

DOT/FAA/AR-96/21

Office of Aviation Research  
Washington, D.C. 20591

# Composite Failure Analysis Handbook Update 1

WL-TR-93-4004

Wright Laboratory  
Air Force Materiel Command  
Wright-Patterson Air Force Base, OH 45433

August 1997

Final Report

DTIC QUALITY INSPECTED 2

19971009 020

This document is available to the U.S. public  
through the National Technical Information  
Service, Springfield, Virginia 22161.



U.S. Department of Transportation  
Federal Aviation Administration




Materials Directorate  
Air Force Materiel Command

## Notice

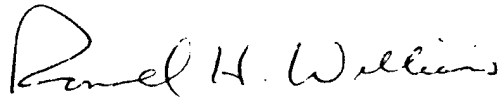
When Government drawings, specifications, or other data are used for any purpose other than in connection with a definitely Government-related procurement, the United States Government incurs no responsibility or any obligation whatsoever. The fact that the government may have formulated or in any way supplied the said drawings, specifications, or other data, is not to be regarded by implication, or otherwise in any manner construed, as licensing the holder, or any other person or corporation; or as conveying any rights or permission to manufacture, use, or sell any patented invention that may in any way be related thereto.

This report is releasable to the National Technical Information Service (NTIS). At NTIS it will be available to the general public including foreign nations.

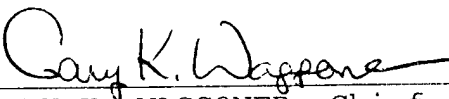
This technical report has been reviewed and is approved for publication.



PATRICIA L. STUMPPFF  
Struct & Elect FA Section  
Materials Integrity Branch  
Systems Support Division  
Materials Directorate



RONALD H. WILLIAMS, Br Chf  
Materials Integrity Branch  
Systems Support Division  
Materials Directorate



GARY K. WAGGONER, Chief  
Systems Support Division  
Materials Directorate

## NOTICE

This document is disseminated under the sponsorship of the U.S. Department of Transportation in the interest of information exchange. The United States Government assumes no liability for the contents or use thereof. The United States Government does not endorse products or manufacturers. Trade or manufacturer's names appear herein solely because they are considered essential to the objective of this report.

1. Report No. DOT/FAA/AR-96/21		2. Government Accession No.		3. Recipient's Catalog No.	
4. Title and Subtitle COMPOSITE FAILURE ANALYSIS HANDBOOK UPDATE 1				5. Report Date August 1997	
				6. Performing Organization Code	
7. Author(s) Greg Walker				8. Performing Organization Report No.	
9. Performing Organization Name and Address Boeing Defense and Space Group Materials, Processes, and Physics Technology P.O. Box 3999 M/S 4H-98 Seattle, WA 98124-2499				10. Work Unit No. (TRAIS)	
				11. Contract or Grant No. C-F33615-86-C-5071 PE-62101 PR-2418 TA-04 WU-47	
12. Sponsoring Agency Name and Address U.S. Department of Transportation Federal Aviation Administration Office of Aviation Research Washington, DC 20591 Wright Laboratory (WL/MLSA/Bldg 652) 2179 Twelfth St., Ste 1 Materials Directorate (AFMC) Wright-Patterson AFB, OH 45433-7718				13. Type of Report and Period Covered Final Report	
				14. Sponsoring Agency Code AAR-431	
15. Supplementary Notes FAA William J. Hughes Technical Center COTR: Donald Oplinger					
16. Abstract <p>This report supplements the data and analyses provided in the previously released "Composite Failure Analysis Handbook," WL-TR-91-4032/DOT/FAA/CT-91/23. It contains fractographic data from failed composite test specimens as well as case histories of failed composite structure.</p> <p>Fractographic data from statically loaded test specimens are presented for carbon/epoxy (AS4/3501-6), carbon/pseudothermoplastic (AS4/KIII), carbon/polyimide (AS4/PMR-15), carbon/thermoplastic (AS4/PEEK), carbon/bismaleimide (AS4/MR-54-4), and carbon and glass low-temperature curing epoxy, (HTA 5131-12K/Rutapox L-20/SL and EC 9-756/K43/Rutapox L-20/SL) materials. Fractographic data are presented for translaminar and interlaminar carbon/resin laminate fatigue specimens, as well as for several failure modes in composite skin nomex honeycomb core specimens. Three failure investigations, including two composite honeycomb structures and one carbon/epoxy laminate structure, are also documented.</p>					
17. Key Words Composites, Composite structures, Failure analysis, Fractography, Adhesive joints, Mechanical joints, Case history studies			18. Distribution Statement This document is available to the public through the National Technical Information Service (NTIS), Springfield, Virginia 22161.		
19. Security Classif. (of this report) Unclassified		20. Security Classif. (of this page) Unclassified		21. No. of Pages 255	22. Price

## FOREWORD

The technical direction for this work was given by Patricia L. Stumpff, Air Force Wright Aeronautical Laboratories, WPAFB, Ohio. Donald F. Sekits was the Boeing program manager, and Gregory M. Walker was the principal investigator.

Additional Boeing people who provided significant contributions to this program included Mike Yamashita, Dr. Russ Crutcher, Linda Nishimura, Dennis Banning, and Steve Barnes.

## TABLE OF CONTENTS

	Page
EXECUTIVE SUMMARY	xv
1. INTRODUCTION	1
1.1 Background	1
1.2 Program Objectives	1
2. TASK 3: EXPANSION OF THE FRACTOGRAPHIC DATABASE	3
2.1 Objective	3
2.2 Approach	3
3. TASK 3: RESULTS	14
3.1 Carbon/Epoxy (3501-6/AS4)	15
3.2 Carbon/Thermoplastic Polyimide (AS4/KIII)	43
3.3 Carbon/Polyimide (AS4/PMR-15)	77
3.4 Carbon/Thermoplastic (AS4/APC-2)	101
3.5 Carbon/Bismaleimide (AS4/MR-54-4)	112
3.6 Fiberglass/Thermoset (EC 9-756-K43/Rutapox L-20/SL)	119
3.7 Carbon/Thermoset (HTA-5131-12K/Rutapox L-20/SL)	137
3.8 Honeycomb Structures (3501-6 Face Sheets/Nomex Honeycomb)	150
4. TASK 6: VERIFICATION OF THE COMPOSITE FAILURE ANALYSIS SYSTEM	184
4.1 Objective	184
4.2 Approach	184
4.3 Reports	184
APPENDICES	
A—SIMPLE ANGLE COMPONENT	
B—METAL CORE HONEYCOMB SANDWICH	
C—GROB AIRCRAFT WING	

## LIST OF FIGURES

Figure	Page
2-1 Specimen Configurations for Expansion of the Fractographic Database	4
2-2 Specimen Configurations for Fatigue and Short-Term Environmental Exposure	5
2-3 Test Plan for Expansion of the Fractographic Database (SOW 4.3.3)	6
2-4 Test Plan for Effects of Fatigue on Fracture Surfaces (SOW 4.3.4)	7
2-5 Test Plan for Short-Term Environmental Exposure (SOW 4.3.5)	8
2-6 Test Plan for Long-Term Environmental Exposure (SOW 4.3.6)	9
2-7 Failure Analysis of Honeycomb Sandwich (SOW 4.3.7)	10
2-8 Cross-Sectional Microscopic Analysis of Composites (SOW 4.3.9)	11
2-9 Fractography of Glass/150°F Cured Epoxy and Carbon/150°F Cured Epoxy (SOW 4.3.10)	12
3.1-1 Optical Fractographs of 3501-6/AS4 Interlaminar Mode II (Shear) Fatigue, Low-Stress Loading, 270°F	17
3.1-2 SEM Fractographs of a 3501-6/AS4 Interlaminar Mode II (Shear) Fatigue Fracture Surface, Low Stress, 270°F	18
3.1-3 Optical Fractographs of 3501-6/AS4 Interlaminar Mode II (Shear) Fatigue, High-Stress Loading, 270°F	19
3.1-4 SEM Fractographs of a 3501-6/AS4 Interlaminar Mode II Fatigue Fracture Surface, High Stress, 270°F	20
3.1-5 Optical Fractographs of a 3501/AS4 Interlaminar Mode I (Tensile) Fatigue Fracture Surface, 270°F	21
3.1-6 SEM Fractographs of a 3501/AS4 Interlaminar Mode I (Tensile) Fatigue Fracture Surface, 270°F	22
3.1-7 Optical Fractographs of 3501-6/AS4 Interlaminar Mode I Tension, Specimen Exposed to Deicing Fluid	23
3.1-8 SEM Fractographs of 3501-6/AS4 Interlaminar Mode I Tension, Specimen Exposed to Deicing Fluid	24
3.1-9 SEM Fractographs of a 3501-6/AS4 ± 45° Tensile Specimen Exposed to Deicing Fluid, Interlaminar Surface	25
3.1-10 SEM Fractographs of a 3501-6/AS4 ± 45° Tensile Specimen Exposed to Deicing Fluid, Translaminar Surface	26
3.1-11 Optical Fractographs of 3501-6/AS4 Interlaminar Mode I Tension Specimen Tested at -20°F (Freezing Condition)	27
3.1-12 Optical Fractographs of 3501-6/AS4 Interlaminar Mode I Tension Specimen Tested at -20°F (Freezing Condition)	28

3.1-13	SEM Fractographs of a 3501-6/AS4 $\pm$ 45° Tensile Specimen Tested at -20°F, Interlaminar Surface	29
3.1-14	SEM Fractographs of a 3501-6/AS4 $\pm$ 45° Tensile Specimen Tested at -20°F, Translaminar Surface	30
3.1-15	Optical Fractographs of 3501-6/AS4 Interlaminar Mode I Tension, Specimen Exposed to UV Radiation	31
3.1-16	SEM Fractographs of 3501-6/AS4 Interlaminar Mode I Tension, Specimen Exposed to UV Radiation	32
3.1-17	SEM Fractographs of a 3501-6/AS4 $\pm$ 45° Tensile Specimen Exposed to UV Radiation, Interlaminar Surface	33
3.1-18	SEM Fractographs of a 3501-6/AS4 $\pm$ 45° Tensile Specimen Exposed to UV Radiation, Translaminar Surface	34
3.1-19	Optical Fractographs of 3501-6/AS4 Interlaminar Mode I (Tension), Specimen Thermally Cycled Prior to Loading	35
3.1-20	SEM Fractographs of a 3501-6/AS4 Interlaminar Mode I Tension Fracture Surface, Thermally Cycled	36
3.1-21	SEM Fractographs of a 3501-6/AS4 $\pm$ 45° Tensile Specimen Thermally Cycled, Interlaminar Surface	37
3.1-22	SEM Fractographs of a 3501-6/AS4 $\pm$ 45° Tensile Specimen Thermally Cycled, Translaminar Surface	38
3.1-23	Optical Fractography of 3501-6/AS4 Interlaminar Mode I Tension Specimen, Moisture/Dryout Cycled	39
3.1-24	SEM Fractographs of a 3501-6/AS4 Interlaminar Mode I Tensile Fracture Surface Tested After Moisture/Dryout Cycling	40
3.1-25	SEM Fractographs of a 3501-6/AS4 $\pm$ 45° Tensile Specimen Tested After Moisture/Dryout Cycling, Interlaminar Surface	41
3.1-26	SEM Fractographs of a 3501-6/AS4 $\pm$ 45° Tensile Specimen Tested After Moisture/Dryout Cycling, Translaminar Surface	42
3.2-1	Optical Fractography of KIII/AS4 Interlaminar Mode I Tension Specimen Tested at RT/Dry	45
3.2-2	SEM Fractographs of a KIII/AS4 Interlaminar Mode I Shear Fracture Surface Tested at RT/Dry	46
3.2-3	Optical Fractography of KIII/AS4 Interlaminar Mode I Tension Specimen Tested at 400°F/Dry	47
3.2-4	SEM Fractographs of a KIII/AS4 Interlaminar Mode I (Tension) Fracture Surface, 400°F	48
3.2-5	Optical Fractography of KIII/AS4 Interlaminar Mode II Shear Specimen Tested at RT/Dry	49
3.2-6	SEM Fractographs of a KIII/AS4 Interlaminar Mode II Shear Fracture Surface	50
3.2-7	Optical Fractography of KIII/AS4 Interlaminar Mode II Shear Specimen Tested at 400°F/Dry	51

3.2-8	SEM Fractographs of a KIII/AS4 Interlaminar Mode II (Shear) Fracture Surface, 400°F	52
3.2-9	SEM Fractographs of a KIII/AS4 N4ptT Specimen, Transverse Fracture Surface, Room Temperature	53
3.2-10	SEM Fractographs of a KIII/AS4 N4ptT Specimen, Interlaminar Surface, Room Temperature	54
3.2-11	Optical Fractographs of a KIII/AS4 Interlaminar Mode I (Tensile) Fatigue Fracture Surface, RT	55
3.2-12	SEM Fractographs of a KIII/AS4 Interlaminar Mode I (Tensile) Fatigue Fracture Surface, RT	56
3.2-13	Optical Fractographs of KIII/AS4 Interlaminar Mode I (Tensile) Fatigue Fracture, 350°F	57
3.2-14	SEM Fractographs of a KIII/AS4 Interlaminar Mode I (Tensile) Fatigue Fracture Surface, 350°F	58
3.2-15	Optical Fractographs of a KIII/AS4 Interlaminar Mode II (Shear) Fatigue, Room Temperature, High Stress	59
3.2-16	SEM Fractographs of a KIII/AS4 Interlaminar Mode II (Shear) Fatigue Fracture Surface, Room Temperature	60
3.2-17	Optical Fractographs of KIII/AS4 Interlaminar Mode II (Shear) Fatigue, 350°F High Stress	61
3.2-18	SEM Fractographs of a KIII/AS4 Interlaminar Mode II (Shear) Fatigue Fracture Surface, 350°F	62
3.2-19	SEM Fractographs of a KIII/AS4 Interlaminar Mode II Shear Fracture Surface Exposed to Hydraulic Fluid for 7 Days	63
3.2-20	SEM Fractographs of a KIII/AS4 Interlaminar Mode II Shear Fracture Surface Exposed to JP4 Jet Fuel for 7 Days	64
3.2-21	SEM Fractographs of a KIII/AS4 Interlaminar Mode II Shear Fracture Surface Exposed to Ultrasonic Agitation in Distilled Water for 24 Hours	65
3.2-22	SEM Fractographs of a KIII/AS4 Interlaminar Mode II Shear Fracture Surface Exposed to MEK for 24 Hours	66
3.2-23	SEM Fractographs of a KIII/AS4 Interlaminar Mode II Shear Fracture Surface Exposed to Acetone for 24 Hours	67
3.2-24	SEM Fractographs of a KIII/AS4 Interlaminar Mode II Shear Fracture Surface Exposed to Soap Solution for 24 Hours	68
3.2-25	SEM Fractographs of a KIII/AS4 Interlaminar Mode II Shear Fracture Surface Exposed to Fire Retardant Foam for 7 Days	69
3.2-26	SEM Fractographs of a KIII/AS4 Interlaminar Mode I Tension Fracture Surface Exposed to Hydraulic Fluid for 7 Days	70
3.2-27	SEM Fractographs of a KIII/AS4 Interlaminar Mode I Tension Fracture Surface Exposed to JP4 Jet Fuel for 7 Days	71
3.2-28	SEM Fractographs of a KIII/AS4 Interlaminar Mode I Tension Fracture Surface Exposed to Ultrasonic Agitation in Distilled Water for 24 Hours	72



3.2-29	SEM Fractographs of a KIII/AS4 Interlaminar Mode I Tension Fracture Surface Exposed to MEK for 24 Hours	73
3.2-30	SEM Fractographs of a KIII/AS4 Interlaminar Mode I Tension Fracture Surface Exposed to Acetone for 24 Hours	74
3.2-31	SEM Fractographs of a KIII/AS4 Interlaminar Mode I Tension Fracture Surface Exposed to Soap Solution for 24 Hours	75
3.2-32	SEM Fractographs of a KIII/AS4 Interlaminar Mode I Tension Fracture Surface Exposed to Fire Retardant Foam for 7 Days	76
3.3-1	SEM Fractographs of a PMR-15/AS4 Interlaminar Mode I Tension Fracture Surface, RT/Dry	79
3.3-2	High-Magnification SEM Fractographs of a PMR-15/AS4 Interlaminar Mode I Tension Fatigue Fracture Surface, RT/Dry	80
3.3-3	Optical Fractographs of PMR-15/AS4 Interlaminar Mode I (Tensile) Fatigue Fracture Surface, 350°F	81
3.3-4	SEM Fractographs of a PMR-15/AS4 Interlaminar Mode I (Tensile) Fatigue Fracture Surface, 350°F	82
3.3-5	Optical Fractographs of PMR-15/AS4 Interlaminar Mode II (Shear) Fatigue, Room Temperature, High Stress	83
3.3-6	SEM Fractographs of a PMR-15/AS4 Interlaminar Mode II (Shear) Fatigue Fracture Surface, Room Temperature	84
3.3-7	Optical Fractographs of PMR-15/AS4 Interlaminar Mode II (Shear) Fatigue, 350°F, High Stress	85
3.3-8	SEM Fractographs of a PMR-15/AS4 Interlaminar Mode II (Shear) Fatigue Fracture Surface, 350°F	86
3.3-9	SEM Fractographs of a PMR-15/AS4 Interlaminar Mode I Tension Fracture Surface Exposed to JP4 Jet Fuel for 7 Days	87
3.3-10	SEM Fractographs of a PMR-15/AS4 Interlaminar Mode I Tension Fracture Surface Exposed to Ultrasonic Agitation in Distilled Water for 24 Hours	88
3.3-11	SEM Fractographs of a PMR-15/AS4 Interlaminar Mode I Tension Fracture Surface Exposed to MEK for 24 Hours	89
3.3-12	SEM Fractographs of a PMR-15/AS4 Interlaminar Mode I Tension Fracture Surface Exposed to Hydraulic Fluid for 7 Days	90
3.3-13	SEM Fractographs of a PMR-15/AS4 Interlaminar Mode I Tension Fracture Surface Exposed to Acetone for 24 Hours	91
3.3-14	SEM Fractographs of a PMR-15/AS4 Interlaminar Mode I Tension Fracture Surface Exposed to Soap Solution for 24 Hours	92
3.3-15	SEM Fractographs of a PMR-15/AS4 Interlaminar Mode I Tension Fracture Surface Exposed to Fire Retardant Foam for 7 Days	93

3.3-16	SEM Fractographs of a PMR-15/AS4 Interlaminar Mode II Shear Fracture Surface Exposed to JP4 Jet Fuel for 7 Days	94
3.3-17	SEM Fractographs of a PMR-15/AS4 Interlaminar Mode II Shear Fracture Surface Exposed to Ultrasonic Agitation in Distilled Water for 24 Hours	95
3.3-18	SEM Fractographs of a PMR-15/AS4 Interlaminar Mode II Shear Fracture Surface Exposed to MEK for 24 Hours	96
3.3-19	SEM Fractographs of a PMR-15/AS4 Interlaminar Mode II Shear Fracture Surface Exposed to Hydraulic Fluid for 7 Days	97
3.3-20	SEM Fractographs of a PMR-15/AS4 Interlaminar Mode II Shear Fracture Surface Exposed to Acetone for 24 Hours	98
3.3-21	SEM Fractographs of a PMR-15/AS4 Interlaminar Mode II Shear Fracture Surface Exposed to Soap Solution for 24 Hours	99
3.3-22	SEM Fractographs of a PMR-15/AS4 Interlaminar Mode II Shear Fracture Surface Exposed to Fire Retardant Foam for 7 Days	100
3.4-1	Optical Fractographs of PEEK/AS4 Interlaminar Mode II (Shear) Fatigue, Room Temperature, High Stress	102
3.4-2	SEM Fractographs of a PEEK/AS4 Interlaminar Mode II (Shear) Fatigue Fracture Surface, Room Temperature	103
3.4-3	Optical Fractographs of an APC-2/AS4 Interlaminar Mode II (Shear) Fatigue Fracture Surface, 250°F	104
3.4-4	SEM Fractographs of an APC-2/AS4 Interlaminar Mode II (Shear) Fatigue Fracture Surface, 250°F	105
3.4-5	Optical Fractographs of an APC-2/AS4 Interlaminar Mode I (Tensile) Fatigue Fracture Surface, RT	106
3.4-6	SEM Fractographs of an APC-2/AS4 Interlaminar Mode I (Tensile) Fatigue Fracture Surface, RT	107
3.4-7	Optical Fractographs of an APC-2/AS4 Interlaminar Mode I (Tensile) Fatigue Fracture Surface, 250°F	108
3.4-8	SEM Fractographs of an APC-2/AS4 Interlaminar Mode I (Tensile) Fatigue Fracture Surface, 250°F	109
3.4-9	SEM Fractographs of a PEEK/AS4 Interlaminar Mode I Tension Fracture Surface Exposed to MEK for 24 Hours	110
3.4-10	SEM Fractographs of a PEEK/AS4 Interlaminar Mode II Shear Fracture Surface Exposed to MEK for 24 Hours	111
3.5-1	Optical Fractographs of BMI/AS4 Interlaminar Mode I Tension Specimen Tested at RT/Dry	113
3.5-2	SEM Fractographs of an AS4/BMI Interlaminar Mode I Tension Specimen Tested at RT/Dry	114

3.5-3	Optical Fractographs of BMI/AS4 Interlaminar Mode II Shear Specimen Tested at RT/Dry	115
3.5-4	SEM Fractographs of an AS4/BMI Interlaminar Mode II Shear Specimen Tested at RT/Dry	116
3.5-5	SEM Fractographs of an AS4/BMI Translaminar Tension RT/Dry Fracture	117
3.5-6	Macro photographs of BMI/AS4 Translaminar Tension Specimen Tested at 450°F/Dry	118
3.6-1	Optical Fractographs of a Rutapox/FG Fabric Interlaminar Mode I (Tensile) Fracture Surface, RT	121
3.6-2	SEM Fractographs of a Rutapox/FG Fabric Interlaminar Mode I (Tensile) Fracture Surface, RT	122
3.6-3	Optical Fractographs of a Rutapox/FG Fabric Interlaminar Mode I (Tensile) High-Rate Fracture Surface, RT	123
3.6-4	SEM Fractographs of a Rutapox/FG Fabric Interlaminar Mode I (Tensile) High-Rate Fracture Surface, RT	124
3.6-5	SEM Fractographs of a Rutapox/FG Fabric Interlaminar Mode II (Shear) Fracture Surface, RT	125
3.6-6	SEM Fractographs of a Rutapox/FG Fabric Interlaminar Mode II (Shear) Hot/Wet Fracture Surface, RT	126
3.6-7	SEM Fractographs of a Rutapox/FG Fabric $\pm 45^\circ$ Tensile Fracture Surface, RT	127
3.6-8	SEM Fractographs of a Rutapox/FG Rovings $\pm 45^\circ$ Tensile Fracture Surface, RT	128
3.6-9	SEM Fractographs of a Rutapox/FG Fabric Open Hole Tension Fracture Surface, RT	129
3.6-10	SEM Fractographs of a Rutapox/FG Rovings Open Hole Compression Fracture Surface, RT	130
3.6-11	SEM Fractographs of a Rutapox/FG Roving 4ptNT Specimen Fracture Surface, RT	131
3.6-12	SEM Fractographs of a Rutapox/FG Roving 4ptNT Fracture Surface, Hot/Wet	132
3.6-13	SEM Fractographs of a Rutapox/FG Fabric Interlaminar Mode I (Tensile) Fracture Surface Exposed to JP4 Jet Fuel for 7 Days	133
3.6-14	SEM Fractographs of a Rutapox/FG Fabric Interlaminar Mode I (Tensile) Fracture Surface Exposed to Acetone for 7 Days	134
3.6-15	SEM Fractographs of a Rutapox/FG Fabric Interlaminar Mode I (Tensile) Fracture Surface Exposed to MEK for 7 Days	136
3.6-16	SEM Fractographs of a Rutapox/FG Fabric Interlaminar Mode I (Tensile) Fracture Surface Exposed to Hydraulic Fluid for 7 Days	137
3.7-1	Optical Fractographs of a Rutapox/Graphite Fabric Interlaminar Mode I (Tensile) Fracture Surface, RT	139
3.7-2	SEM Fractographs of a Rutapox/Graphite Fabric Interlaminar Mode I (Tensile) Fracture Surface, RT	140
3.7-3	Optical Fractographs of a Rutapox/Graphite Fabric Interlaminar Mode I (Tensile) High-Rate Fracture Surface, RT	141

3.7-4	SEM Fractographs of a Rutapox/Graphite Fabric Interlaminar Mode I (Tensile) High-Rate Fracture Surface, RT	142
3.7-5	SEM Fractographs of a Rutapox/Graphite Fabric Interlaminar Mode II (Shear) Fracture Surface, RT	143
3.7-6	SEM Fractographs of a Rutapox/Graphite Fabric Interlaminar Mode II (Shear) Hot/Wet Fracture Surface, RT	144
3.7-7	SEM Fractographs of a Rutapox/Graphite Roving 4ptNT Fracture Surface, Hot/Wet	145
3.7-8	SEM Fractographs of a Rutapox/Graphite Roving 4ptNT Fracture Surface, RT	146
3.7-9	SEM Fractographs of a Rutapox/Graphite Fabric $\pm 45^\circ$ Tensile Fracture Surface, RT	147
3.7-10	SEM Fractographs of a Rutapox/Graphite Fabric Open Hole Tension Fracture Surface, RT	148
3.7-11	SEM Fractographs of a Rutapox/Graphite Rovings Open Hole Compression Fracture Surface, RT	149
3.8-1	Fibers Torn and Bent in the Direction of the Propagation of the Failure	153
3.8-2	Orientation of the Continuous Ribbons in the Honeycomb Denoting the Ribbon Direction and the Associated Meniscus Set	153
3.8-3	Trilobate Resin Structure at the Ribbon Juncture Forming a Pair of Menisci or a Meniscus Set	153
3.8-4	Failure Patterns in the Resin Menisci Indicating the Propagation Directions	154
3.8-5	The Failure Front Doesn't Travel as a Straight Line and May, for Short Distances, Change Direction	154
3.8-6	The Wallner Line Pattern for a Failure Propagating Normal to the Ribbon Direction	155
3.8-7	The Wallner Line Pattern for a Failure Propagating Inward From Both Sides Indicating a Vertical or Twisting Failure	155
3.8-8	Failure Type for Mode I Honeycomb Sandwich Failures	156
3.8-9	Optical Fractographs of Mode I Sandwich, Control Specimen	157
3.8-10	Optical Fractographs of Mode I Sandwich, Aged Adhesive Specimen	159
3.8-11	Optical Fractographs of Mode I Sandwich, Stronger Core Used (8-lb) Specimen	161
3.8-12	Optical Fractographs of Mode I Sandwich Specimen, Undercured Adhesive	163
3.8-13	Optical Fractographs of Mode I Sandwich Specimen, Undercured Face Sheet	165
3.8-14	Illustration of the Position of the Two Photographs and Four Drawings of Each Sample	167
3.8-15	Linear Distribution of the Three Crack Modes Near the Honeycomb/Adhesive/Carbon Fiber Composite Interface and the Amount of Cracking Through the Honeycomb	168
3.8-16	Control Sample 1—2.4X Reduction	169

3.8-17	Control Sample 2—2.4X Reduction	170
3.8-18	Control Sample 3—2.4X Reduction	171
3.8-19	Aged Adhesive Sample 6A1—2.4X Reduction	172
3.8-20	Aged Adhesive Sample 6A2—2.4X Reduction	173
3.8-21	Aged Adhesive Sample 6A3—2.4X Reduction	174
3.8-22	Improper Core Sample 7A1—2.4X Reduction	175
3.8-23	Improper Core Sample 7A2—2.4X Reduction	176
3.8-24	Improper Core Sample 7A3—2.4X Reduction	177
3.8-25	Undercured Adhesive Sample 8A1—2.4X Reduction	178
3.8-26	Undercured Adhesive Sample 8A2—2.4X Reduction	179
3.8-27	Undercured Adhesive Sample 8A3—2.4X Reduction	180
3.8-28	Undercured Face Sheet Sample 9A1—2.4X Reduction	181
3.8-29	Undercured Face Sheet Sample 9A2—2.4X Reduction	182
3.8-30	Undercured Face Sheet Sample 9A3—2.4X Reduction	183

## EXECUTIVE SUMMARY

This document is a first revision of the Composite Failure Analysis Handbook, dated February 1992, which was issued jointly by the Air Force and the FAA under report numbers WL-TR-91-4032 and DOT/FAA/CT-91/23, respectively.

The Composite Failure Analysis Handbook was developed to meet an obvious need on the part of accident investigators for key information on the failure characteristics of organic matrix fiber reinforced composites undergoing failure due to structural loading. The scope of the Handbook included:

- Failure analysis logic networks
- Guidelines for data gathering and handling techniques for field representatives
- Fractographic techniques for composite failure analysis
- Data base on fractographic characteristics of composite material failures
- Description of case studies illustrating the validity of the failure analysis system presented in the Handbook

In addition to carbon-, aramid-, boron-, and glass-reinforced epoxies, the fractographic data base of the Handbook dealt with carbon reinforced polyimide, bismaleimide, and thermoplastic material systems. Both static and fatigue loaded specimens were considered for in-plane loading parallel ("translaminar") and normal ("intralaminar") to the fibers as well as out-of-plane ("interlaminar") loading and in-plane shear loading. Effects of environment on the failure characteristics presented included those of elevated temperature and humidity.

Subsequent to the initiation of effort leading to development of the Handbook it became apparent that information in addition to what had been planned for the first release of the Handbook was desirable, as a result of which the present document was developed. In addition to providing for an expansion of the fractographic database, additional case studies are provided. In particular, new fractographic results are provided both on material types previously considered (AS4/3501-6 carbon epoxy and AS4/APC-2 carbon thermoplastic) and on a number of additional carbon reinforced organic matrix materials (AS4/KIII carbon reinforced thermoplastic polyimide, C3K8-HS/PMR-15 versus the AS4/PMR-14 carbon polyimide considered in the first release, and AS4-5250-3 versus the AS4/MR-54-4 carbon bismaleimide of the first release). In addition, carbon and glass reinforced forms of the 150°F curing German resin "Rutapox" L-20/SL encountered in the European aircraft industry were characterized. This present Update 1 also provides characterization results not available previously on honeycomb reinforced sandwich materials containing carbon epoxy skins.

In addition to new composite material systems, characterization results are provided for additional loading modes, including open hole compression and tension. Results are also provided for structural fatigue exposures of the new materials, as well as for the carbon epoxy materials previously considered for elevated temperature environments. New results on environmental degradation effects of JP4 jet fuel, hydraulic fluid, and other potentially degrading substances encountered in the aircraft service environment are presented.

New case studies aimed at verifying the failure analysis procedures provided by the Handbook include an assessment of a failed aircraft wing component and evaluation of failure processes in a honeycomb sandwich specimen and a simple angle component.

## SECTION 1 INTRODUCTION

### 1.1 Background

With increasing use of carbon-fiber-reinforced plastics for structural applications, a handbook was needed that would assist in analyzing failed structural components. To address this concern, a number of contracts were initiated by the Air Force and the FAA to develop such a document, which ultimately resulted in the initial publication of a composite failure analysis handbook. This handbook included all of the essential information and procedures needed to thoroughly analyze a composite structural component failure. However, because of continual developments in composite materials technology and their applications, it is necessary for the handbook to be a "living document" and to be updated routinely.

### 1.2 Program Objectives

WRDC Contract F33615-85-C-5010, "Post Failure Analysis Compendium for Composite Structures," was one of the contracts that provided information for the publication of the handbook. As an expansion to this contract, another contract (F33615-86-C-5071, "Composite Failure Analysis Handbook") was awarded that consisted of the following tasks:

- Task 1:           Development of Handling and Data Gathering Techniques for Field Representatives
  
- Task 2:           Expansion of Fractographic Techniques in Composite Failure Analysis
  
- Task 3:           Expansion of the Fractographic Database
  
- Task 4:           Development of Data Formats
  
- Task 5:           Documentation of Material Properties
  
- Task 6:           Verification of the Composite Failure Analysis System (by performing a demonstration on two structural test items)
  
- Task 7:           Documentation

- Task 8: Administrative Management

- Task 9: Meetings

Tasks 1, 2, 4, and 5 were completed under the original contract, with the results of this work having been presented in the final interim report. Tasks 3, 6, and 7 were expanded as an add-on contract to the original contract (F33615-86-C-5071). This report summarizes the work done as a part of the add-on contract to these tasks.



## SECTION 2

### TASK 3: EXPANSION OF THE FRACTOGRAPHIC DATABASE

#### 2.1 Objective

The objective for this task was to provide additional fractographic information for the existing database. The task included examining material systems that have been previously studied but tested under different conditions, which were not covered under the original SOW. In addition, other composite material systems not previously examined were studied: a thermoset epoxy from Germany (Rutapox) using both fiberglass and carbon reinforcing fibers, a toughened thermoset (BMI/AS4), a pseudothermoplastic (KIII/AS4), and a thermoplastic (LARC-TPI/AS4).

#### 2.2 Approach

The overall approach to the fractographic database expansion followed a sequence that involved purchasing the materials, fabricating test panels and specimens, testing the specimens according to an Air Force-approved test matrix, and documenting the fracture surfaces.

Purchasing the materials was essentially routine, except for the LARC-TPI and the Rutapox materials. The major problem with LARC-TPI is in achieving uniform wetting of the fibers with the resin matrix material. This was attempted twice by Mitsui Toatsu Chemicals. In both cases, they failed to produce a uniform prepreg material for subsequent fabrication. Because this program was not a development project, further work on this material was stopped. The other material that was difficult to purchase was the Rutapox resin. A number of difficulties were encountered in the purchasing procedure because the material was from a foreign source (Germany) for a U.S. Air Force program. Consequently, there was a long delay in receiving the material.

Fabrication of the panels and specimens was also routine based on the standard processing parameters of the materials. Figures 2-1 and 2-2 show the types of specimens used to obtain the variety of fracture modes. All material was ordered in prepreg form, except for the Rutapox materials. Since this material is used primarily with fiberglass and carbon fiber fabrics, no prepreg forms were available. Consequently, it was initially proposed that a prepreg form, using the resin and fiberglass or carbon tows, would be made at Boeing and used to fabricate the panel. However, after further investigation, that was determined to be unfeasible. It was then decided to lay up most of the panels using the fabric material. A few of the panels would still require a hand layup using the tows so as to produce a pure translamellar fracture.

Except for the LARC-TPI material, testing, with several modifications as noted, was performed according to the proposed test matrix, shown in Figures 2-3 through 2-9. These tests were designed to provide a number of different fracture modes from which the fractography would be documented. Because most of the tests and specimens were considered to be standard, very few problems were encountered. Most of the problems appeared during fatigue testing, specifically the open hole tension and compression tests. The fatigue tests were limited by the number of cycles due to financial and schedule constraints. As a result, the open hole tension (OHT) and open hole compression

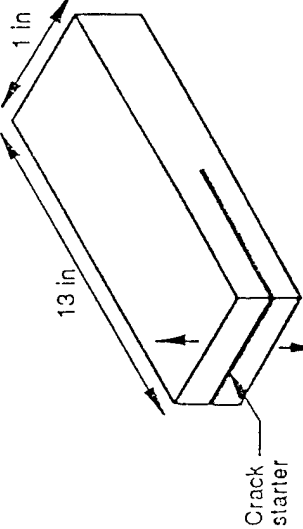
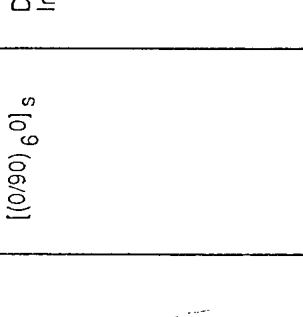
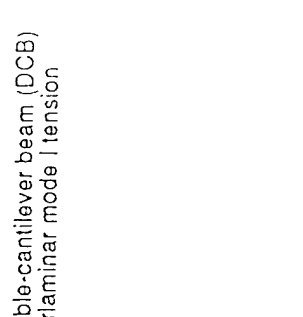
Specimen types	Specimen geometry	Ply layup	Test and fracture type
1		$[(0/90)_{\bar{6}}\bar{0}]_s$	Double-cantilever beam (DCB) Interlaminar mode I tension
2		$[(0/90)_{\bar{6}}\bar{0}]_s$	End-notched flexure (ENF) Interlaminar mode II shear
3		(0/90) 8s	Notched four-point tension (N4ptT) Translaminar tension

Figure 2-1. Specimen Configurations for Expansion of the Fractographic Database

Specimen types	Specimen geometry	Ply layup	Test and fracture type
4		(0) <sub>26</sub>	Double cantilever beam (DCB) Interlaminar Mode I tension
5		(0) <sub>26</sub>	End-notched flexure (ENF) Interlaminar Mode II shear
6		(0/90) <sub>4S</sub>	Open hole tension (OHT) Translaminar tension
7		(0) <sub>16</sub>	Open hole compression (OHC) Translaminar compression
8		(±45) <sub>2S</sub>	±45 deg tensile test ±45 deg inplane shear

Figure 2-2. Specimen Configurations for Fatigue and Short-Term Environmental Exposure

Material system	Specimen types	Environments at fracture	Number of specimens		Comments
			Per test	Total	
<b>Thermoplastics</b>					
<ul style="list-style-type: none"> <li>T-800/LARC-TPI Carbon/polyimide</li> <li>AS4/KIII Carbon/Avimid (R) KIII</li> </ul>	1, 2	RT/dry, 450°F/dry	3	12	Notched four-point compression not tested due to post-failure damage of the carbon fibers.
	3	RT/dry, 450°F/dry	3	6	
	1, 2	RT/dry, 400°F/dry	3	12	
	3	RT/dry, 400°F/dry	3	6	
<b>Thermosets</b>					
<ul style="list-style-type: none"> <li>AS4/BMI Carbon/bismaleimide</li> <li>Carbon/150°F curing epoxy</li> <li>Glass/150°F curing epoxy</li> </ul>	1, 2	RT/dry, 450°F/dry	3	12	Same as above.
	3	RT/dry, 450°F/dry	3	6	
	1, 2	RT/dry, elevated temperature/wet	3	12	
	3	RT/dry, elevated temperature/wet	3	6	
	1, 2	RT/dry, elevated temperature/wet	3	12	
	3	RT/dry, elevated temperature/wet	3	6	

Figure 2-3. Test Plan for Expansion of the Fractographic Database (SOW 4.3.3)

Material system	Specimen type	Environments at fracture	Stress levels (at RT)	Number of specimens	
				Per test	Total
3501-6/AS4	4, 5, 6, 7	RT/dry* and 270°F/dry	High and low	3	36
PMR-15/AS4	4, 5, 6, 7	RT/dry and 450°F/dry	High	3	24
KIII/AS4	4, 5, 6, 7	RT/dry and 400°F/dry	High	3	24
PEEK/AS4	4, 5, 6, 7	RT/dry and 350°F/dry	High	6	24

\* For RT/dry specimen type 6 and 7 only (RT/dry specimen type 4 and 5 were tested under C-5010 contract)

Figure 2-4. Test Plan for Effects of Fatigue on Fracture Surfaces (SOW 4.3.4)

Material system	Test specimen type (type 1 and 2)	Post-fracture exposure/exposure time, in days						
		JP4 fuel	Hydraulic fluid	Fire retardant foam	NOX soap	Acetone	Methylethylketone	Ultrasonic cleaning
<b>Thermosets</b>								
AS4/PMR-15	Interlaminar Mode I tension (DCB) and Mode II shear (ENF)	7	7	7	1	1	1	1
Glass/epoxy	Interlaminar Mode I tension (DCB) and Mode II shear (ENF)	7	7	7	1	1	1	1
<b>Thermoplastics</b>								
AS4/PEEK	Interlaminar Mode I tension (DCB) and Mode II shear (ENF)	7	7	7	1	1	1	1
AS4/KIII	Interlaminar Mode I tension (DCB) and Mode II shear (ENF)	7	7	7	1	1	1	1

Figure 2-5. Test Plan for Short-Term Environmental Exposure (SOW 4.3.5)

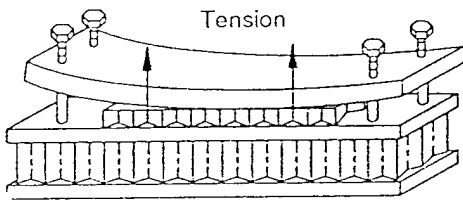
SS9130/O/180-90

Material system	Environmental conditioning	Specimen type, configuration and lay-up	Number of specimens	
			Per test	Total
AS4/3501-6 carbon/350°F cured epoxy	Deicing fluid	<ul style="list-style-type: none"> <li>• Tensile test</li> </ul>	3	6
	Freezing		3	6
	Rain erosion	<ul style="list-style-type: none"> <li>• Double cantilever beam</li> </ul>	3	6
	UV radiation		3	6
	Thermal cycling	3	6	
	Moisture/dryout cycles	3	6	

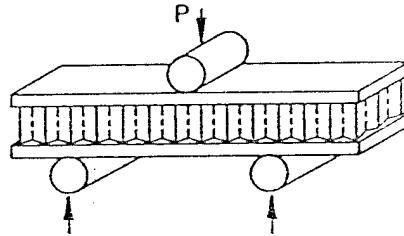
Figure 2-6. Test Plan for Long-Term Environmental Exposure (SOW 4.3.6)

Material system	Parameter	Specimen type		No. of specimens		Comments
		SCB	BS	Per test	Total	
AS4/3501-6 face sheets and Nomex honeycomb cores	Environmental <ul style="list-style-type: none"> <li>Control specimen</li> <li>Humidity</li> <li>Fluid</li> </ul>	X	X	3	6	RT/dry Humidity chamber at elevated temperature Immerse specimen before test
		X	X	3	6	
		X	X	3	6	
	Loading during exposure <ul style="list-style-type: none"> <li>Creep</li> <li>Fatigue</li> </ul>	X	X	3	6	Apply and maintain load Cyclic axial loading
		X	X	3	6	
	Processing anomaly <ul style="list-style-type: none"> <li>Aged adhesive</li> <li>Undercured adhesive</li> <li>Undercured face sheet</li> <li>Improper core selection</li> </ul>	X	X	3	6	Overaged adhesive Undercured adhesive Undercured composite face sheet Core density, core cell type
		X	X	3	6	
		X	X	3	6	
		X	X	3	6	

Specimen configuration:



Single cantilever beam (SCB)  
Mode I sandwich test



Bending shear (BS)  
Mode II sandwich test

Figure 2-7. Failure Analysis of Honeycomb Sandwich (SOW 4.3.7)

C0019-08.01 L7220 D4ai



Material system	Optical microscopy			
	Undamage	Impact	Fatigue	Thermal cycling
AS4/3501-6 Carbon/350°F cured epoxy	✓	✓	✓	✓
1581/F155 S-glass/250°F cured epoxy; fabric style 181-150	✓	✓		
Kevlar 49/F155 Kevlar/250°F cured epoxy; fabric style 285	✓	✓		
IM7/8551-7 Carbon/toughened epoxy	✓	✓		
4/5505 Boron/350°F cured epoxy	✓	✓		
Rütapox L20-SL Glass/150°F cured epoxy	✓		✓	
Rütapox L20-SL Carbon/150°F cured epoxy	✓		✓	
AS4/PEEK Carbon/thermoplastic	✓	✓		
C-3000/PMR-15 Carbon/high temperature thermoset; 8H satin	✓	✓		
AS4/KIII Carbon/pseudothermoplastic	✓			

Figure 2-8. Cross-Sectional Microscopic Analysis of Composites (SOW 4.3.9)

Material system	Parameters	Specimen type	Environment at failure	Number of specimens	
				Per test	Total
Carbon/150°F cured epoxy and glass/150°F cured epoxy	Static	6, 7, 8	RT/dry	3	18
	Fatigue	4, 5, 6, 7	RT/dry	3	24
	Creep	4, 5	RT/dry	3	12
	High rate load	4, 5	RT/dry	3	12

Figure 2-9. Fractography of Glass/150°F Cured Epoxy and Carbon/150°F Cured Epoxy (SOW 4.3.10)

(OHC) specimens did not exhibit the desired amount of damage to effectively document a transverse fatigue fracture surface. The rest of the fatigue specimens were cycled enough to produce an adequate fracture surface for documentation.

Fractographic documentation was done following testing of the specimens using optical and scanning electron microscopy. An exception was the work done to document the fractures and damage in the tested honeycomb specimens. For the single cantilevered beam specimen, the fractured honeycomb material and resin meniscus regions were examined. The three-point bending shear specimens could only be analyzed initially by external observation, such as the deformation of the face sheets and the honeycomb side of the specimens. Other techniques were used to further document the honeycomb core damage, however they were unable to provide satisfactory results.

**SECTION 3**  
**TASK 3: RESULTS**

**SECTION 3.1**  
**CARBON/EPOXY**  
**3501-6/AS4**

**3.1.1 Introduction**

This section presents the results of additional fractography performed on AS4/3501-6 graphite/thermoset (Gr/Ep) test coupons. This material system is used in many aerospace applications and is considered a "baseline" thermoset composite system. Consequently, this system has been studied extensively to make the most complete fractographic database as a baseline for the other composite system.

The additional fractography includes examination of interlaminar fracture coupons that were subjected to fatigue loading at high- and low-stress levels, both at room temperature and 270°F (dry). Also, a number of interlaminar and translaminar coupons were subjected to different long-term environmental exposures then statically tested.

**3.1.2 Fatigue**

**Interlaminar Mode II (Shear) High and Low Stress Levels, RT and 270°F/Dry**

The typical mode II crack propagation features were easily identified on the surfaces of both specimens. In addition, indications of fatigue loading, in the form of fatigue crack growth increments or striations, were visible on the low-stressed specimen. They were observed only on the exposed fibers at the high optical and SEM magnifications. Even though the high-stressed fracture surface was thoroughly examined, no striations were found. Figures 3.1-1 through 3.1-4 show optical and SEM fractographs of interlaminar mode II fatigue at high and low stress levels.

**Interlaminar Mode I (Tensile) Low Stress Level, 270°F/Dry**

The mode I crack propagation features were not easily seen on the fracture surfaces (Figures 3.1-5 & 3.1-6) unlike a typical static load fracture surface. There were more features indicative of mode II (shear), such as hackles, throughout the surfaces. But these corresponded to the fiber pullout fractures than the overall crack propagation. Neither did these features generally indicate the overall crack propagation direction.

**3.1.3 Long-Term Environmental Exposure**

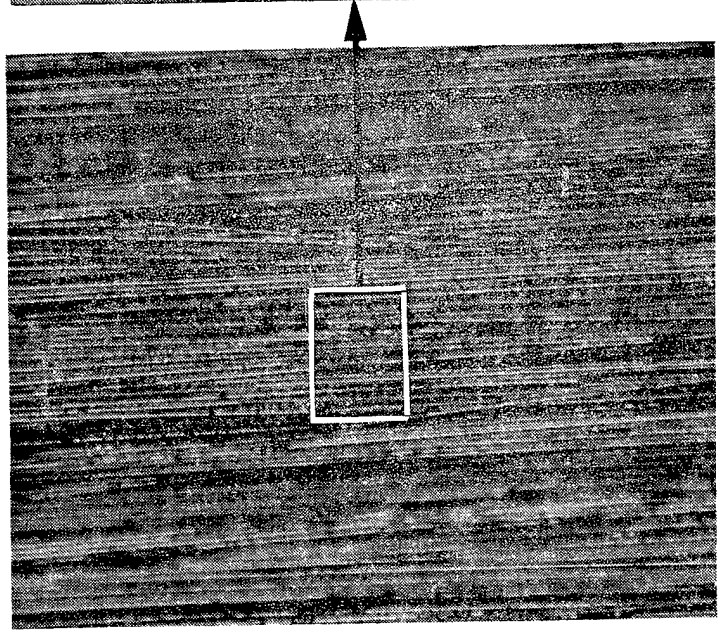
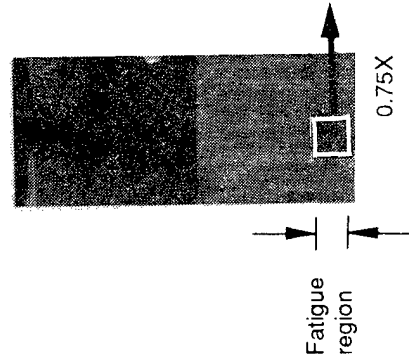
Interlaminar mode I and translaminar ( $\pm 45^\circ$  tensile) specimens (Figures 3.1-7 - 3.1-26) were exposed to the following environmental conditions:

- Soaking in deicing fluid for 14 days
- Freezing the specimens at -20°F for 14 days
- Exposure to UV radiation per MIL-STD-810

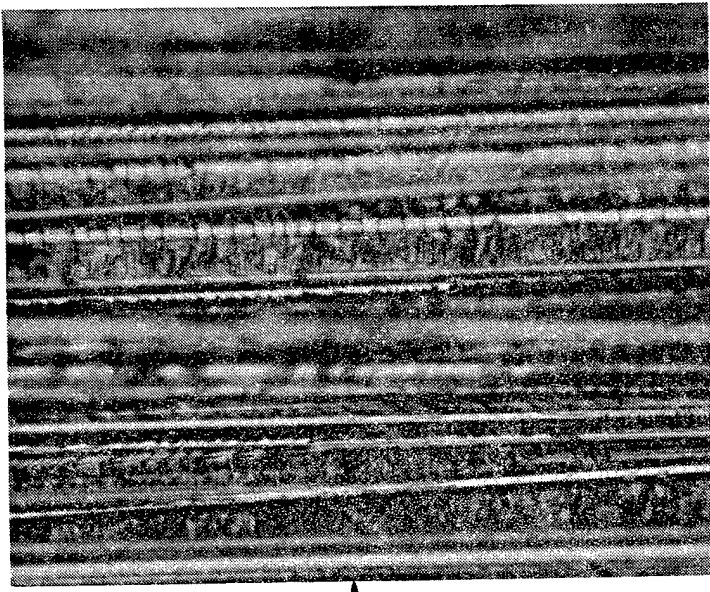
- Thermal cycling between -65° F and 140°F for 2000 cycles
- Moisture - Dryout cycling for 4 monthly periods

Following the exposures, the specimens were then tested and examined. Fractographic analysis of the surface morphologies revealed no abnormal or unusual surface features on any of the specimens.

Crack growth direction  
↓



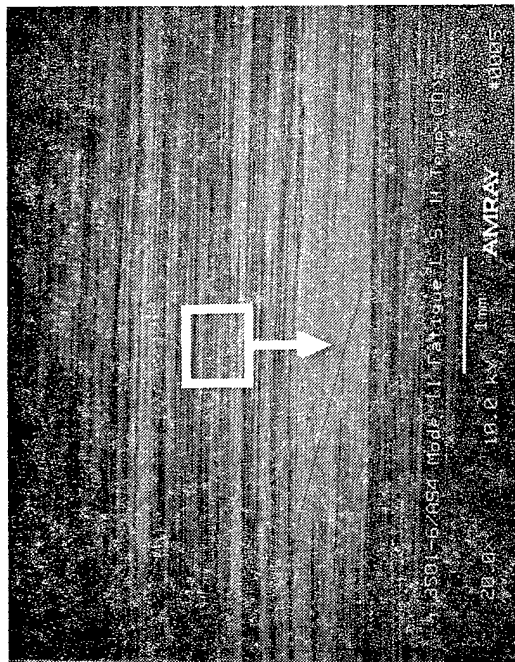
100X



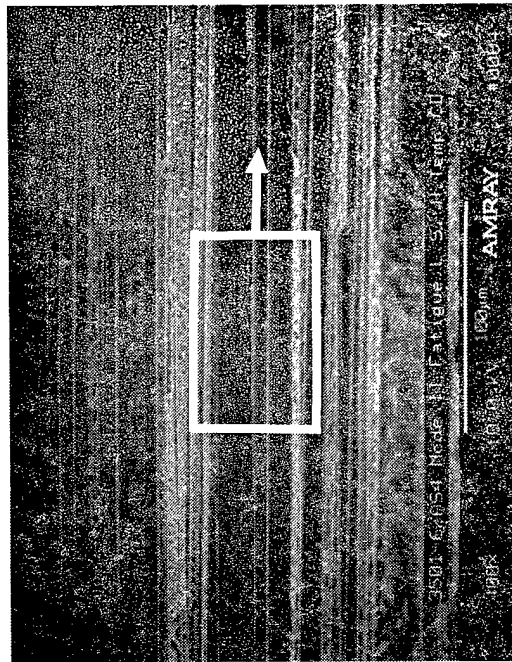
400X

Figure 3.1-1. Optical Fractographs of 3501-6/AS4 Interlaminar Mode II (Shear) Fatigue, Low Stress Loading, 270°F

49754.14 9-5571 D8 fh

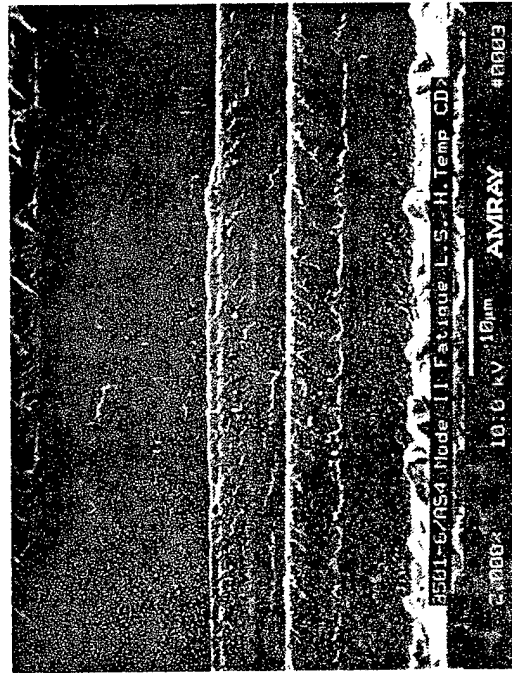


60 degree tilt (a) 20X



60 degree tilt (b) 400X

Mechanically induced crack direction



60 degree tilt (c) 2000X

Figure 3.1-2. SEM Fractographs of a 3501-6/AS4 Interlaminar Mode II (Shear) Fatigue Fracture Surface, Low Stress, 270°F



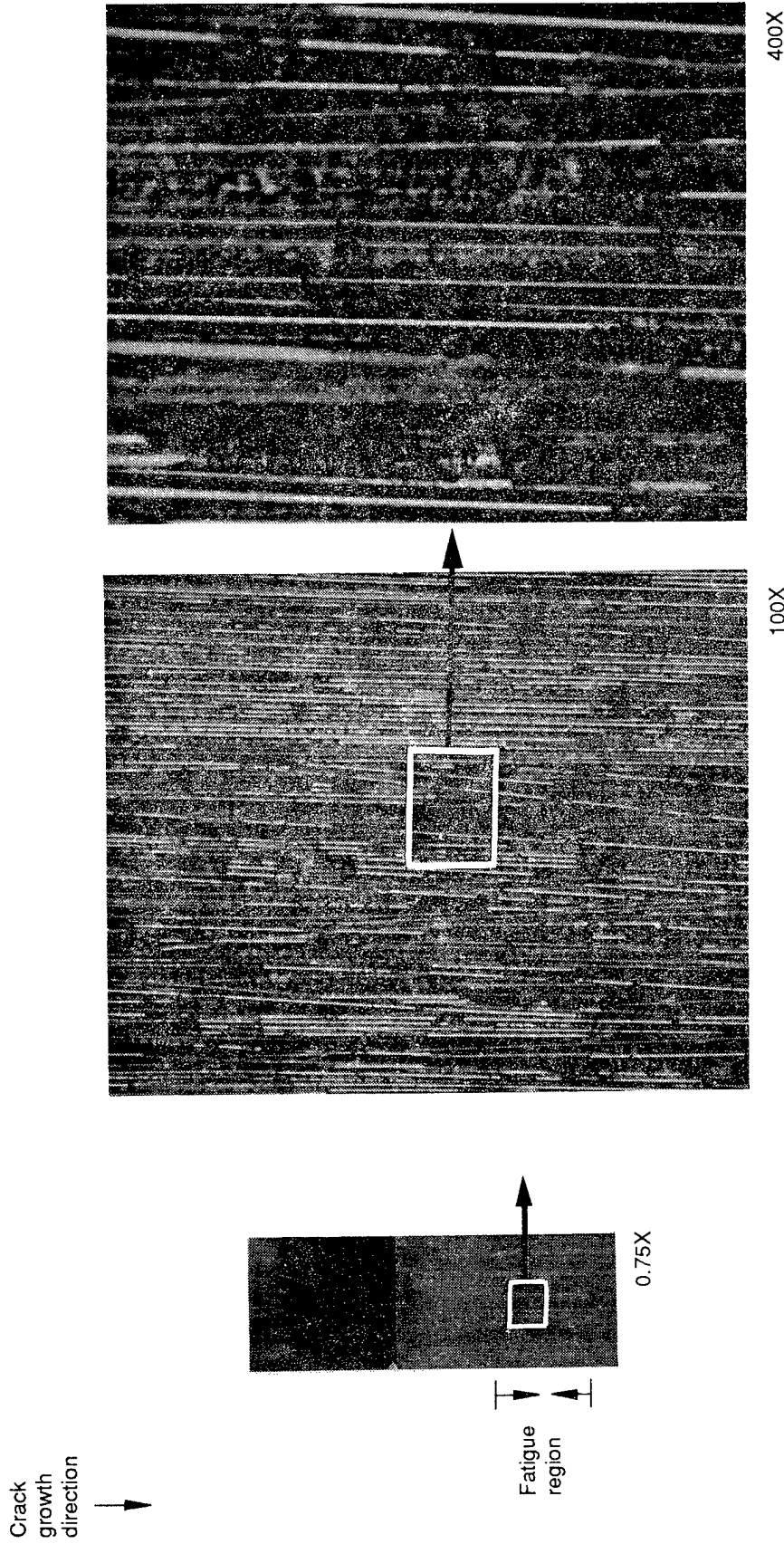
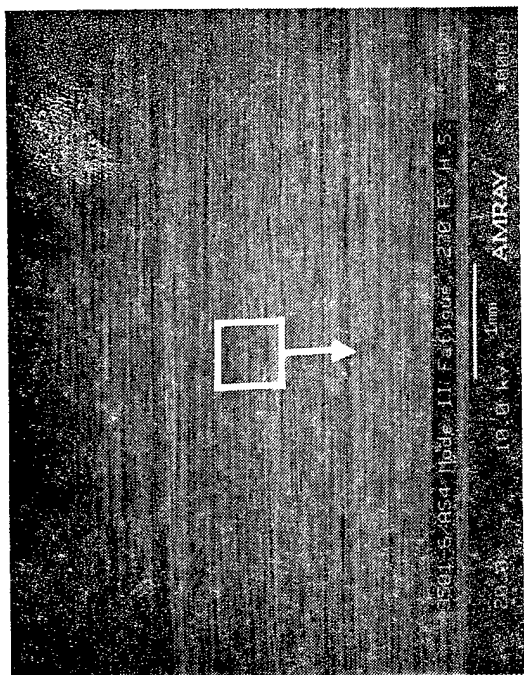


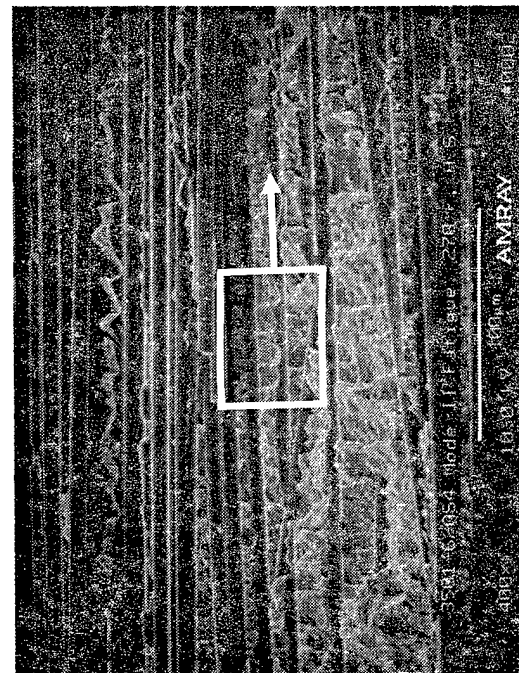
Figure 3.1-3. Optical Fractographs of 3501-6/AS4 Interlaminar Mode II (Shear) Fatigue, High-Stress Loading, 270°F

49754.15 9-5571 D8 fh

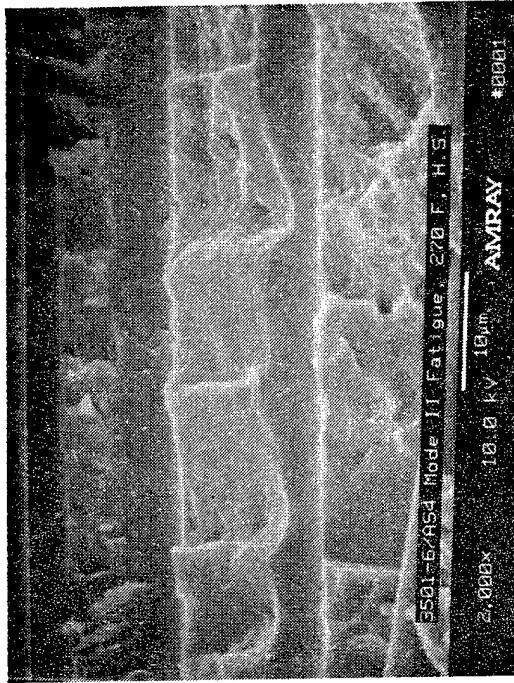


60 degree tilt (a) 20X

Mechanically induced  
crack direction →



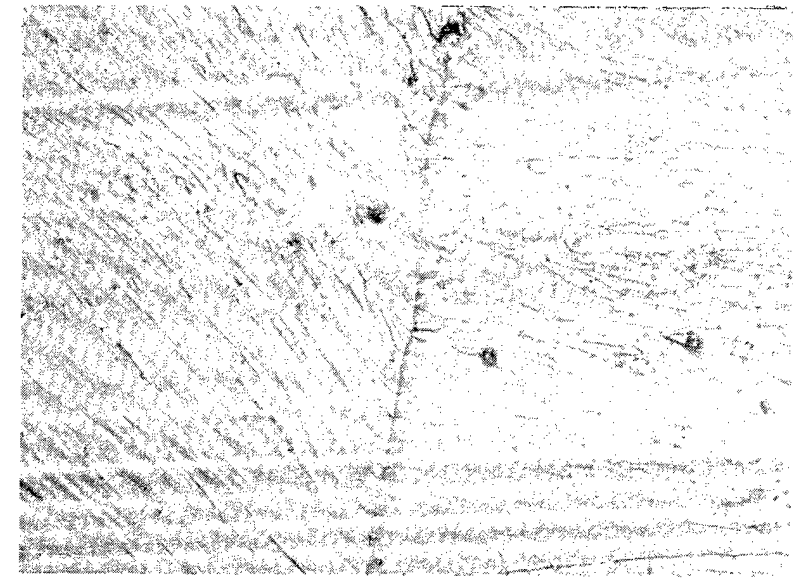
60 degree tilt (b) 400X



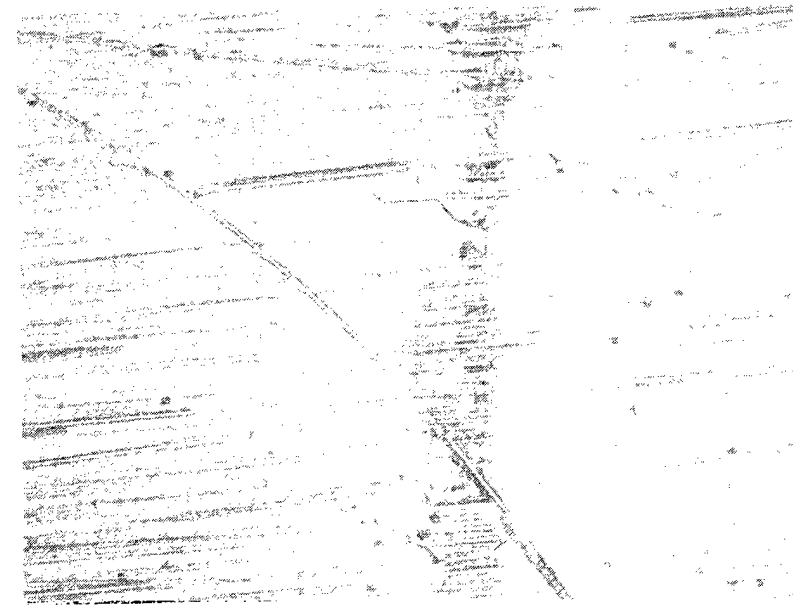
60 degree tilt (c) 2000X

Figure 3.1-4. SEM Fractographs of a 3501-6/AS4 Interlaminar Mode II Fatigue Fracture Surface, High Stress, 270°F

2405.09 9-5576 D1ai



400X



100X



0.44X

Figure 3.1-5. Optical Fractographs of a 3501/AS4 Interlaminar Mode I (Tensile) Fatigue Fracture Surface, 270° F

Mechanically Induced  
Crack Direction

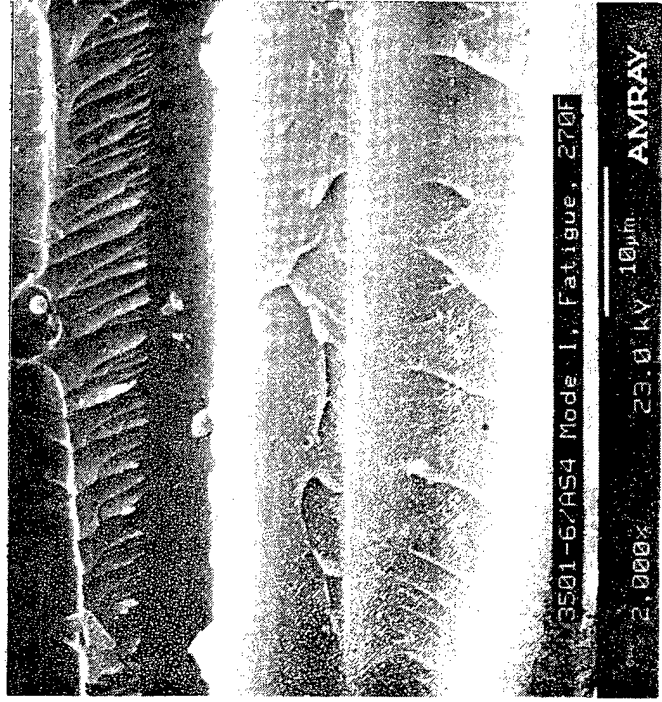
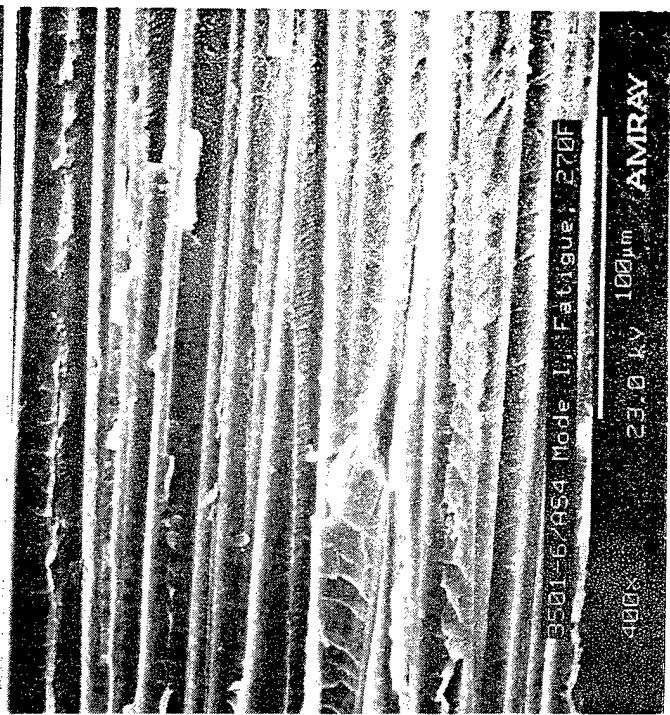
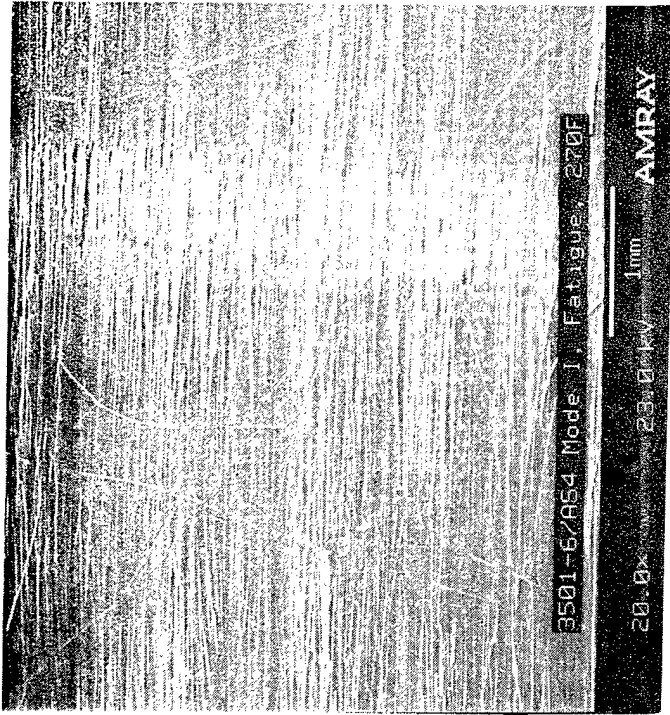
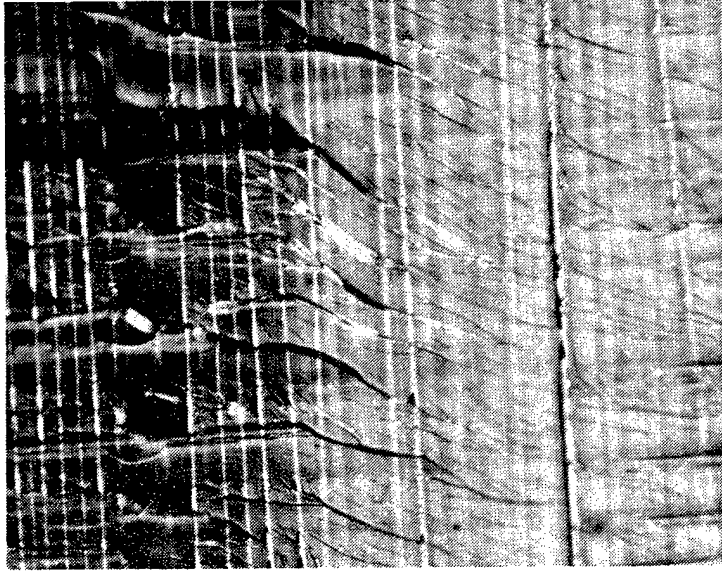
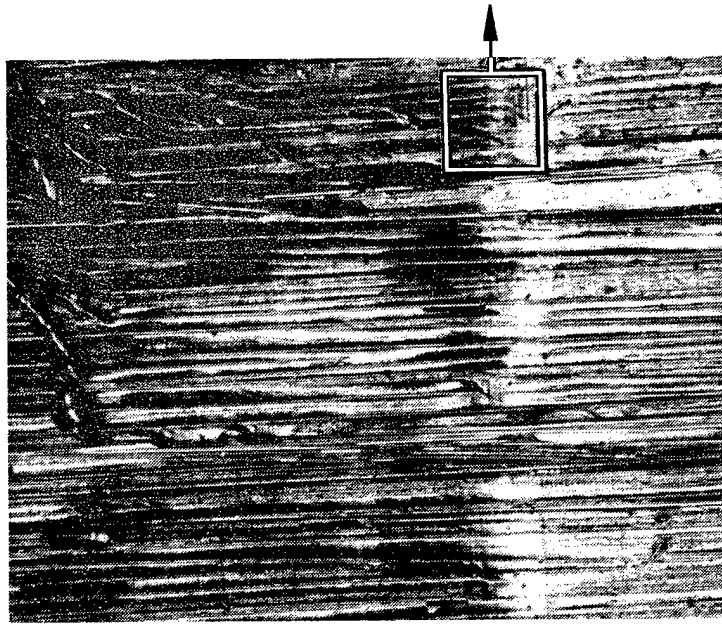


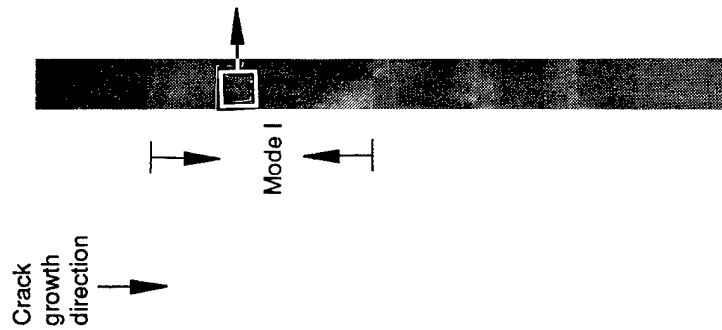
Figure 3.1-6. SEM Fractographs of a 3501/AS4 Interlaminar Mode I (Tensile) Fatigue Fracture Surface, 270° F



400 X

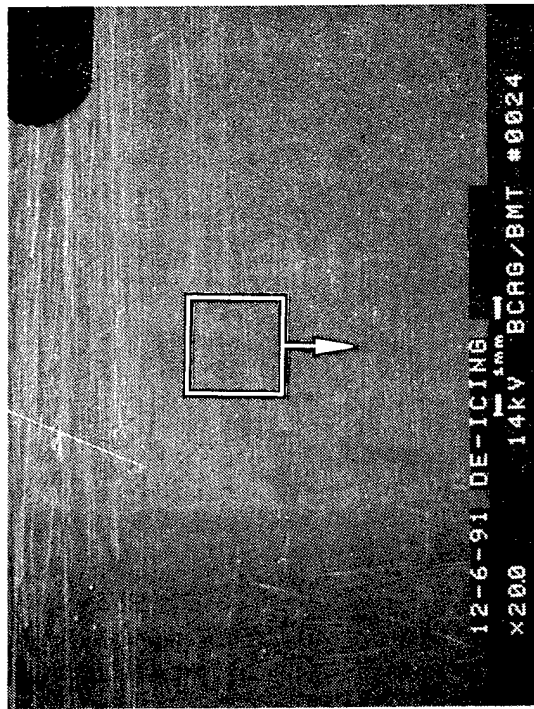


100 X



0.28 X

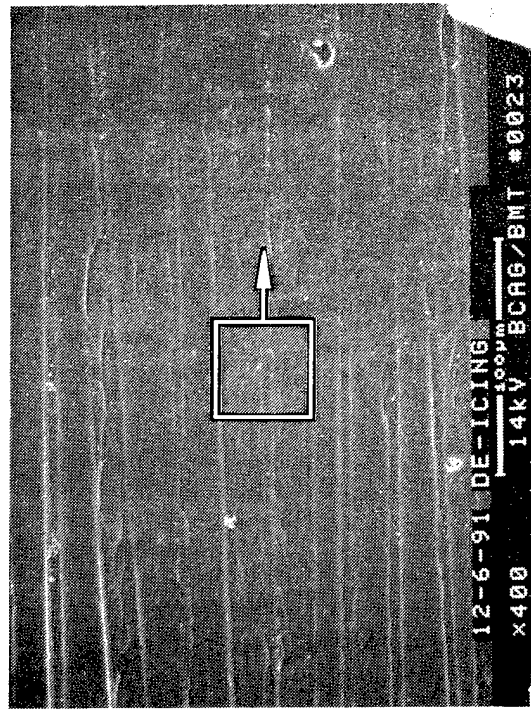
Figure 3.1-7. Optical Fractographs of 3501-6/AS4 Interlaminar Mode I Tension, Specimen Exposed to Deicing Fluid



30-degree tilt

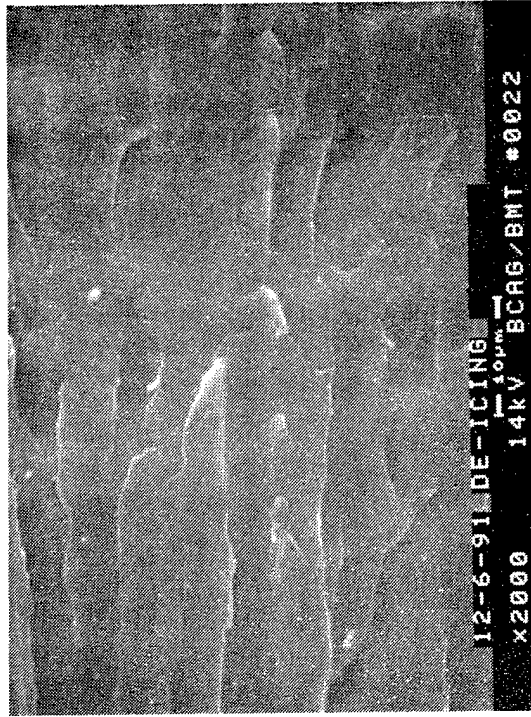
20 X

Mechanically induced  
crack direction



30-degree tilt

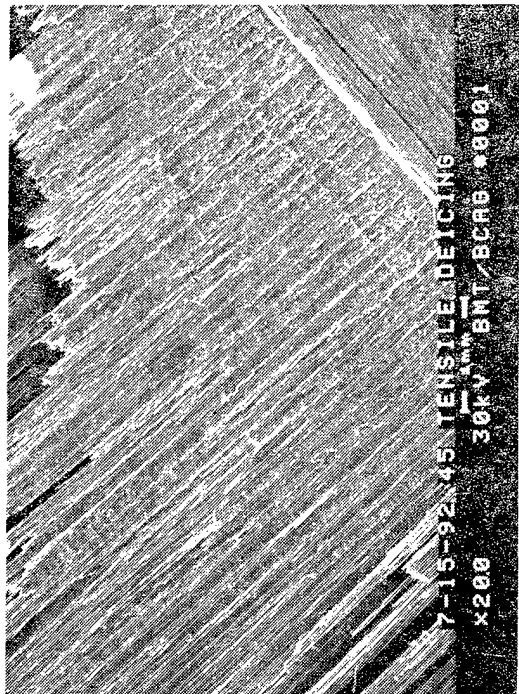
400 X



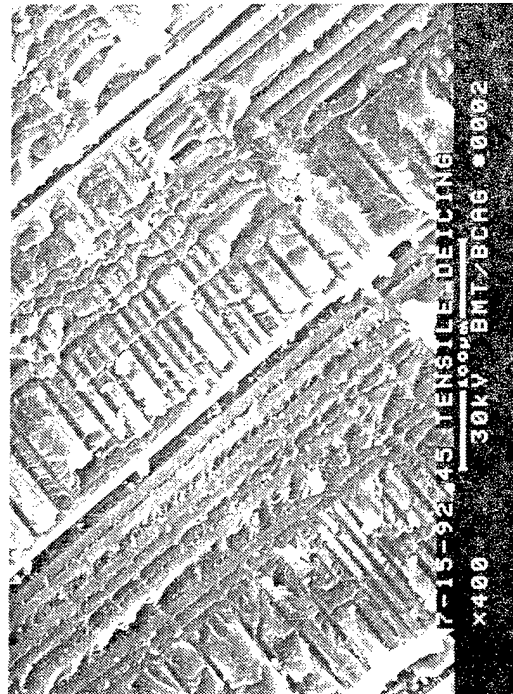
30-degree tilt

2,000 X

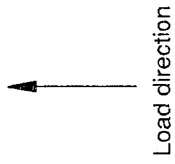
Figure 3.1-8. SEM Fractographs of 3501-6/AS4 Interlaminar Mode I Tension, Specimen Exposed to Deicing Fluid



60 degree tilt (a) 20X



60 degree tilt (b) 400X



60 degree tilt (c) 2000X

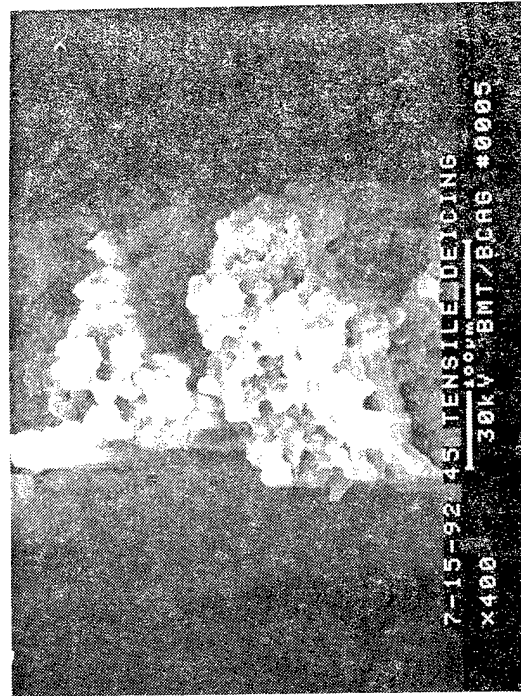
Figure 3.1-9. SEM Fractographs of a 3501-6/AS4 ± 45 Tensile Specimen Exposed to Deicing Fluid, Interlaminar Surface

49754.32 9-5571 D1 ai



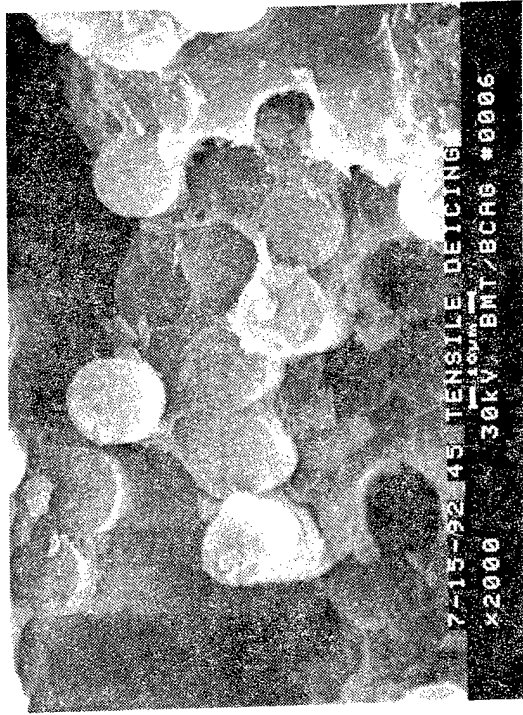
20X

(a)



400X

(b)



2000X

(c)

Figure 3.1-10. SEM Fractographs of a 3501-6/AS4 ± 45 Tensile Specimen Exposed to Deicing Fluid, Translaminar Surface

49754.33 9-5571 D1 ai



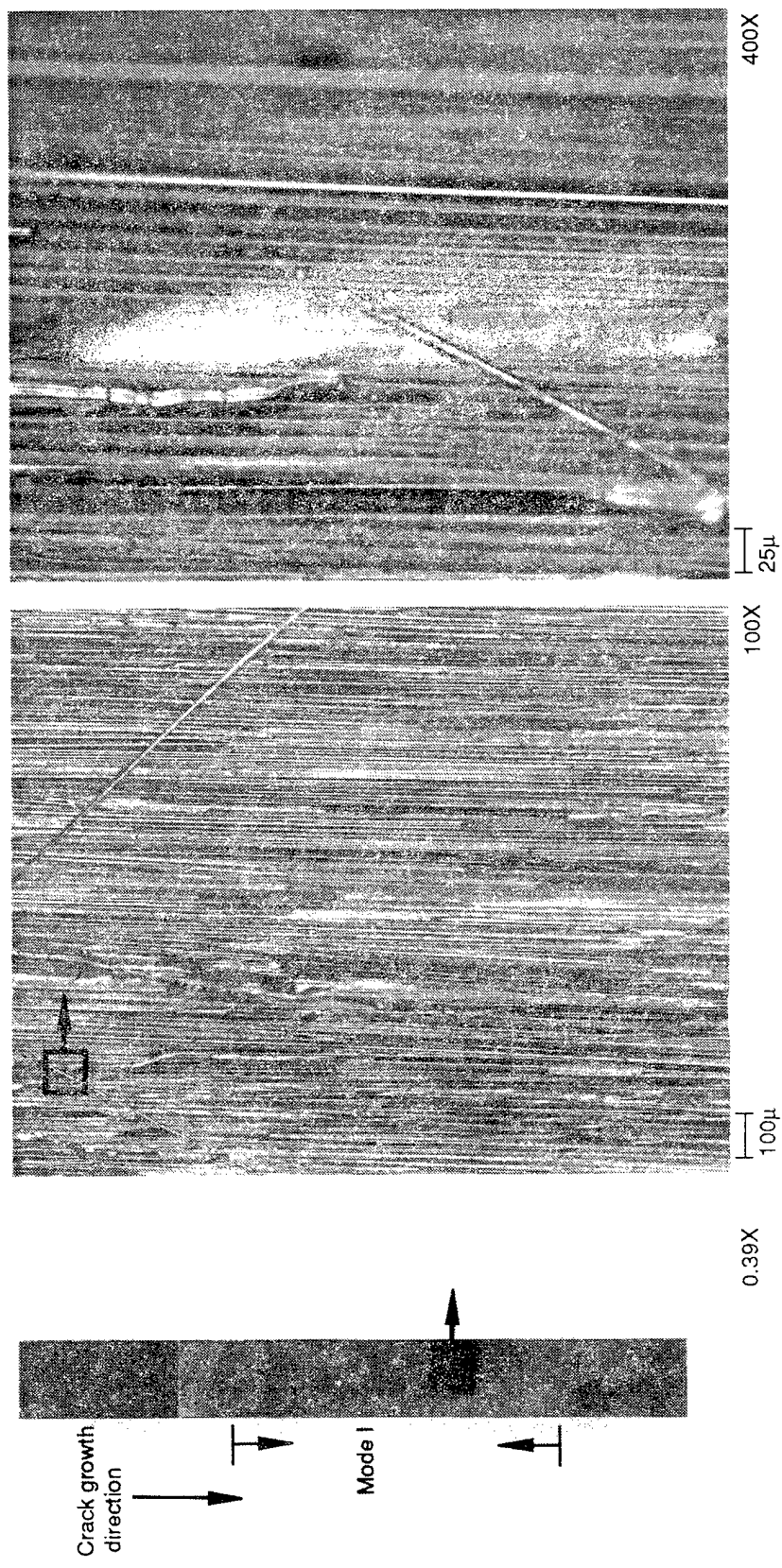


Figure 3.1-11. Optical Fractographs of 3501-6/AS4 Interlaminar Mode I Tension Specimen Tested at -20°F (Freezing Condition)

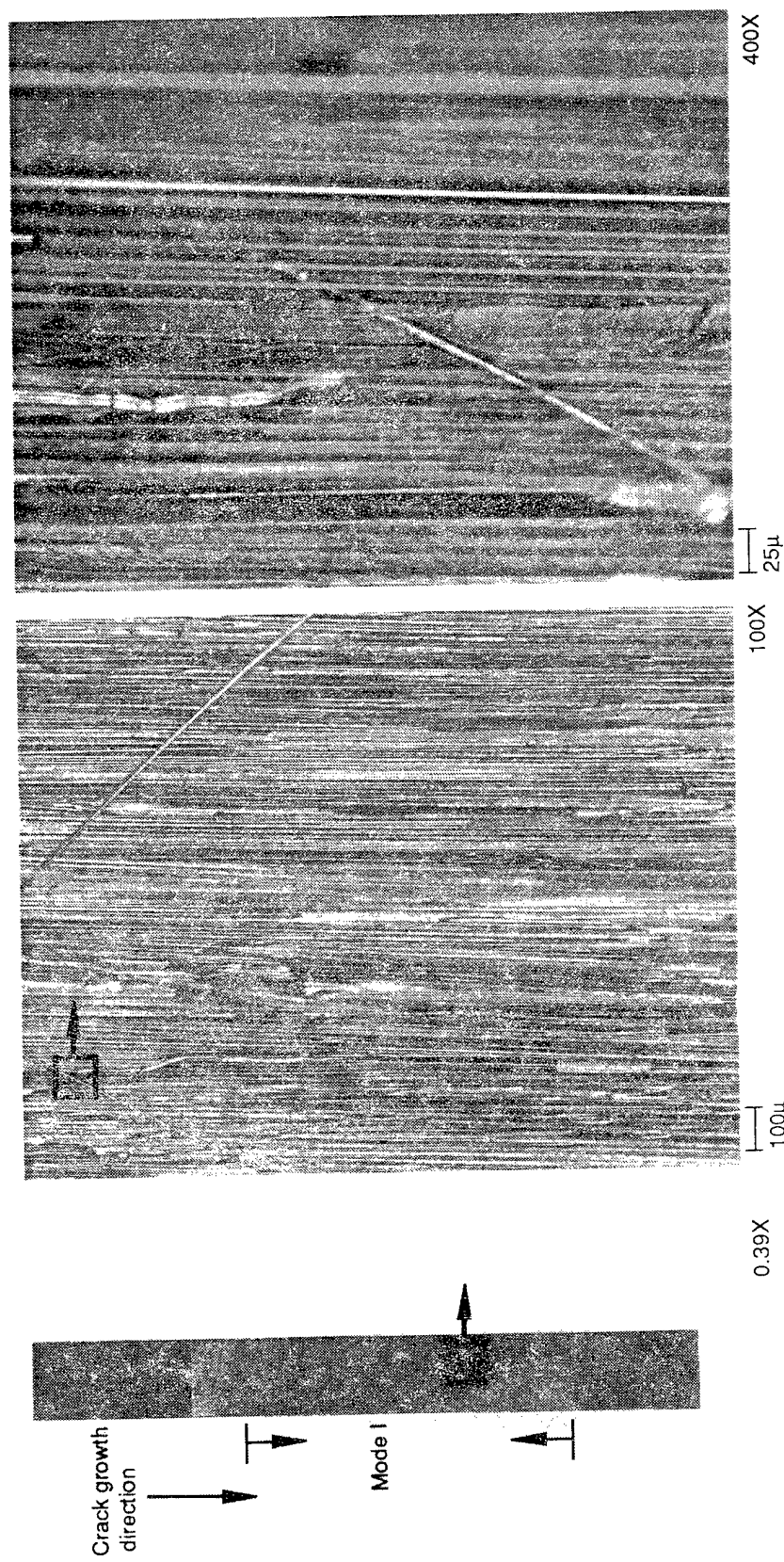


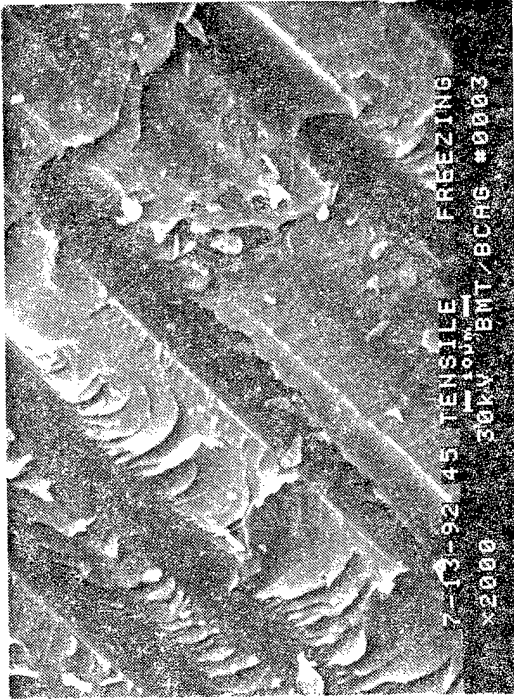
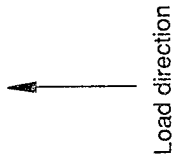
Figure 3.1-12. Optical Fractographs of 3501-6/AS4 Interlaminar Mode I Tension Specimen Tested at -20°F (Freezing Condition)



(a) 20X



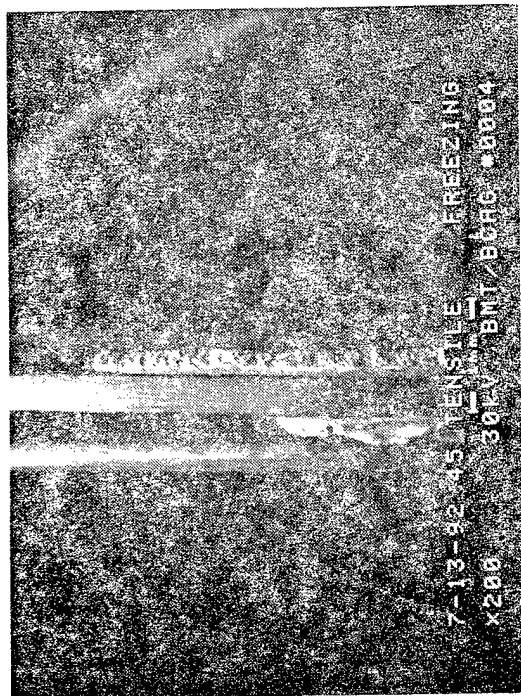
(b) 400X



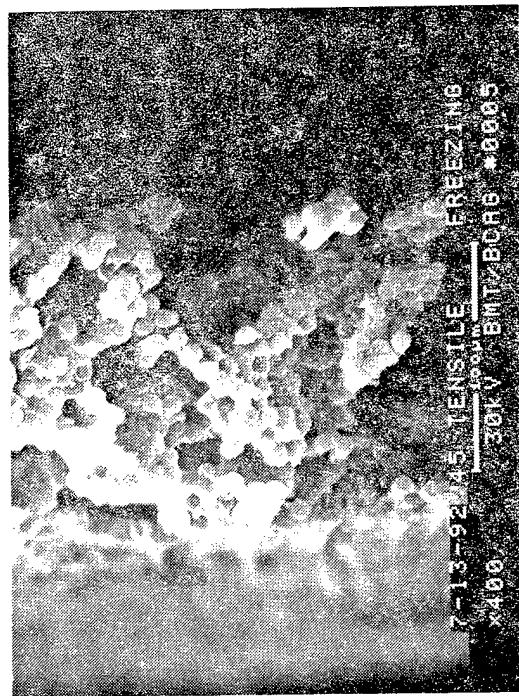
(c) 2000X

Figure 3.1-13. SEM Fractographs of a 3501-6/AS4 ± 45 Tensile Specimen Tested at -20° F, Interlaminar Surface

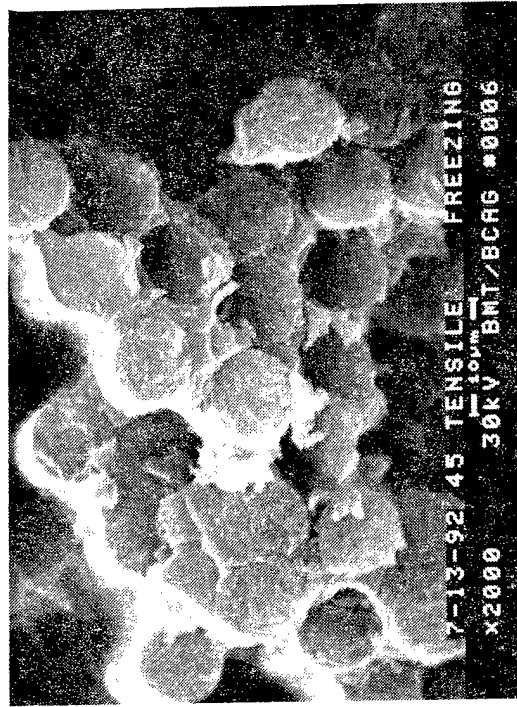
49754.36 9-5571 D1 ai



(a) 20X



(b) 400X



(c) 2000X

Figure 3.1-14. SEM Fractographs of a 3501-6/AS4 ± 45 Tensile Specimen Tested at -20° F, Translaminar Surface

49754.37 9-5571 D1 ai

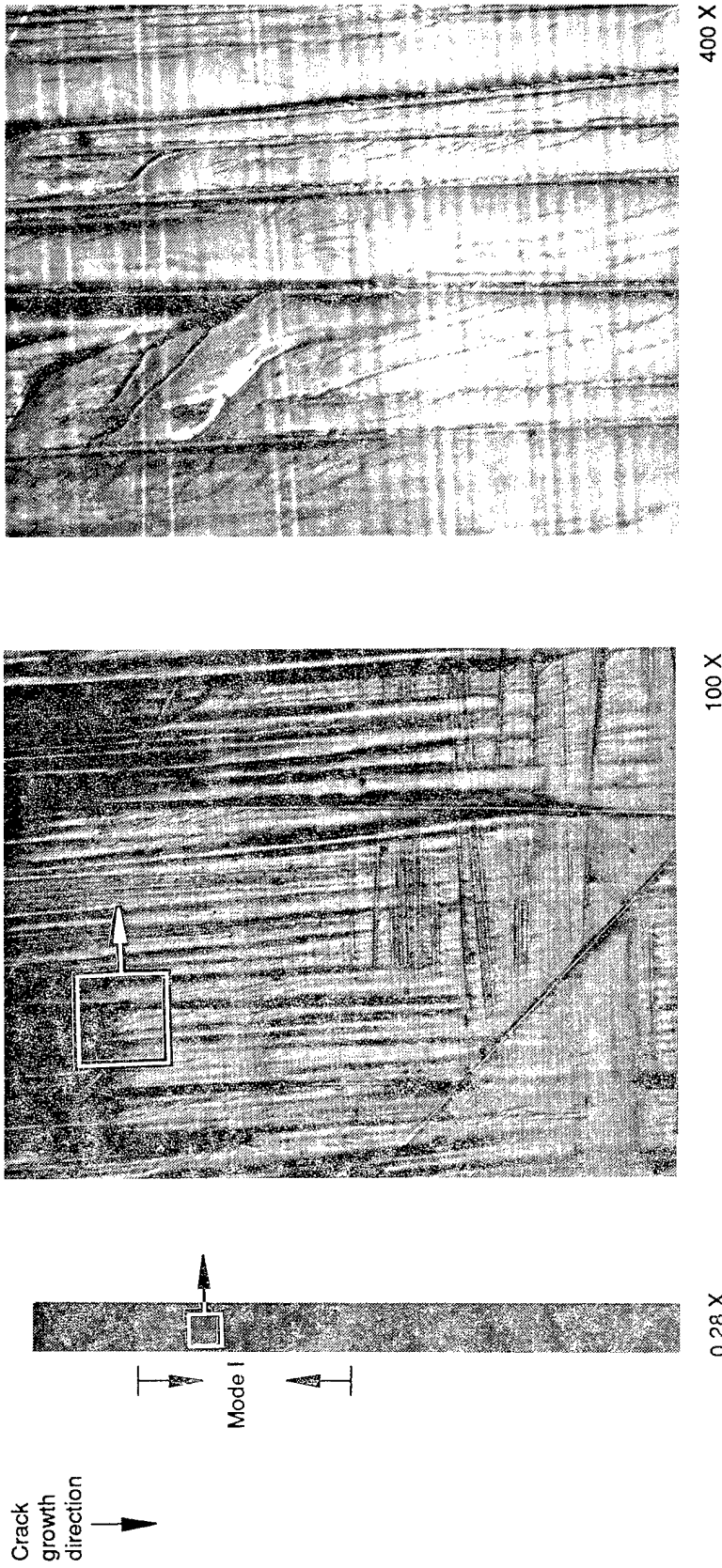
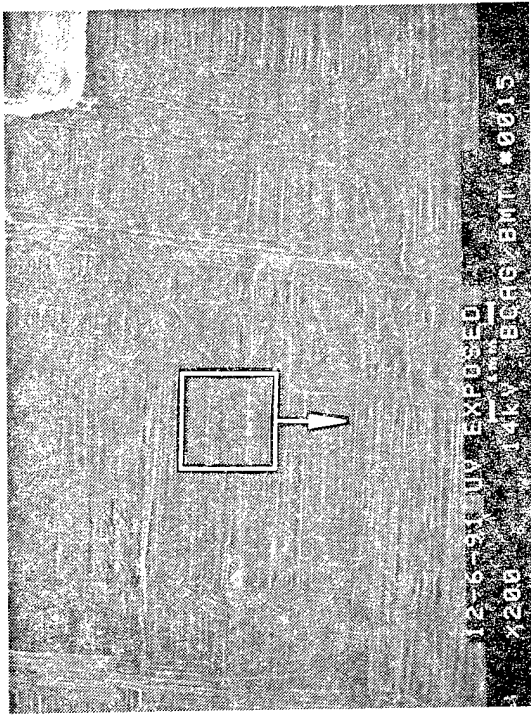

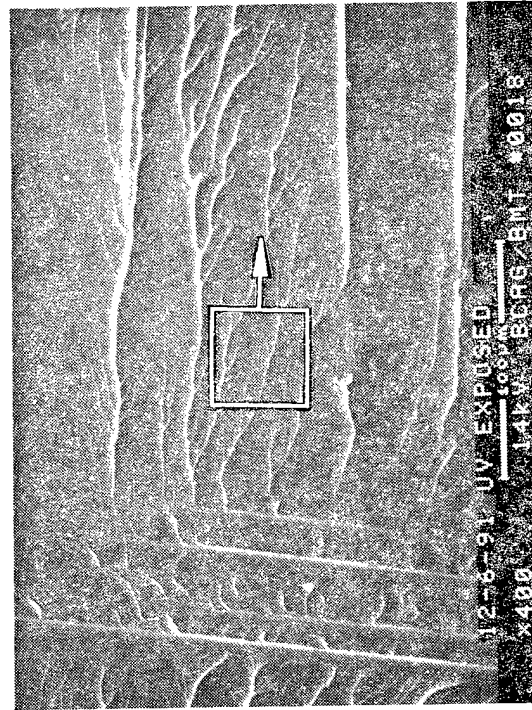


Figure 3.1-15. Optical Fractographs of 3501-6/AS4 Interlaminar Mode I Tension, Specimen Exposed to UV Radiation

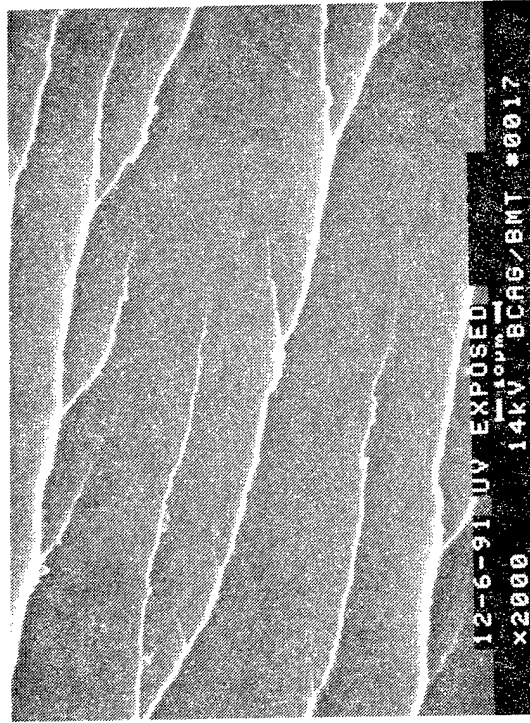


30-degree tilt 20 X

Mechanically induced crack direction  


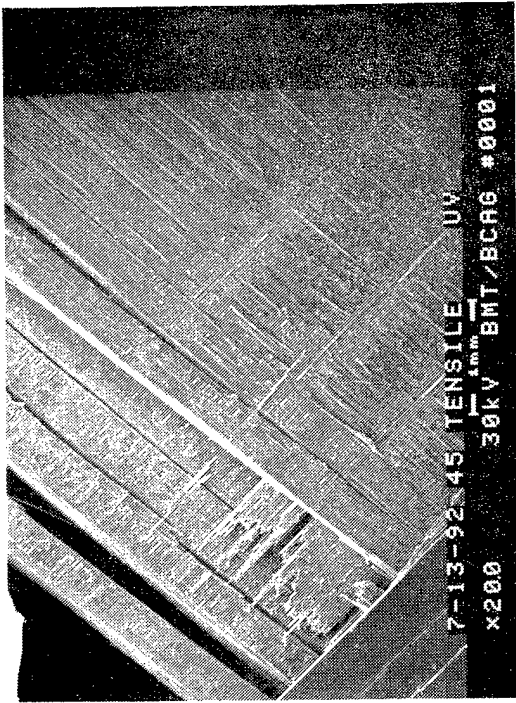


30-degree tilt 400 X

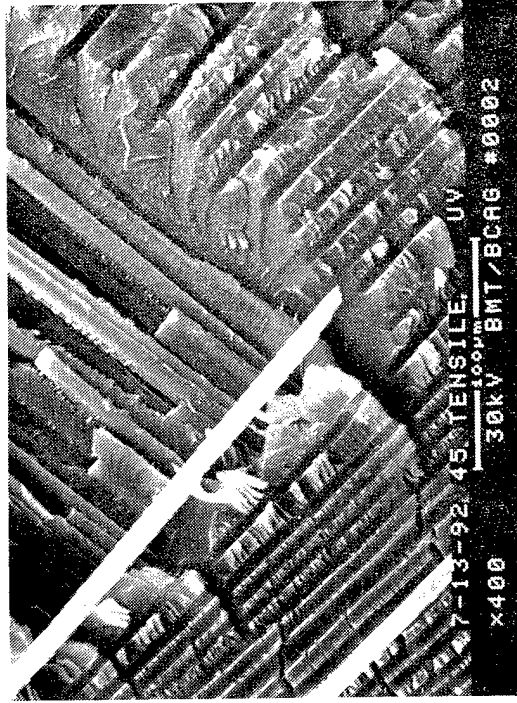


30-degree tilt 2,000 X

Figure 3.1-16. SEM Fractographs of 3501-6/AS4 Interlaminar Mode I Tension, Specimen Exposed to UV Radiation

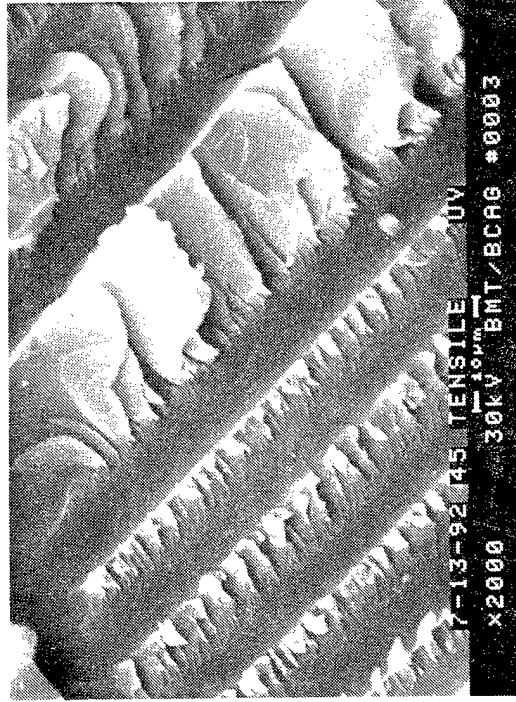


60 degree tilt (a) 20X



60 degree tilt (b) 400X

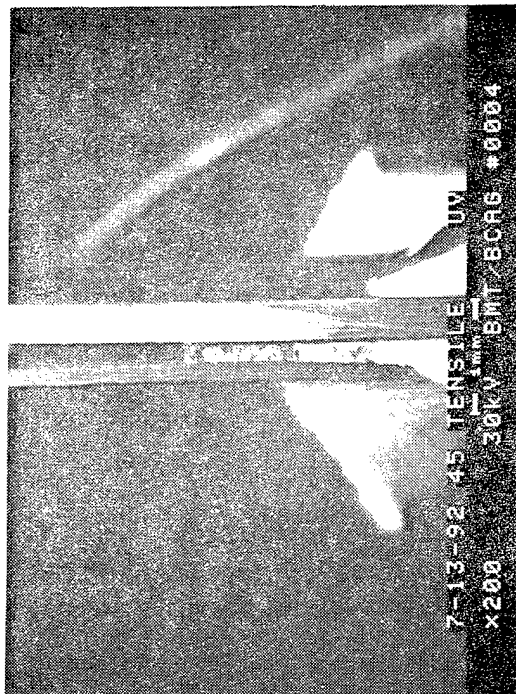
↑  
Load direction



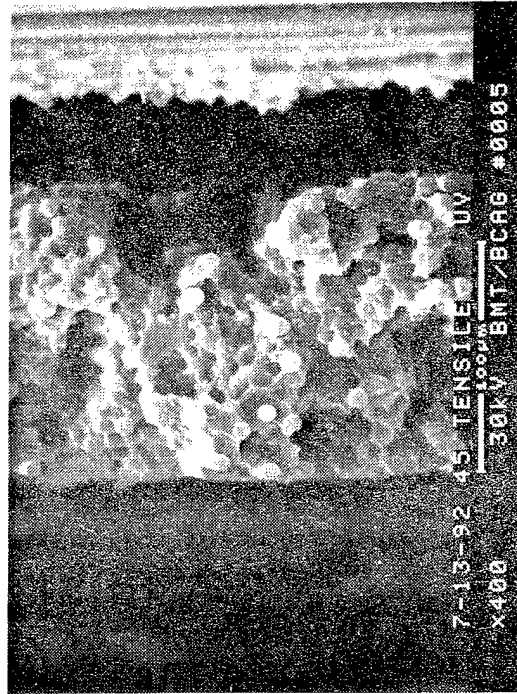
60 degree tilt (c) 2000X

Figure 3.1-17. SEM Fractographs of a 3501-6/AS4 ± 45 Tensile Specimen Exposed to UV Radiation, Interlaminar Surface

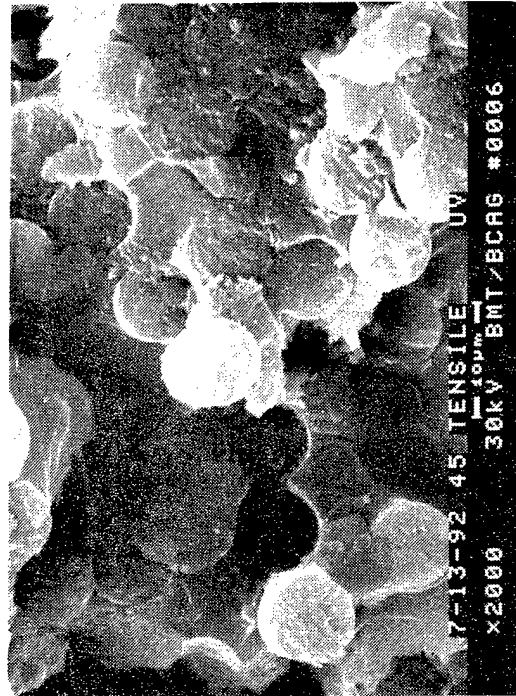
49754.30 9-5571 D1 ai



(a) 20X



(b) 400X



(c) 2000X

Figure 3.1-18. SEM Fractographs of a 3501-6/AS4 ± 45 Tensile Specimen Exposed to UV Radiation, Translaminar Surface

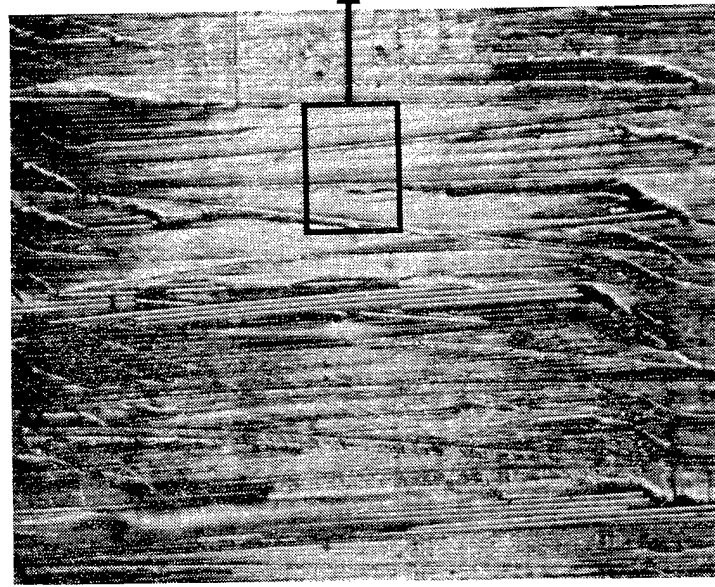


Crack growth direction

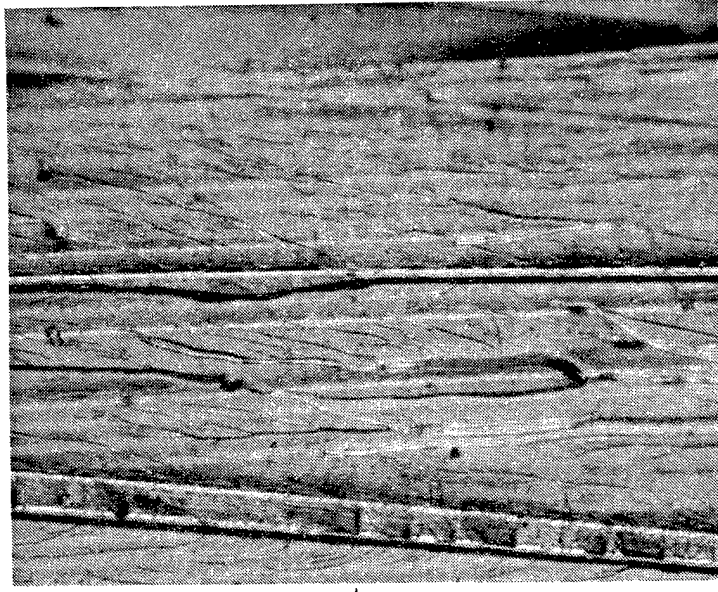


Mode I

0.28X



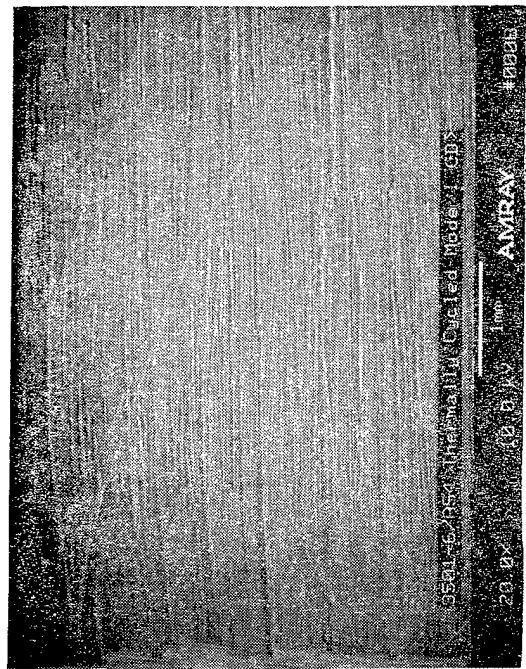
100X



400X

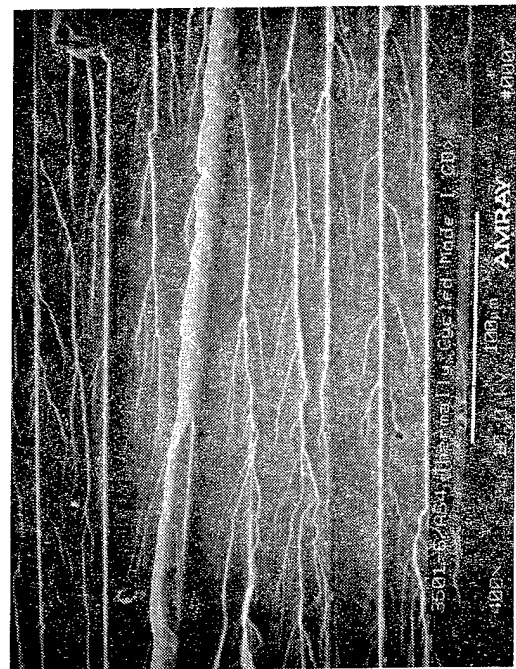
Figure 3.1-19. Optical Fractographs of 3501-6/AS4 Interlaminar Mode I (Tension), Specimen Thermally Cycled Prior to Loading

49754.08 9-5571 D8 fh

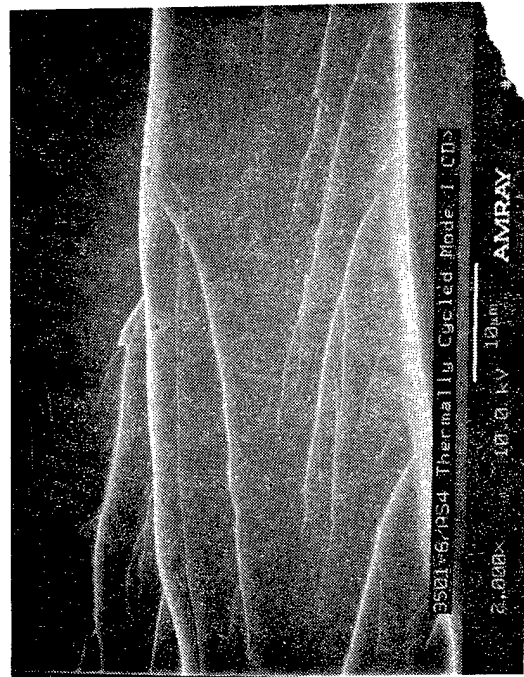


30 degree tilt (a) 20X

Mechanically induced crack direction

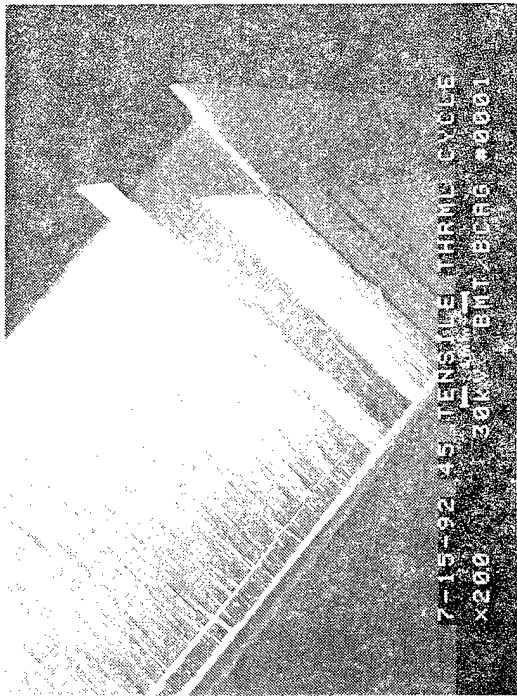


30 degree tilt (b) 400X

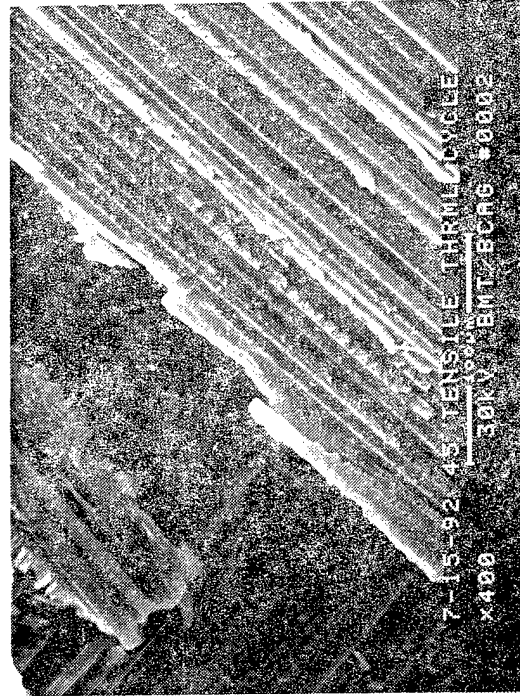


30 degree tilt (c) 2000X

Figure 3.1-20. SEM Fractographs of a 3501-6/AS4 Interlaminar Mode I Tension Fracture Surface, Thermally Cycled

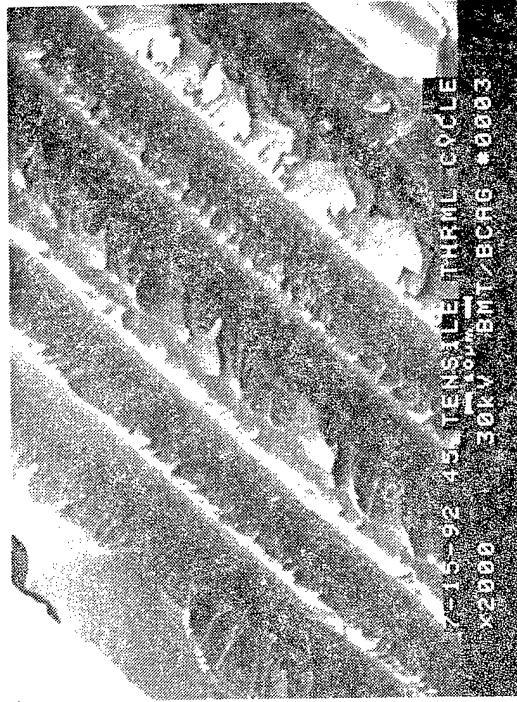


60 degree tilt (a) 20X



60 degree tilt (b) 400X

A ↑  
Load direction



60 degree tilt (c) 2000X

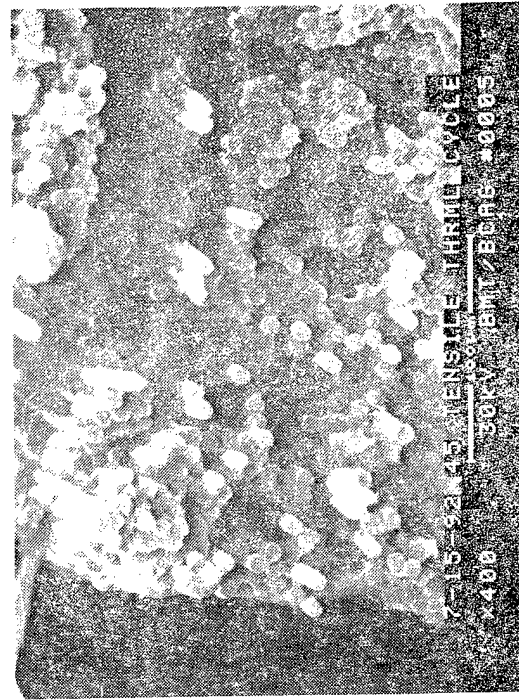
Figure 3.1-21. SEM Fractographs of a 3501-6/AS4 ± 45 Tensile Specimen Thermally Cycled, Interlaminar Surface

49754.34 9-5571 D1 ai



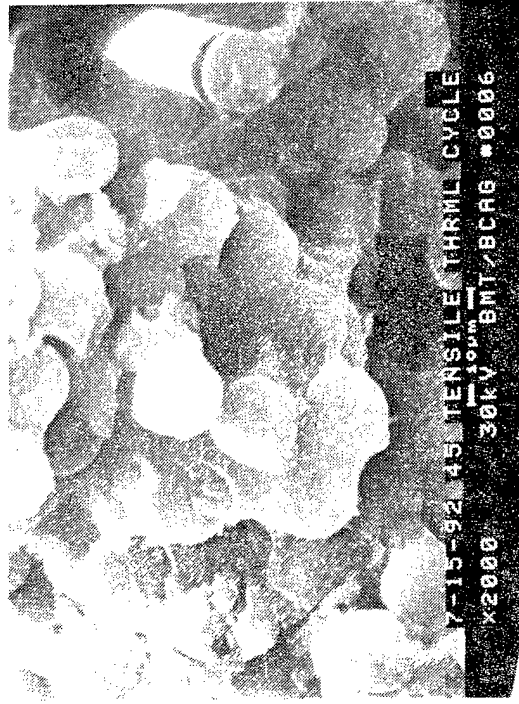
20X

(a)



400X

(b)



2000X

(c)

Figure 3.1-22. SEM Fractographs of a 3501-6/AS4 ± 45 Tensile Specimen Thermally Cycled, Translaminar Surface

49754.35 9-5571 D1 ai

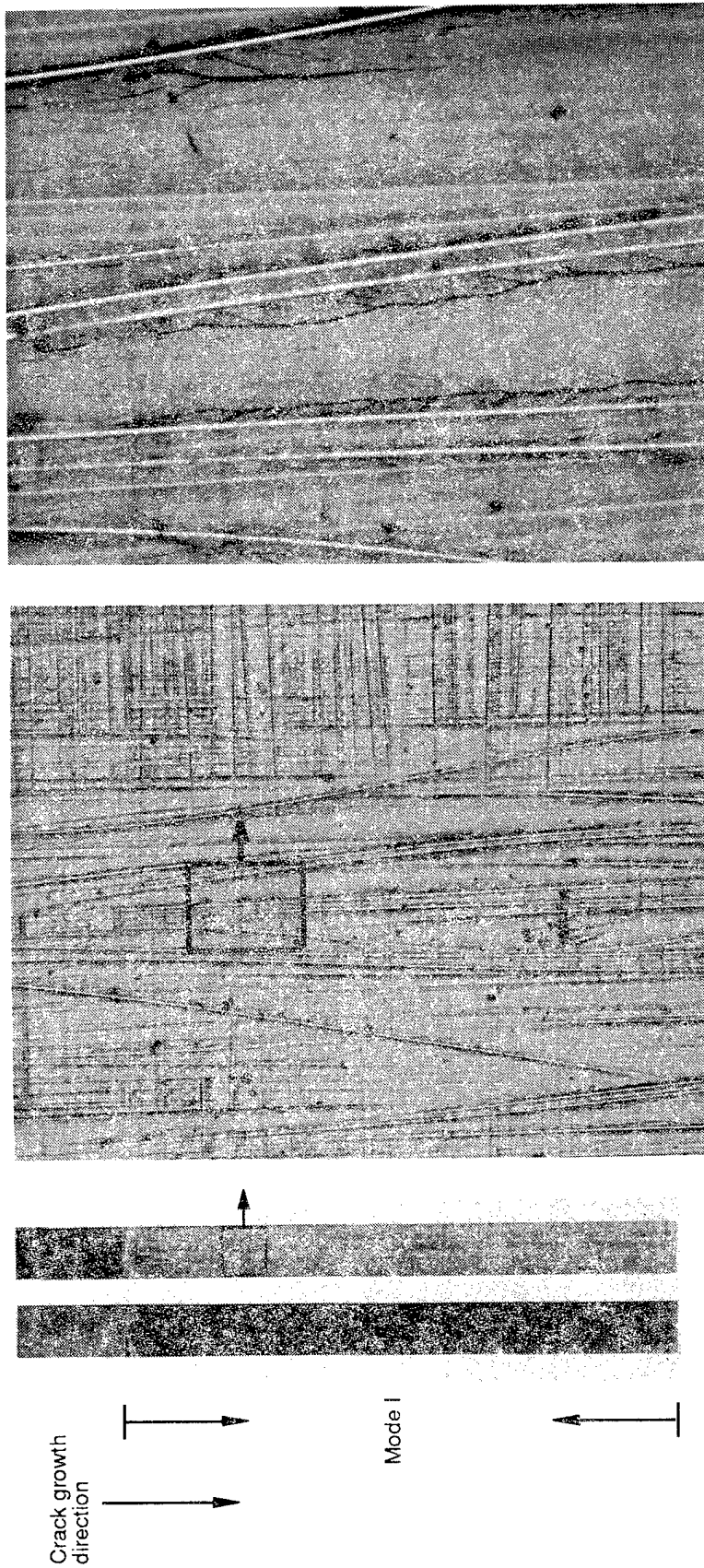
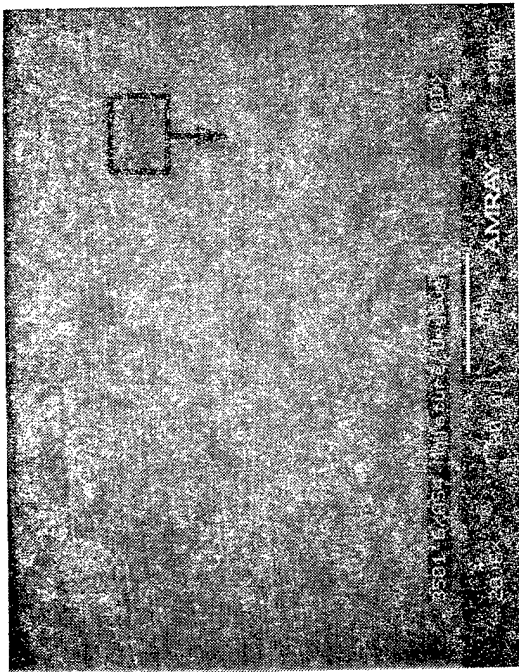
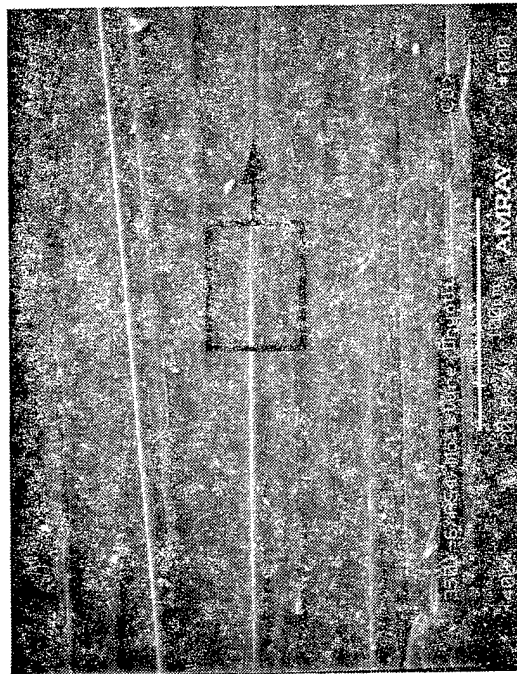


Figure 3.1-23. Optical Fractography of 3501-6/AS4 Interlaminar Mode I Tension Specimen, Moisture/Dryout Cycled

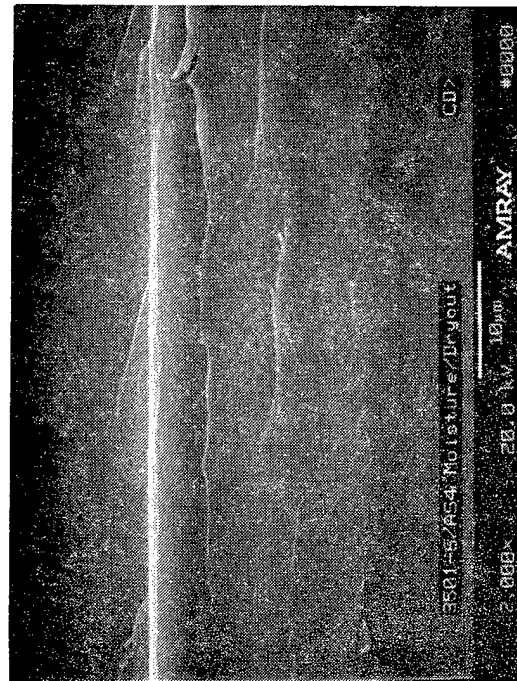


30 degree tilt (a) 20X



30 degree tilt (b) 400X

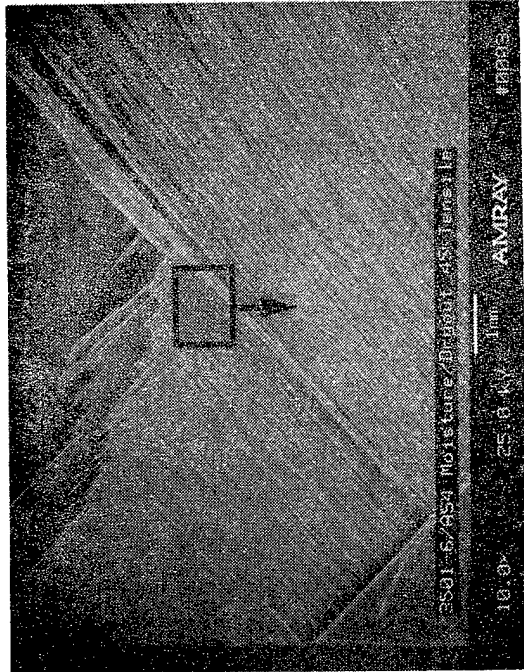
Mechanically induced  
crack direction →



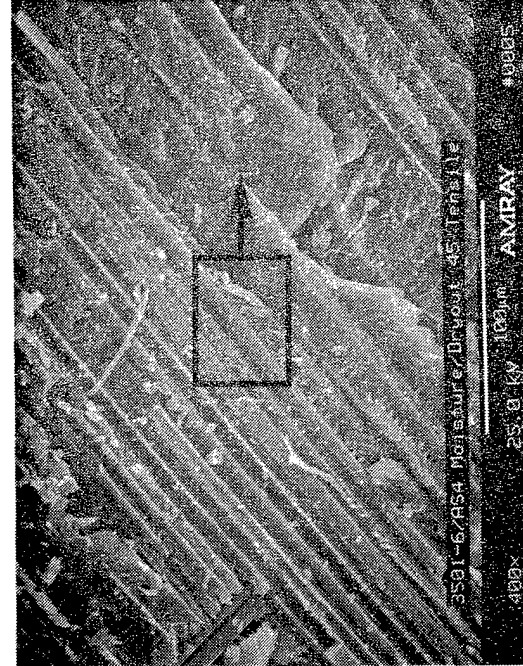
30 degree tilt (c) 2000X

Figure 3.1-24. SEM Fractographs of a 3501-6/AS4 Interlaminar Mode I Tensile Fracture Surface Tested After Moisture/Dryout Cycling

49829.13 9-5576 D1ai



(a) 20X



(b) 400X

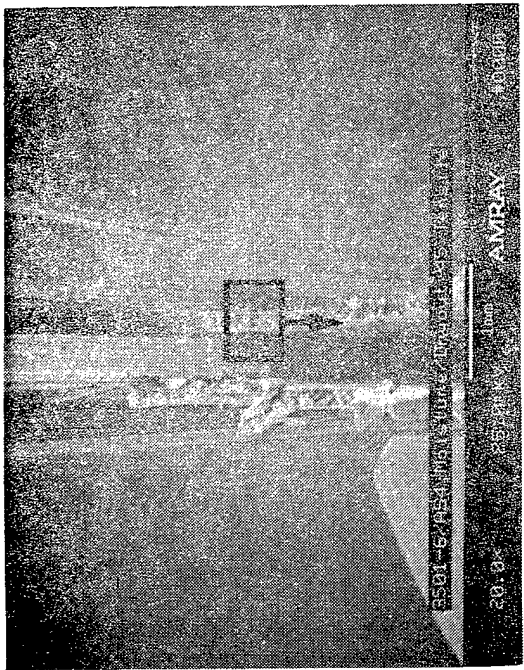
↑  
Loading direction



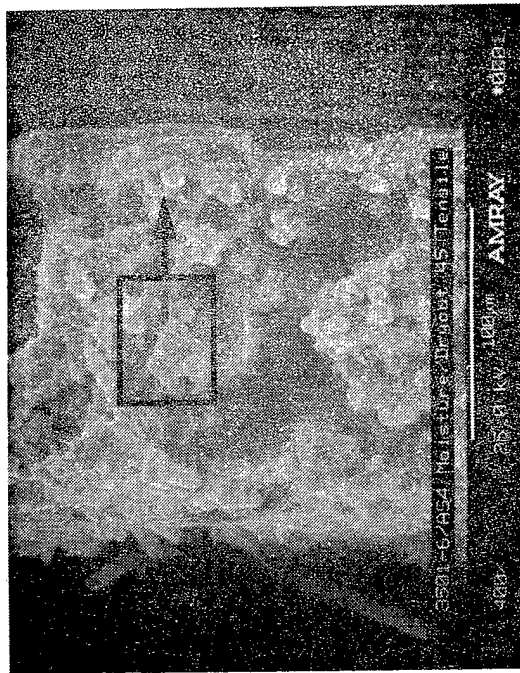
(c) 2000X

Figure 3.1-25. SEM Fractographs of a 3501-6/AS4 ±45° Tensile Specimen Tested After Moisture/Dryout Cycling, Interlaminar Surface

49829.11 9-5576 D1ai

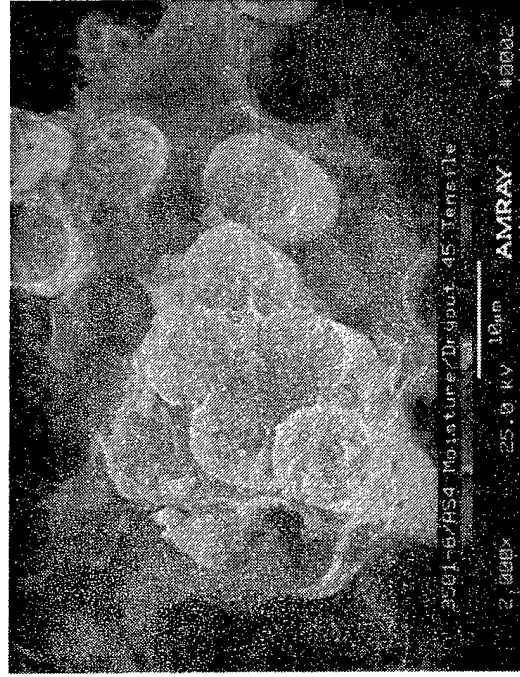


(a) 20X



(b) 400X

Mechanically induced crack direction



(c) 2000X

Figure 3.1-26. SEM Fractographs of a 3501-6/AS4  $\pm 45^\circ$  Tensile Specimen Tested After Moisture/Dryout Cycling, Translaminar Surface  
49829.12.9.5576 D1ai



**SECTION 3.2**  
**CARBON/THERMOPLASTIC POLYIMIDE**  
**AS4/KIII**

**3.2.1 Introduction**

This section presents the results of fractography performed on the AS4/KIII graphite/thermoplastic polyimide (Gr/TPP) test coupons. The Gr/TPP composite system is a high-temperature thermoplastic that is being considered for a variety of applications in aerospace structures. The tests performed include both interlaminar and translaminar test coupons. These test coupons were loaded statically at room temperature and at 400°F (dry). Sections from the room temperature coupons were individually exposed to various environments to determine whether the surface morphology would be affected by these conditions. In addition, interlaminar mode II (shear) test coupons were subjected to cyclic loading to produce a fatigue crack fracture surface for characterization.

**3.2.2 Static Loading**

**Interlaminar Mode I (Tension), RT/Dry**

The fracture morphology of the specimens exhibited similar features as those of the PEEK material system, which is a true thermoplastic. On a macroscopic scale, numerous loose fibers were on the surface due to fiber pull-out. Microscopically, these features include the slow ductile peeling of the matrix craze filaments, which produce a limited river pattern and some cusps, which are generally associated with mode II (shear) loading (Figures 3.2-1 and 3.2-2).

**Interlaminar Mode I (Tension), 400°F/Dry**

This fracture surface was generally similar to the RT surface but with minor differences such as fibers pulled out from the surface and slightly larger matrix craze filaments (Figures 3.2-3 and 3.2-4).

**Interlaminar Mode II (Shear), RT/Dry**

As with the mode I (tensile) case, the mode II (shear) surface morphology exhibited features similar to those of the PEEK specimens, except that there were no loose fibers on the surface. This morphology was also similar to the KIII/AS4 mode I surface, making it difficult to determine the loading condition (Figures 3.2-5 and 3.2-6).

**Interlaminar Mode II (Shear), 400°F/Dry**

There were no significant differences between the fracture morphology of the RT and the elevated temperature test specimens as shown in Figures 3.2-7 and 3.2-8.

### **Translaminar Mode I (Tension), RT/Dry**

The overall appearance of the room temperature fracture morphology was typical of a notched four-point tensile specimen, exhibiting a very jagged surface. The fracture origins on the fiber ends were easily visible and generally indicated the overall mechanically induced crack direction (Figure 3.2-9). The interlaminar surfaces (Figure 3.2-10) were identical to the mode I fracture morphology as described above.

The specimen tested at 400°F did not fracture transversely; it only bent and buckled. Consequently, no fractographic data is available for this fracture configuration.

### **3.2.3 Fatigue**

#### **Interlaminar Mode I (Tension), RT and 350°F/Dry**

Both the RT (Figures 3.2-11 & 3.2-12) and the 350°F tested specimens (Figures 3.2-13 & 3.2-14) exhibited similar fracture features which appeared to resemble a mode II (shear) morphology. The resin material between the fibers contained hackles which indicated the overall crack growth orientation. No rivermarks or other distinctive mode I features were observed.

#### **Interlaminar Mode II (Shear), RT and 350°F/Dry**

Examination of the fracture surfaces did not reveal any definite indications of fatigue, except for a feature that may be related to the cyclic loading. This feature appeared to be typical of a mode II hackle. However, when observed at high magnification the feature appears to be wider and thinner than similar hackles on statically loaded specimens. This feature was observed both on the RT specimen (Figures 3.2-15 and 3.2-16) and the 350°F tested specimens (Figures 3.2-17 and 3.2-18).

### **3.2.4 Short-Term Environmental Exposure**

#### **Interlaminar Mode II Surfaces**

Examination of the mode II surfaces (Figure 3.2-19 through Figure 3.2-25) exposed to the various environments revealed that the hydraulic fluid (Figure 3.2-19) and JP4 jet fuel (Figure 3.2-20) slightly degraded the fracture features. The fibers appeared to be "cleaner" when compared to the control specimens. However, this did not alter the surface morphology enough to prevent identification of the mode II fracture features, such as the cusp and matrix filaments.

#### **Interlaminar Mode I Surfaces**

None of the exposure conditions appeared to have degraded the fracture features (Figure 3.2-26 through Figure 3.2-32).

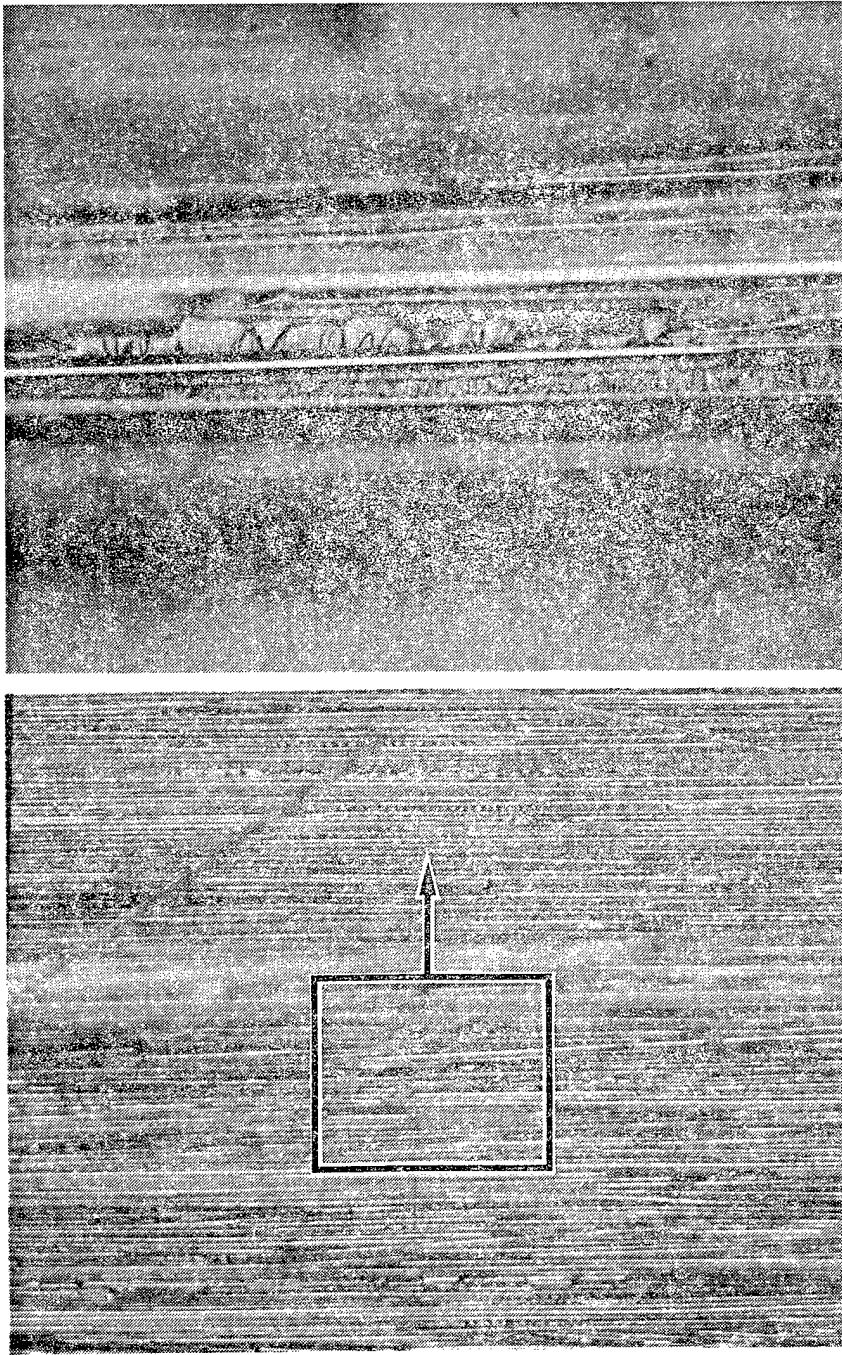
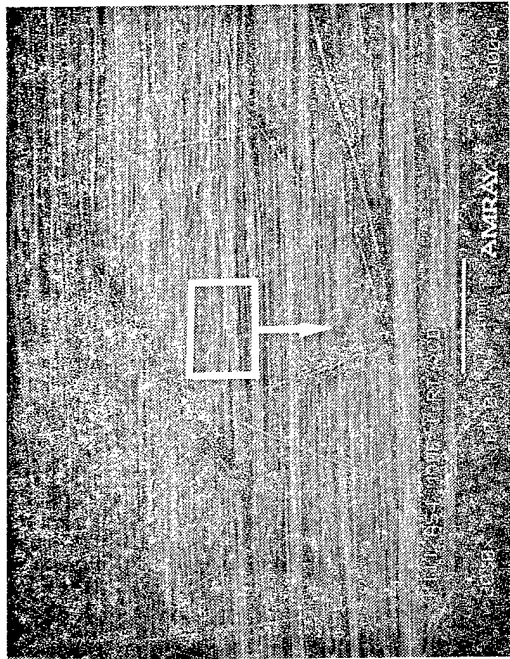
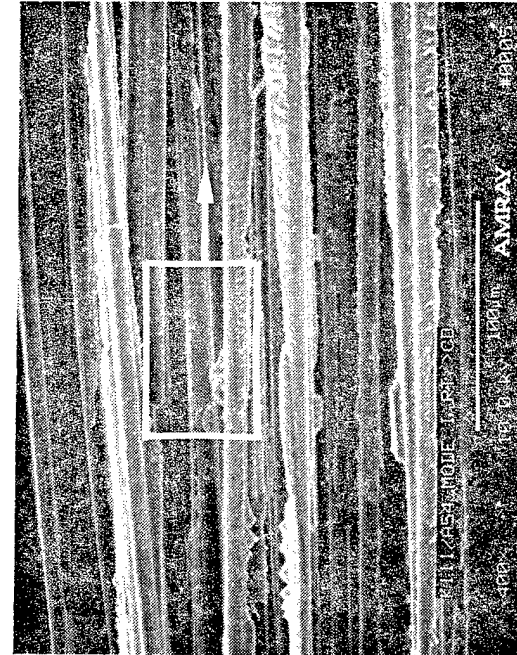


Figure 3.2-1. Optical Fractography of KI/II/AS4 Interlaminar Mode I Tension Specimen Tested at RT/Dry

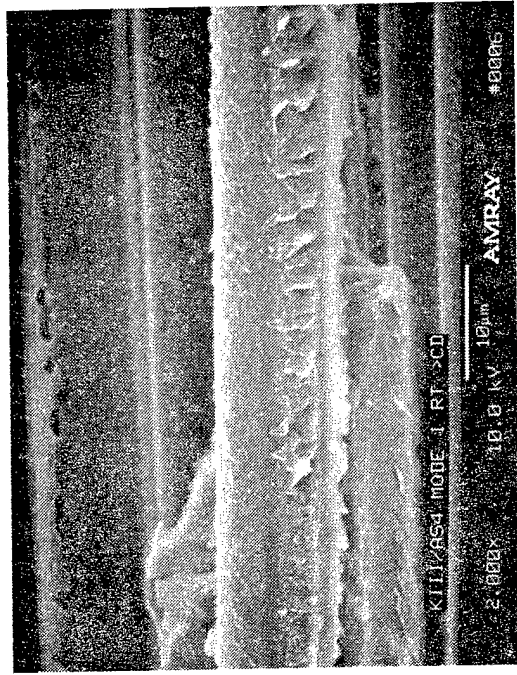


30 degree tilt (a) 20X



30 degree tilt (b) 400X

Mechanically induced  
crack direction →



30 degree tilt (c) 2000X

Figure 3.2-2. SEM Fractographs of a KIII/AS4 Interlaminar Mode I Shear Fracture Surface Tested at RT/Dry

2405.09 9-5576 D1ai

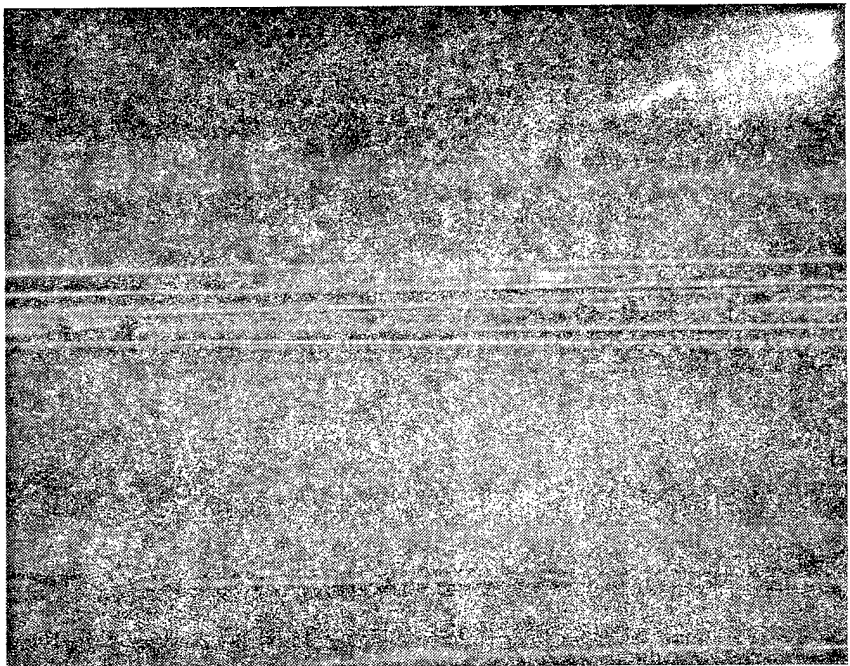
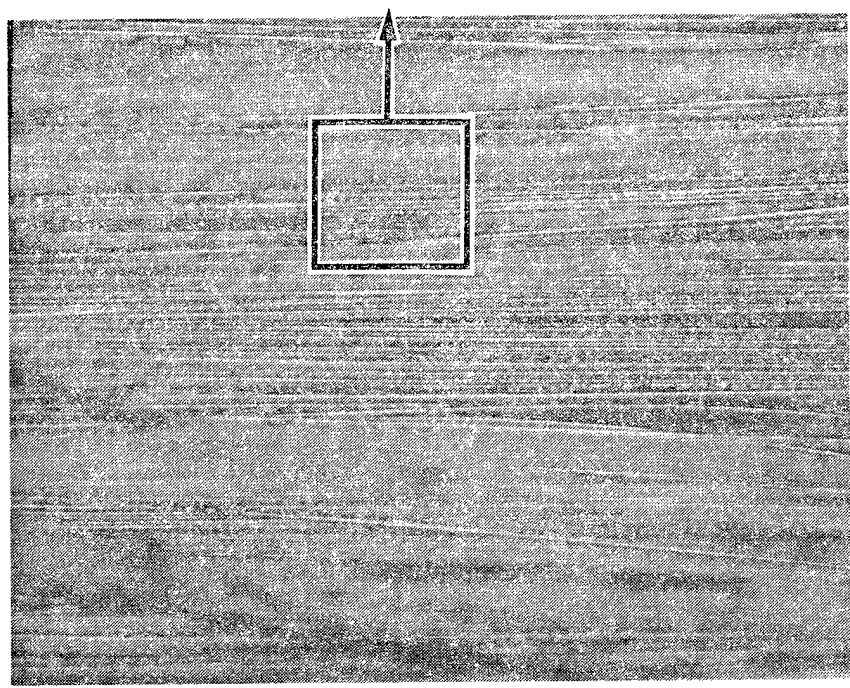
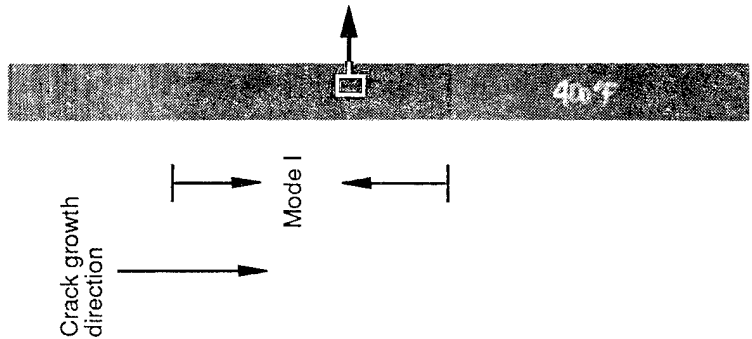
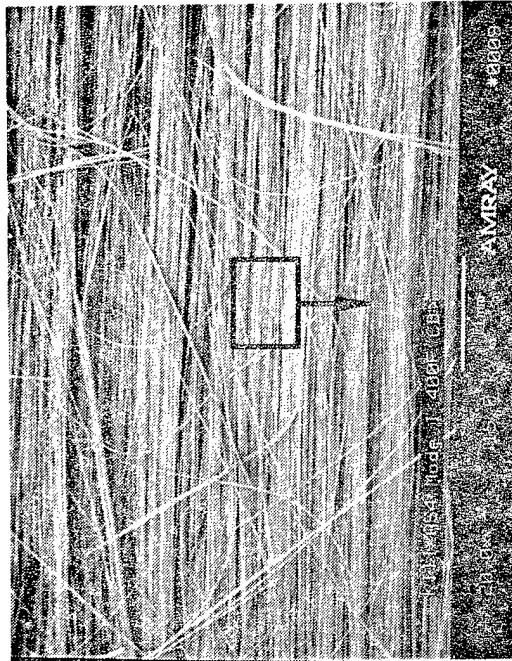
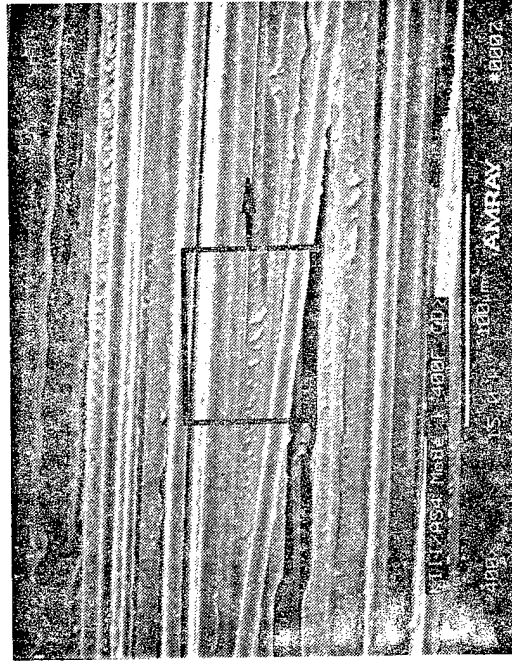


Figure 3.2-3. Optical Fractography of K111/AS4 Interlaminar Mode I Tension Specimen Tested at 400°F/Dry



30 degree tilt (a) 20X

Mechanically induced crack direction ↑



30 degree tilt (b) 400X



30 degree tilt (c) 2000X

Figure 3.2-4. SEM Fractographs of a K111/AS4 Interlaminar Mode I (Tension) Fracture Surface, 400°F

49754.23 9-5571 D1 ai

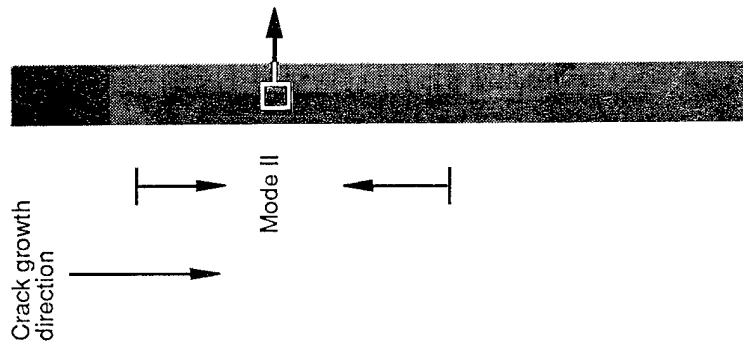
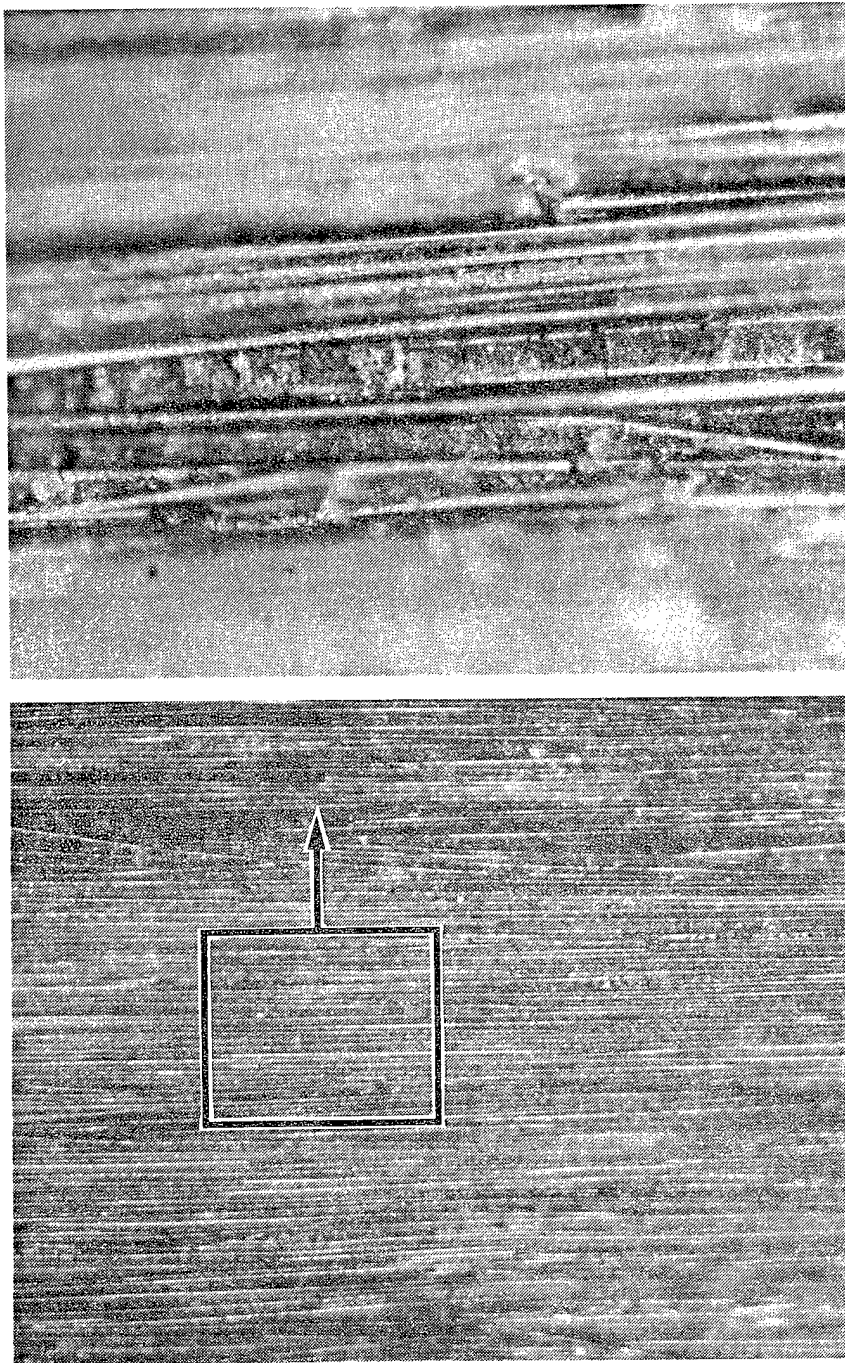
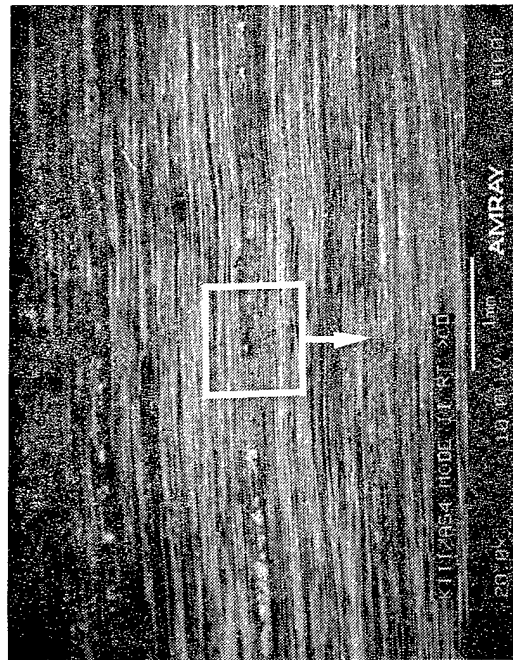
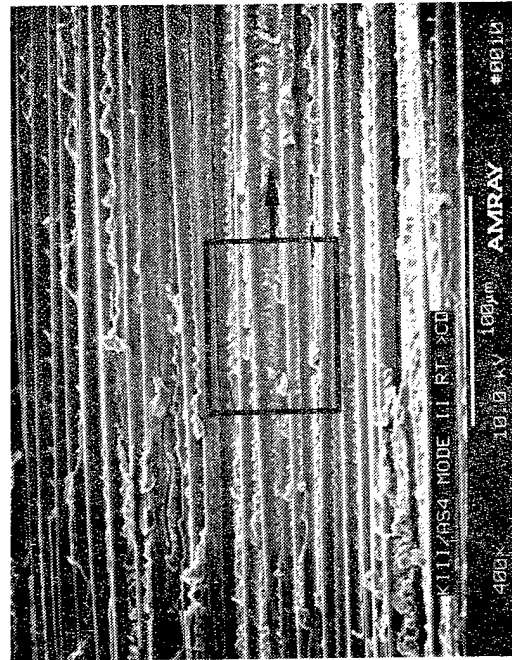


Figure 3.2-5. Optical Fractography of KIII/AS4 Interlaminar Mode II Shear Specimen Tested at RT/Dry

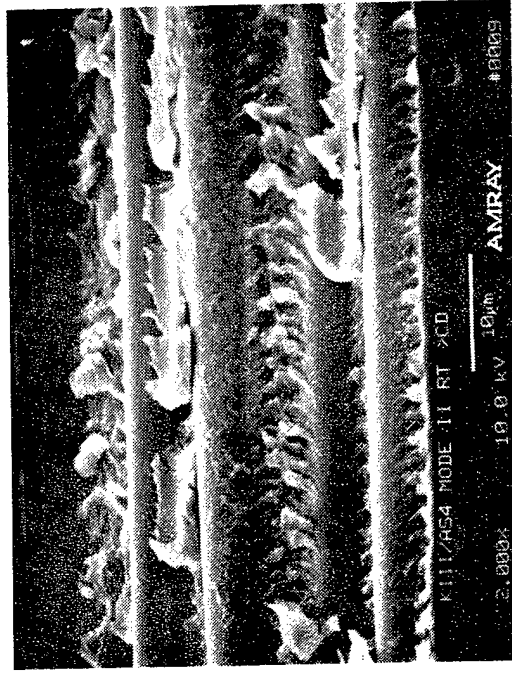


60 degree tilt (a) 20X



60 degree tilt (b) 400X

Mechanically induced  
crack direction

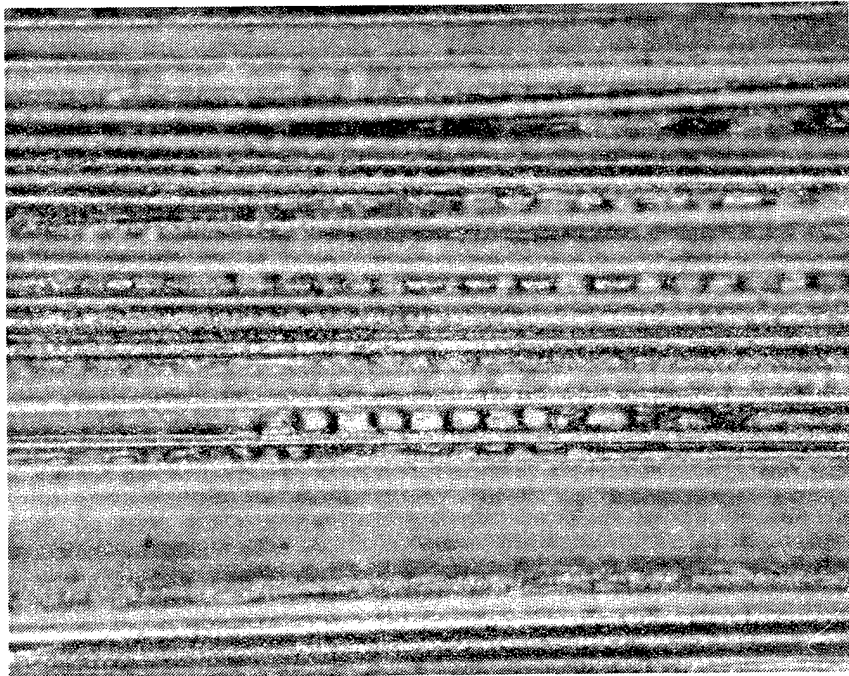


60 degree tilt (c) 2000X

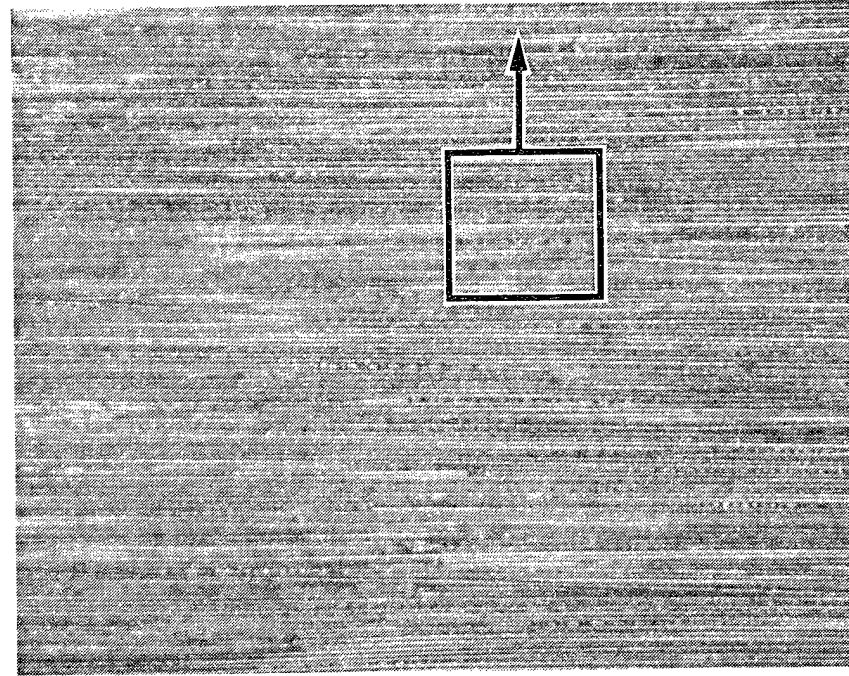
Figure 3.2-6. SEM Fractographs of a KIII/AS4 Interlaminar Mode II Shear Fracture Surface

2405.08 9-5576 D1a:





400 X



100 X

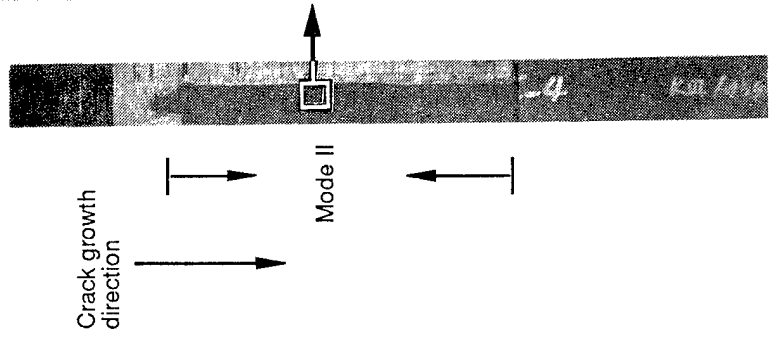
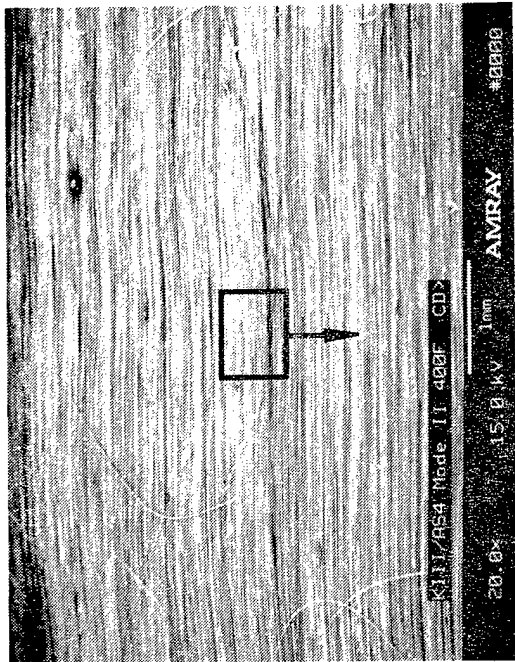
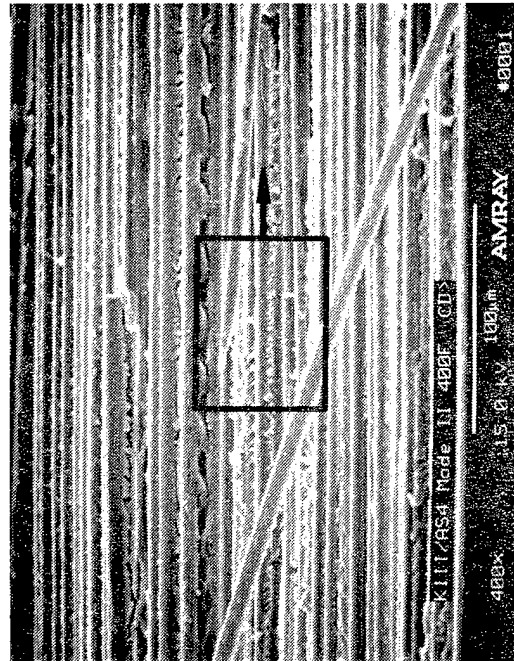


Figure 3.2-7. Optical Fractography of KIII//AS4 Interlaminar Mode II Shear Specimen Tested at 400° F/Dry

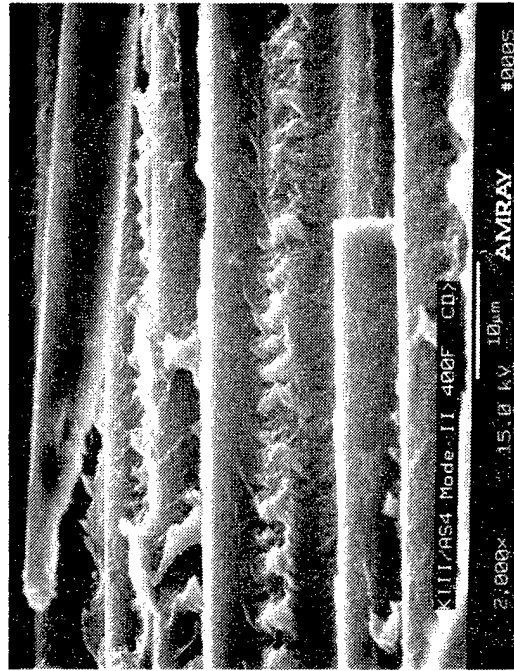


60 degree tilt (a) 20X



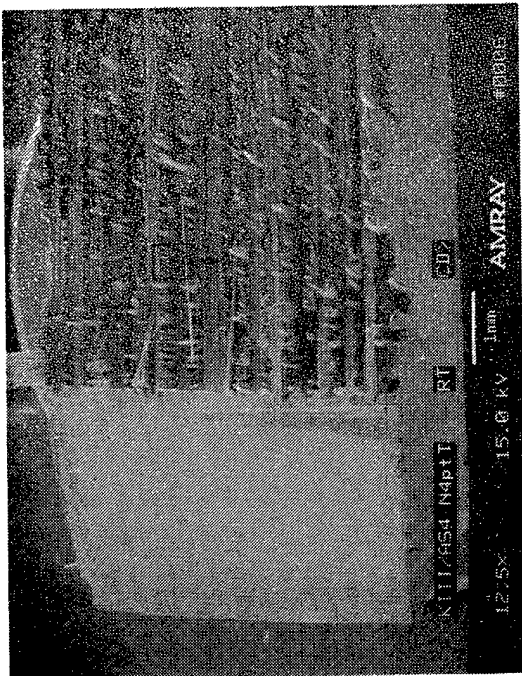
60 degree tilt (b) 400X

Mechanically induced crack direction



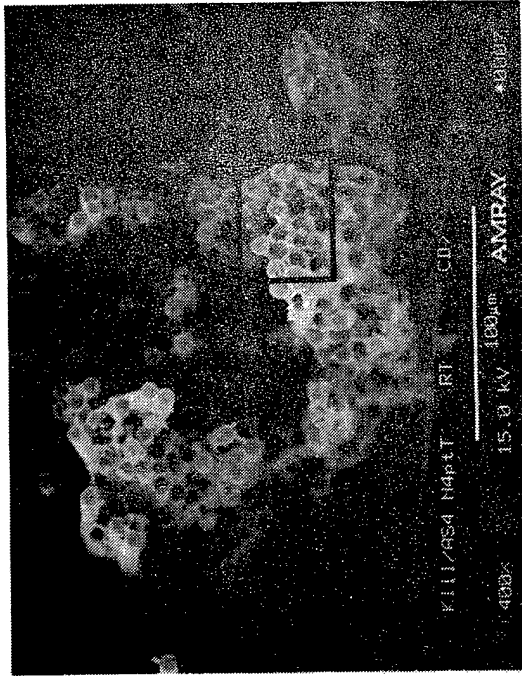
60 degree tilt (c) 2000X

Figure 3.2-8. SEM Fractographs of a KIII/AS4 Interlaminar Mode II (Shear) Fracture Surface, 400°F

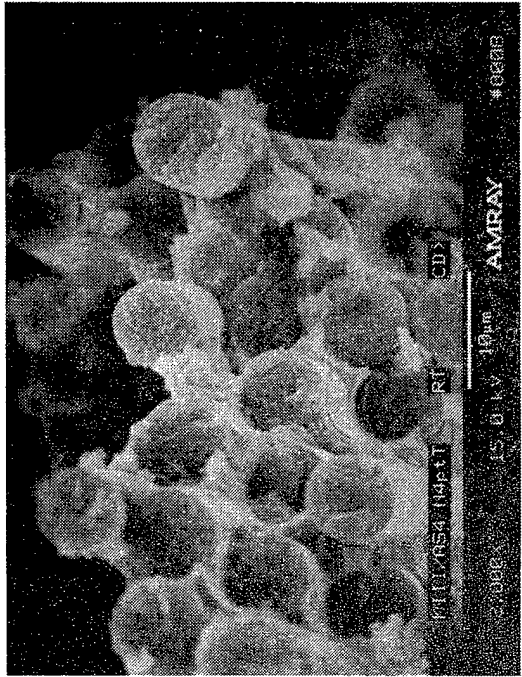


(a) 12.5X

Mechanically induced crack direction



(b) 400X

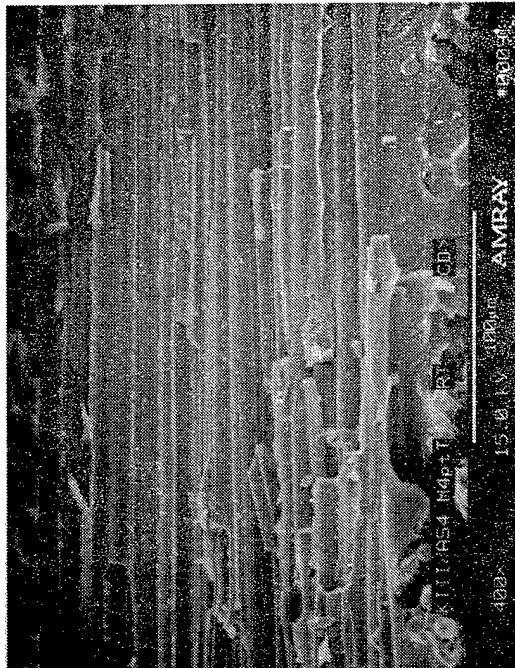


(c) 2000X

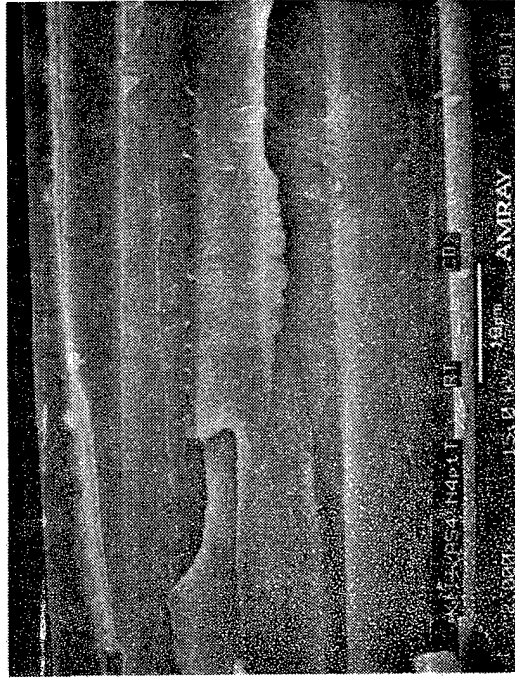
Figure 3.2-9. SEM Fractographs of a K111/AS4 N4ptT Specimen, Transverse Fracture Surface, Room Temperature

49829.10 9-5576 D1ai

Mechanically induced  
crack direction

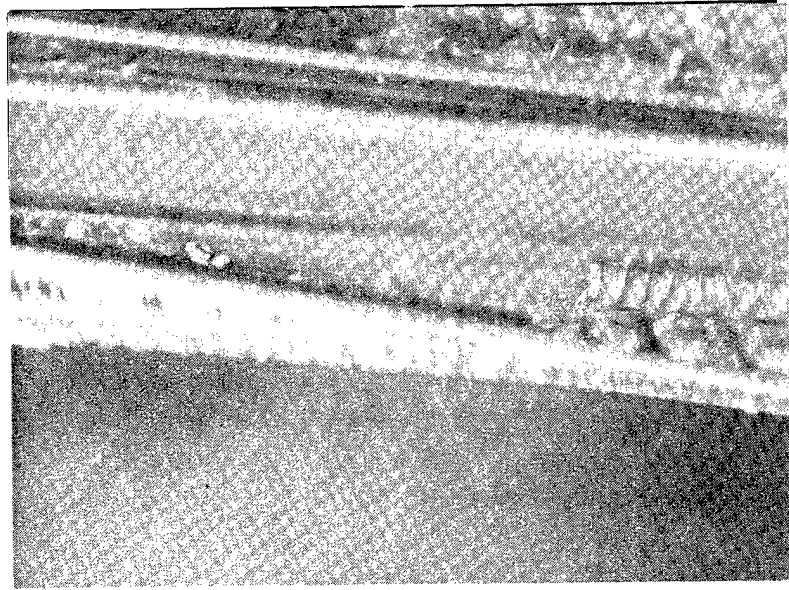


(a) 400X

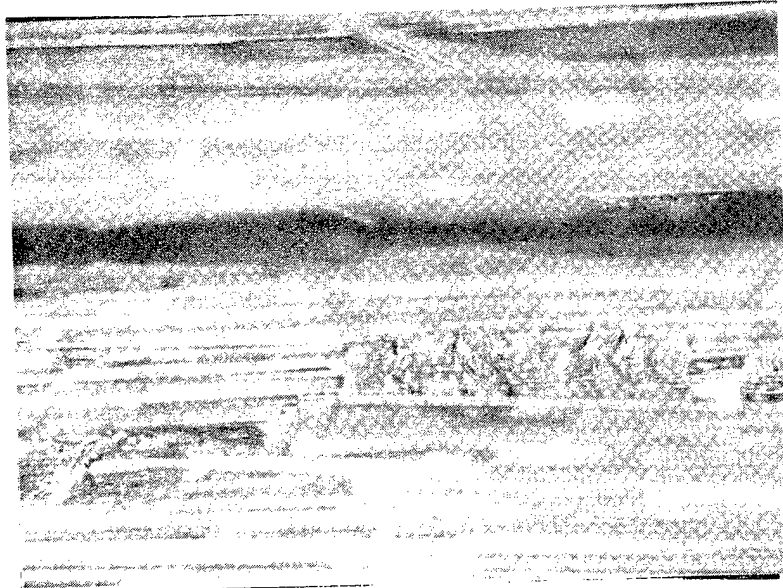


(b) 2000X

Figure 3.2-10. SEM Fractographs of a KII//AS4 N4ptT Specimen, Interlaminar Surface, Room Temperature



400X



100X

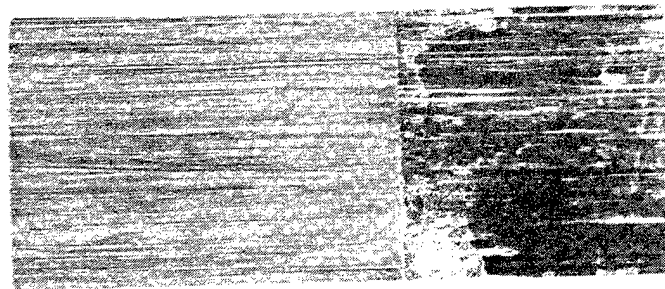


Figure 3.2-11. Optical Fractographs of a KIII/AS4 Interlaminar Mode I (Tensile) Fatigue Fracture Surface, RT



Mechanically Induced  
Crack Direction →

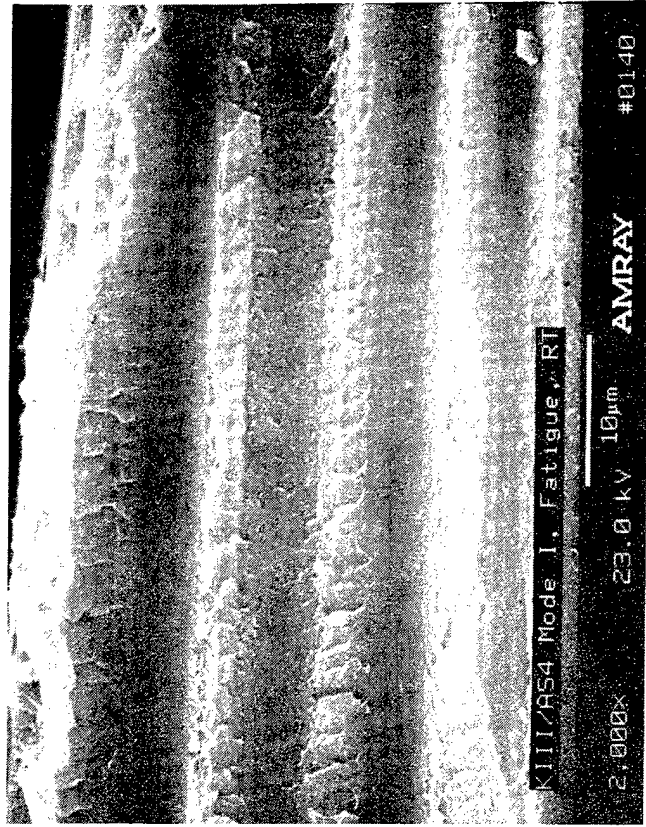
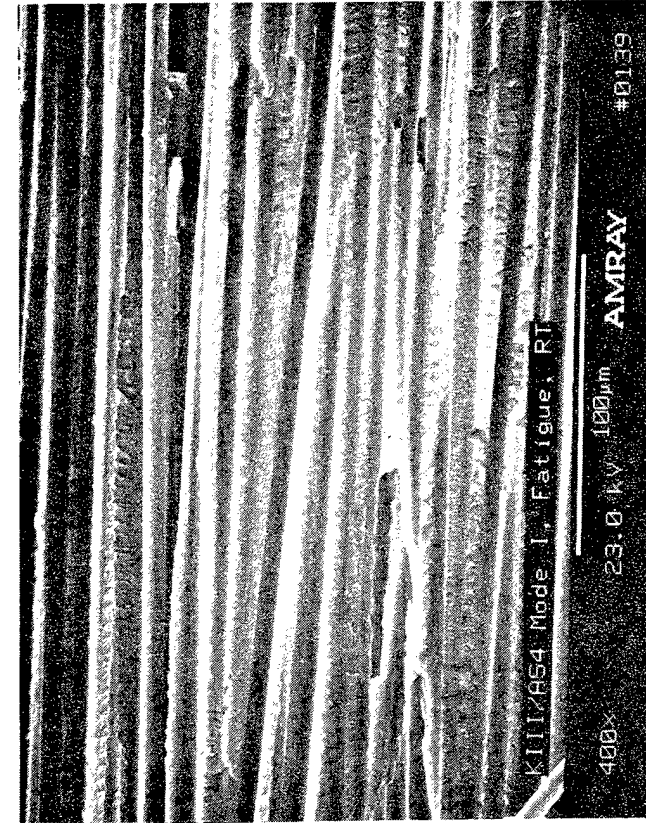
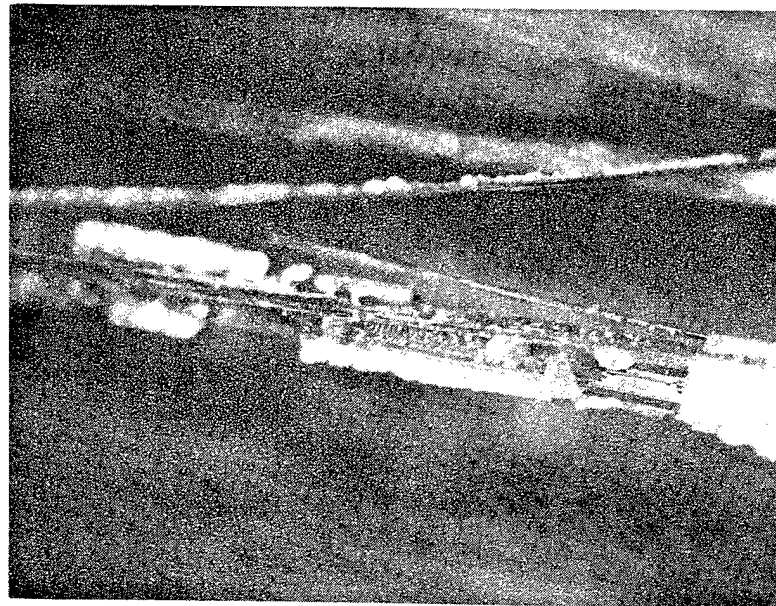
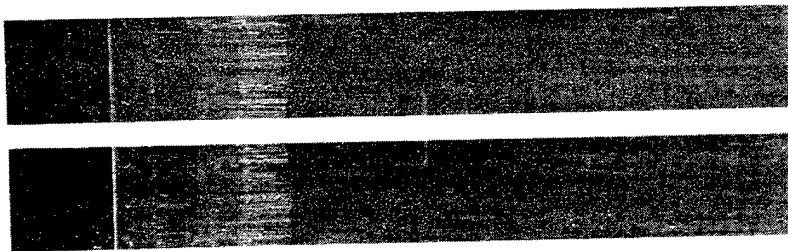
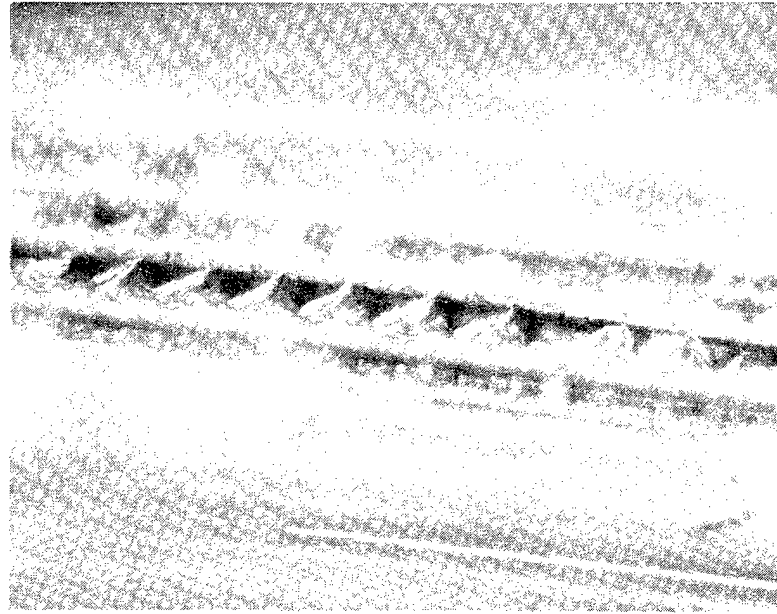


Figure 3.2-12. SEM Fractographs of a KIII/AS4 Interlaminar Mode I (Tensile) Fatigue Fracture Surface, RT



100X



400X

Figure 3.2-13. Optical Fractographs of a KIII/AS4 Interlaminar Mode I (Tensile) Fatigue Fracture Surface, 350° F

Mechanically Induced  
Crack Direction  
↑

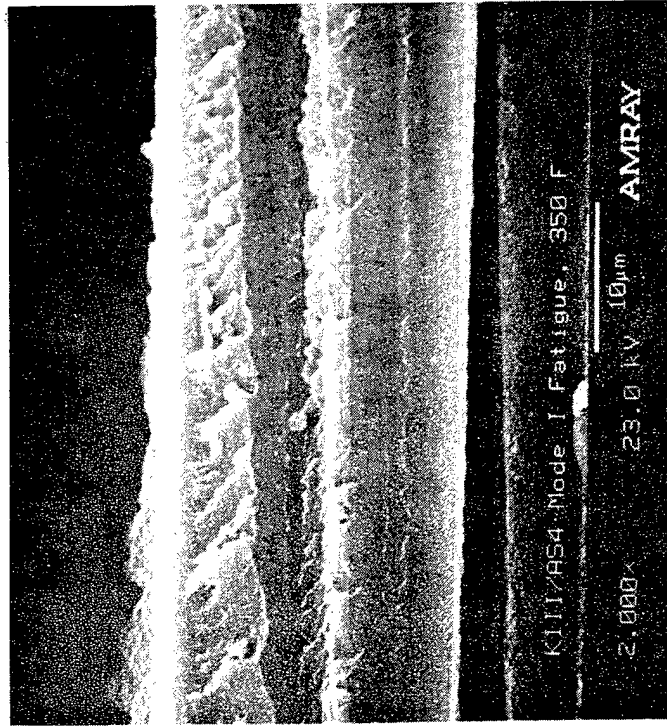
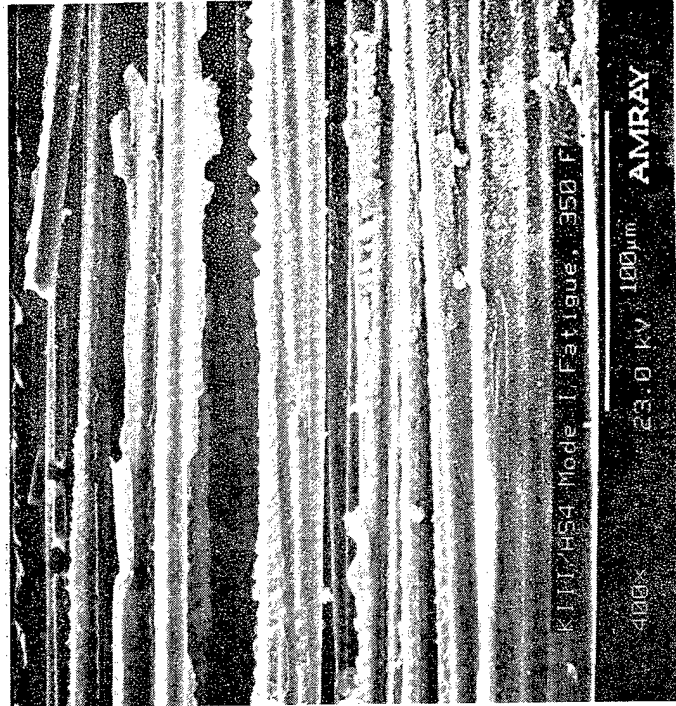
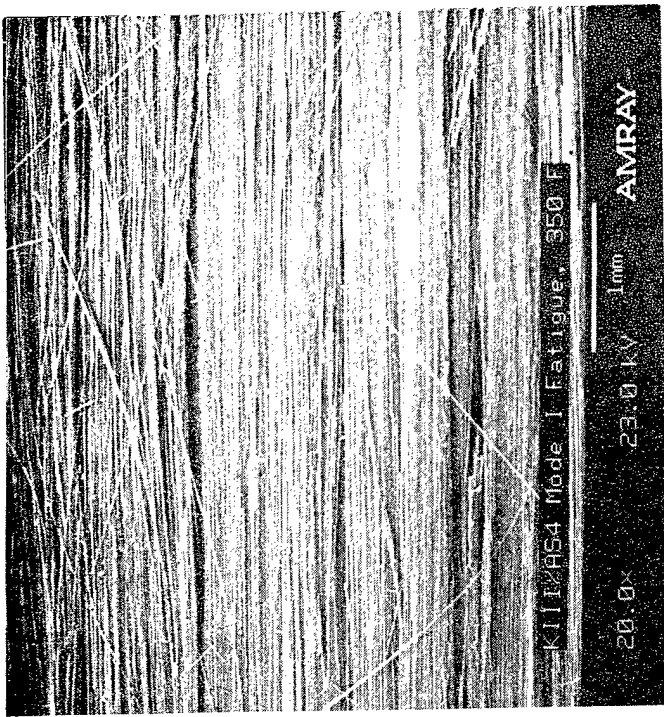
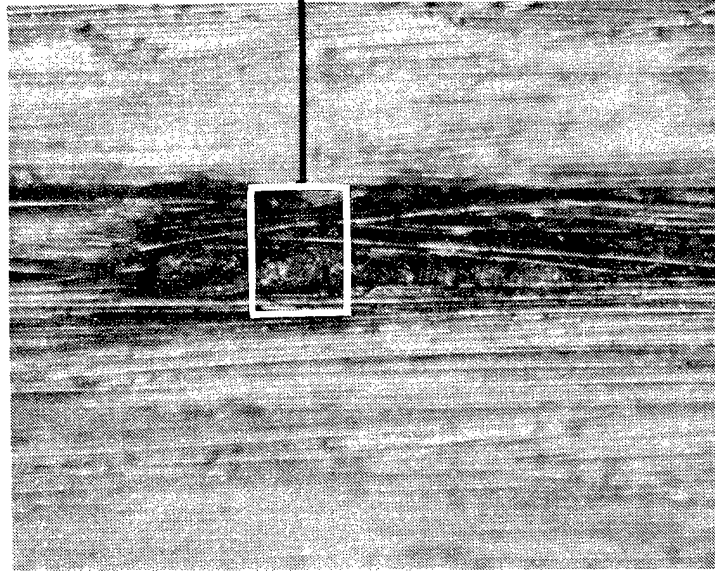
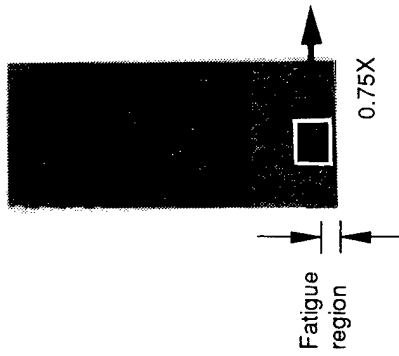


Figure 3.2-14. SEM Fractographs of a KIII/AS4 Interlaminar Mode I (Tensile) Fatigue Fracture Surface, 350° F



Crack growth direction  
↑



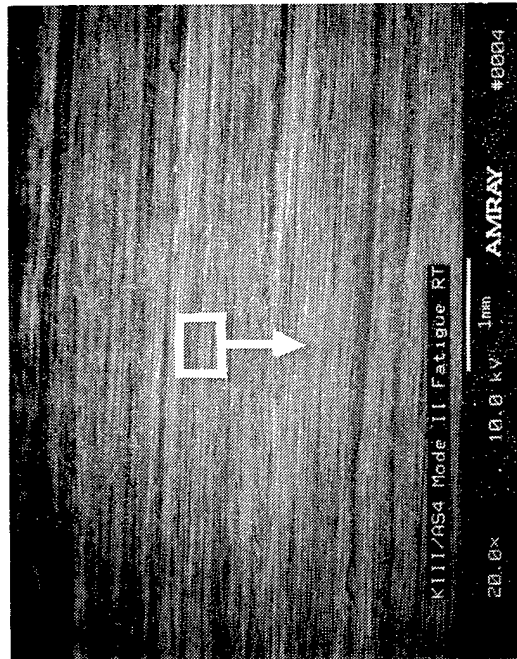
100X



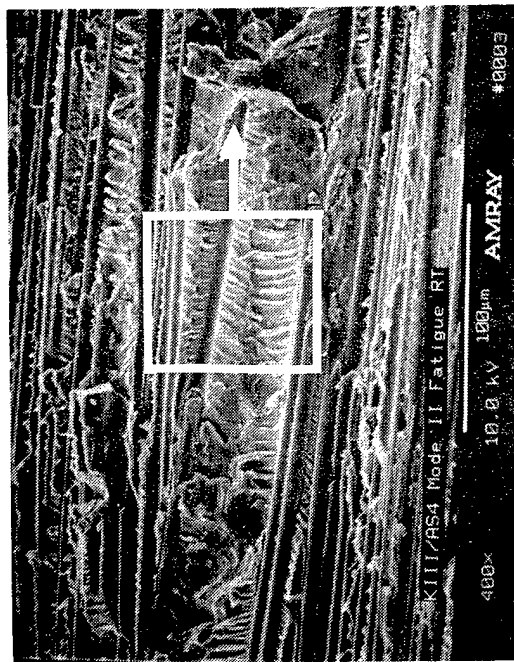
400X

Figure 3.2-15. Optical Fractographs of KIII/AS4 Interlaminar Mode II (Shear) Fatigue, Room Temperature, High Stress

49754.11 9-5571 D8 fh

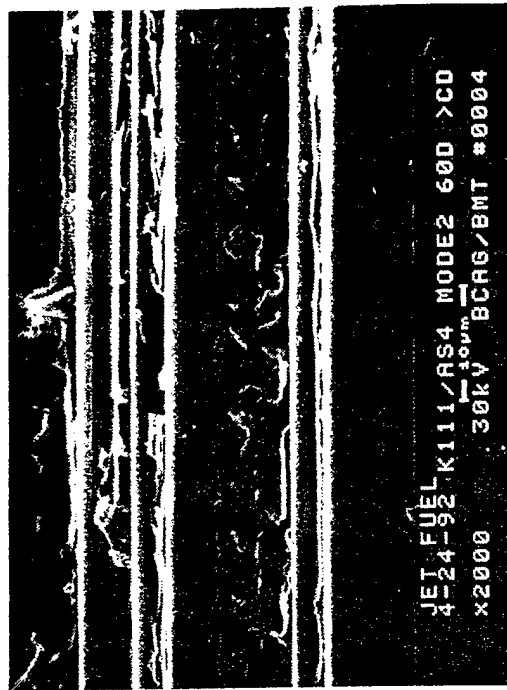


60 degree tilt (a) 20X



60 degree tilt (b) 400X

Mechanically induced  
crack direction

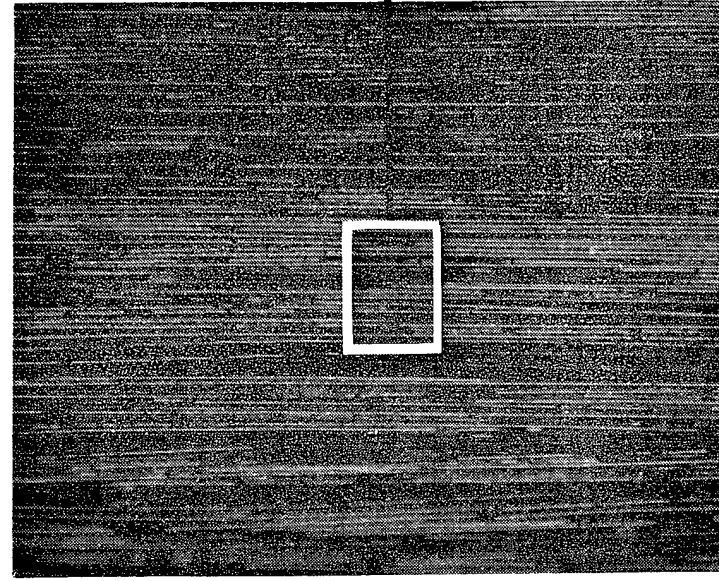
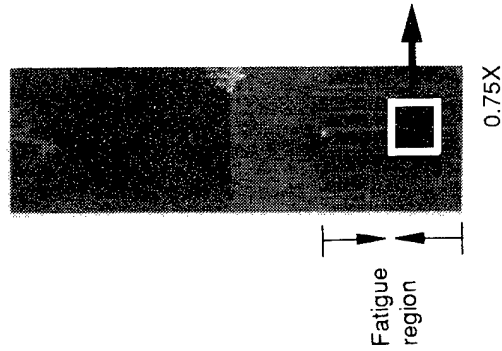


60 degree tilt (c) 2000X

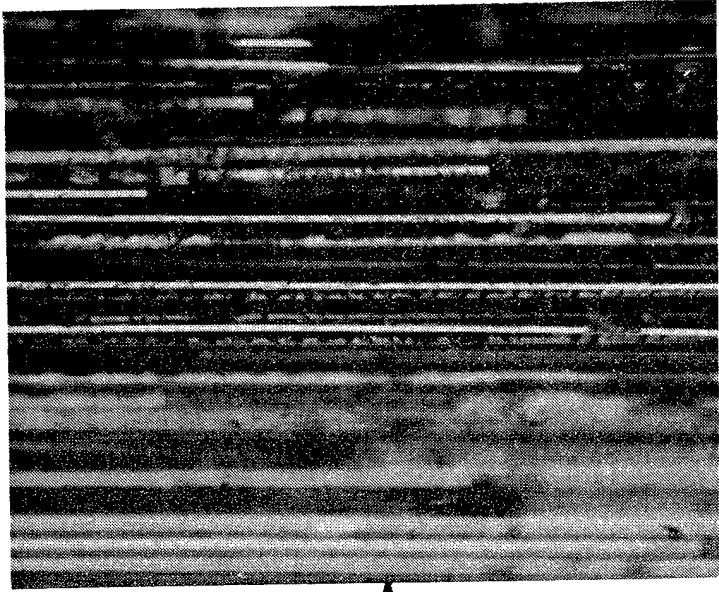
Figure 3.2-16. SEM Fractographs of a K111/AS4 Interlaminar Mode II (Shear) Fatigue Fracture Surface, Room Temperature

49754.25 9-5571 D1 ai

Crack growth direction  
→



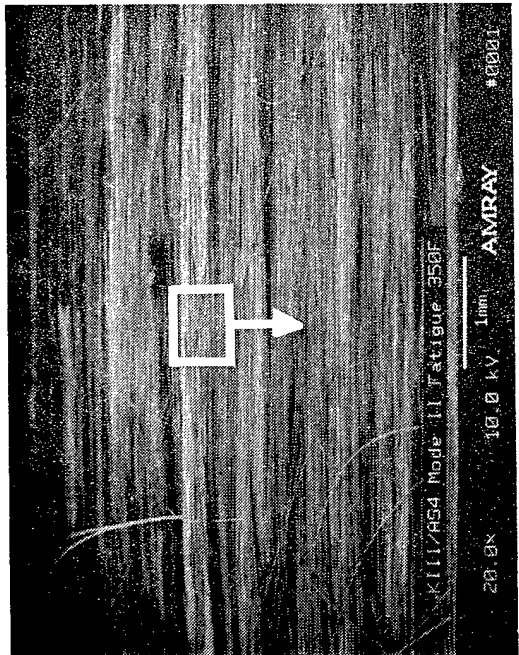
100X



400X

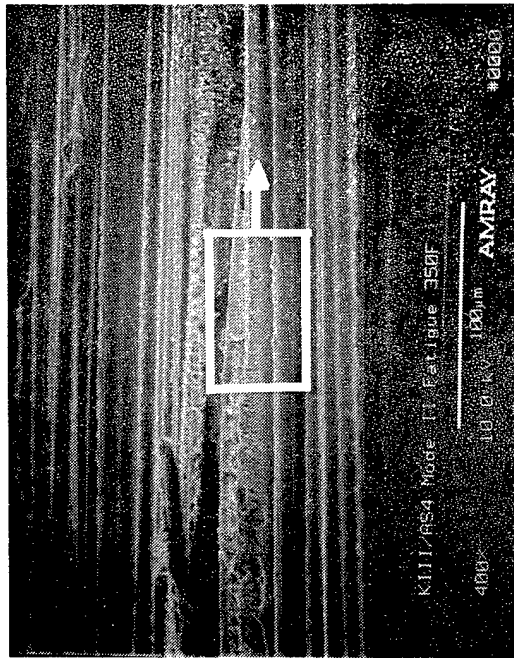
Figure 3.2-17. Optical Fractographs of K111/AS4 Interlaminar Mode II (Shear) Fatigue, 350° F, High Stress

49754.10 9-5571 D8 fh

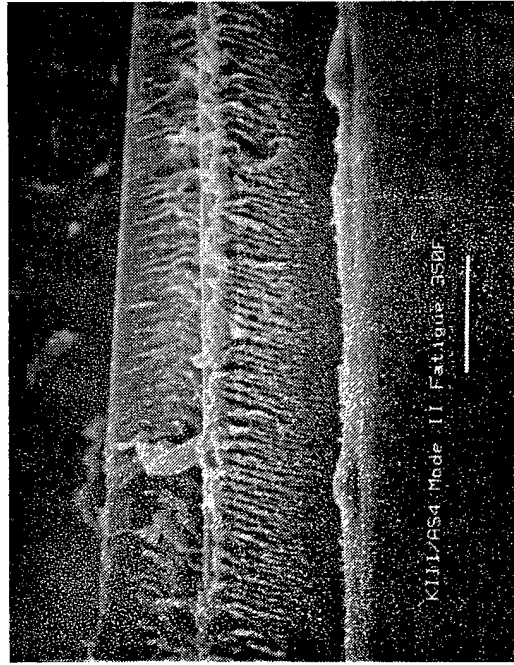


60 degree tilt (a) 20X

Mechanically induced  
crack direction



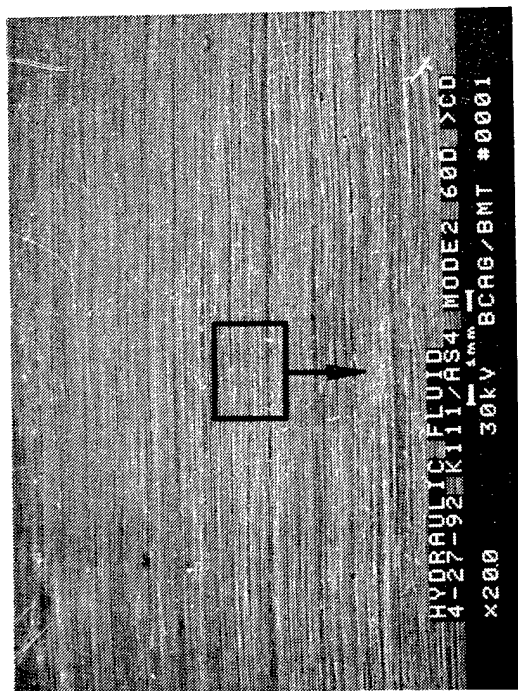
60 degree tilt (b) 400X



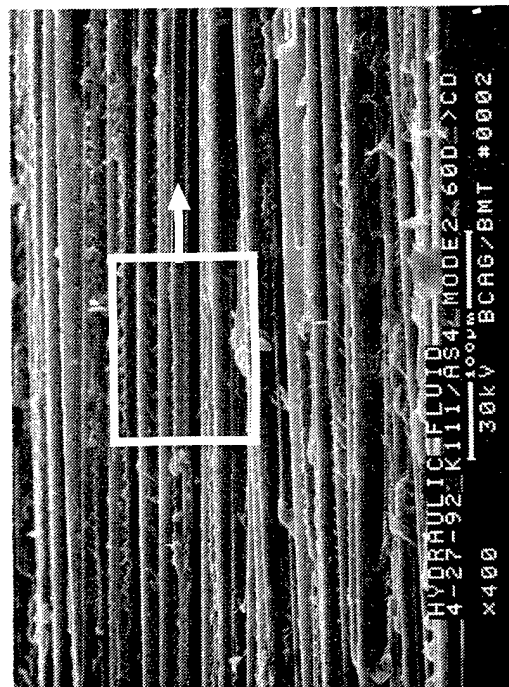
60 degree tilt (c) 2000X

Figure 3.2-18. SEM Fractographs of a K111/RS4 Interlaminar Mode II (Shear) Fatigue Fracture Surface, 350° F

49754.26 9-5571 D1 ai

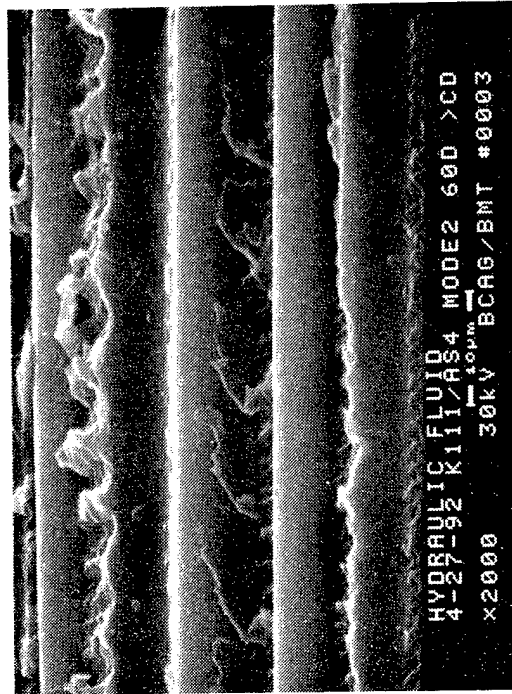


60 degree tilt (a) 20X



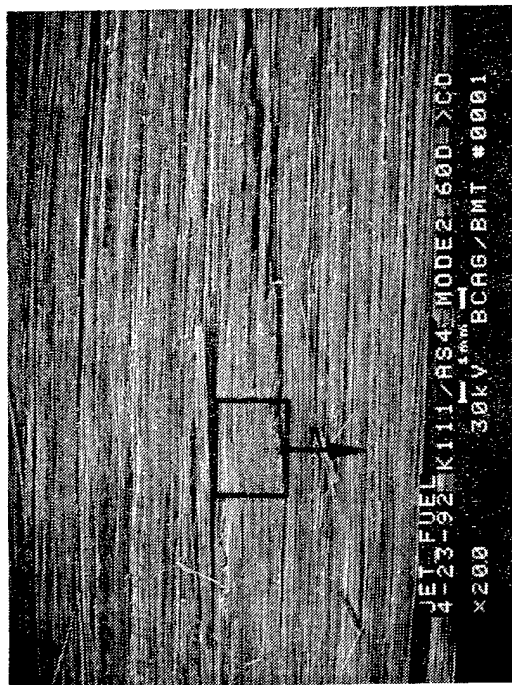
60 degree tilt (b) 400X

Mechanically induced  
crack direction

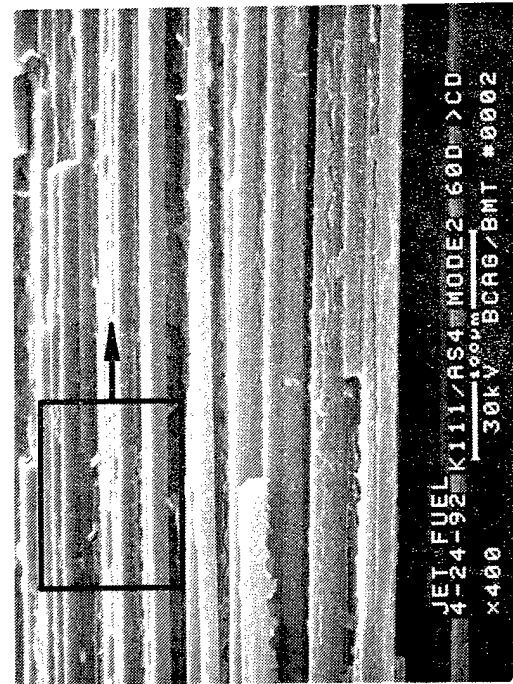


60 degree tilt (c) 2000X

Figure 3.2-19. SEM Fractographs of a K111/AS4 Interlaminar Mode II Shear Fracture Surface Exposed to Hydraulic Fluid for 7 Days

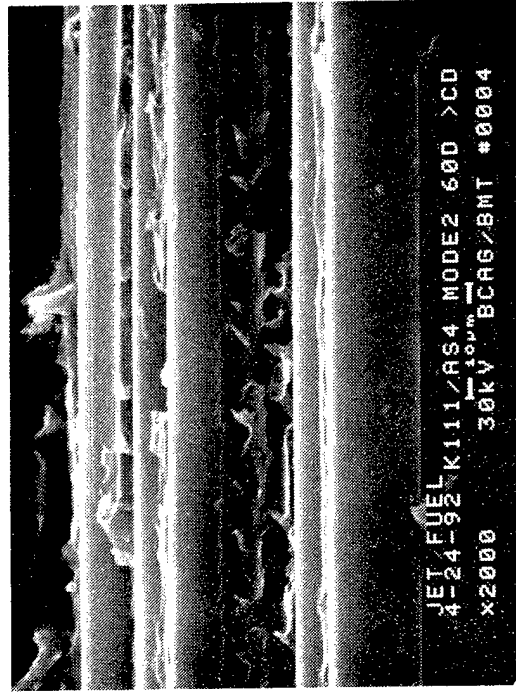


60 degree tilt (a) 200X



60 degree tilt (b) 400X

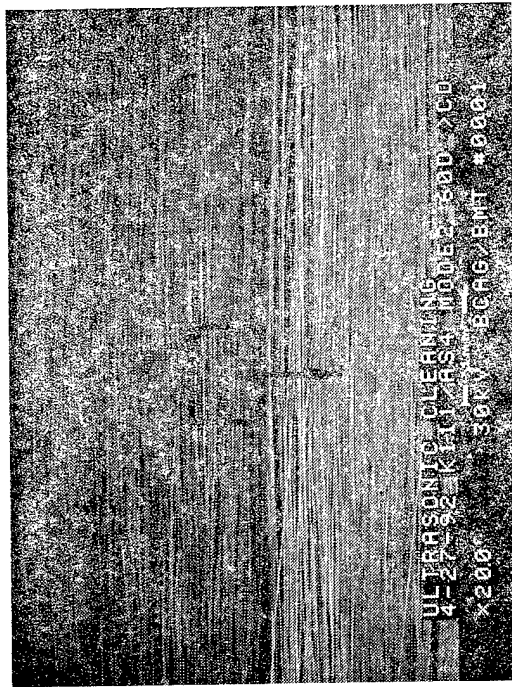
Mechanically induced crack direction



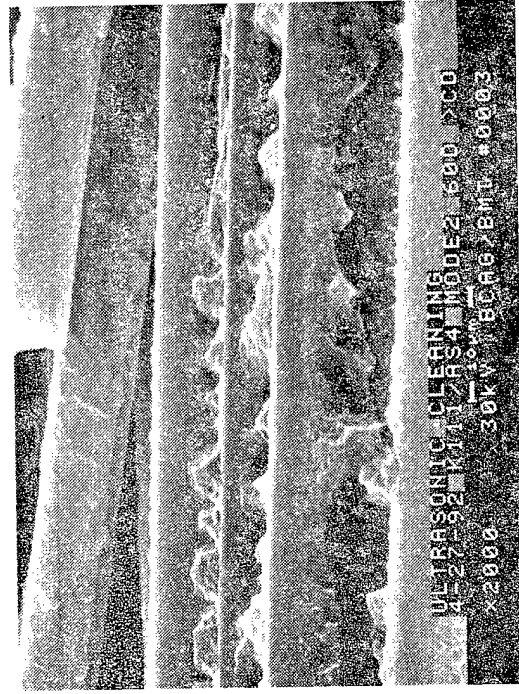
60 degree tilt (c) 2000X

Figure 3.2-20. SEM Fractographs of a K111/AS4 Interlaminar Mode II Shear Fracture Surface Exposed to JP4 Jet Fuel for 7 Days

2405.06 9-5576 D1ai



60 degree tilt (a) 20X

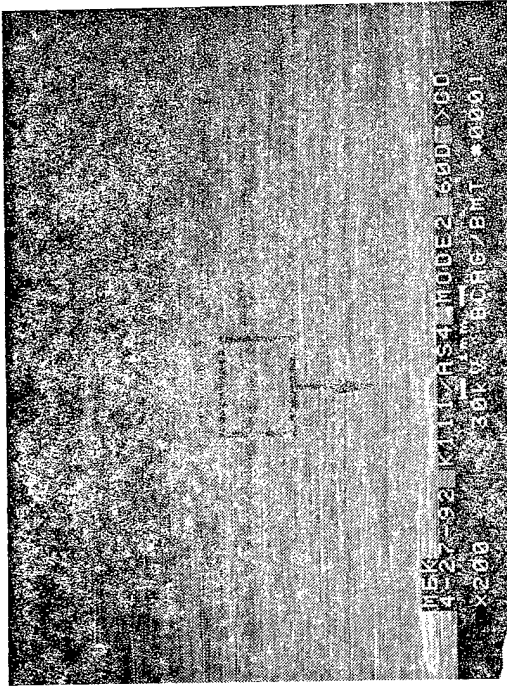


60 degree tilt (c) 2000X

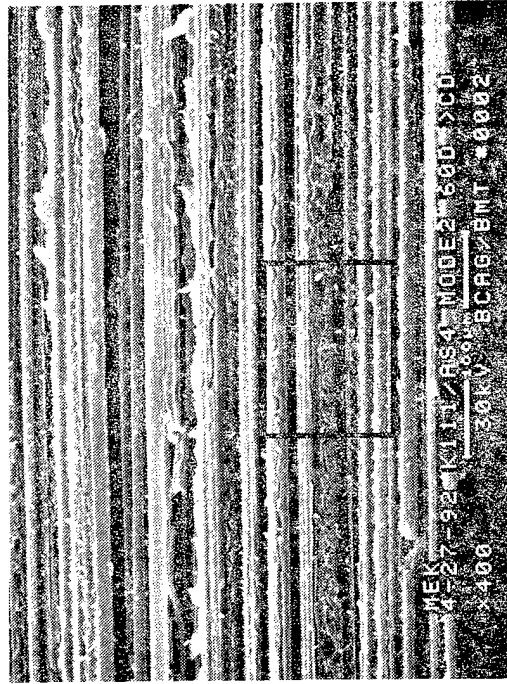


60 degree tilt (b) 400X

Figure 3.2-21. SEM Fractographs of a K1117/AS4 Interlaminar Mode II Shear Fracture Surface Exposed to Ultrasonic Agitation in Distilled Water for 24 Hours  
2405.01 9-5576 D1ai

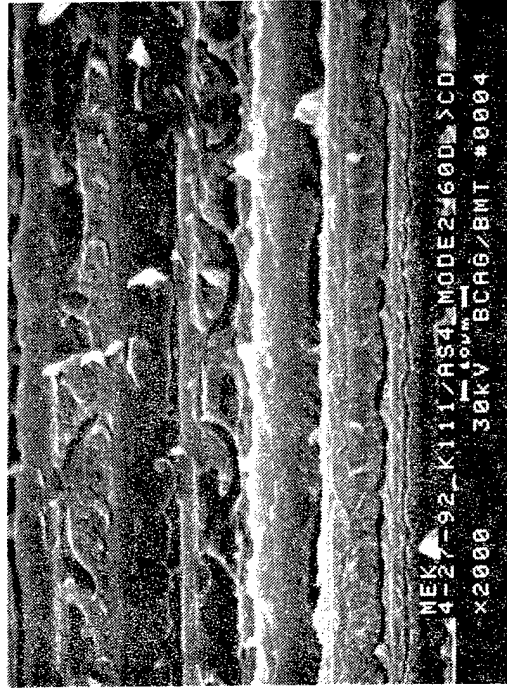


60 degree tilt (a) 20X



60 degree tilt (b) 400X

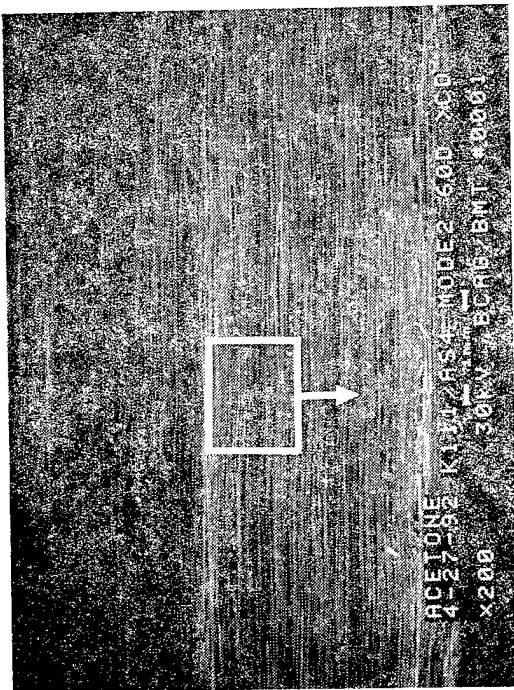
Mechanically induced  
crack direction



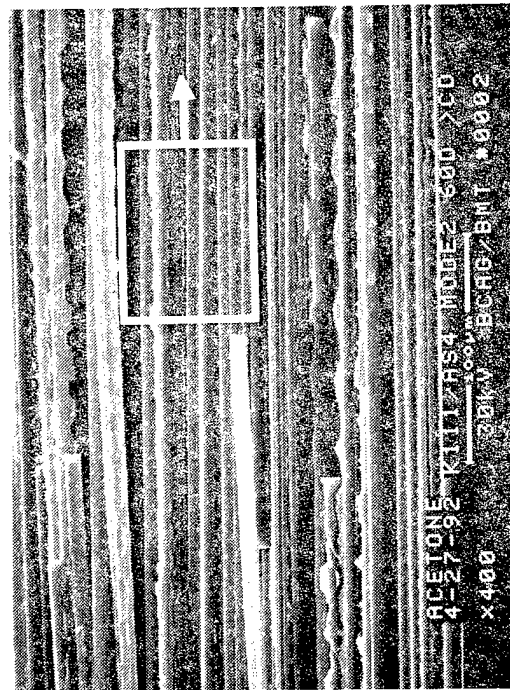
60 degree tilt (c) 2000X

Figure 3.2-22. SEM Fractographs of a K111/AS4 Interlaminar Mode II Shear Fracture Surface Exposed to MEK for 24 Hours



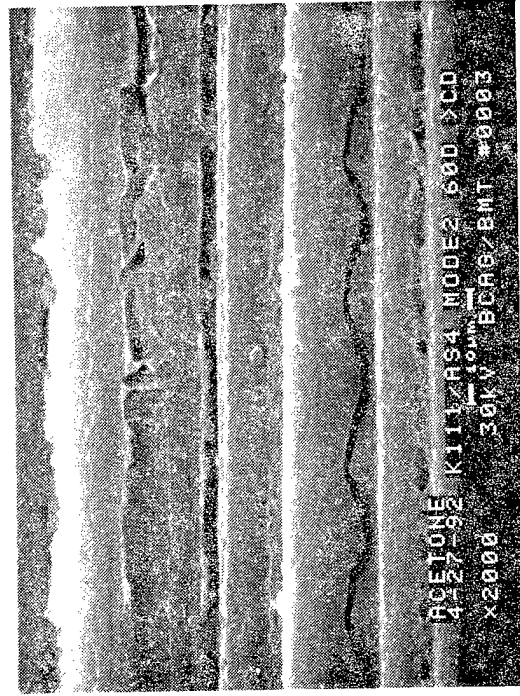


60 degree tilt (a) 20X



60 degree tilt (b) 400X

Mechanically induced  
crack direction

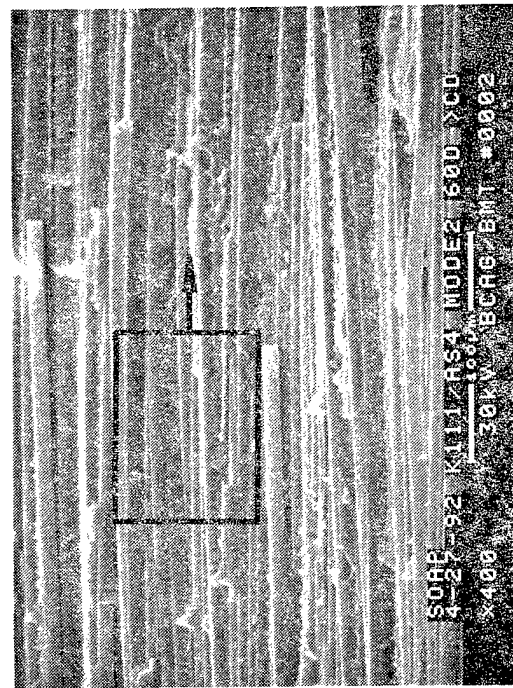


60 degree tilt (c) 2000X

Figure 3.2-23. SEM Fractographs of a K111/AS4 Interlaminar Mode II Shear Fracture Surface Exposed to Acetone for 24 Hours

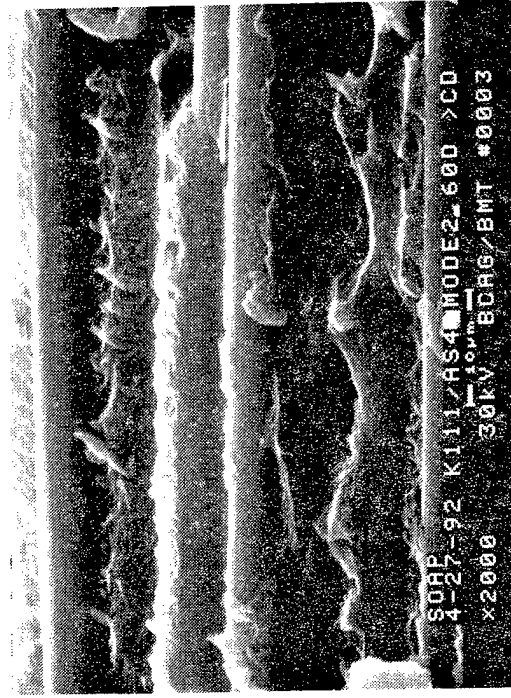


60 degree tilt (a) 20X



60 degree tilt (b) 400X

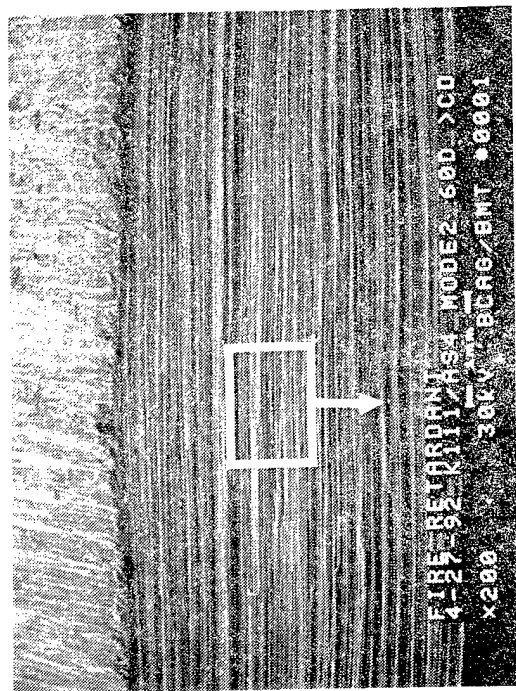
Mechanically induced crack direction



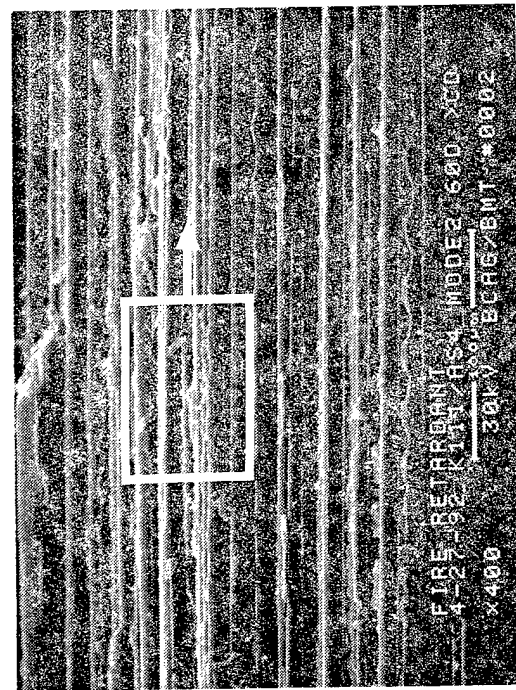
60 degree tilt (c) 2000X

Figure 3.2-24. SEM Fractographs of a K111/AS4 Interlaminar Mode II Shear Fracture Surface Exposed to Soap Solution for 24 Hours

2405.04 9-5576 D1ai

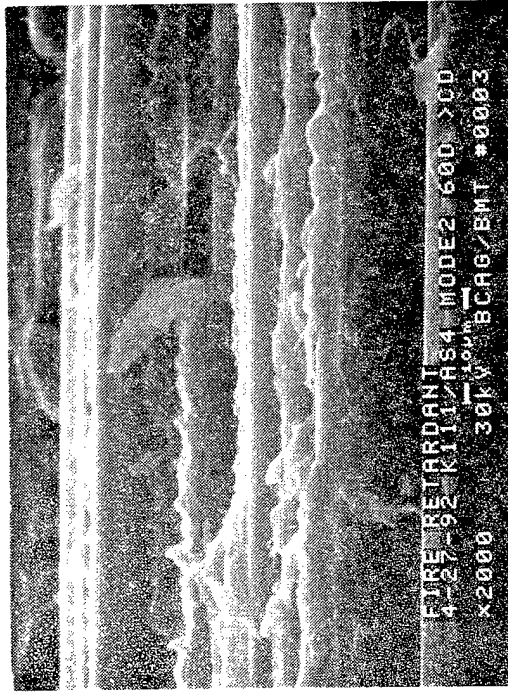


60 degree tilt (a) 20X



60 degree tilt (b) 400X

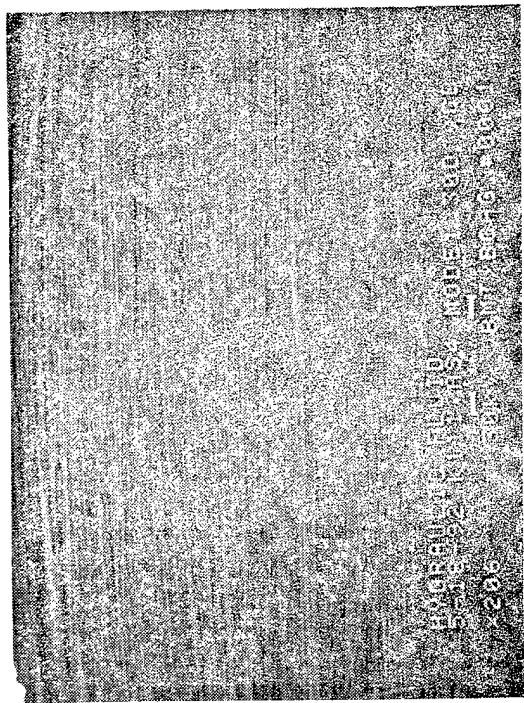
Mechanically induced  
crack direction



60 degree tilt (c) 2000X

Figure 3.2-25. SEM Fractographs of a K111/ASA4 Interlaminar Mode II Shear Fracture Surface Exposed to Fire Retardant Foam for 7 Days

2405.05 9-5576 D1ai

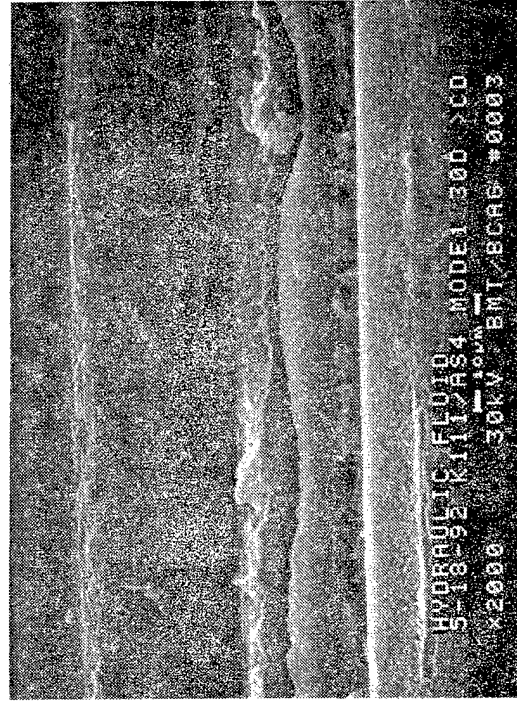


30 degree tilt (a) 20X



30 degree tilt (b) 400X

Mechanically induced  
crack direction



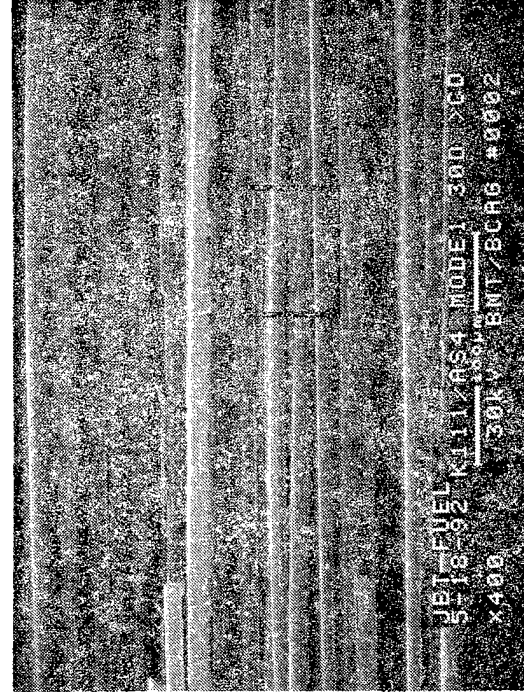
30 degree tilt (c) 2000X

Figure 3.2-26. SEM Fractographs of a Kill/AS4 Interlaminar Mode I Tension Fracture Surface Exposed to Hydraulic Fluid for 7 Days

49754.01 9-5571 D8 ai

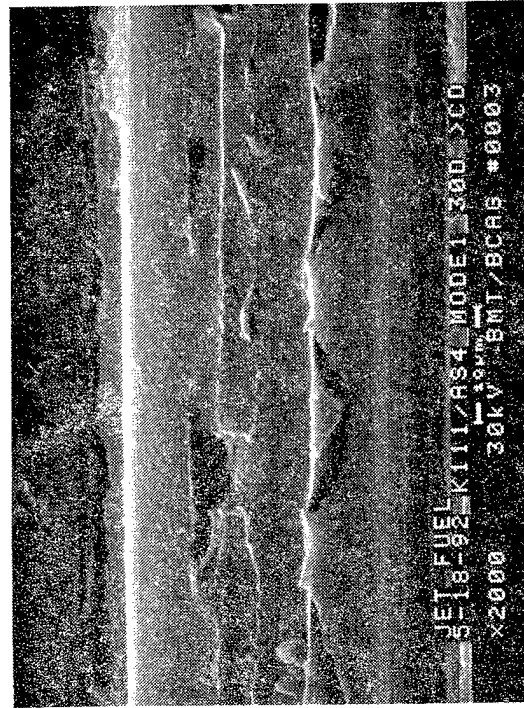


30 degree tilt (a) 20X



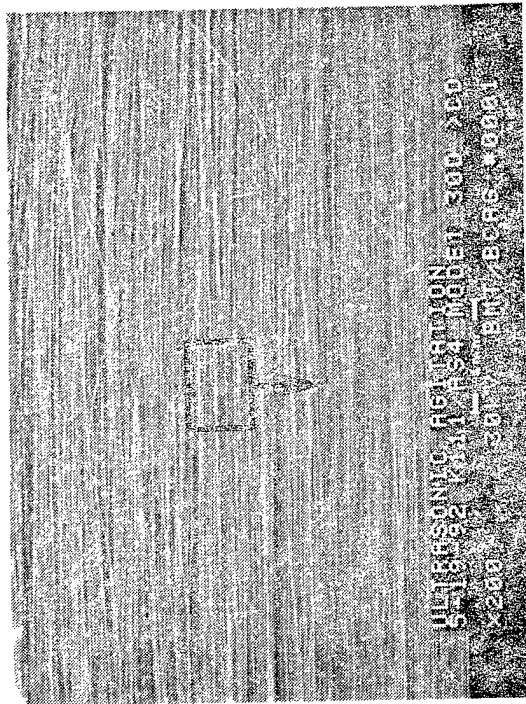
30 degree tilt (b) 400X

Mechanically induced crack direction  
 ↑



30 degree tilt (c) 2000X

Figure 3.2-27. SEM Fractographs of a K111AS4 Interlaminar Mode I Tension Fracture Surface Exposed to JP4 Jet Fuel for 7 Days

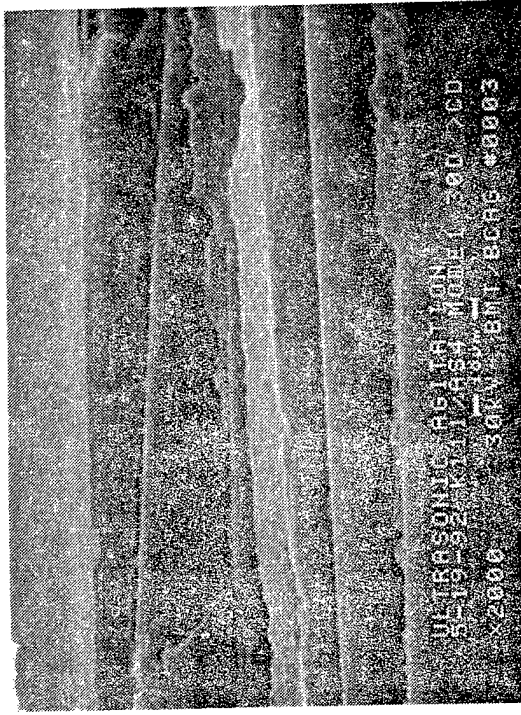
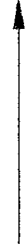


30 degree tilt (a) 20X



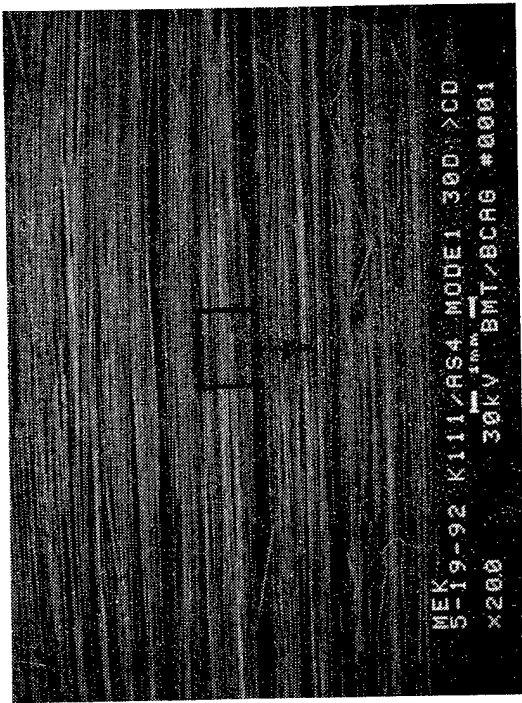
30 degree tilt (b) 400X

Mechanically induced crack direction

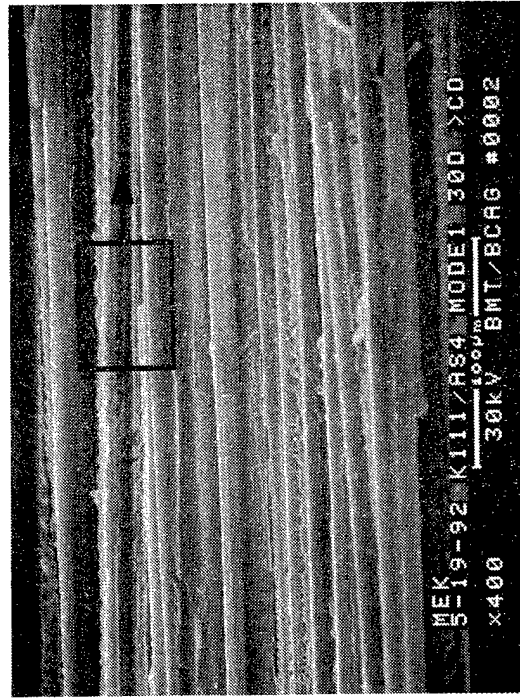


30 degree tilt (c) 2000X

**Figure 3.2-28. SEM Fractographs of a KIII /AS4 Interlaminar Mode I Tension Fracture Surface Exposed to Ultrasonic Agitation in Distilled Water for 24 hours**

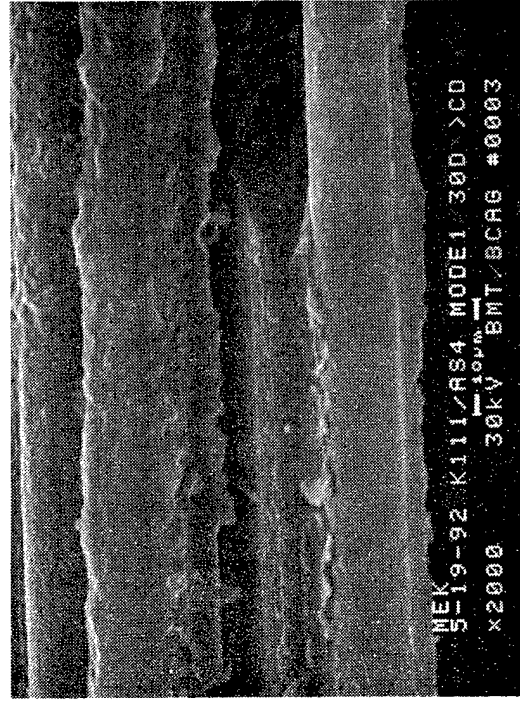


30 degree tilt (a) 20X



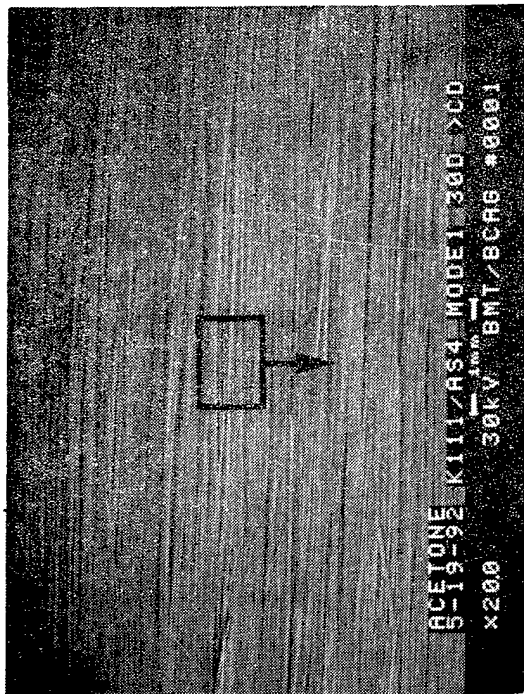
30 degree tilt (b) 400X

Mechanically induced crack direction

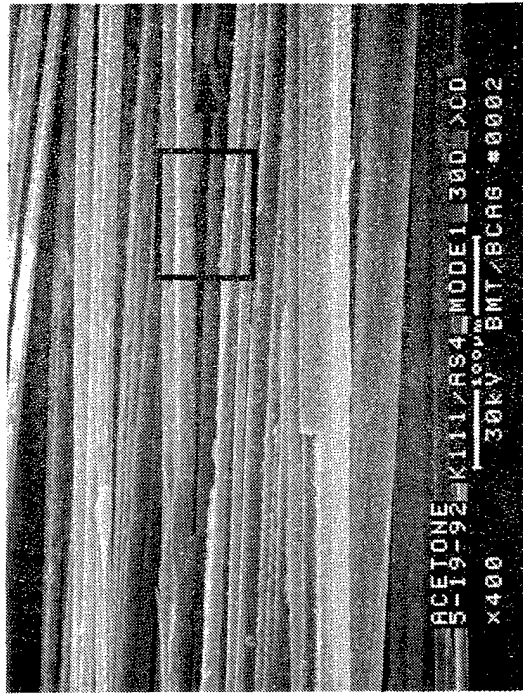


30 degree tilt (c) 2000X

Figure 3.2-29. SEM Fractographs of a K111/AS4 Interlaminar Mode I Tension Fracture Surface Exposed to MEK for 24 Hours

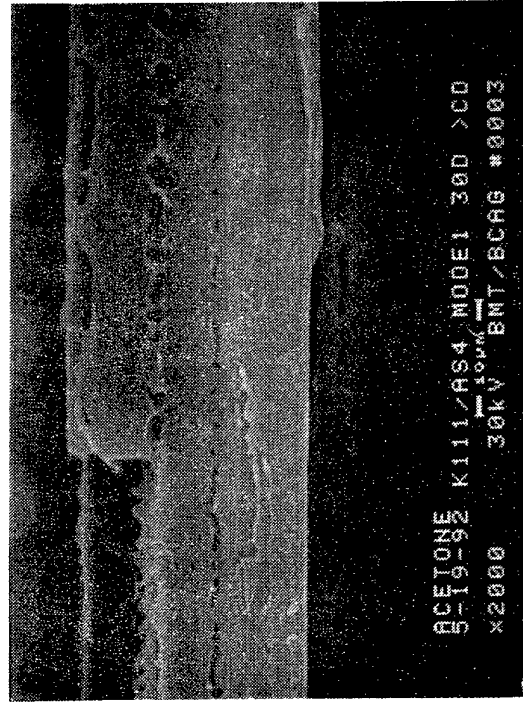


30 degree tilt (a) 20X



30 degree tilt (b) 400X

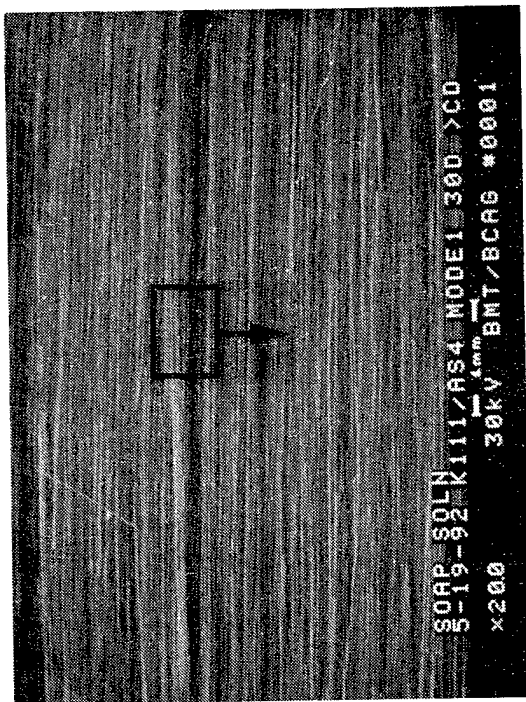
Mechanically induced crack direction



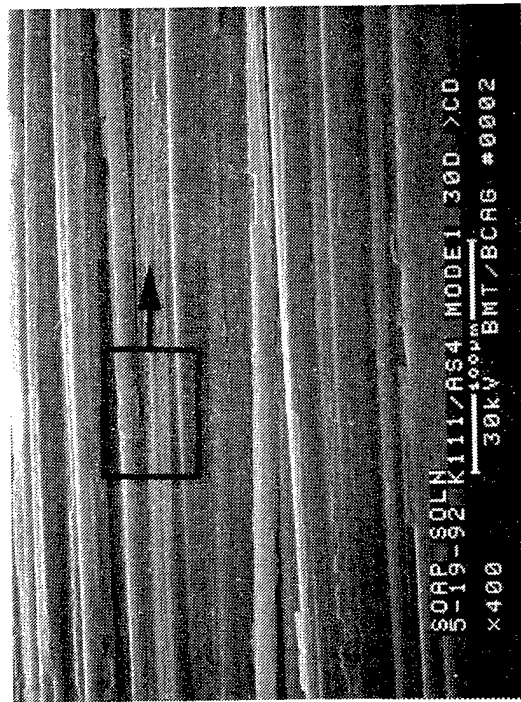
30 degree tilt (c) 2000X

Figure 3.2-30. SEM Fractographs of a K111/AS4 Interlaminar Mode I Tension Fracture Surface Exposed to Acetone for 24 hours



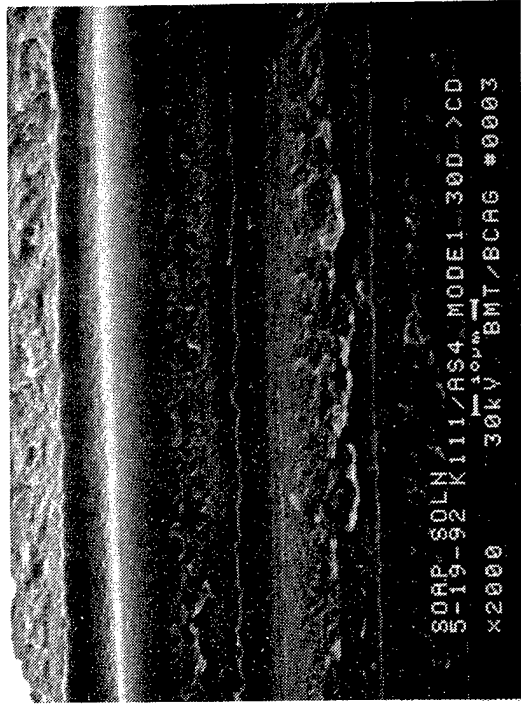


30 degree tilt (a) 20X



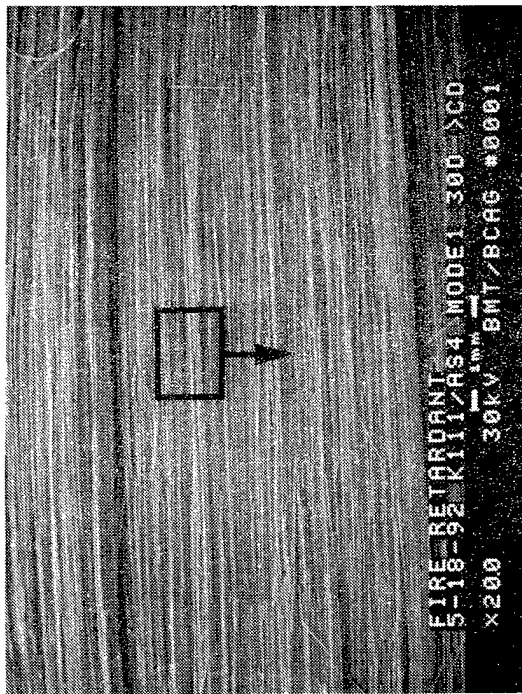
30 degree tilt (b) 400X

Mechanically induced crack direction

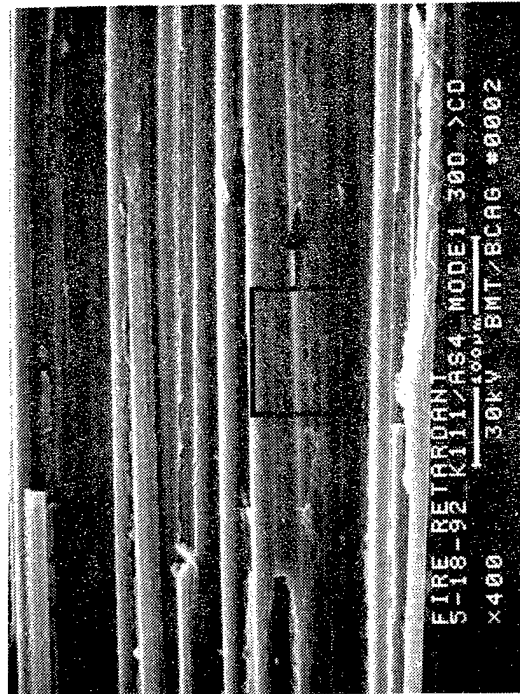


30 degree tilt (c) 2000X

Figure 3.2-31. SEM Fractographs of a K111/AS4 Interlaminar Mode I Tension Fracture Surface Exposed to Soap Solution for 24 hours

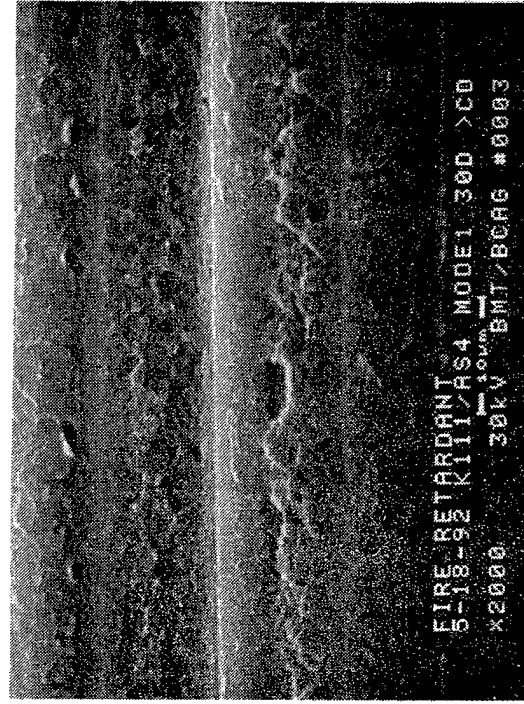


30 degree tilt (a) 20X



30 degree tilt (b) 400X

Mechanically induced crack direction



30 degree tilt (c) 2000X

Figure 3.2-32. SEM Fractographs of a KIII/AS4 Interlaminar Mode I Tension Fracture Surface Exposed to Fire Retardant Foam for 7 Days

**SECTION 3.3**  
**CARBON/POLYIMIDE**  
**AS4/PMR-15**

**3.3.1 Introduction**

This section contains additional data for the AS4/PMR-15 graphite/polyimide (Gr/PI) fractographic database. The additional tests were designed to allow the characterization of interlaminar fracture surfaces, which were the result of fatigue crack growth and surfaces that have been affected by various environmental exposures.

**3.3.2 Fatigue**

**Interlaminar Mode I (Tension), RT and 350°F/Dry**

The overall surface morphology exhibited similar features as the fracture surface of a statically loaded specimen (Figure 3.3-1). Rivermarks and hackles were observed including fatigue striations. However, the striation features, which were usually located in fiber pull out troughs, were very difficult to identify even at very high magnifications (Figure 3.3-2a). These striations were also observed in resin rich regions, which resembled typical "beach marks" in fatigued metals (Figure 3.3-2b).

However the 350°F specimen fracture surface did not exhibit the typical mode I (tension) features. The fracture features were not distinct enough to determine the overall crack propagation direction

**Interlaminar Mode II (Shear), RT and 350°F/Dry**

The morphology of both the RT and 350°F (Figures 3.3-4 through 3.3-8) specimen surfaces exhibited characteristic shear features, such as hackles and cusps, in addition to fatigue striations (Figures 3.3-6 & 3.3-8). The striations were spaced very close together compared to the striations on the 3501-6/AS4 specimens. On the high-temperature specimen, the striations could only be identified above 5000X (See Figure 3.3-6). Because of this, locating the striations was very difficult and required a careful examination at various angles and tilts before the striations could be identified .

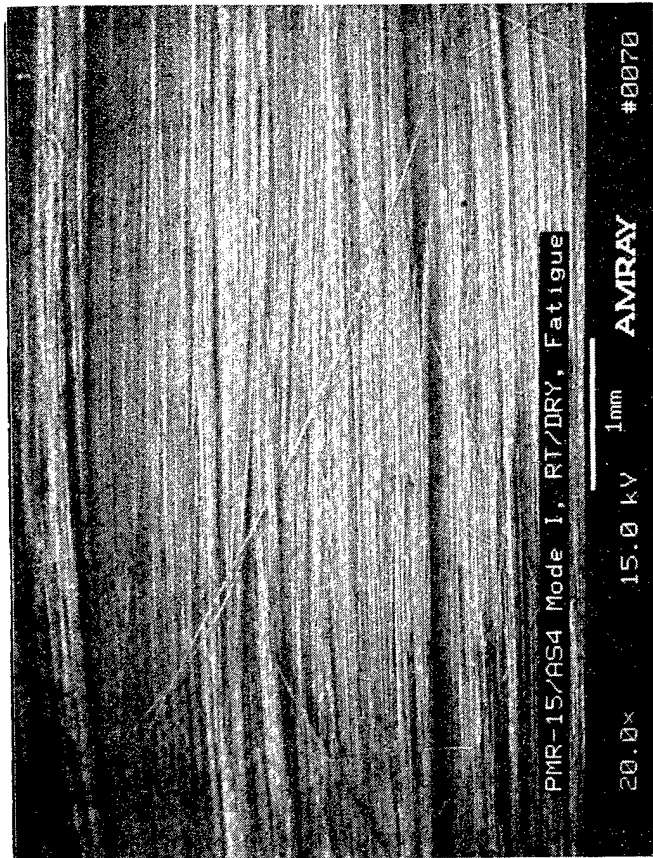
**3.3.3 Short-Term Environmental Exposure**

**Interlaminar Mode I (Tensile) Surfaces**

The effects of the exposure did not affect the fracture morphology to any noticeable degree. All of the characteristic mode I surface features were easily identified (Figure 3.3-9 through 3.3-15).

**Interlaminar Mode II (Shear) Surfaces**

Of all of the environments (Figures 3.3-16 through 3.3-22), only the exposure to the fire retardant (Figure 3.3-16) and the hydraulic fluid (Figure 3.3-19) slightly degraded the resin microflow features observed on the mode II surface. Even though these features were degraded, the surface was readily identified as a result of a mode II fracture.



Mechanically induced  
 crack direction

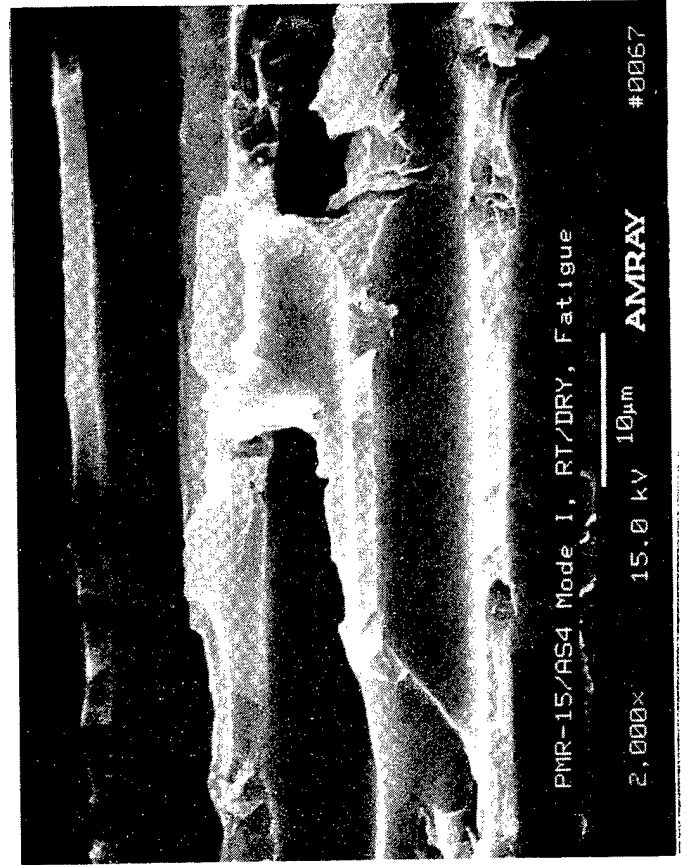
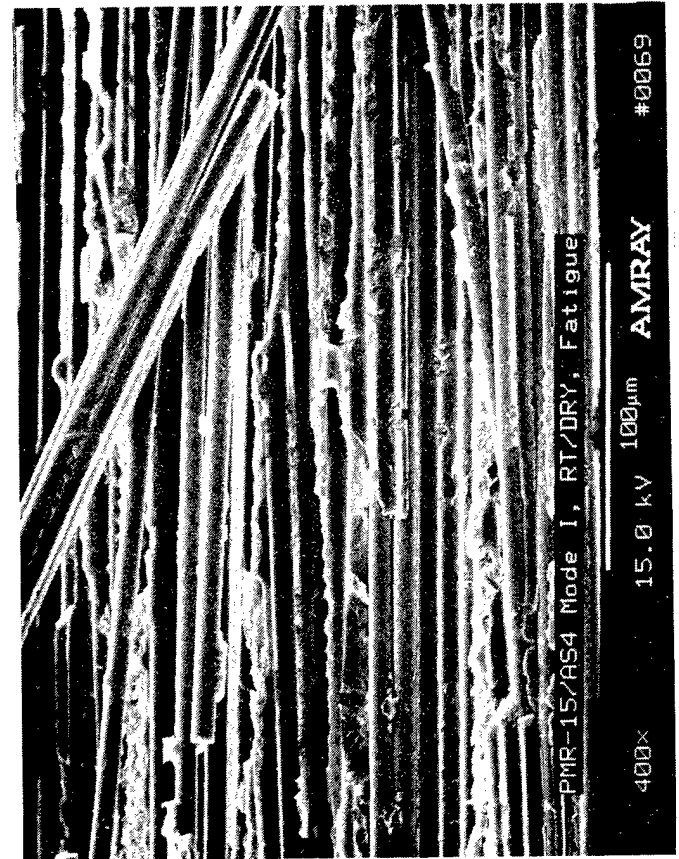
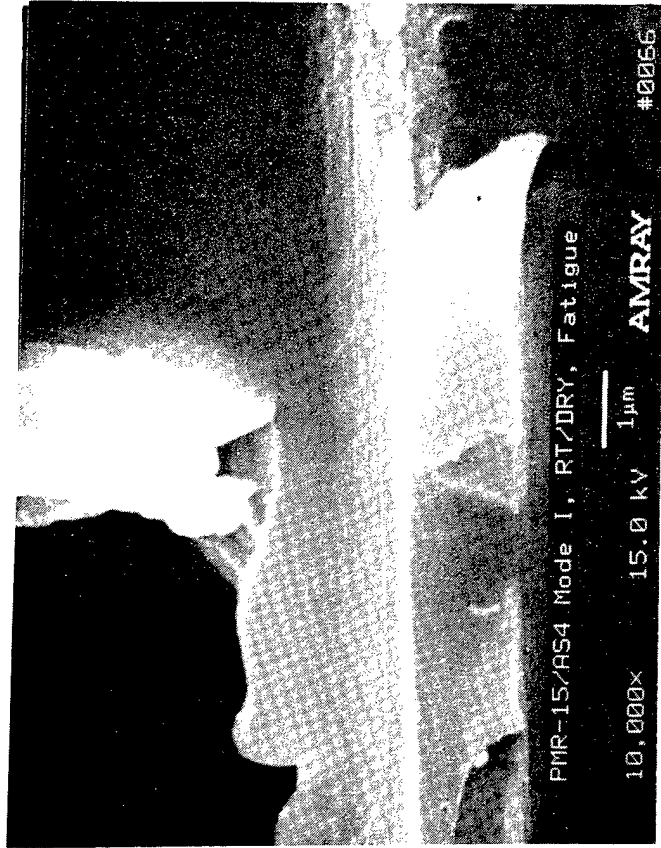
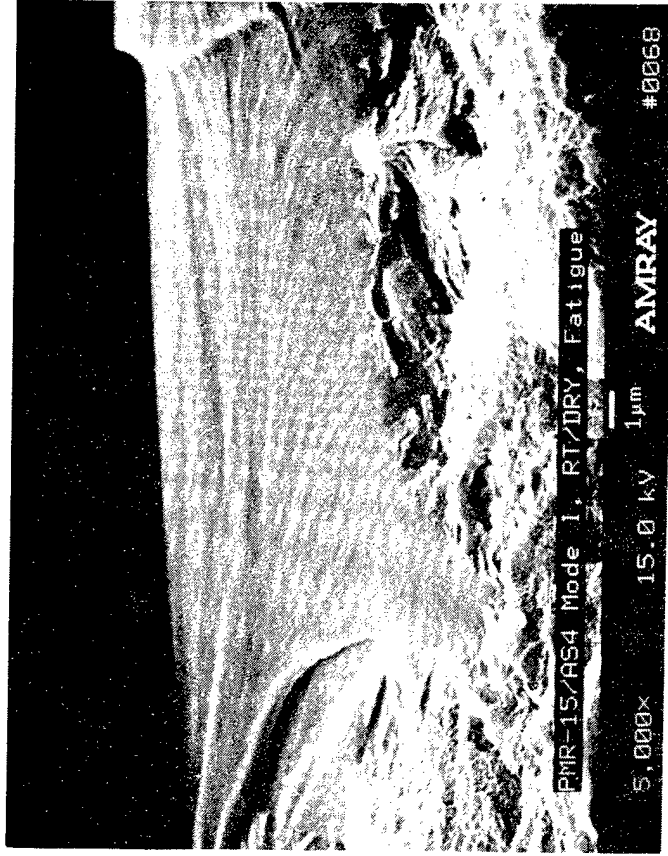


Figure 3.3-1. SEM Fractographs of a PMR-15/AS4 Interlaminar Mode I Tension Fatigue Fracture Surface, RT/Dry

Mechanically induced  
crack direction

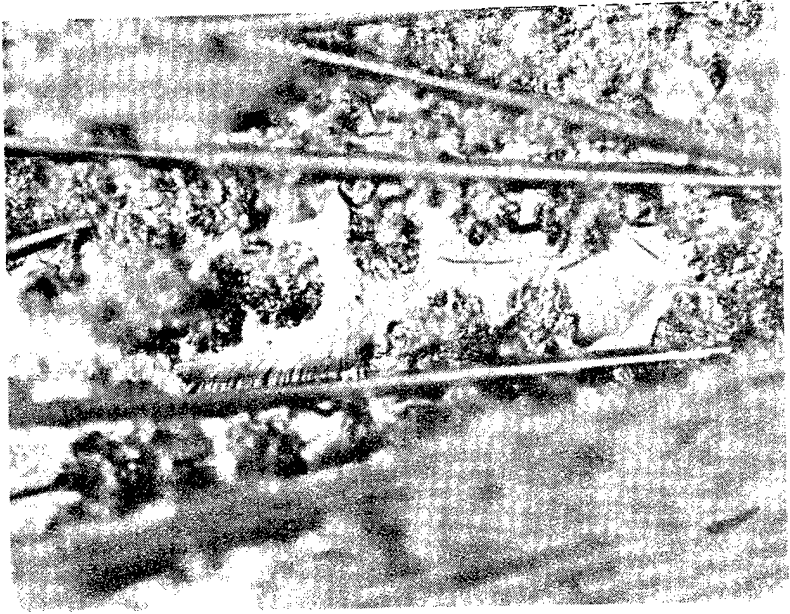
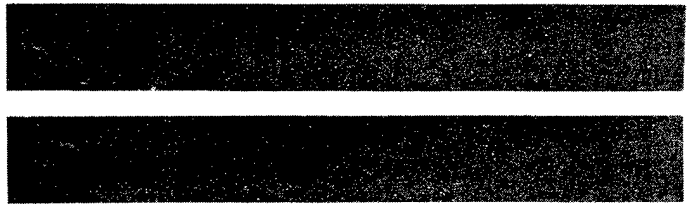


(a)

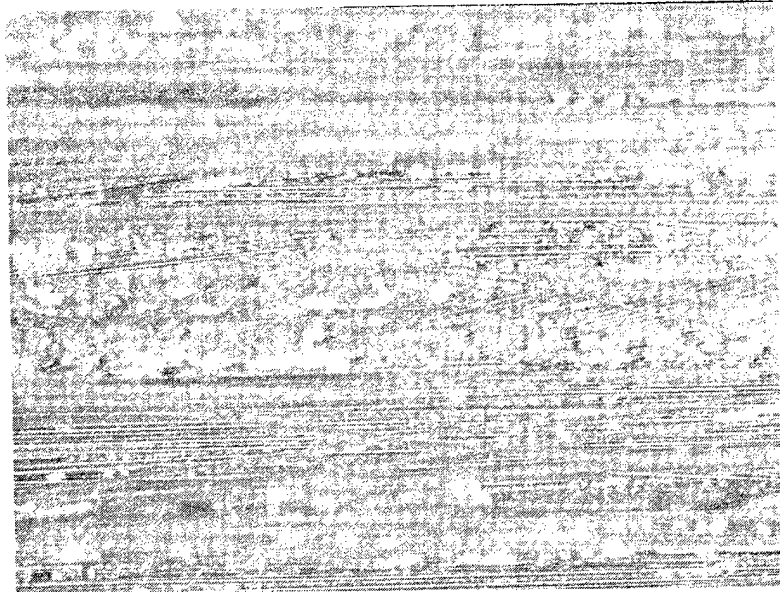


(b)

Figure 3.3-2. High-Magnification SEM Fractographs of a PMR-15/AS4 Interlaminar Mode I Tension Fatigue Fracture Surface, RT/Dry



400X



100X

Figure 3.3-3. Optical Fractographs of a PMR-15/AS4 Interlaminar Mode I (Tensile) Fatigue Fracture Surface, 350° F

Mechanically Induced  
Crack Direction  
↑

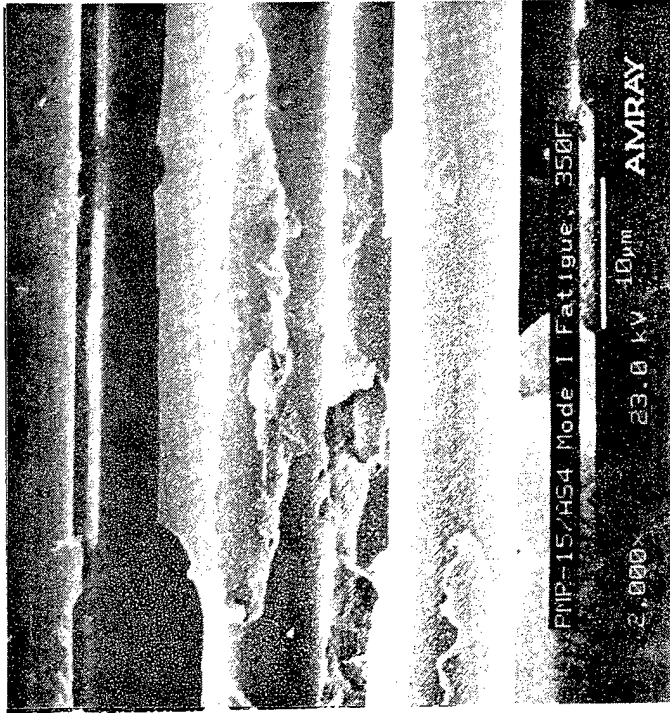
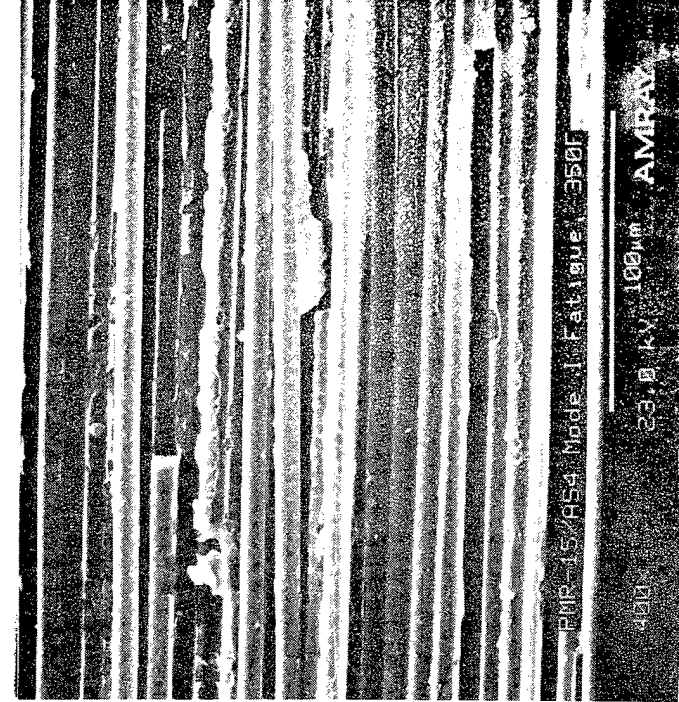
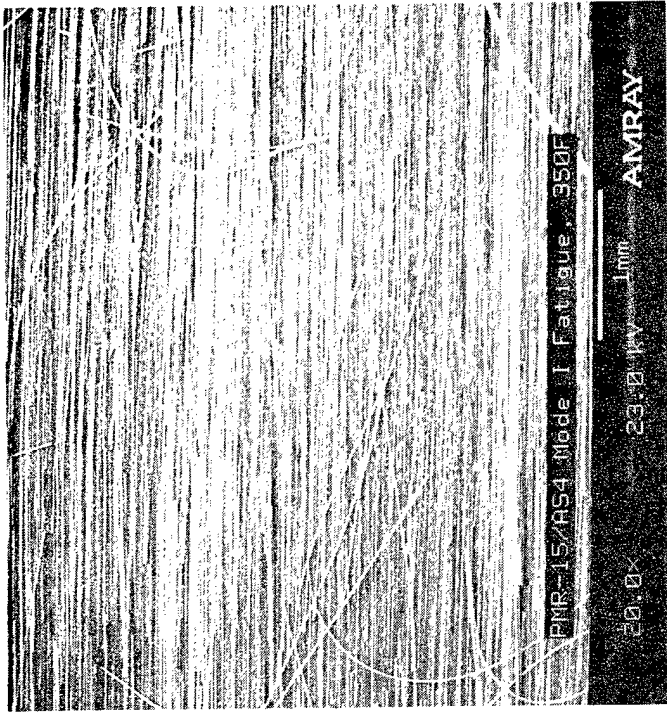
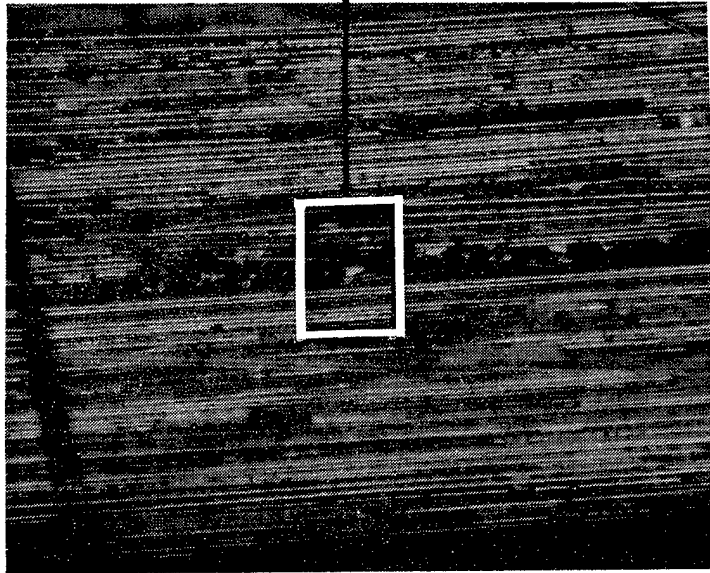
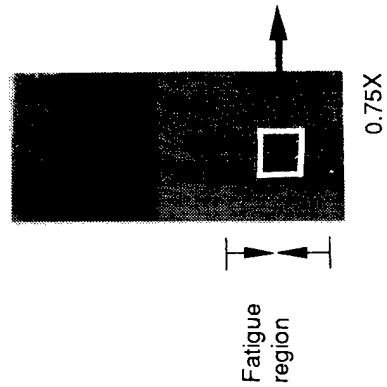


Figure 3.3-4. SEM Fractographs of a PMR-15/AS4 Interlaminar Mode I (Tensile) Fatigue Fracture Surface, 350° F



Crack growth direction  
↑



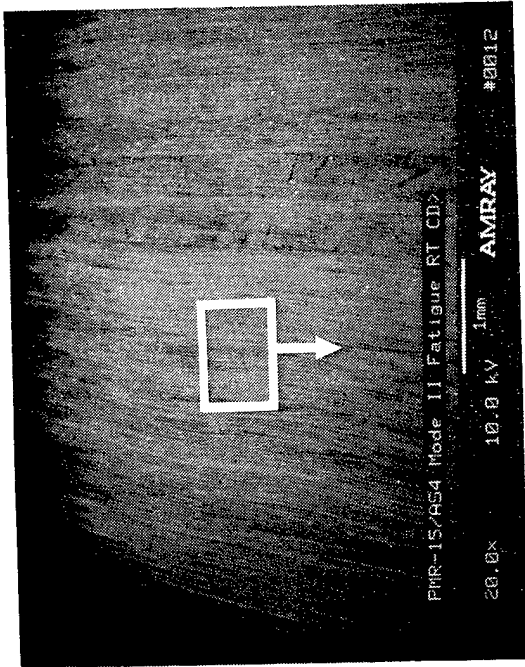
400X

100X

0.75X

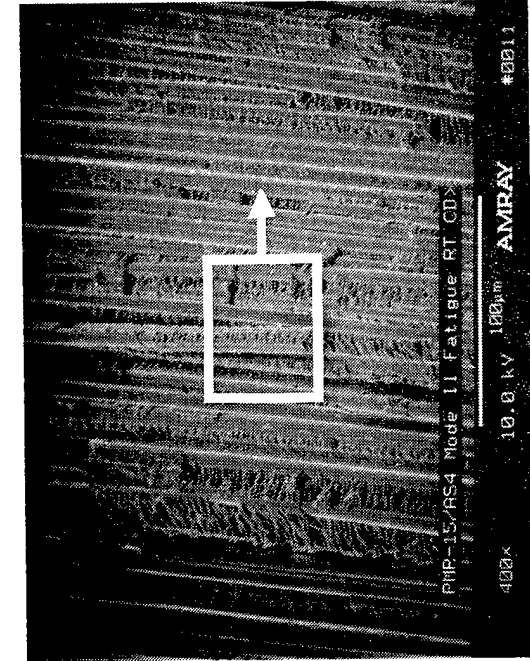
Figure 3.3-5. Optical Fractographs of PMR-15/AS4 Interlaminar Mode II (Shear) Fatigue, Room Temperature, High Stress

49754.13 9-5571 D8 fh

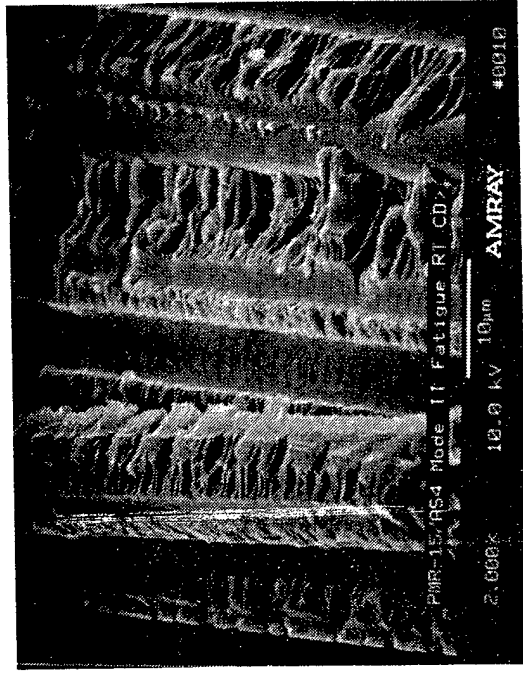


60 degree tilt (a) 20X

Mechanically induced  
crack direction



60 degree tilt (b) 400X

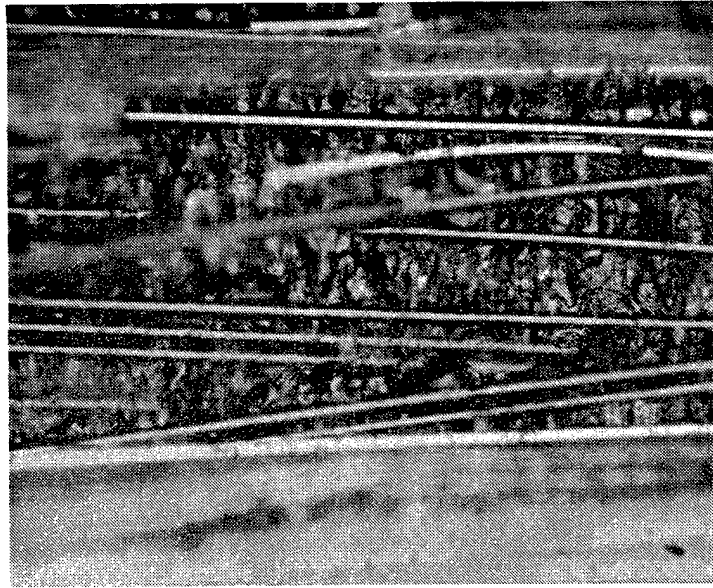
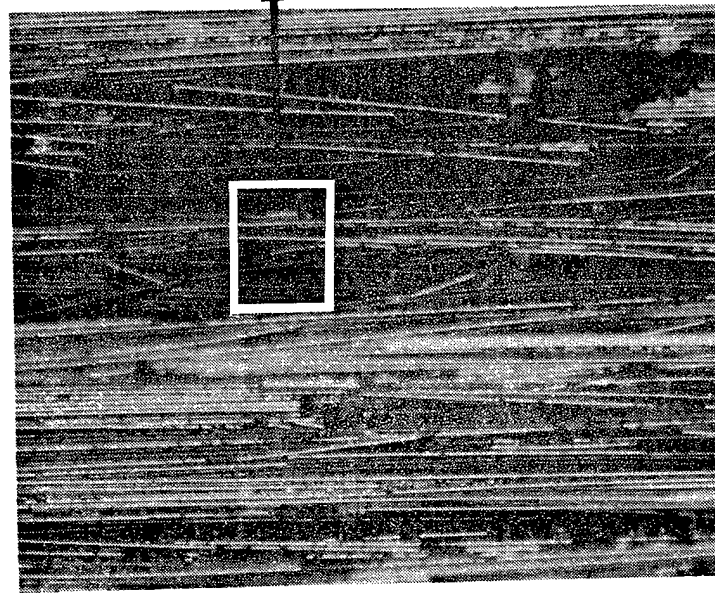
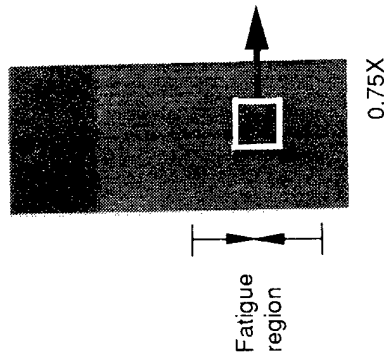


30 or 60 degree tilt (c) 2000X

Figure 3.3-6. SEM Fractographs of a PMR-15/AS4 Interlaminar Mode II (Shear) Fatigue Fracture Surface, Room Temperature

49754.22 9-5571 D1 ai

Crack growth direction  
↑

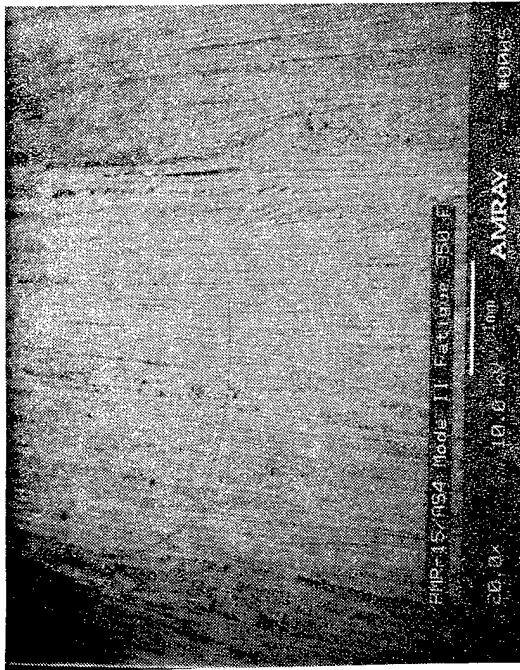


400X

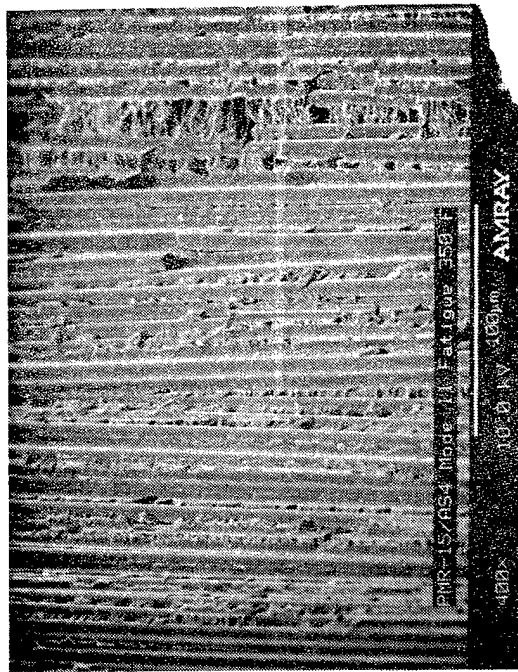
100X

Figure 3.3-7. Optical Fractographs of PMR-15/AS4 Interlaminar Mode II (Shear) Fatigue, 350° F, High Stress

49754.12 9-5571 D8 fh

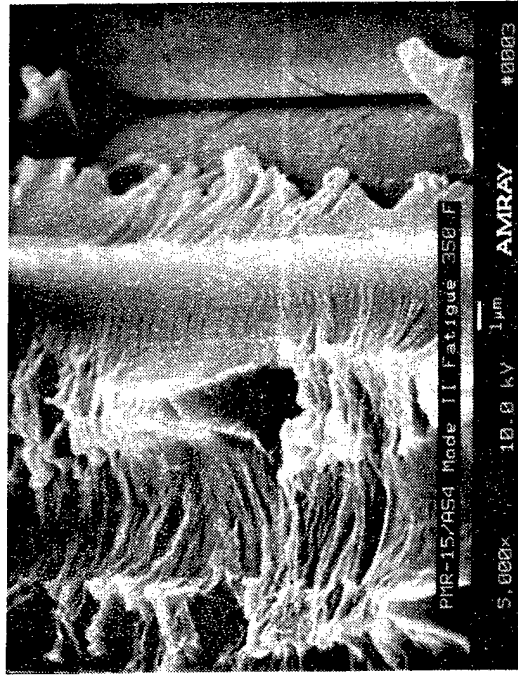


60 degree tilt (a) 20X



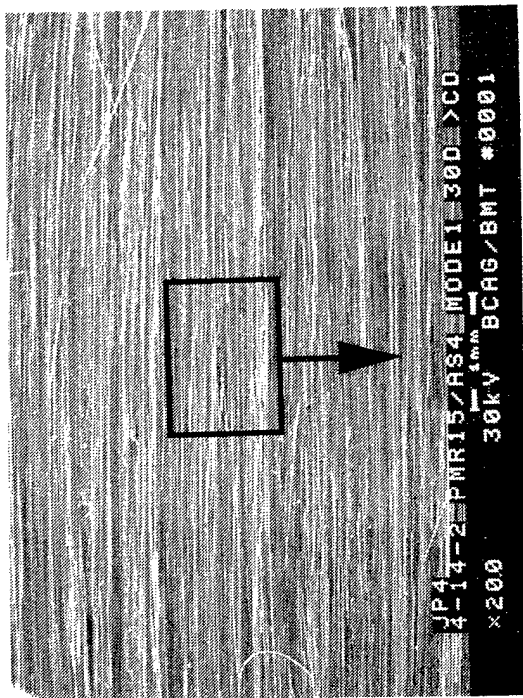
60 degree tilt (b) 400X

Mechanically induced crack direction

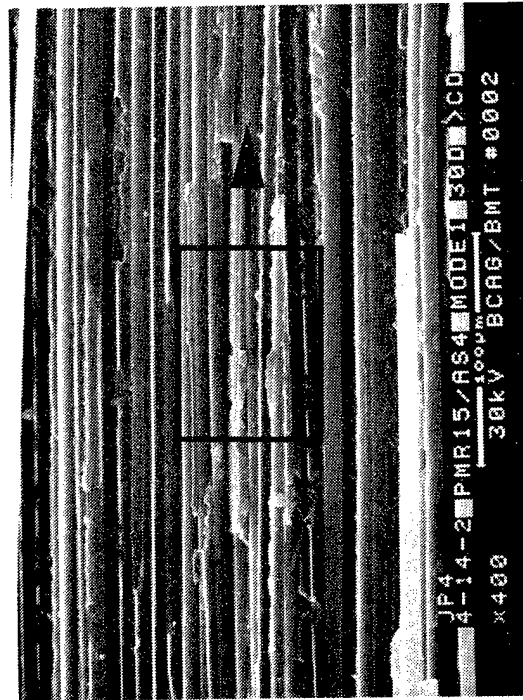


60 degree tilt (c) 5000X

Figure 3.3-8. SEM Fractographs of a PMR-15/AS4 Interlaminar Mode II (Shear) Fatigue Fracture Surface, 350°F

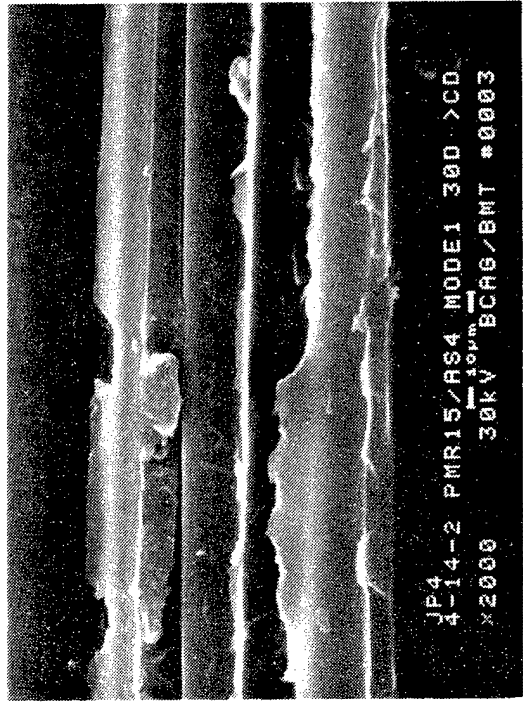


60 degree tilt (a) 200X



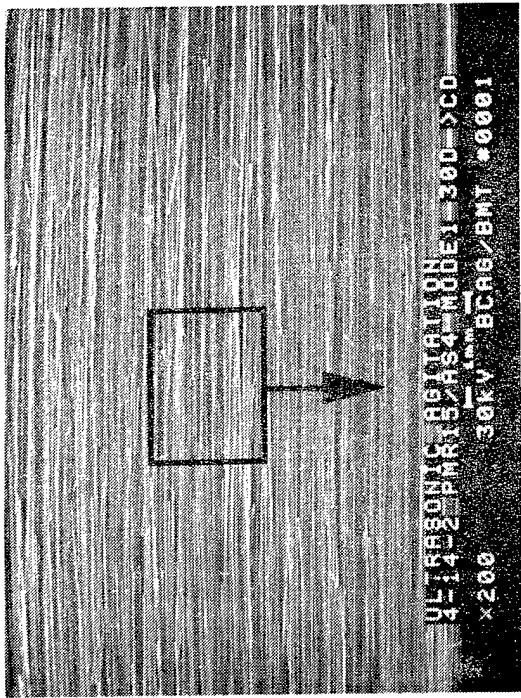
60 degree tilt (b) 400X

Mechanically induced  
crack direction

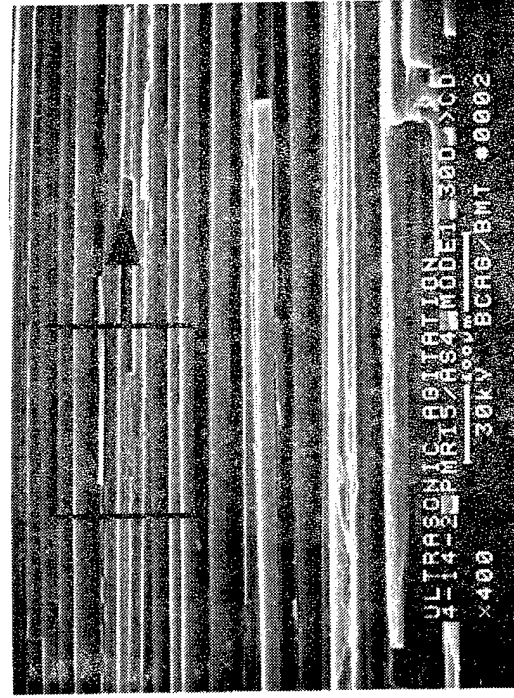


60 degree tilt (c) 2000X

Figure 3.3-9. SEM Fractographs of a PMR-15/AS4 Interlaminar Mode I Tension Fracture Surface Exposed to JP4 Jet Fuel for 7 Days

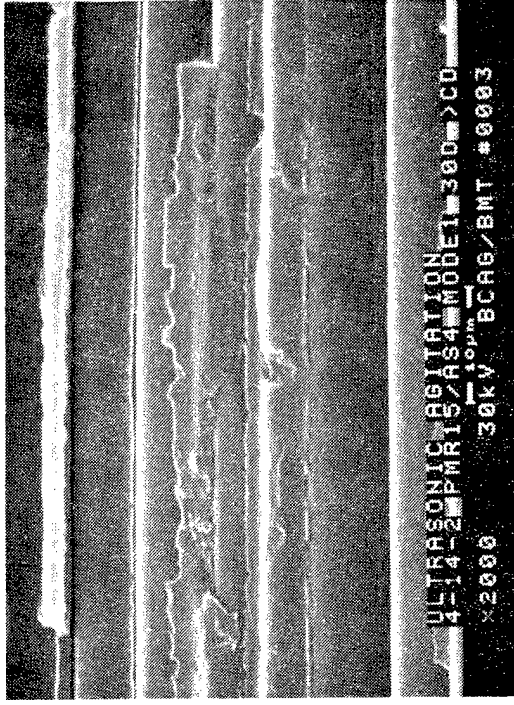


60 degree tilt (a) 20X



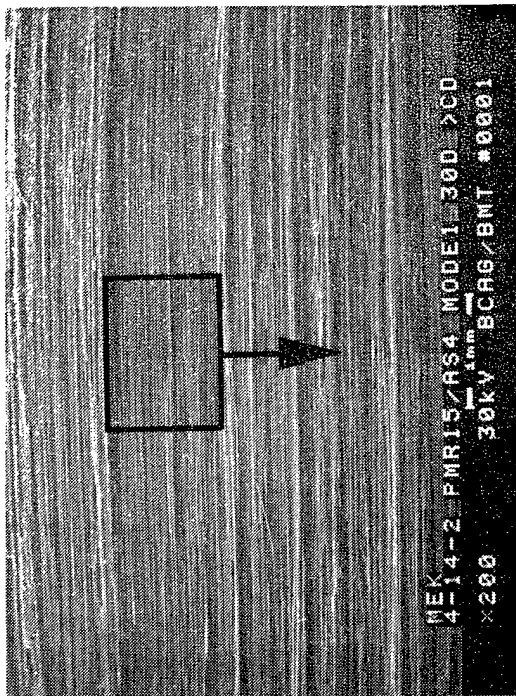
60 degree tilt (b) 400X

Mechanically induced crack direction

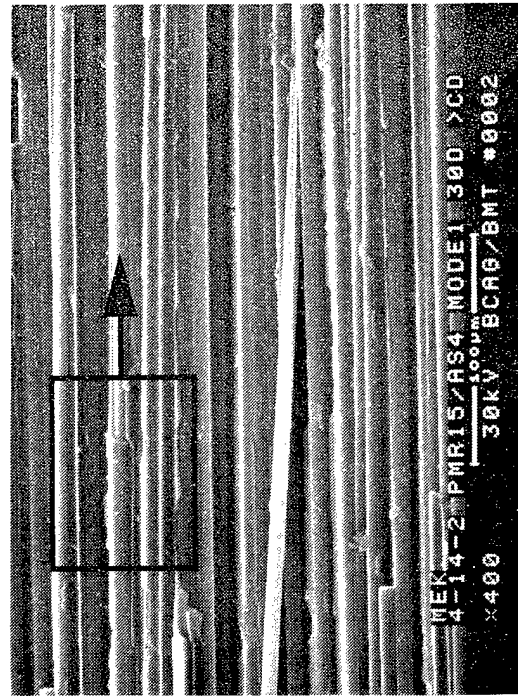


60 degree tilt (c) 2000X

Figure 3.3-10. SEM Fractographs of a PMR-15/AS4 Interlaminar Mode I Tension Fracture Surface Exposed to Ultrasonic Agitation in Distilled Water for 24 hours

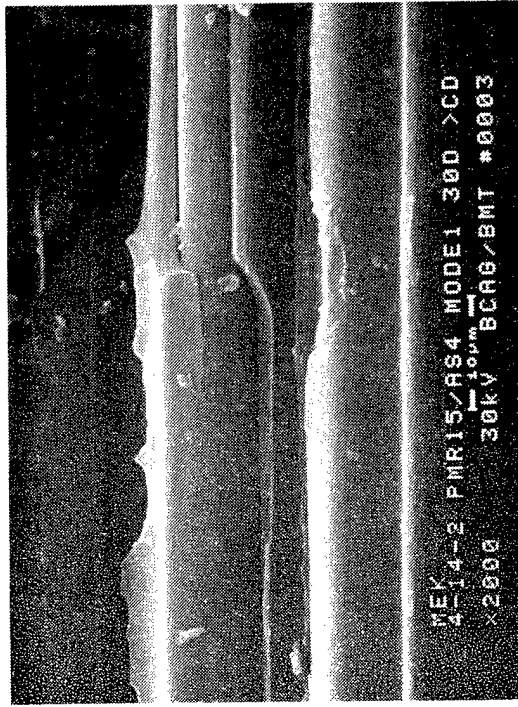


60 degree tilt (a) 20X



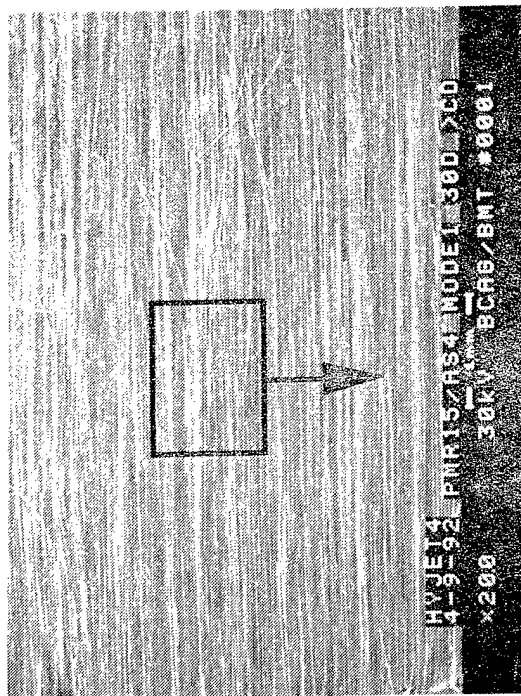
60 degree tilt (b) 400X

Mechanically induced  
crack direction

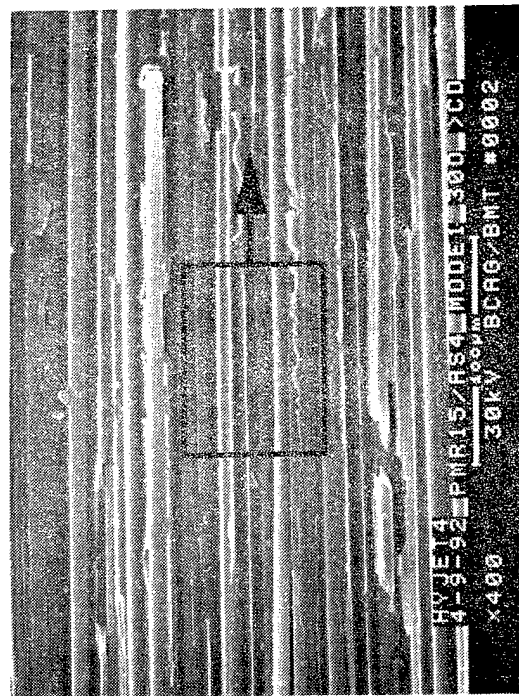


60 degree tilt (c) 2000X

Figure 3.3-11. SEM Fractographs of a PMR-15/AS4 Interlaminar Mode I Tension Fracture Surface Exposed to MEK for 24 hours

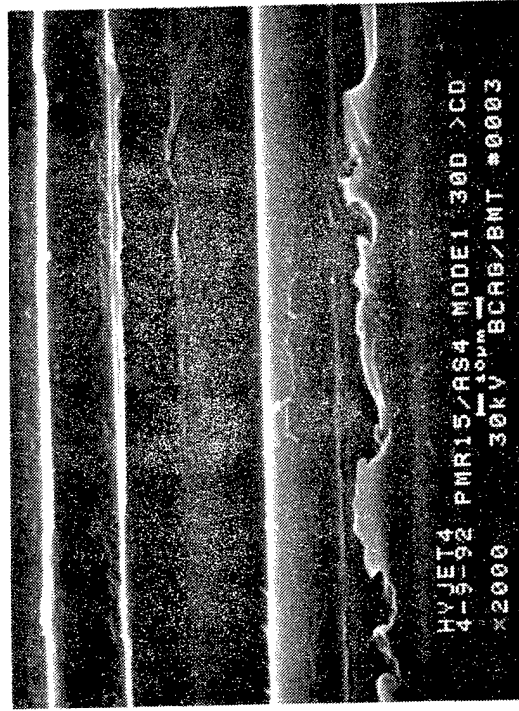


60 degree tilt (a) 20X



60 degree tilt (b) 400X

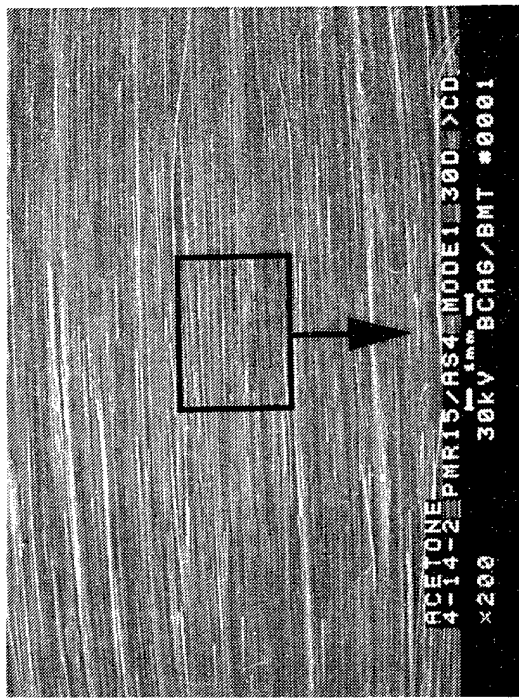
Mechanically induced  
crack direction



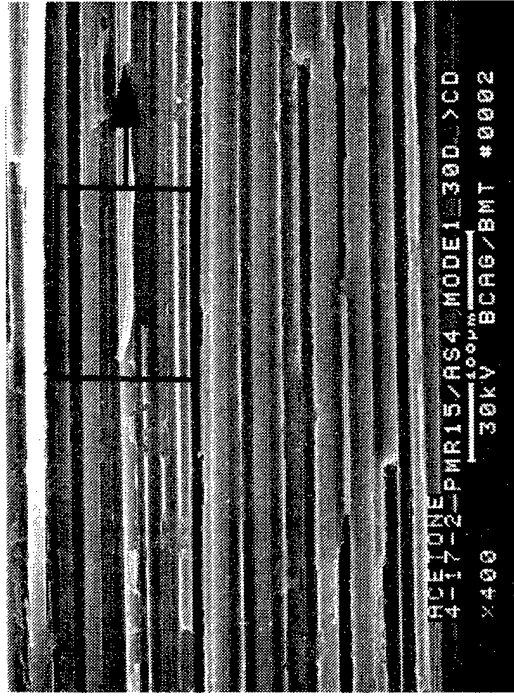
60 degree tilt (c) 2000X

Figure 3.3-12. SEM Fractographs of a PMR-15/AS4 Interlaminar Mode I Tension Fracture Surface Exposed to Hydraulic Fluid for 7 Days



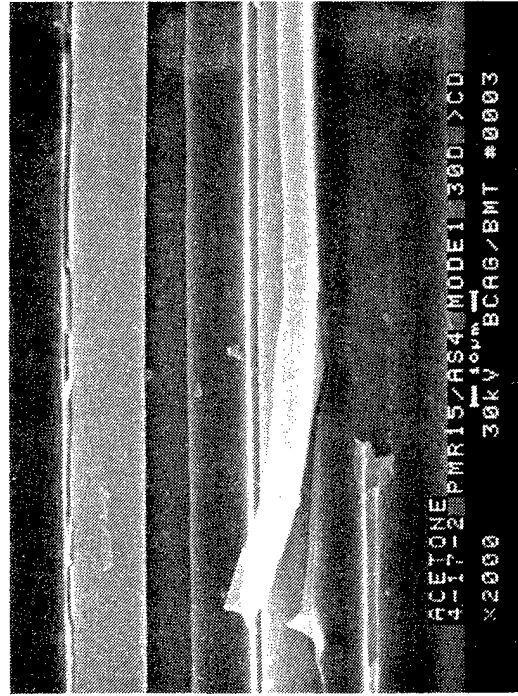


60 degree tilt (a) 20X



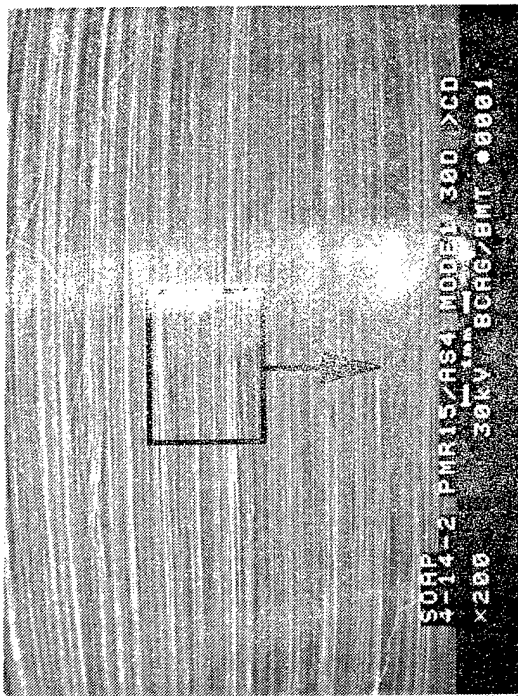
60 degree tilt (b) 400X

Mechanically induced  
crack direction

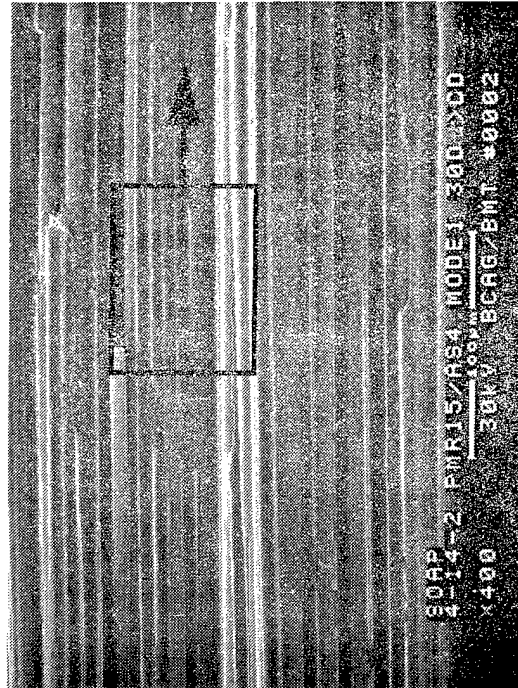


60 degree tilt (c) 2000X

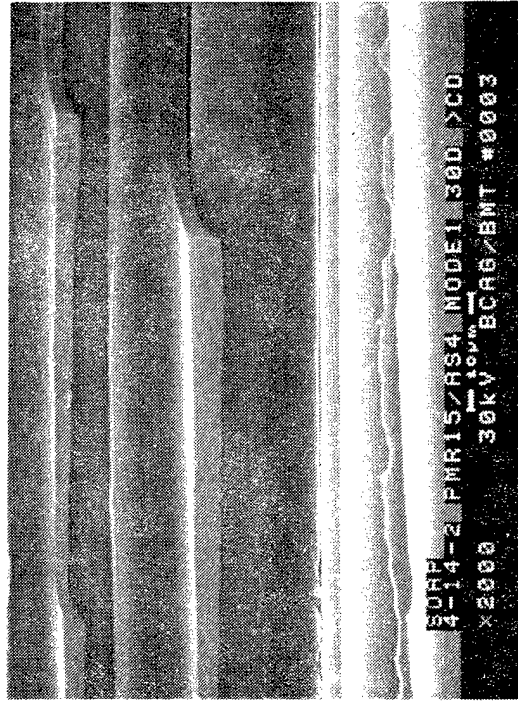
Figure 3.3-13. SEM Fractographs of a PMR-15/AS4 Interlaminar Mode I Tension Fracture Surface Exposed to Acetone for 24 hours



60 degree tilt (a) 20X



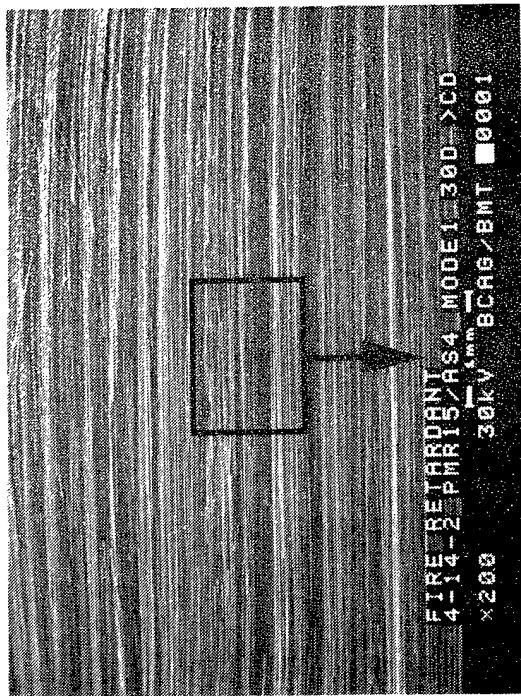
60 degree tilt (b) 400X



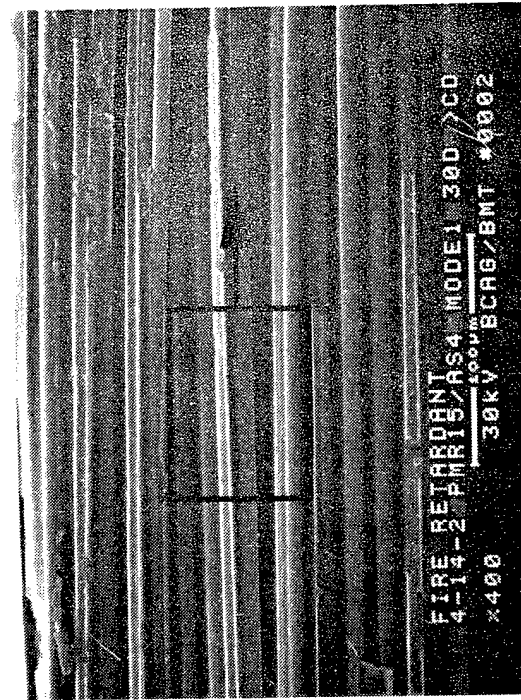
60 degree tilt (c) 2000X

Figure 3.3-14. SEM Fractographs of a PMR-15/AS4 Interlaminar Mode I Tension Fracture Surface Exposed to Soap Solution for 24 hours

2387.04 L7220 D8 ai

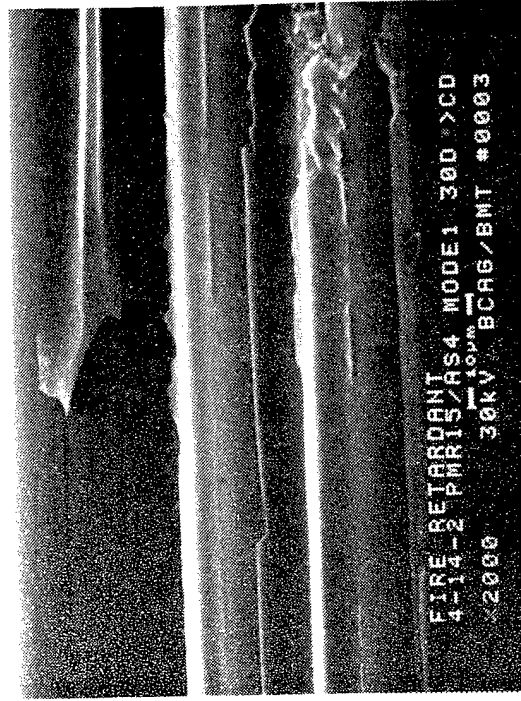


60 degree tilt (a) 20X



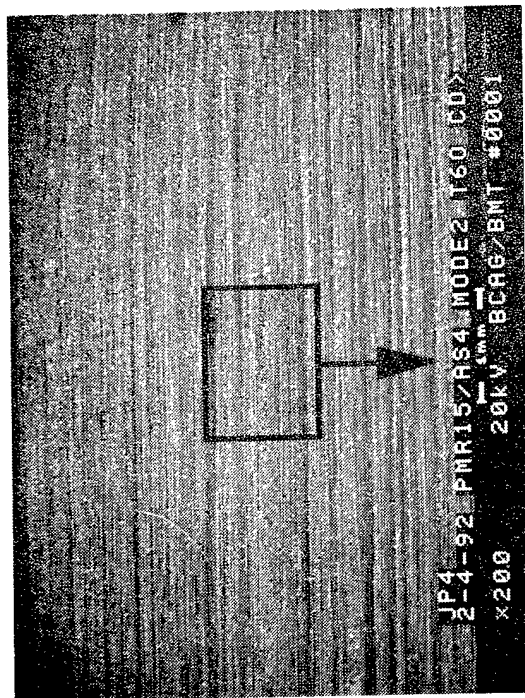
60 degree tilt (b) 400X

Mechanically induced crack direction

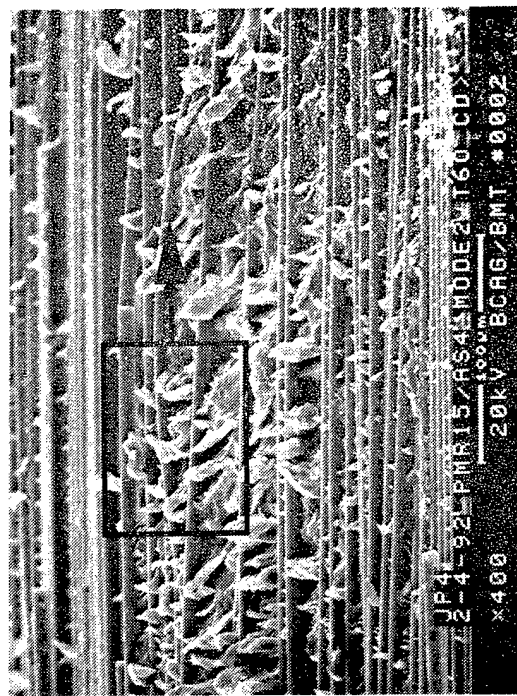


60 degree tilt (c) 2000X

Figure 3.3-15. SEM Fractographs of a PMR-15/AS4 Interlaminar Mode I Tension Fracture Surface Exposed to Fire Retardant Foam for 7 Days

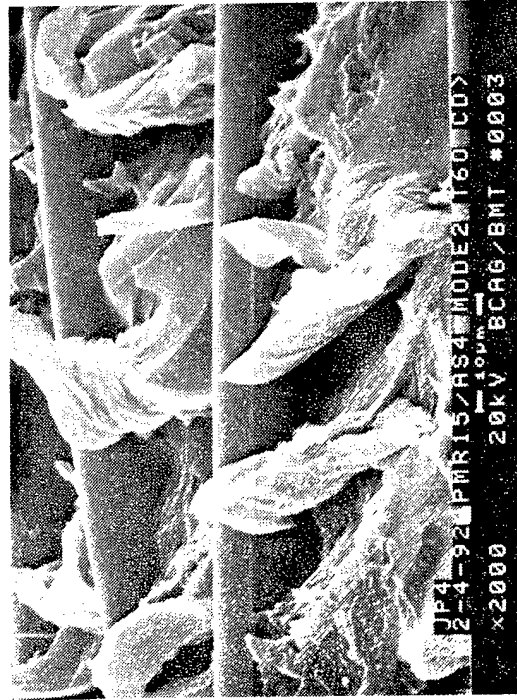


60 degree tilt (a) 20X



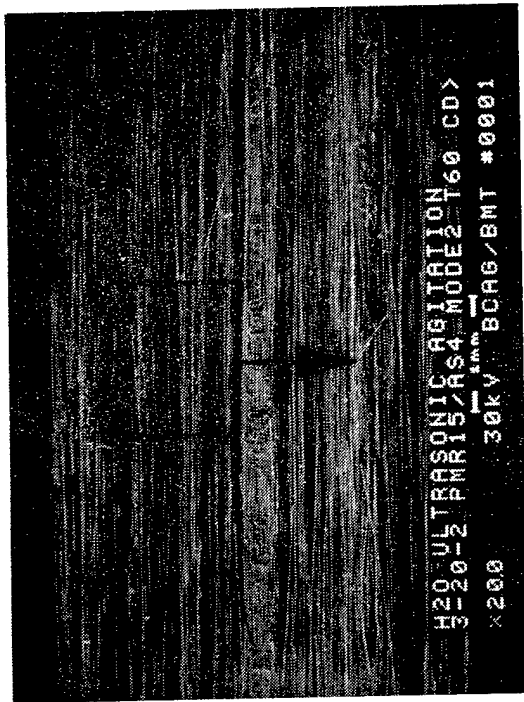
60 degree tilt (b) 400X

Mechanically induced  
crack direction

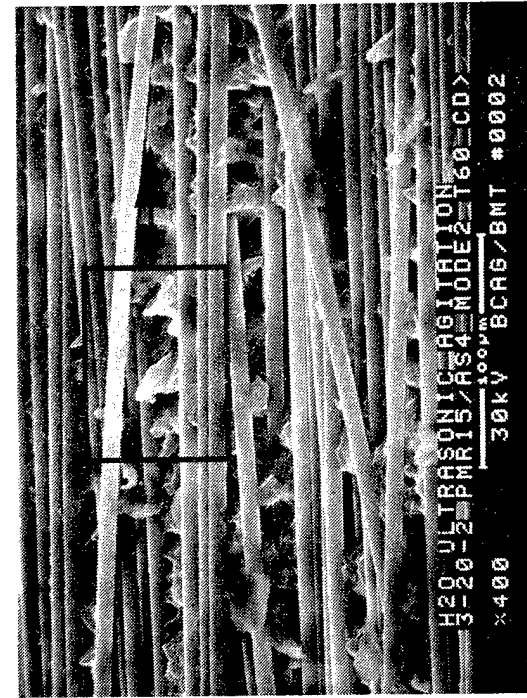


60 degree tilt (c) 2000X

Figure 3.3-16. SEM Fractographs of a PMR-15/AS4 Interlaminar Mode II Shear Fracture Surface Exposed to JP4 Jet Fuel for 7 Days

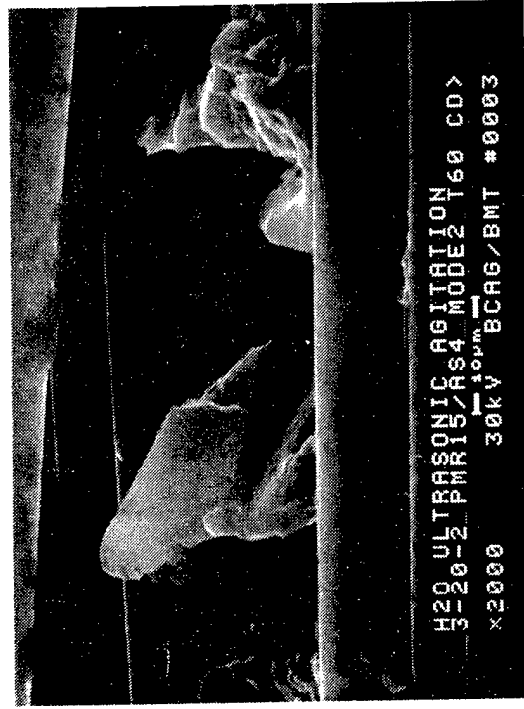


60 degree tilt (a) 20X



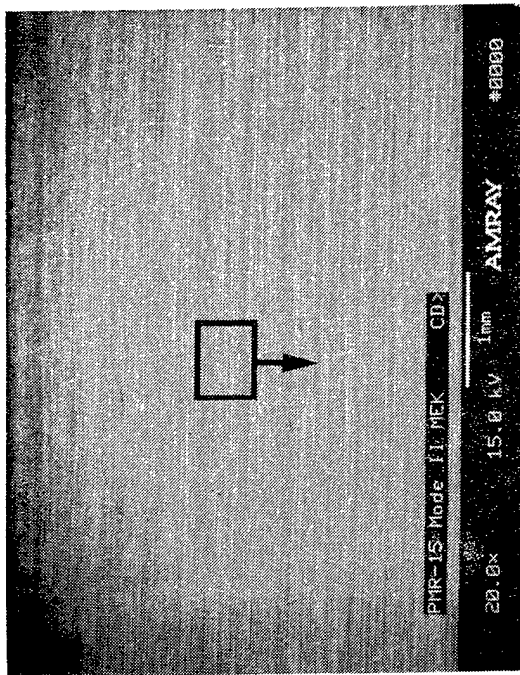
60 degree tilt (b) 400X

Mechanically induced crack direction



60 degree tilt (c) 2000X

Figure 3.3-17. SEM Fractographs of a PMR-15/AS4 Interlaminar Mode II Shear Fracture Surface Exposed to Ultrasonic Agitation in Distilled Water for 24 hours

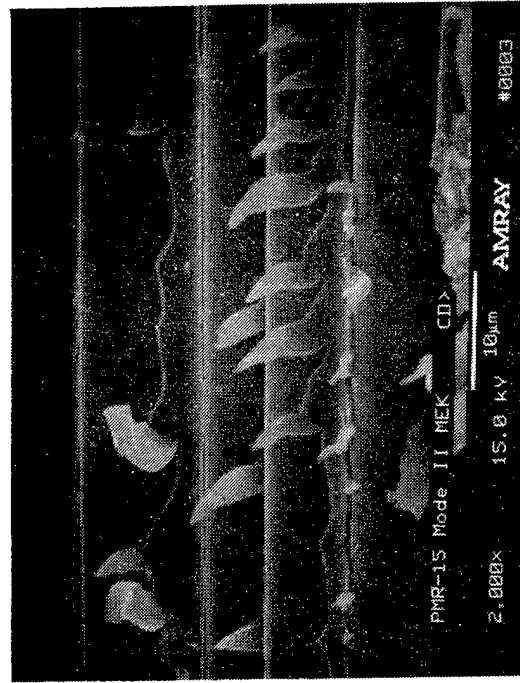


60 degree tilt (a) 20X



60 degree tilt (b) 400X

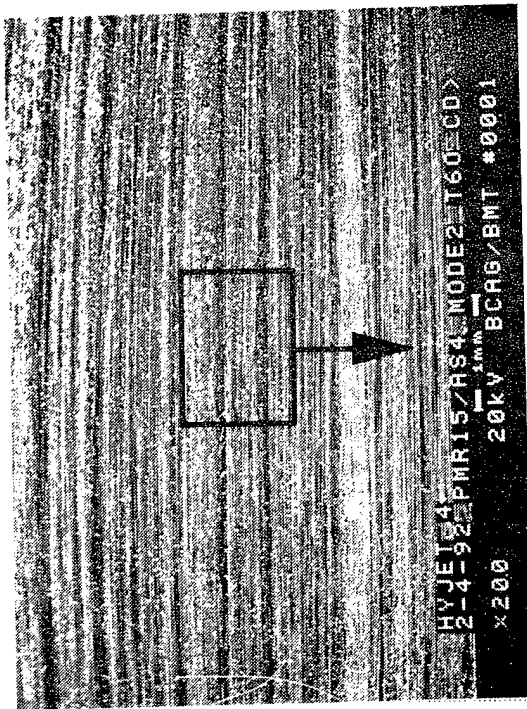
Mechanically induced crack direction



60 degree tilt (c) 2000X

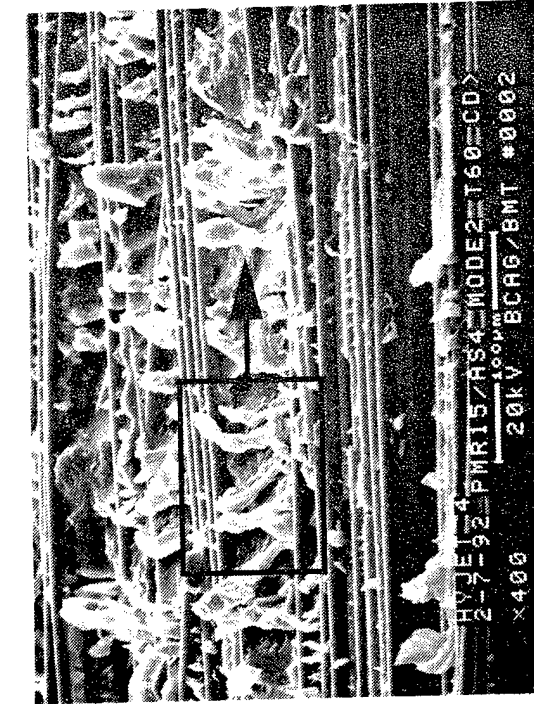
Figure 3.3-18. SEM Fractographs of a PMR-15/AS4 Interlaminar Mode II Shear Fracture Surface Exposed to MEK for 24 Hours

49829.06 9-5576 D1ai

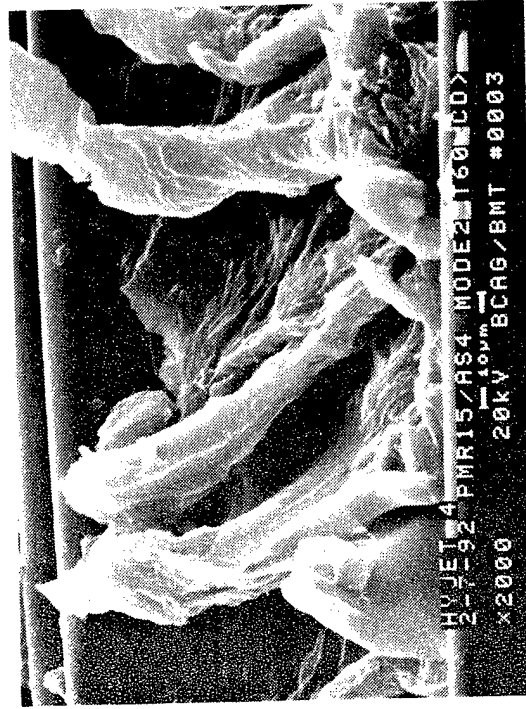


60 degree tilt (a) 20X

Mechanically induced  
crack direction



60 degree tilt (b) 400X

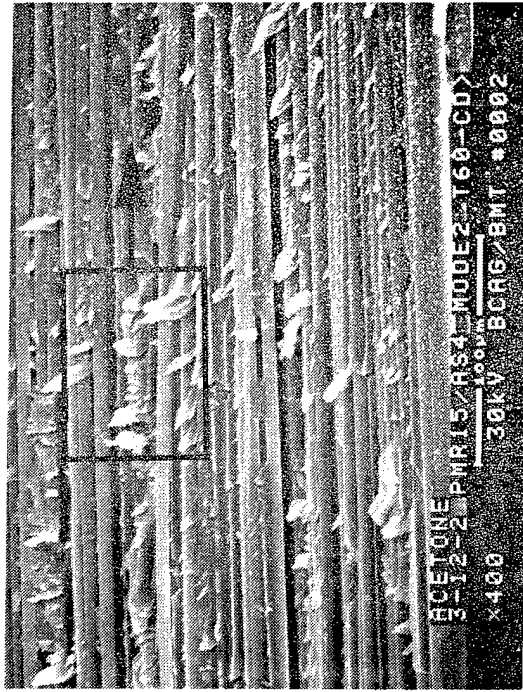


60 degree tilt (c) 2000X

Figure 3.3-19. SEM Fractographs of a PMR-15/AS4 Interlaminar Mode II Shear Fracture Surface Exposed to Hydraulic Fluid for 7 Days

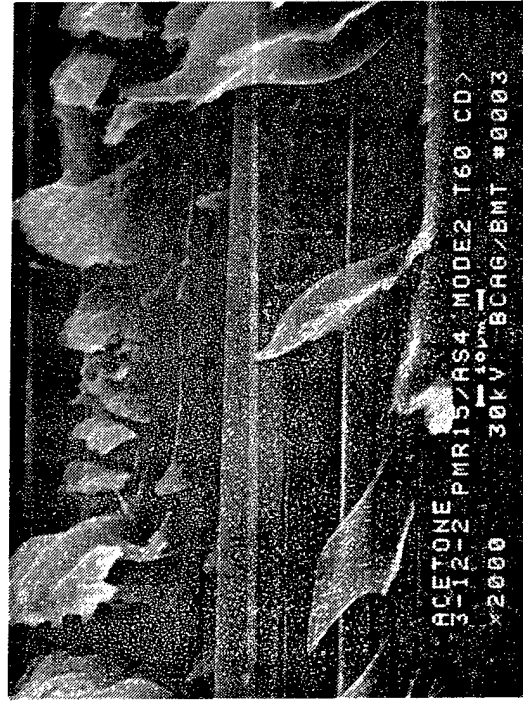


60 degree tilt (a) 20X



60 degree tilt (b) 400X

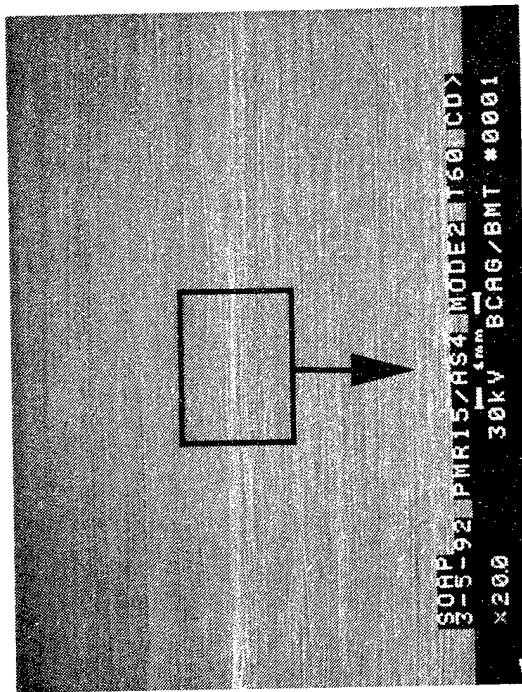
Mechanically induced crack direction



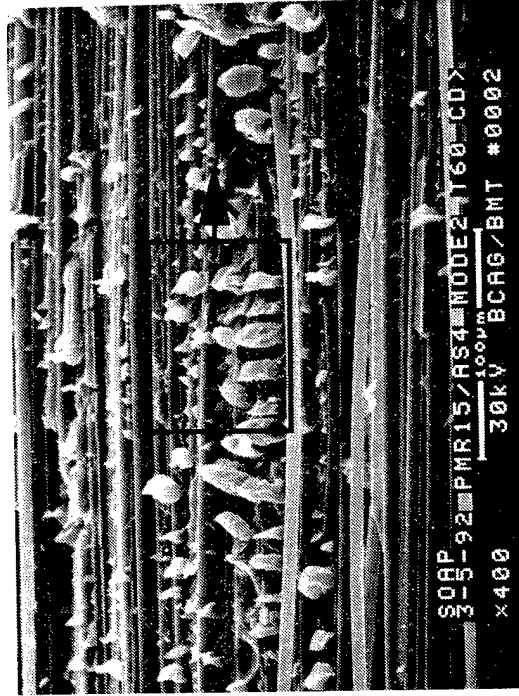
60 degree tilt (c) 2000X

Figure 3.3-20. SEM Fractographs of a PMR-15/AS4 Interlaminar Mode II Shear Fracture Surface Exposed to Acetone for 24 hours




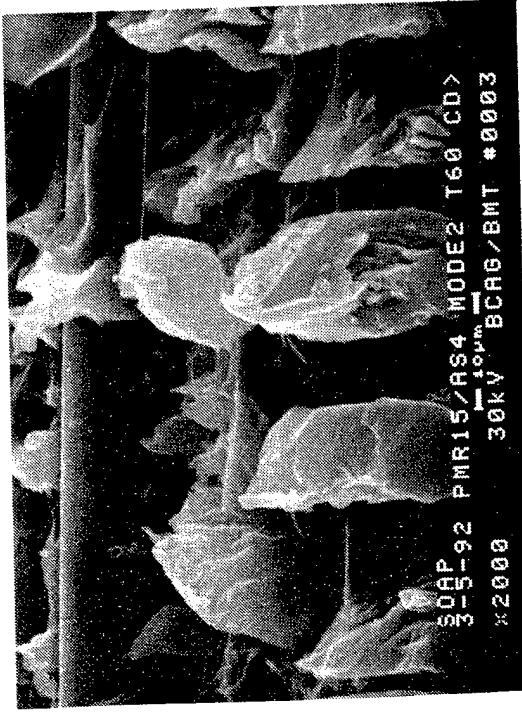


60 degree tilt (a) 20X



60 degree tilt (b) 400X

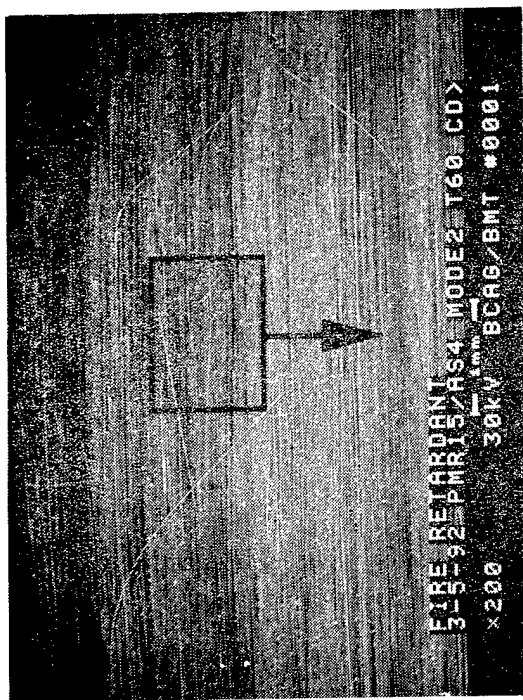
Mechanically induced  
crack direction

60 degree tilt (c) 2000X

Figure 3.3-21. SEM Fractographs of a PMR-15/AS4 Interlaminar Mode II Shear Fracture Surface Exposed to Soap Solution for 24 hours

2857.05 L7220 D8 aiR1

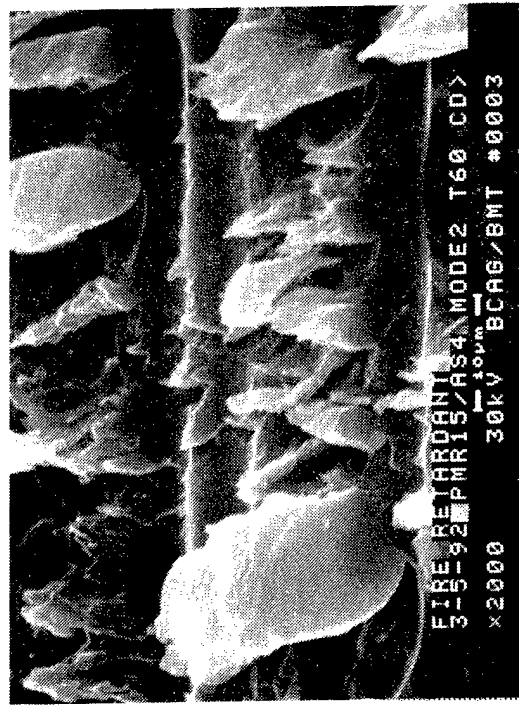


60 degree tilt (a) 20X



60 degree tilt (b) 400X

Mechanically induced crack direction  
 ↑



60 degree tilt (c) 2000X

Figure 3.3-22. SEM Fractographs of a PMR-15/AS4 Interlaminar Mode II Shear Fracture Surface Exposed to Fire Retardant Foam for 7 Days

2357.01 L7220 D8 aiR1

**SECTION 3.4**  
**CARBON/THERMOPLASTIC**  
**AS4/APC-2**

**3.4.1 Introduction**

This section contains additional data for the AS4/APC-2 graphite/polyetheretherketone (Gr/PEEK) fractographic database. The additional tests were designed to allow the characterization of interlaminar fracture surfaces, which were the result of fatigue crack growth and surfaces that have been affected by various environmental exposures.

**3.4.2 Fatigue**

**Interlaminar Mode II (Shear), RT and 250°F/Dry**

As shown in Figures 3.4-1 and 3.4-2, the fracture surface morphology of the RT specimen appeared typical for the mode II (shear) Gr/PEEK fracture surface. However, the hackle feature on this surface was considerably smaller than the statically loaded specimen and was probably unique to the cyclic loading.

The fracture morphology was very different on the specimen tested at 250°F (Figures 3.4-3 and 3.4-4). The resin was pulled out in "ribbons" which did not indicate the overall crack propagation direction.

**Interlaminar Mode I (Tension), RT and 250°F/Dry**

The RT fracture surface (Figures 3.4-5 and 3.4-6) exhibited features similar to large hackles between the fibers, oriented in the direction of the overall crack propagation direction. The plastic craze was also present throughout the entire surface including the large hackles.

The morphology of the 250°F fracture surface (Figures 3.4-7 and 3.4-8) was different from the RT specimen. It consisted of the "ribbons" of resin that appear to have been pulled out from the surface. This was observed on the mode II (shear) fatigue fracture surface. These "ribbons" did not give any indication to the overall crack propagation direction.

**3.4.3 Short-Term Environmental Exposure**

**Interlaminar Mode I and II Surfaces**

Examination of the fracture surface revealed the characteristic surface features for both the mode I (tension) (Figure 3.4-9) and mode II (shear) (Figure 3.4-10), respectively. There appeared to be no degradation in the surface feature due to the exposures.

Crack growth direction →

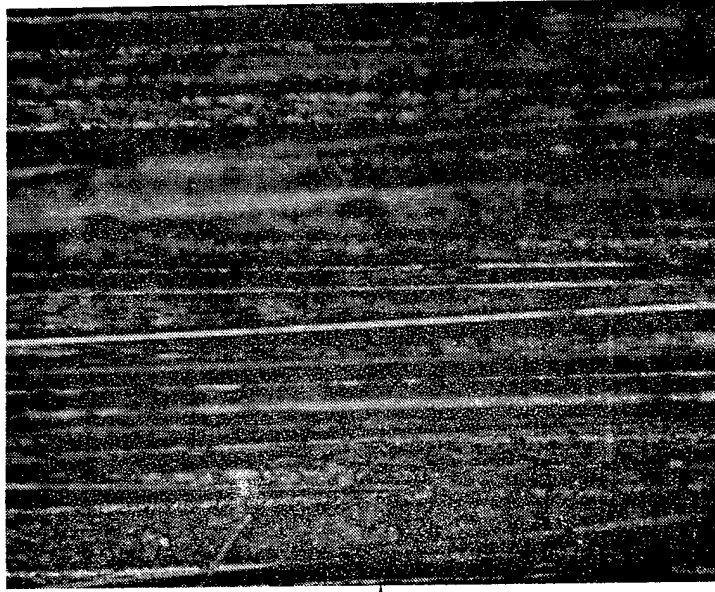
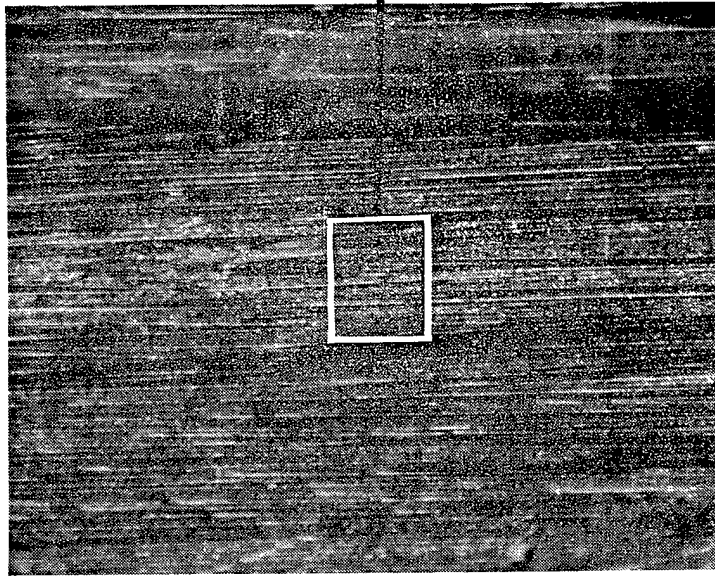
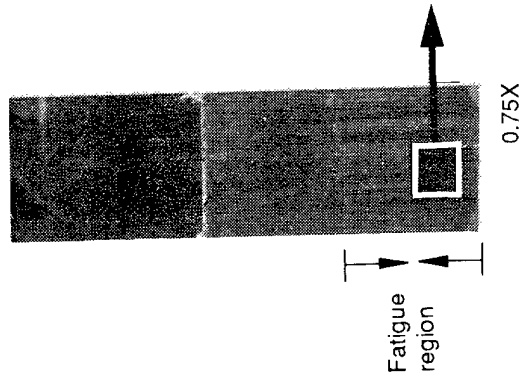
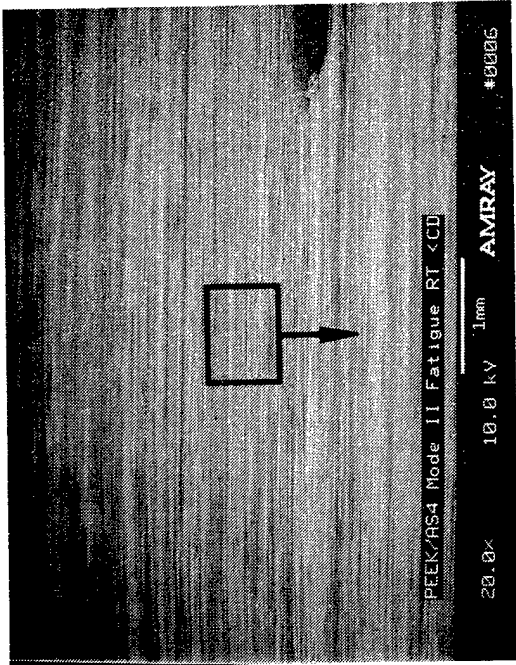
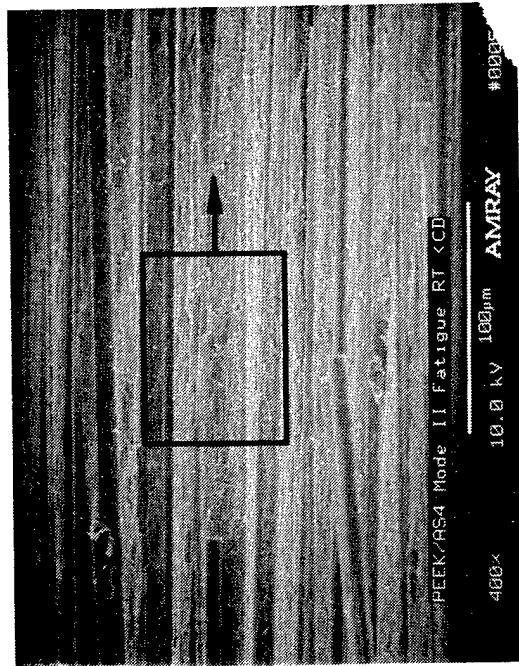


Figure 3.4-1. Optical Fractographs of PEEK/AS4 Interlaminar Mode II (Shear) Fatigue, Room Temperature, High Stress

49754.09 9-5571 D8 fh

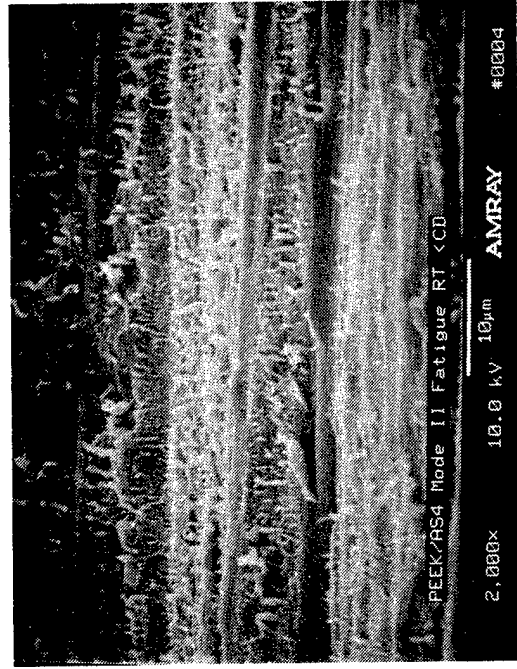


60 degree tilt (a) 20X



60 degree tilt (b) 400X

Mechanically induced  
crack direction



60 degree tilt (c) 2000X

Figure 3.4-2. SEM Fractographs of a PEEK/AS4 Interlaminar Mode II (Shear) Fatigue Fracture Surface, Room Temperature

49754.20 9-5571 D1 ai

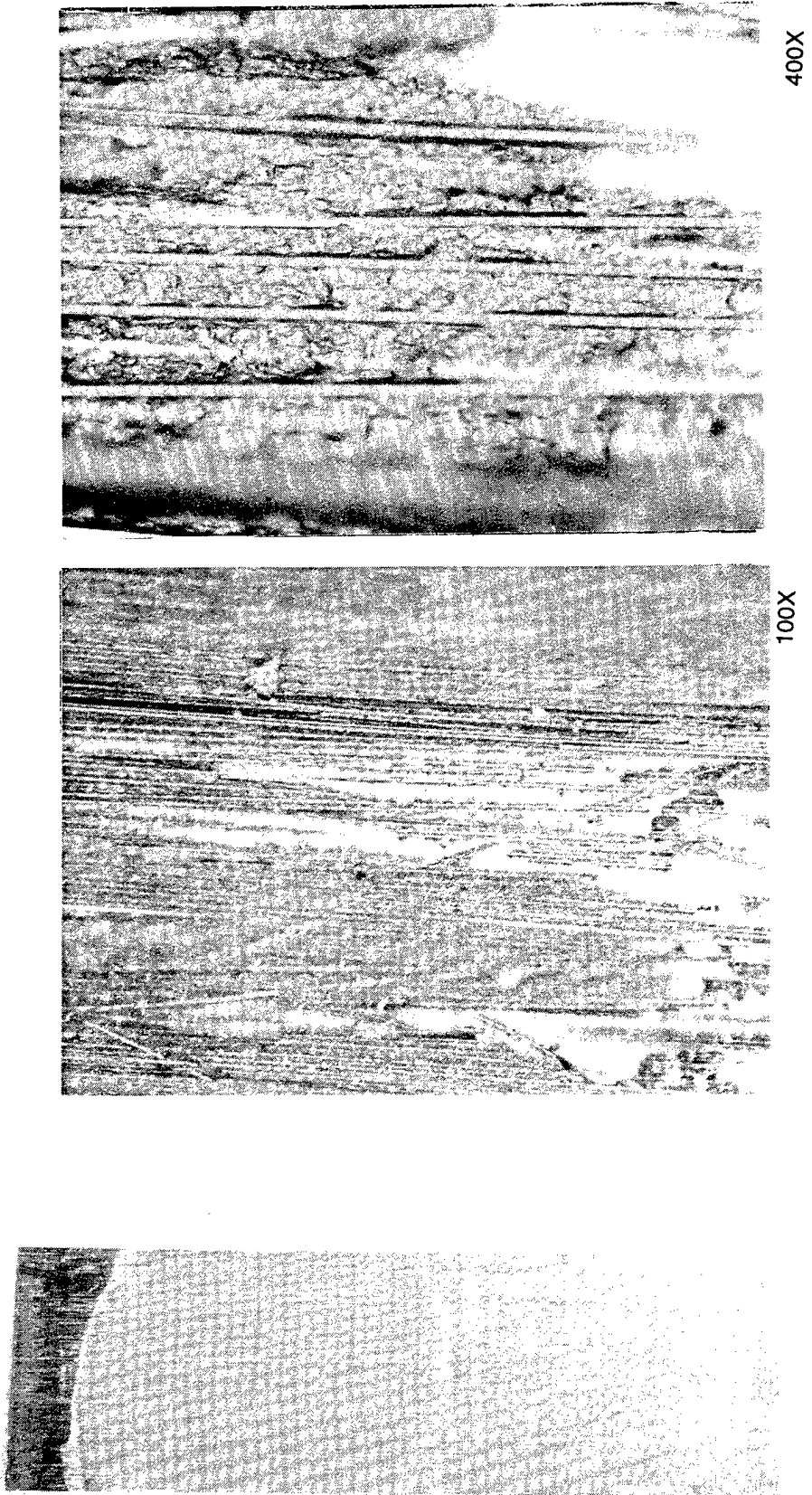
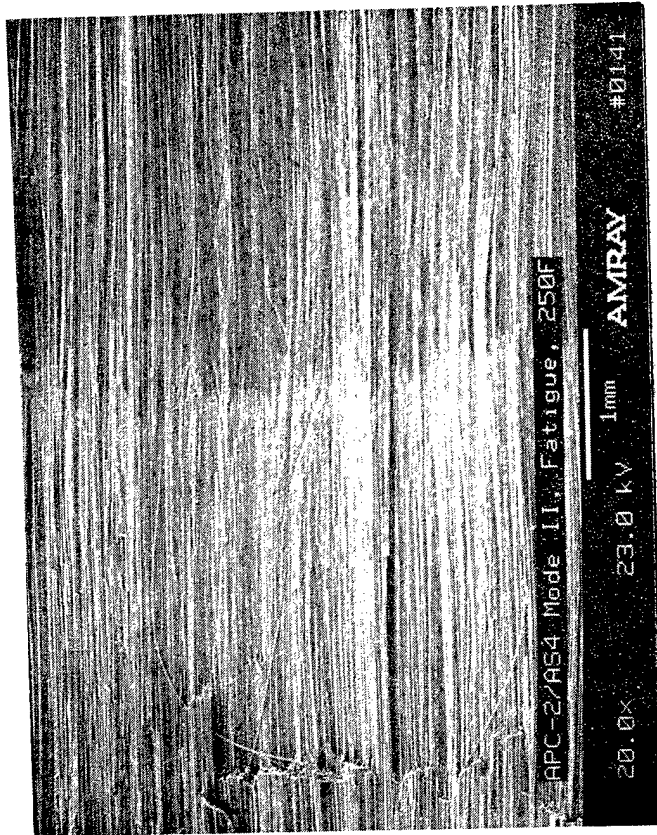


Figure 3.4-3. Optical Fractographs of a APC-2/AS4 Interlaminar Mode II (Shear) Fatigue Fracture Surface, 250° F



Mechanically Induced  
Crack Direction  
↑

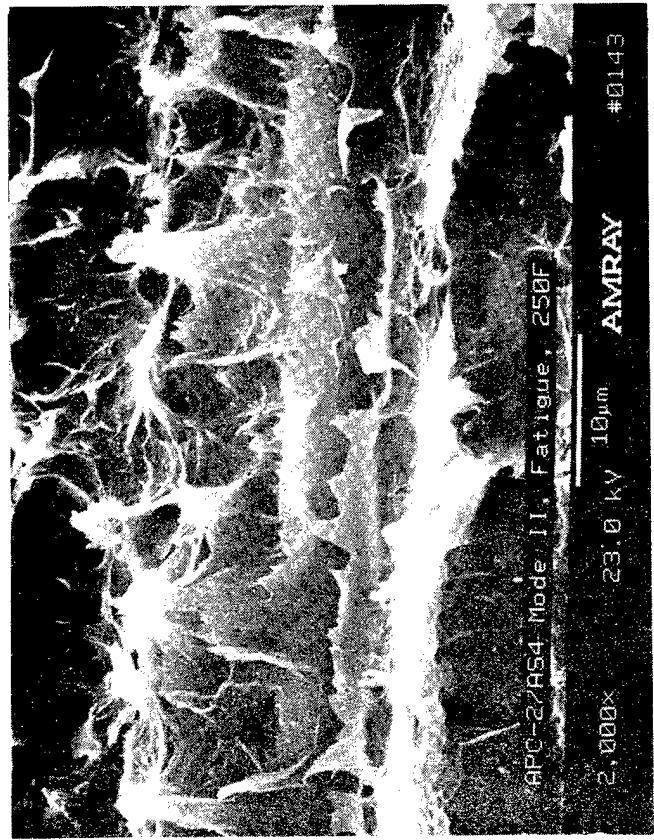
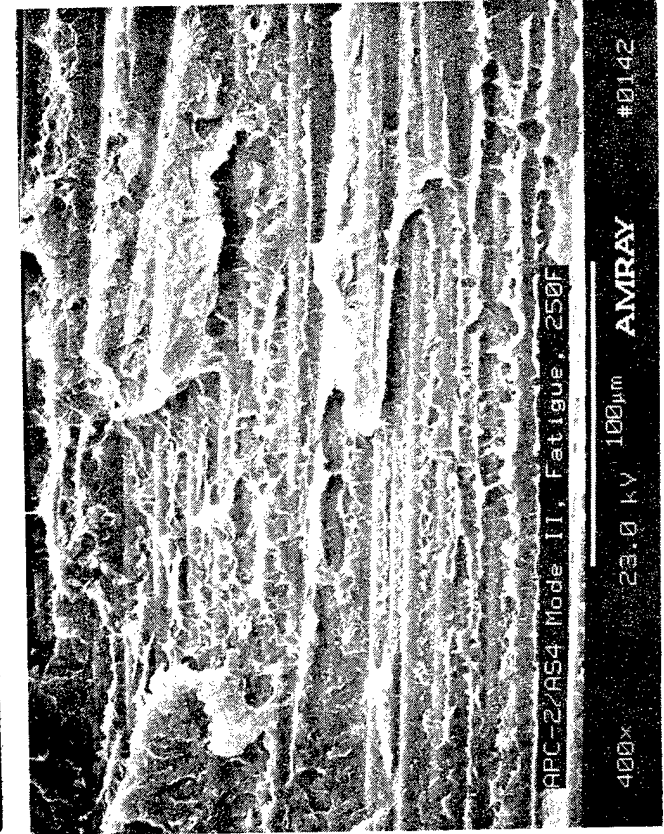


Figure 3.4-4. SEM Fractographs of a APC-2/AS4 Interlaminar Mode II (Shear) Fatigue Fracture Surface, 250° F



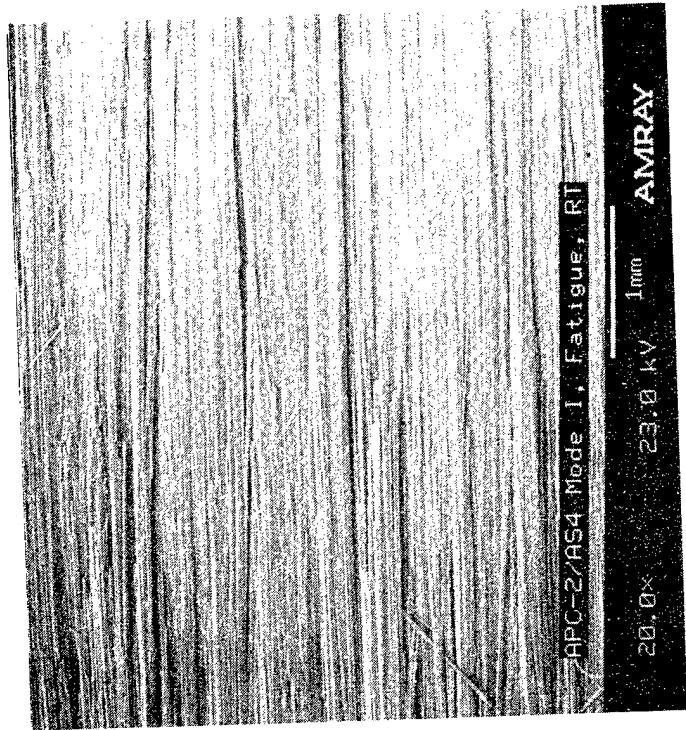
100X



400X

Figure 3.4-5. Optical Fractographs of a APC-2/AS4 Interlaminar Mode I (Tensile) Fatigue Fracture Surface, RT





Mechanically Induced  
Crack Direction

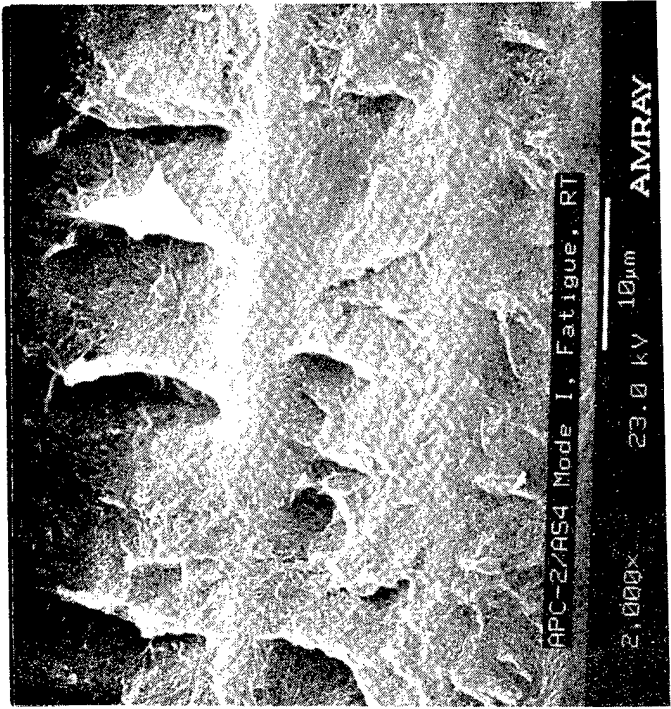
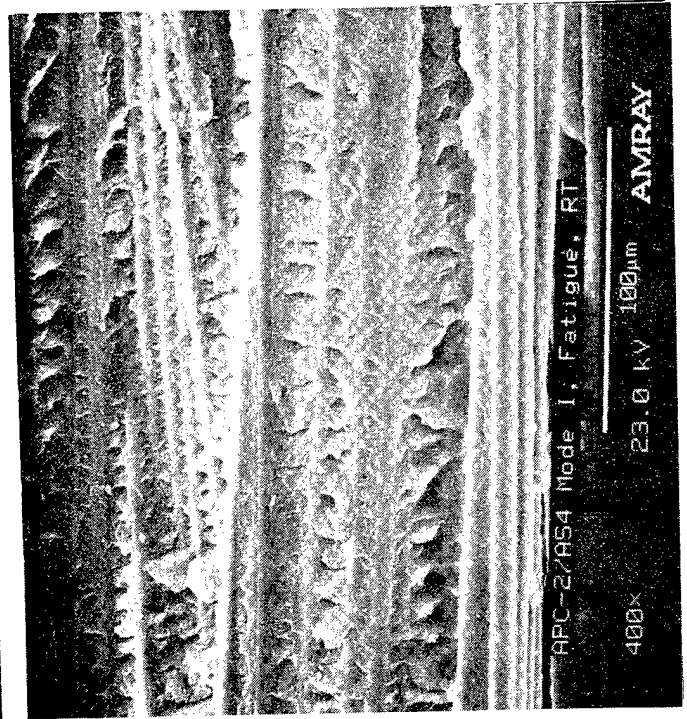
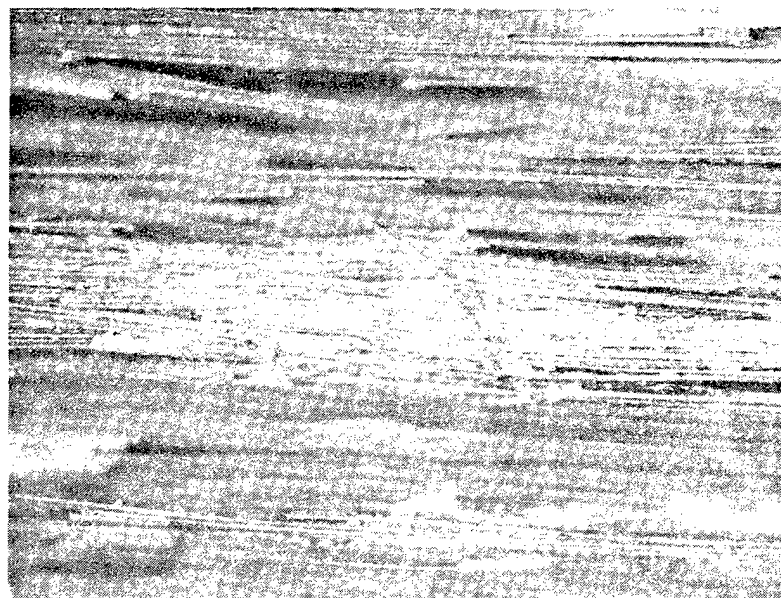


Figure 3.4-6. SEM Fractographs of a APC-2/AS4 Interlaminar Mode I (Tensile) Fatigue Fracture Surface, RT



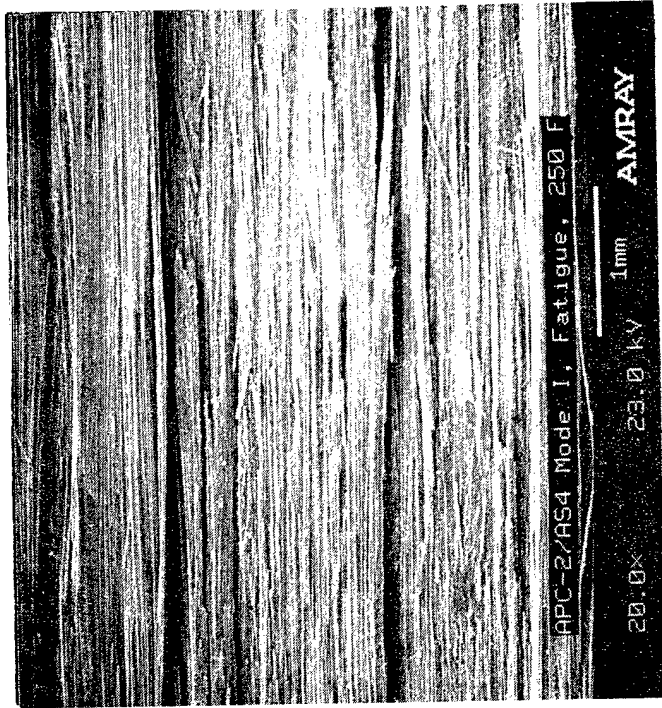
400X



100X



Figure 3.4-7. Optical Fractographs of a APC-2/AS4 Interlaminar Mode I (Tensile) Fatigue Fracture Surface, 250° F



Mechanically Induced  
Crack Direction →

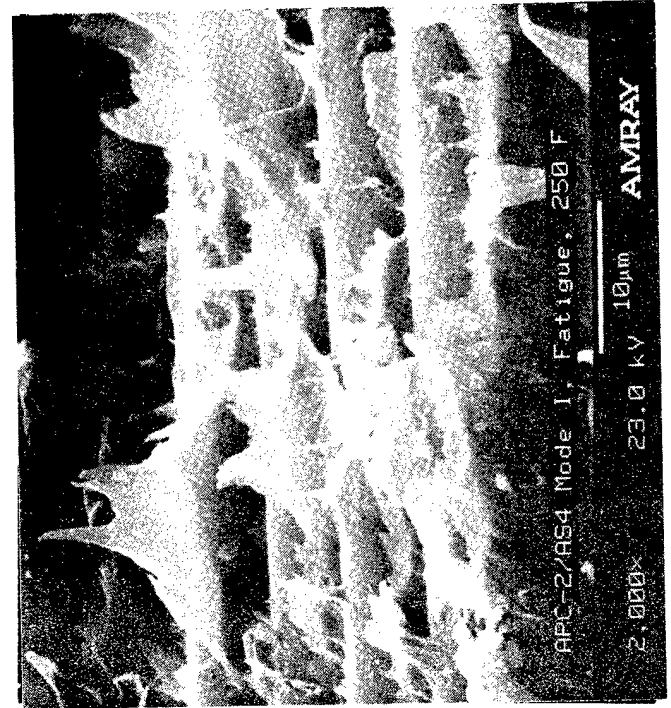
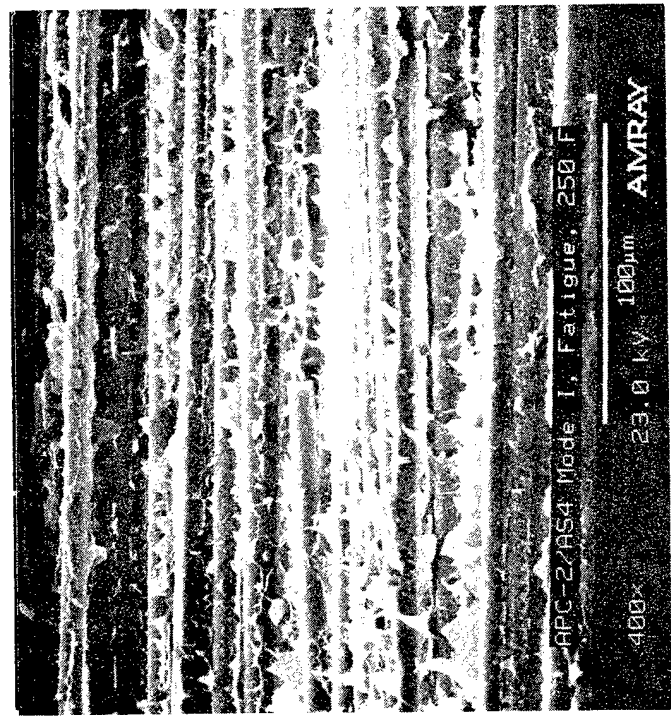
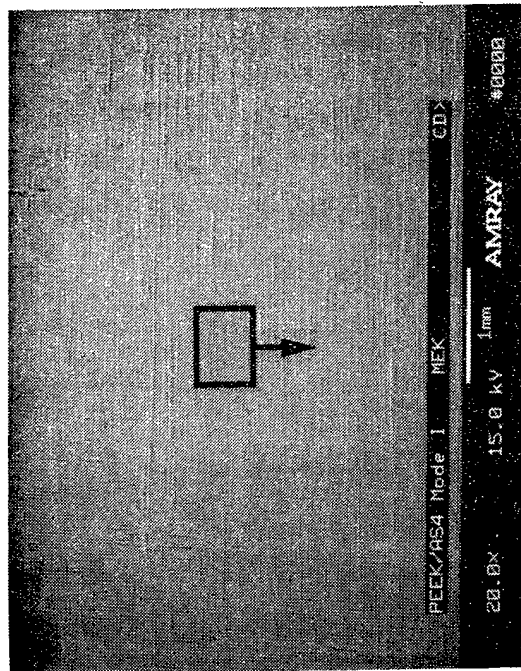
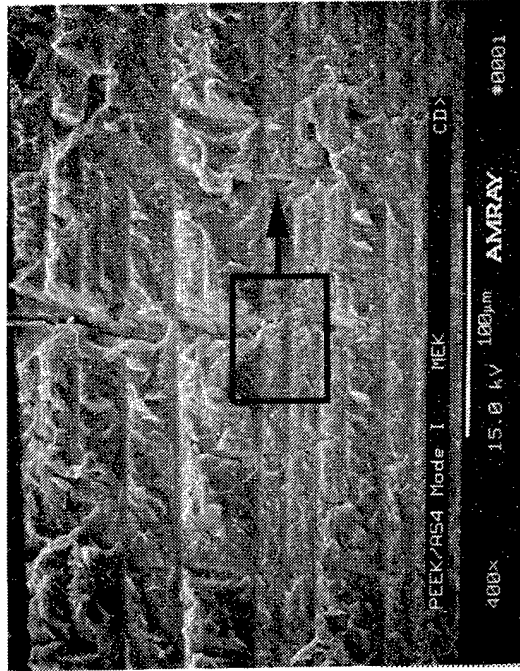


Figure 3.4-8. SEM Fractographs of a APC-2/AS4 Interlaminar Mode I (Tensile) Fatigue Fracture Surface, 250° F

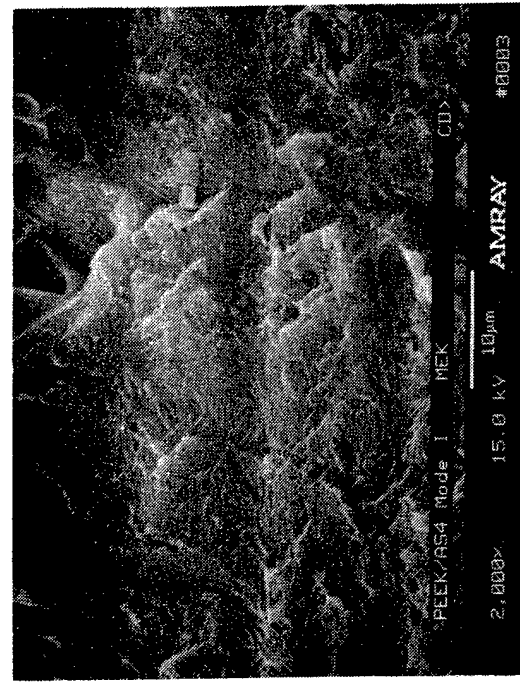


30 degree tilt (a) 20X

Mechanically induced crack direction

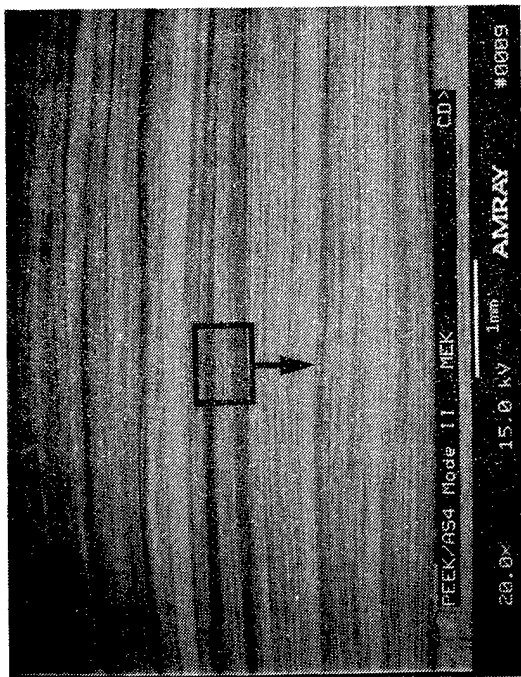


30 degree tilt (b) 400X

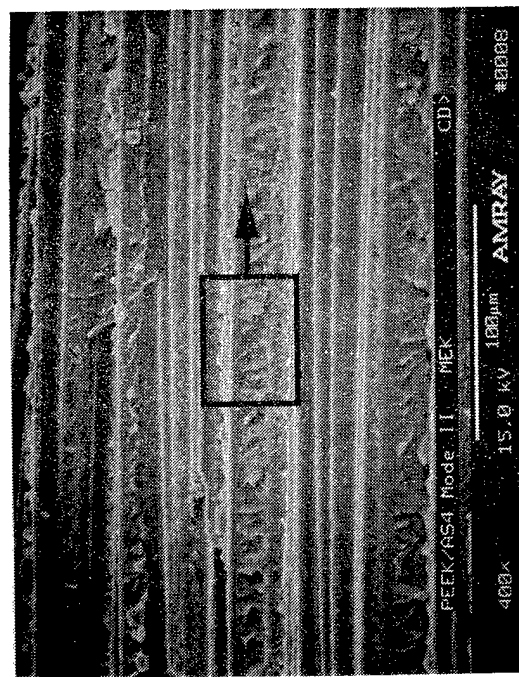


30 degree tilt (c) 2000X

Figure 3.4-9. SEM Fractographs of a PEEK/AS4 Interlaminar Mode I Tension Fracture Surface Exposed to MEK for 24 Hours

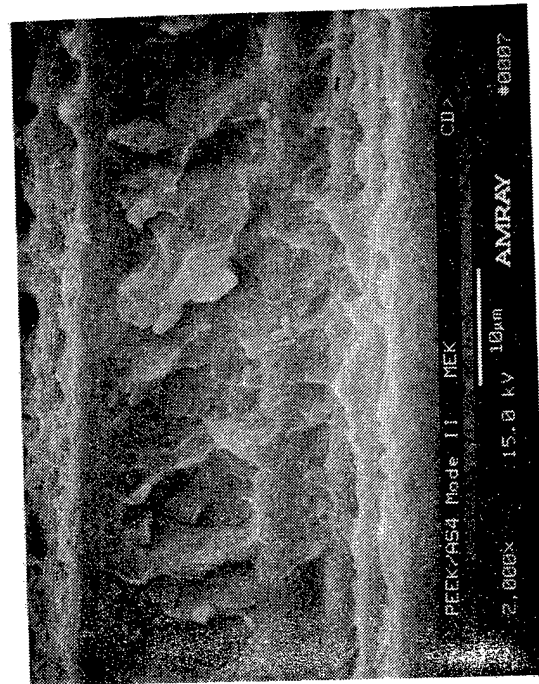


60 degree tilt (a) 20X



60 degree tilt (b) 400X

Mechanically induced crack direction



60 degree tilt (c) 2000X

Figure 3.4-10. SEM Fractographs of a PEEK/AS4 Interlaminar Mode II Shear Fracture Surface Exposed to MEK for 24 Hours

**SECTION 3.5**  
**CARBON/BISMALEIMIDE**  
**AS4/MR-54-4**

**3.5.1 Introduction**

This section contains additional fractography performed on AS4/MR-54-4 graphite/bismaleimide (Gr/BMI) test coupons. Initial fractographic analysis has been previously documented on this system and is included in the handbook. Work under this contract included both interlaminar and translaminar specimens. The coupons were to have been tested at both RT and at 450°F. However, only the specimens tested at RT were documented because the elevated-temperature-tested specimens buckled and did not produce either an interlaminar or a translaminar fracture surface.

**3.5.2 Static Loading**

**Interlaminar Mode I (Tensile), RT/Dry**

Visual observation revealed a smooth, glassy surface typical of an interlaminar mode I tension fracture. However, fragments of loose fibers were apparent on the fracture surface. These fibers were separated from the matrix (possibly due to weak fiber/matrix adhesion). Under the optical microscope, fine rivermarks were observed, indicating the overall crack propagation direction (Figure 3.5-1). As shown in Figure 3.5-2, SEM examination revealed rivermarks between the carbon fibers. These rivermarks indicated the crack growth is consistent with the mechanically induced crack direction.

**Interlaminar Mode II (Shear), RT/Dry**

Visual observation of the fracture surface revealed a flat but milky appearance when held at an angle to the light. The milky appearance is due to the hackle formation created by shear loading, which was observed at higher magnification under the optical microscope (Figure 3.5-3). SEM examination revealed hackles of different sizes, shapes, and tilt angles located between the carbon fibers (Figure 3.5-4).

**Translaminar Tension, RT/Dry**

SEM fractography (Figure 3.5-5) revealed radial patterns on the fiber ends, indicating a resultant crack direction consistent with the mechanically induced direction. The specimen tested at 450° F did not fracture but only bent during the testing (Figure 3.5-6)

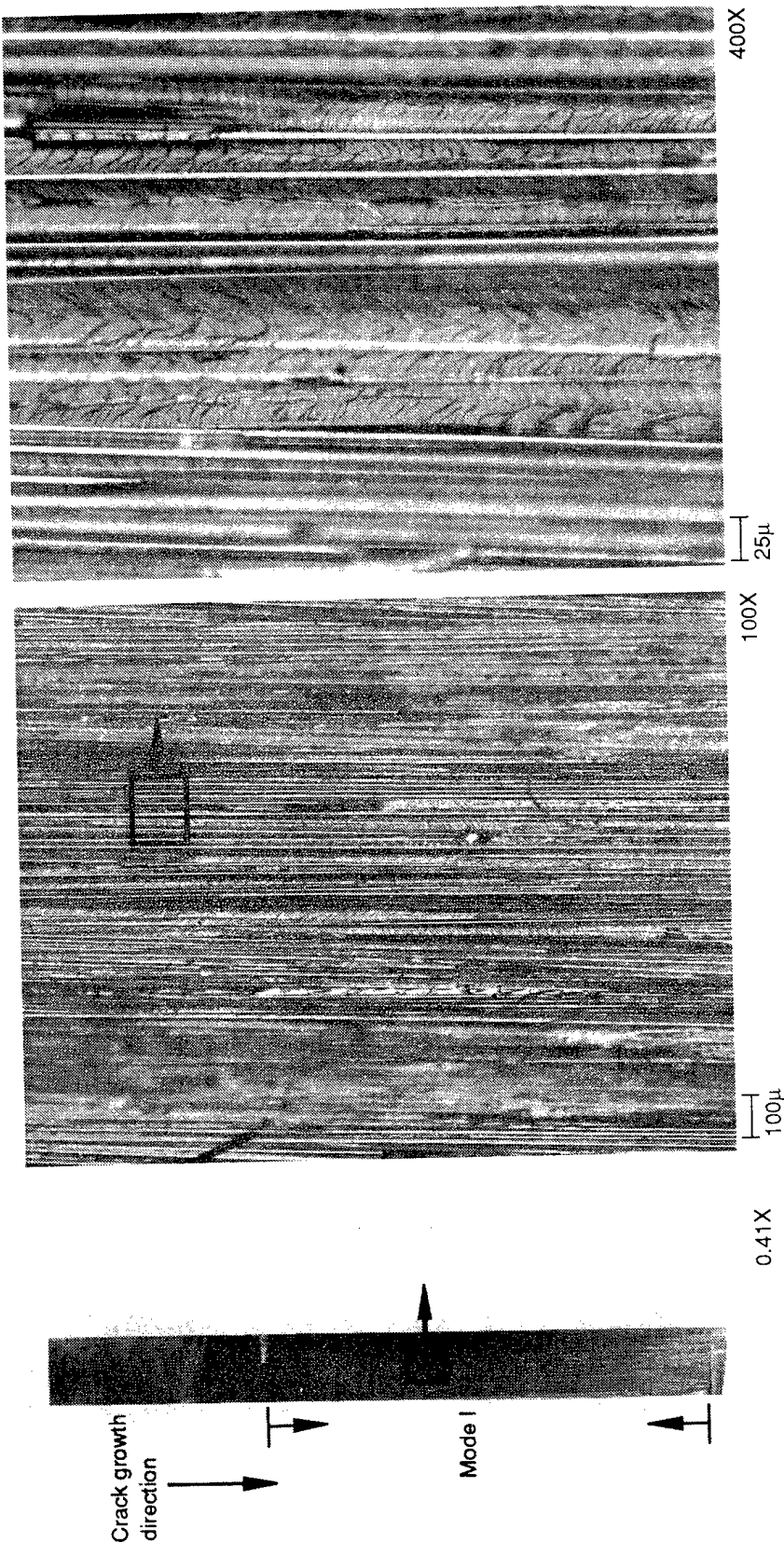
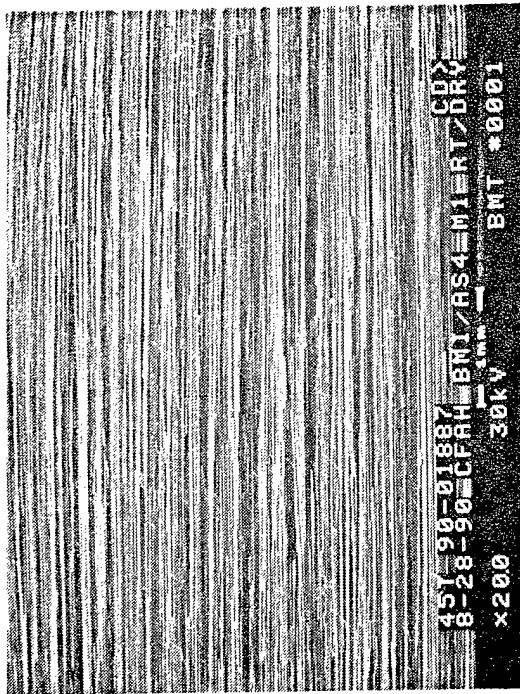


Figure 3.5-1. Optical Fractographs of BM//AS4 Interlaminar Mode I Tension Specimen Tested at RT/Dry



Mechanically induced  
crack direction

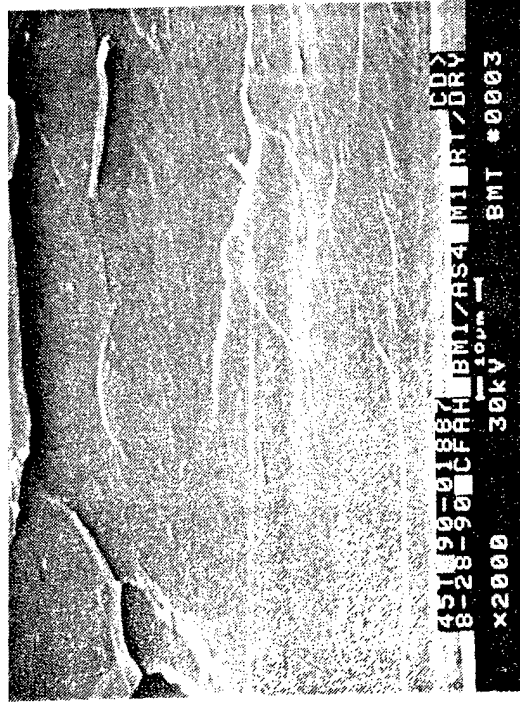
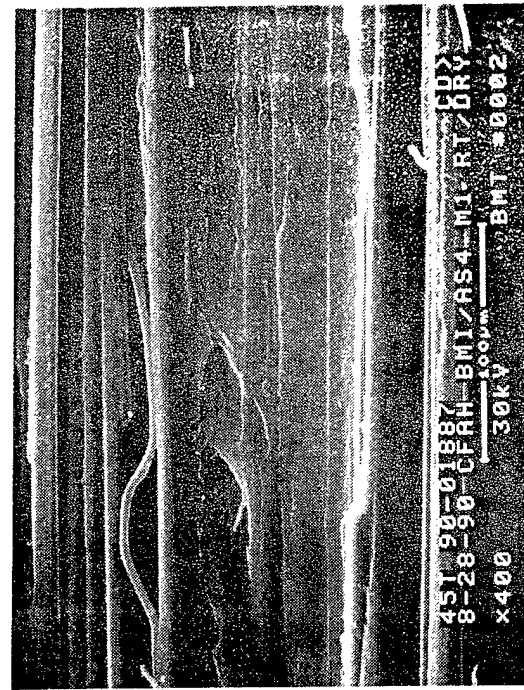


Figure 3.5-2. SEM Fractographs of an AS4/EMI Interlaminar Mode I Tension Specimen Tested at RT/Dry



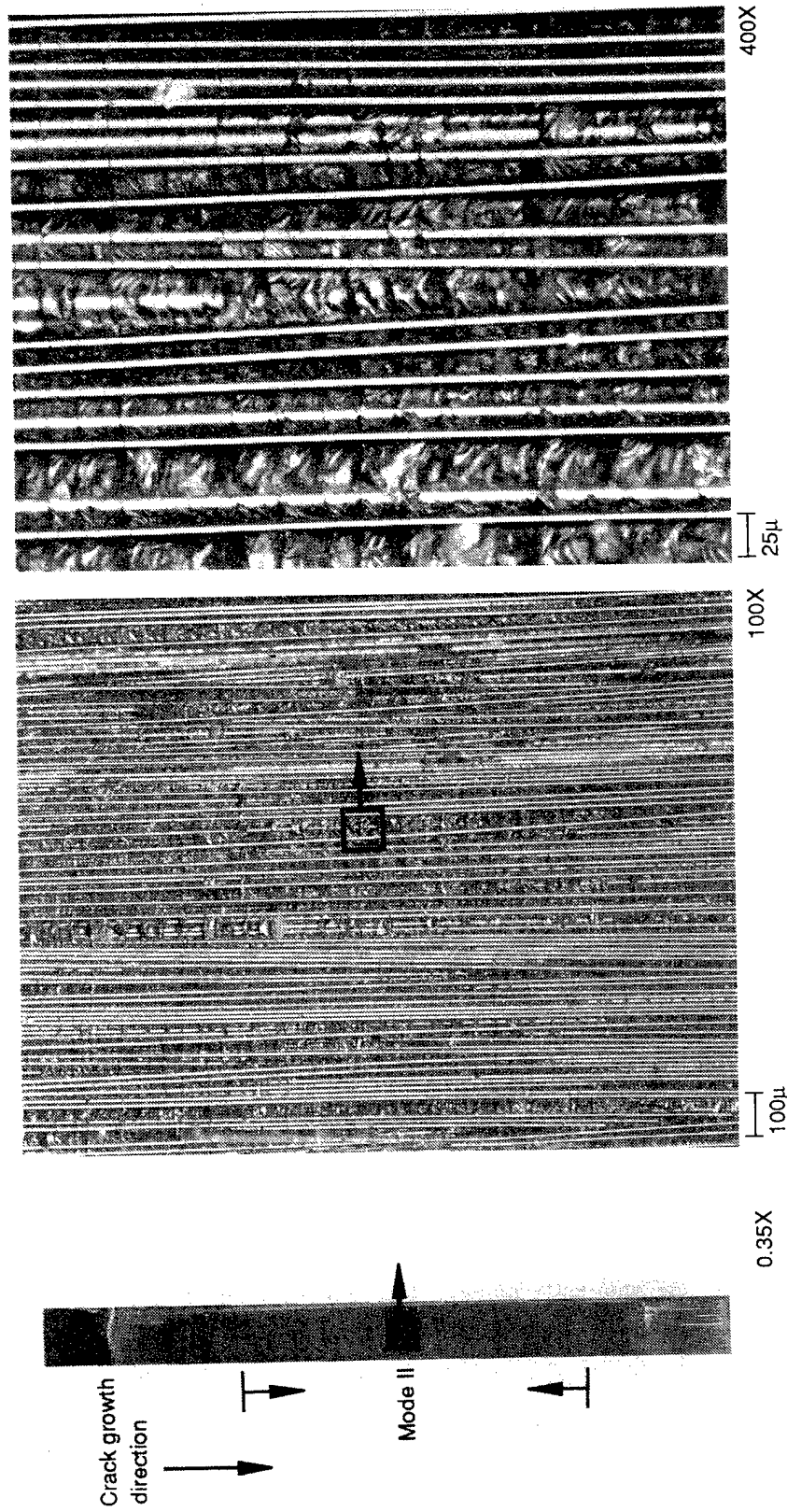
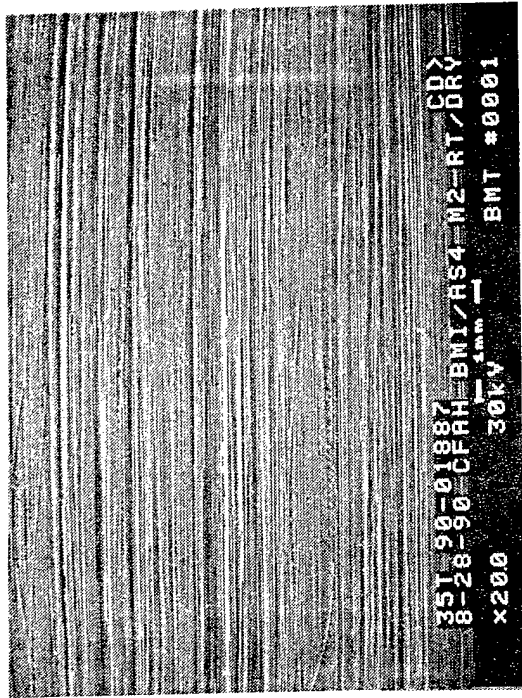


Figure 3.5-3. Optical Fractographs of BMI/AS4 Interlaminar Mode II Shear Specimen Tested at RT/Dry



Mechanically induced  
crack direction

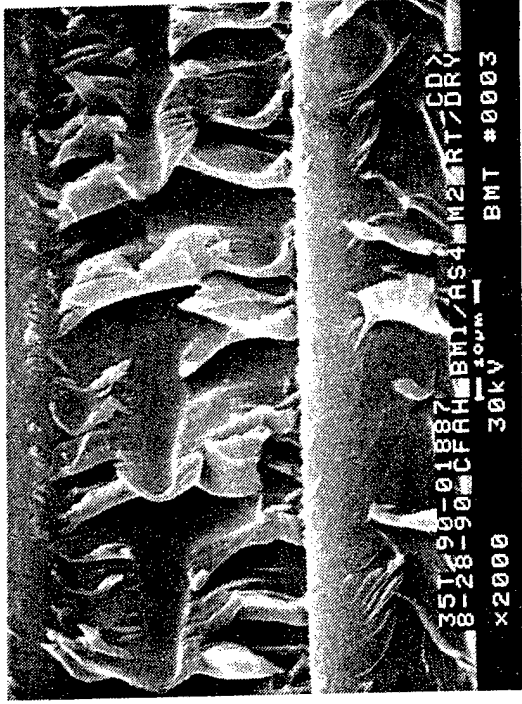
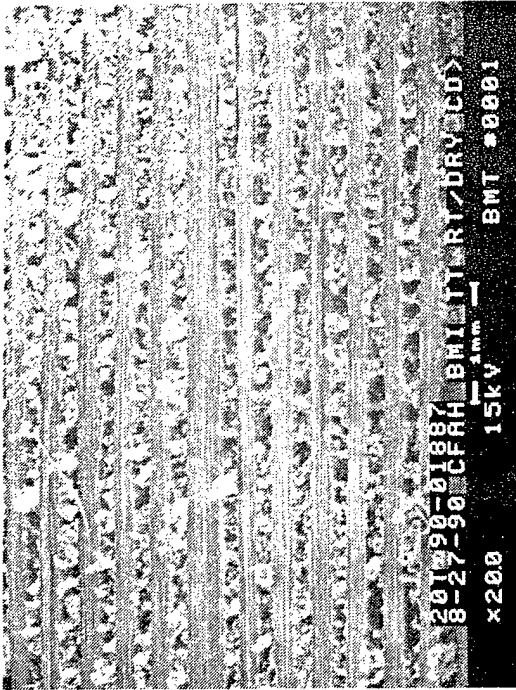


Figure 3.5-4. SEM Fractographs of an AS4/BMI Interlaminar Mode II Shear Specimen Tested at RT/Dry



Mechanically induced crack direction

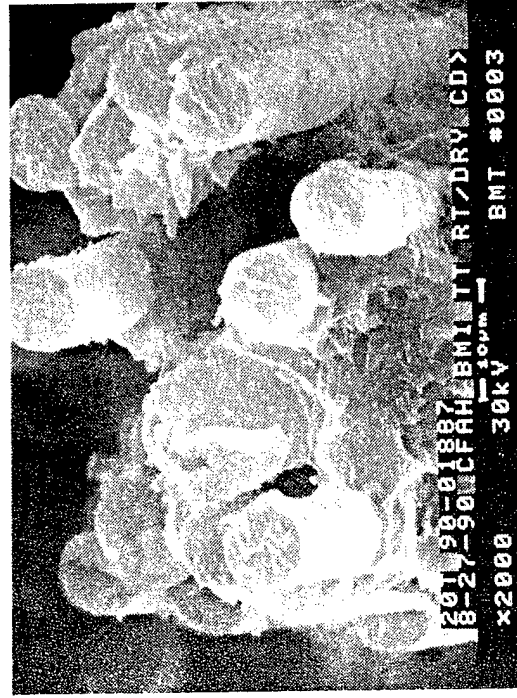
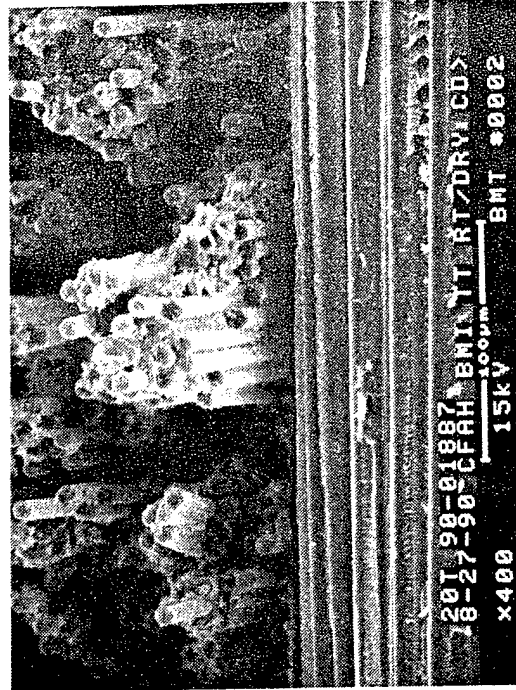
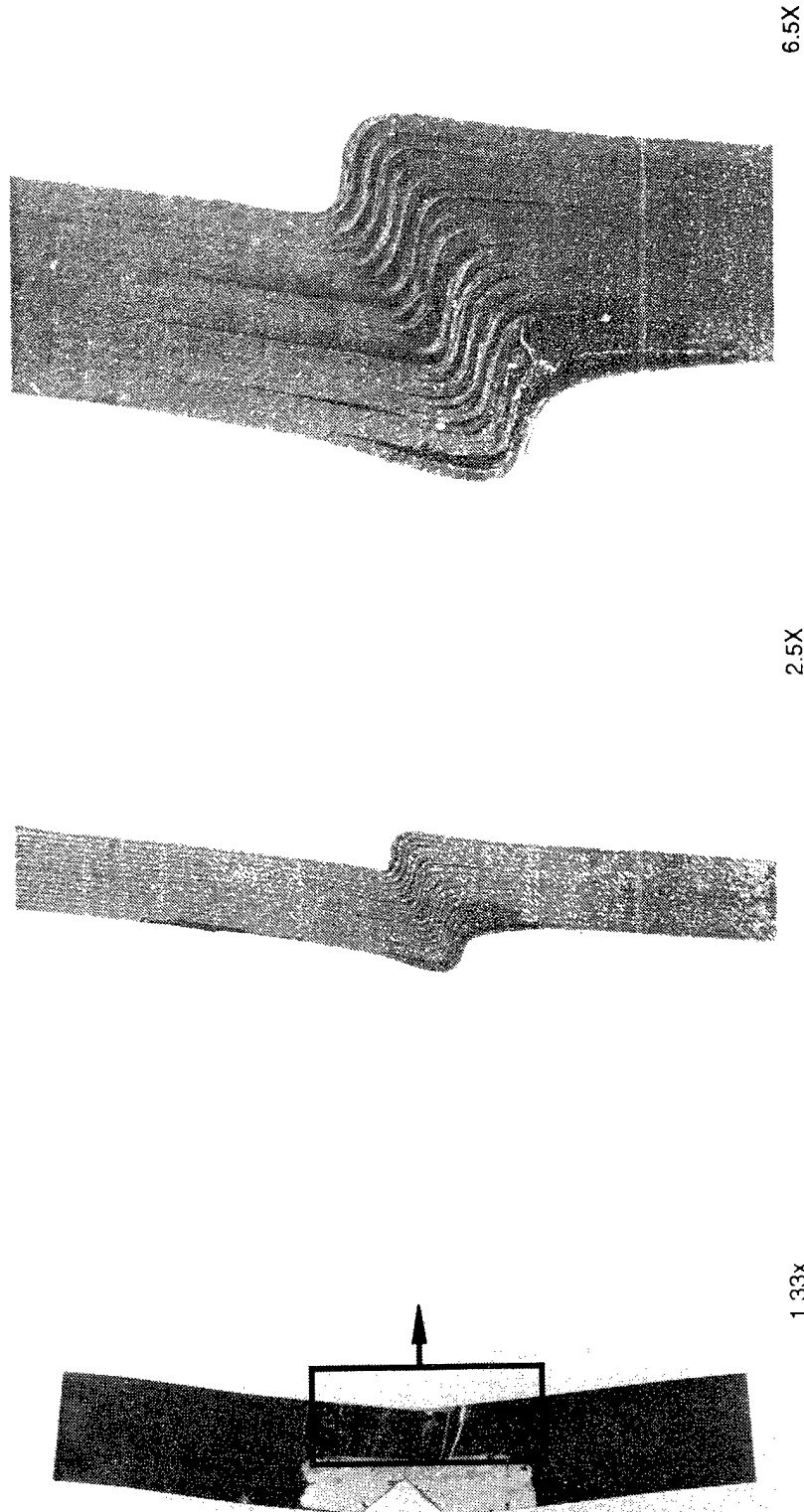


Figure 3.5-5. SEM Fractographs of an AS4/BMI Translaminar Tension RT/Dry Fracture



(a) Face View  
 (b) Cross-Section View  
 Figure 3.5-6. Macrophotographs of BMI/AS4 Translaminar Tension Specimen Tested at 450° F/Dry

**SECTION 3.6**  
**FIBERGLASS/THERMOSET**  
**EC 9-756-K43/RUTAPOX L-20/SL**

**3.6.1 Introduction**

This section shows the results of the fractography on L-20/SL (FG/Rutapox) test coupons. This composite system is currently used by Grob Industries to manufacture lightweight aircraft. Because the primary structures on these aircraft are fabricated using fabric material, the interlaminar test coupons (DCB and ENF) also consisted of fabric made by using a wet hand lay-up technique. However, to evaluate basic fractographic surfaces, additional specimens were machined from panels fabricated using fiber rovings. A general comparison of the two forms reveal similar fracture modes but the fabric did not appear to have as good of fiber wet out as the rovings.

**3.6.2 Static Loading**

**Interlaminar Mode I (Tension), Normal and High Strain Rate RT/Dry**

Visual examination revealed an opaque white fracture surface and an easily discernible fiber fabric weave. As shown in Figure 3.6-1 & 3.6-2, SEM examination revealed very few regions containing rivermarks, which would indicate the crack growth direction. In addition, there were numerous areas of matrix material cracking features that appear to be similar to hackles, which are usually indicative of a mode II shear loading than mode I tensile. The high strain rate test fracture surfaces Figure 3.6-3 & 3.6-4, exhibited a smaller region of fracture between the fabric plies. The "high" spots of the fabric weave were apparently the only areas that had fractured.

**Interlaminar Mode II (Shear), RT/Dry and Hot/Wet**

The fracture surfaces of both specimens exhibited similar features (Figure 3.6-4 & 3.6-5). The fabric tows parallel to the crack propagation orientation contained the hackles typical of a shear loading. Whereas the tows perpendicular to the crack direction exhibited ribbons of resin tearing from the fibers. The torn ends were generally bent towards the crack propagation direction.

The fracture surface of the RT/Dry specimen was composed mainly of resin which indicates that the crack propagated through the interface between the fabric surface (as seen in the Hot/Wet fractographs) and the resin. In addition, voids were also present at the fabric tow intersections

### **±45° Tensile Fracture Specimen**

The fabric specimen fracture surfaces (Figure 3.6-7) were more consolidated as compared to the roving specimen surfaces. There were fewer fiber pullout regions but wetting of the fibers did not appear to be as thorough. Furthermore, unlike the roving specimen, the fabric fiber ends exhibited a fracture morphology indicative of a compression loading. These were also grouped in more bundles compared to the roving specimen fiber ends.

In the specimen made using only rovings (Figure 3.6-8), the fracture surface exhibited primarily mode II fracture features with some limited regions of mode I. The overall appearance was very fibrous with a considerable amount of fiber pullout.

### **Open Hole Tension, Fabric**

The overall fracture surface (Figure 3.6-9) was very fibrous and jagged with numerous regions of mode II (shear). No river patterns, indicative of mode I (tension) fractures, appeared in the intralaminar fracture surfaces. The fracture morphology appeared to resemble a tearing of groups of fibers from the tow bundle with resin attaching to both surfaces of separated fiber bundle. In addition, the fibers did not appear to have complete fiber wet out by the resin.

### **Open Hole Compression, Rovings,**

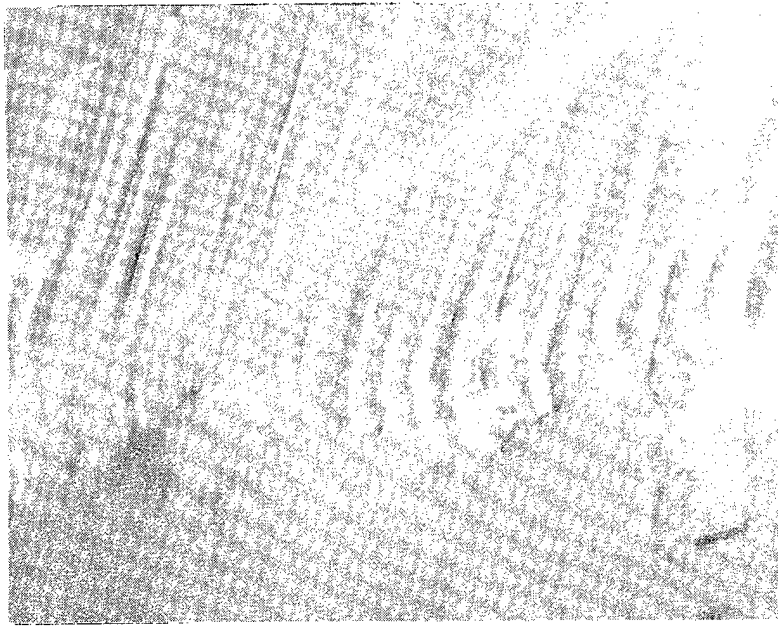
This fracture plane (Figure 3.6-10) was more distorted than the graphite specimen fracture surface but it was a more consistent morphology throughout the surface. The overall surface consisted of fiber bundles which had fractured together in one layer, generally covering the entire fracture surface. The fiber ends and surrounding resin exhibited the classic compression loading morphology.

### **Translaminar Mode I (Tensile), 4ptNT, Rovings, RT/Dry and Hot/Wet**

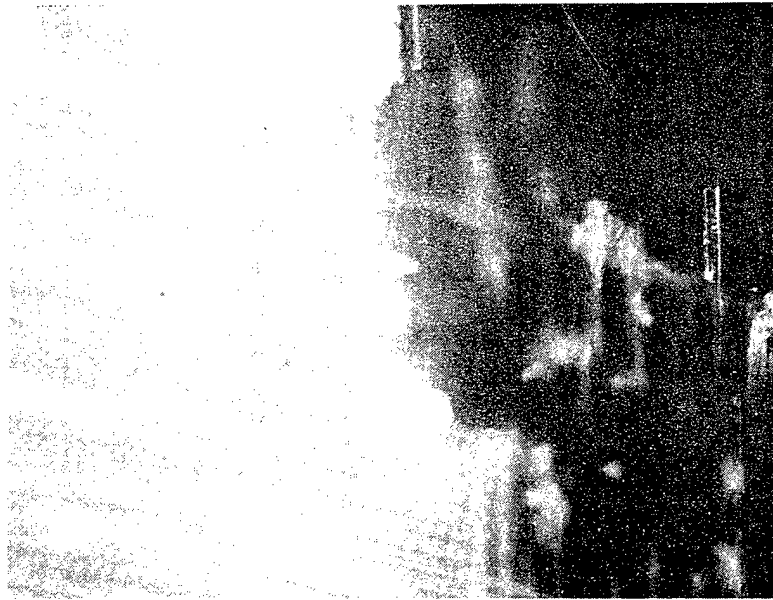
Large amounts of fiber pullout were present throughout the surfaces of both specimens (Figure 3.6-11 & 3.6-12). Fibers that pulled out from along the intralaminar surfaces (the 90° direction tows) were not wetted very thoroughly and the resin fracture surfaces on this fracture surface contained only a few fracture features. Unlike the other roving specimens, there didn't appear to be thorough fiber wet out in these roving specimens.

### **3.6.3 Short-Term Environmental Exposure**

For the Rutapox epoxy resin system, only four specimens were examined that were of the most severe environments; JP4, Acetone, MEK, and Hydraulic Fluid (Figure 3.6-14 through 3.6-16). Examination of the fracture surfaces revealed no degradation of the fracture features regardless of the exposure conditions.



400X



100X

Figure 3.6-1. Optical Fractographs of a Rutapox/FG Fabric Interlaminar Mode I (Tensile) Fracture Surface, RT

Mechanically Induced  
Crack Direction  
↓

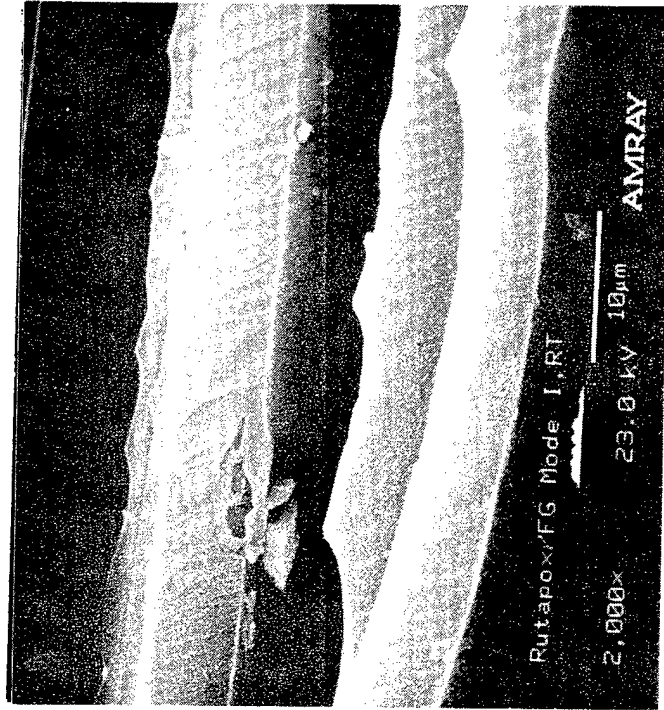
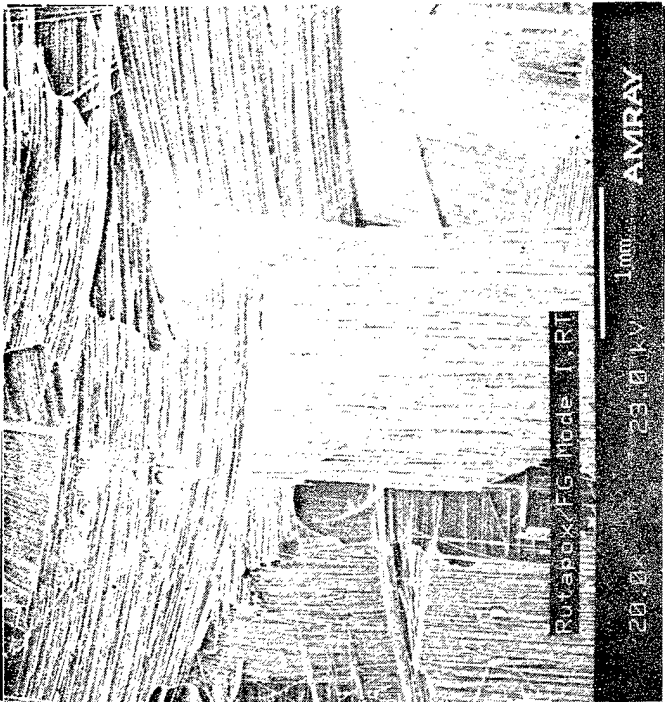
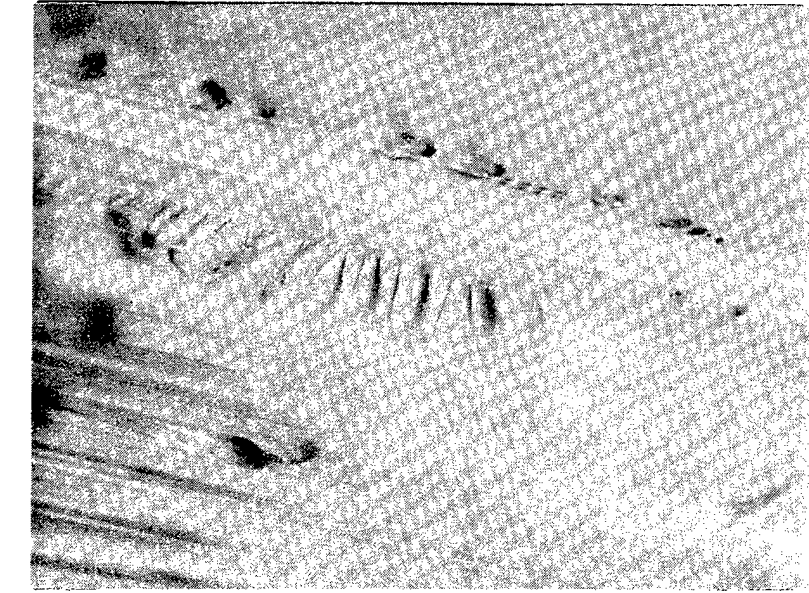
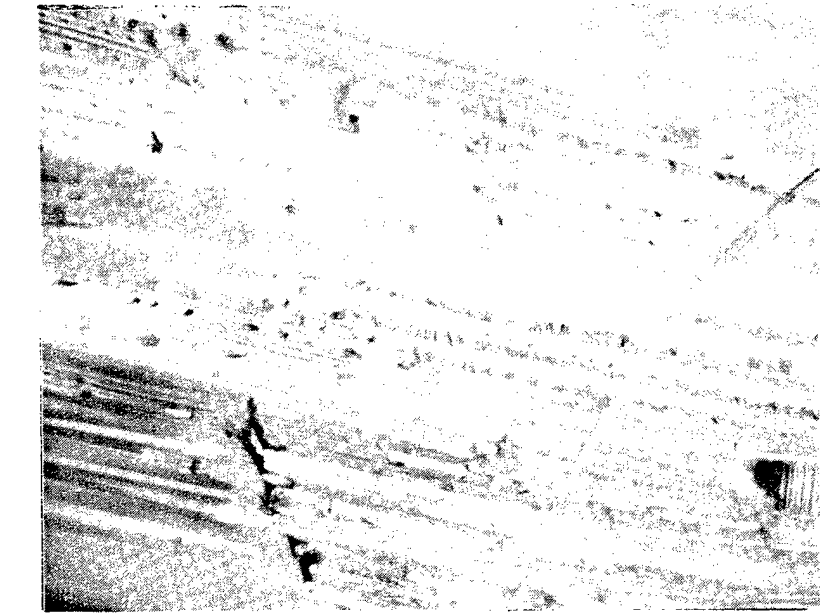


Figure 3.6-2. SEM Fractographs of a Rutapox/FG Fabric Interlaminar Mode I (Tensile) Fracture Surface, RT





400X



100X

Figure 3.6-3. Optical Fractographs of a Rutapox/FG Fabric Interlaminar Mode I (Tensile) High-Rate Fracture Surface, RT

Mechanically Induced  
Crack Direction  
↓

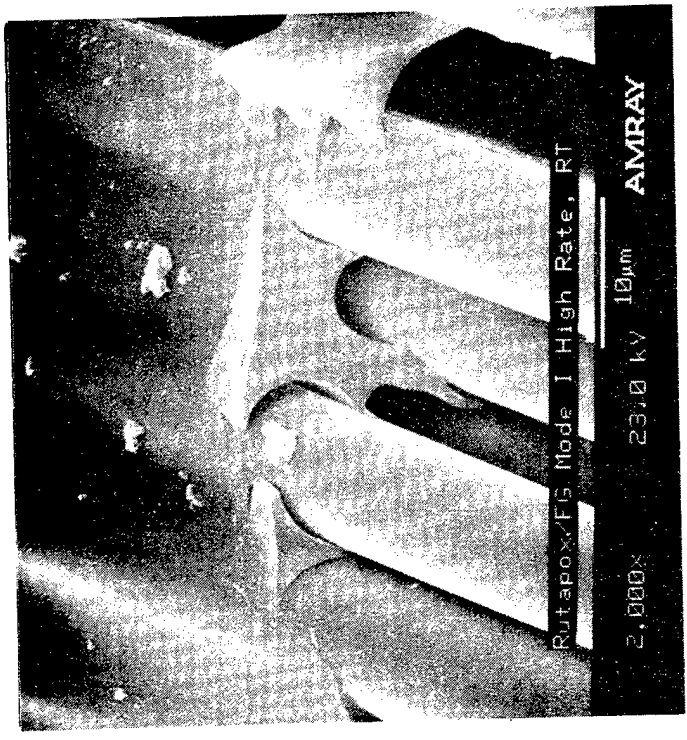
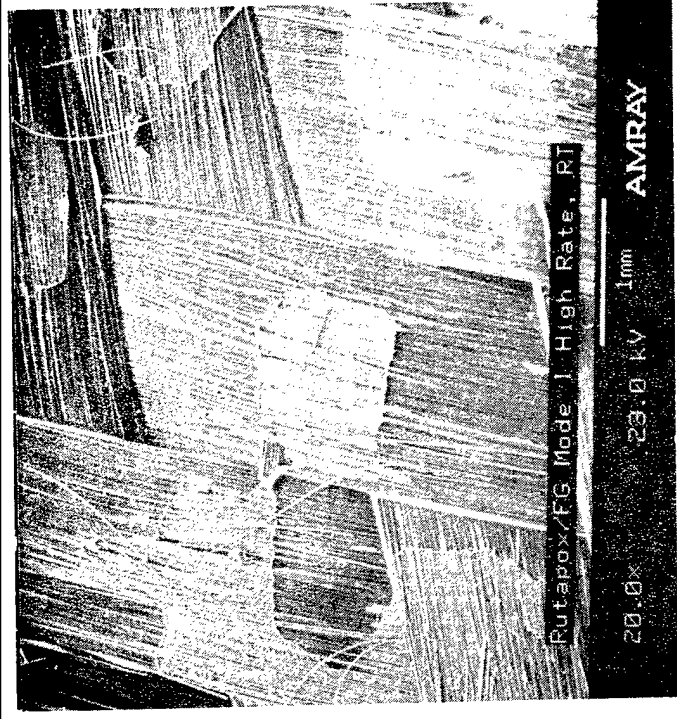


Figure 3.6-4. SEM Fractographs of a Rutapox/FG Fabric Interlaminar Mode I (Tensile) High-Rate Fracture Surface, RT

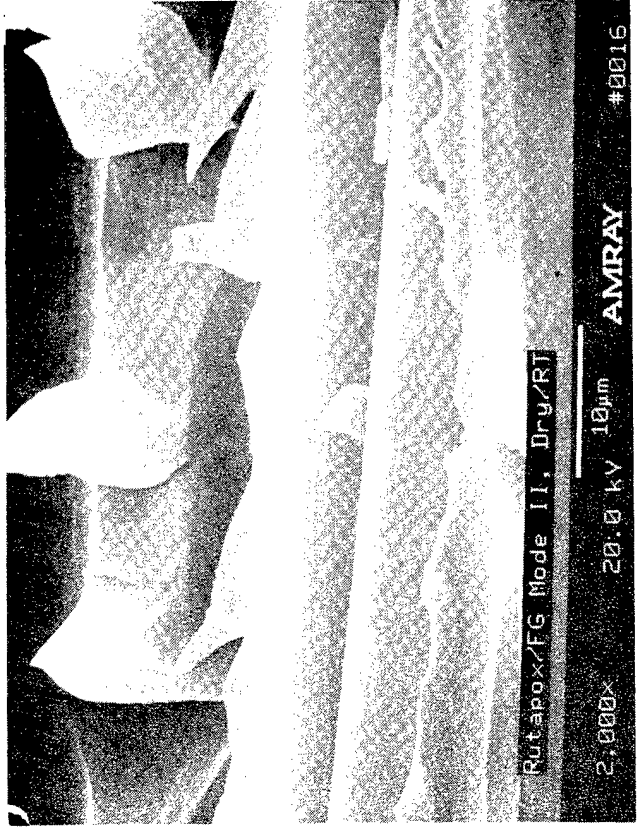
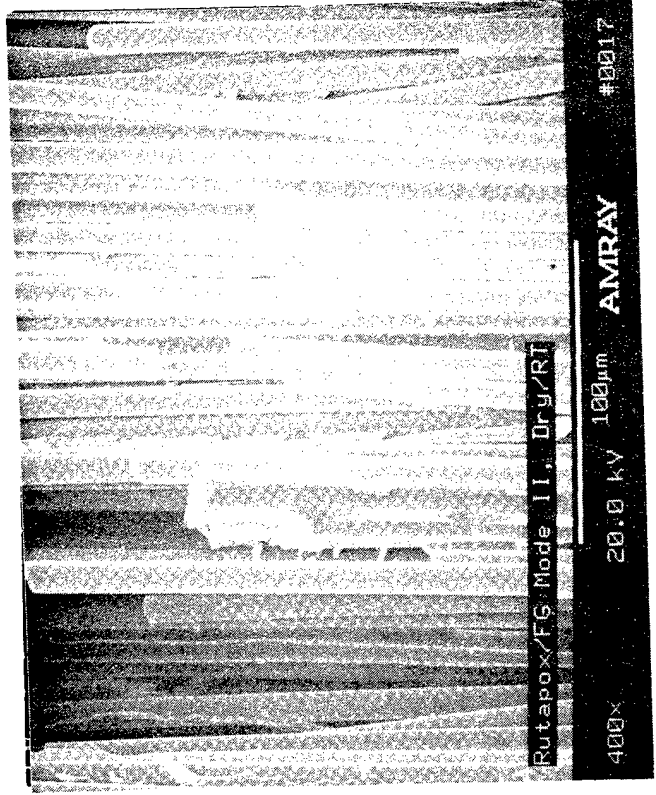
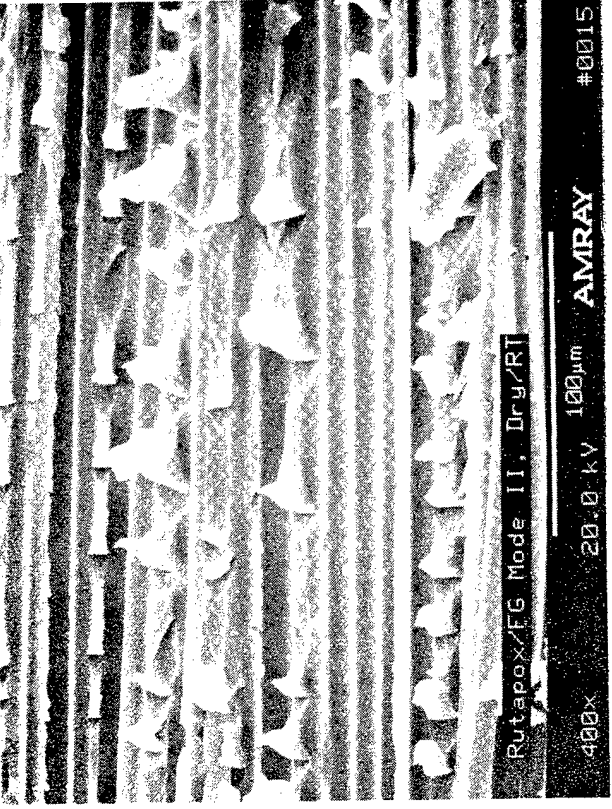
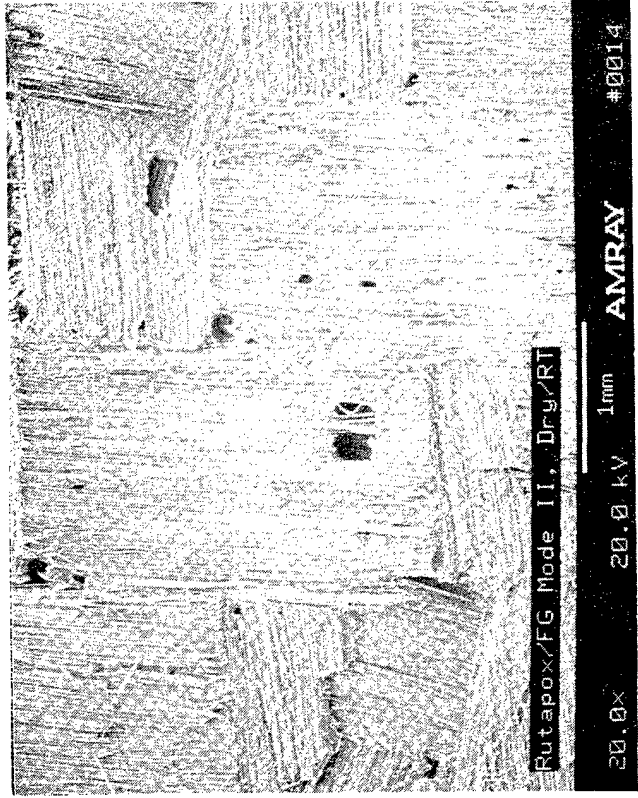


Figure 3.6-5. SEM Fractographs of a Rutapox/FG Fabric Interlaminar Mode II (Shear) Fracture Surface, RT

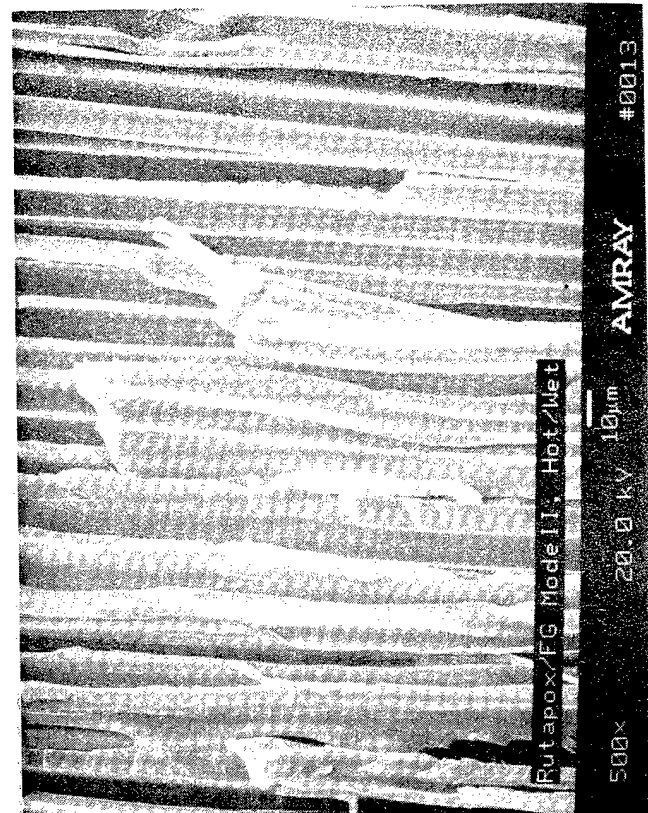
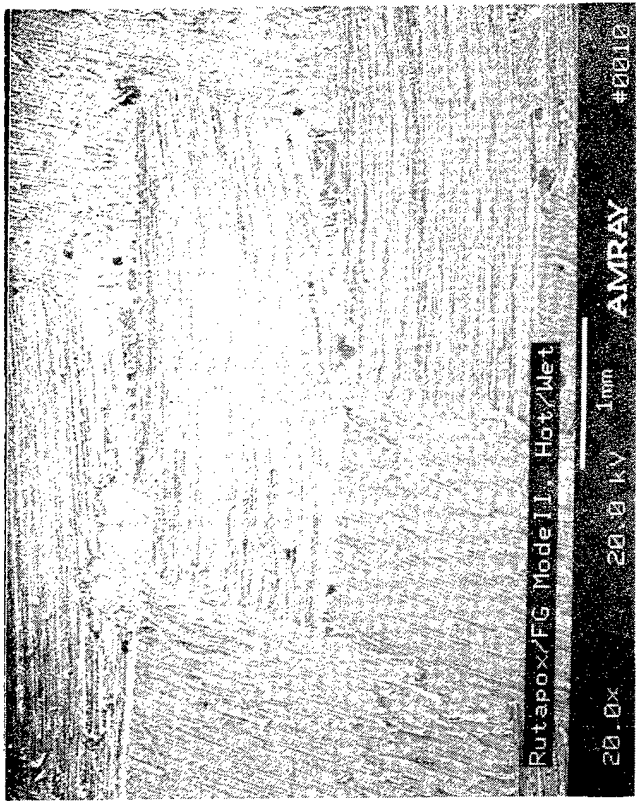
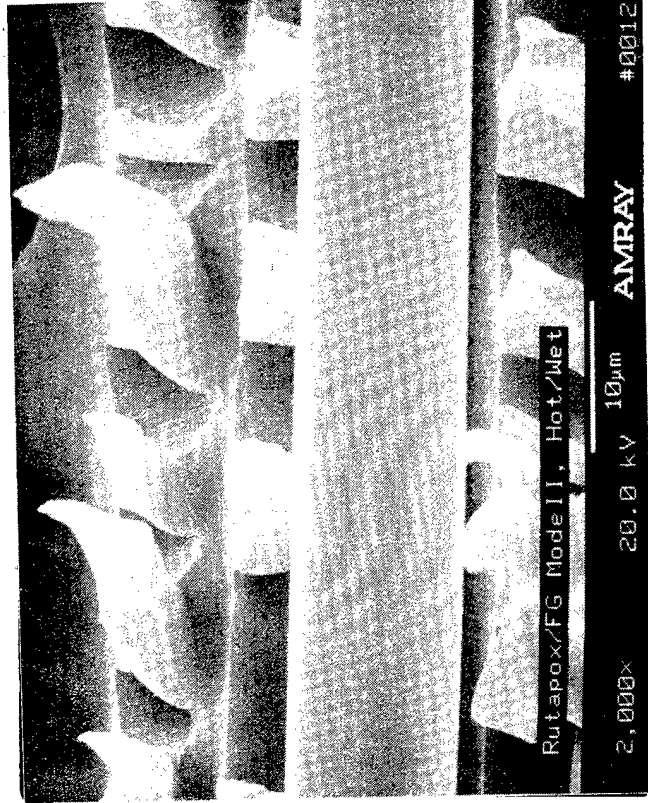
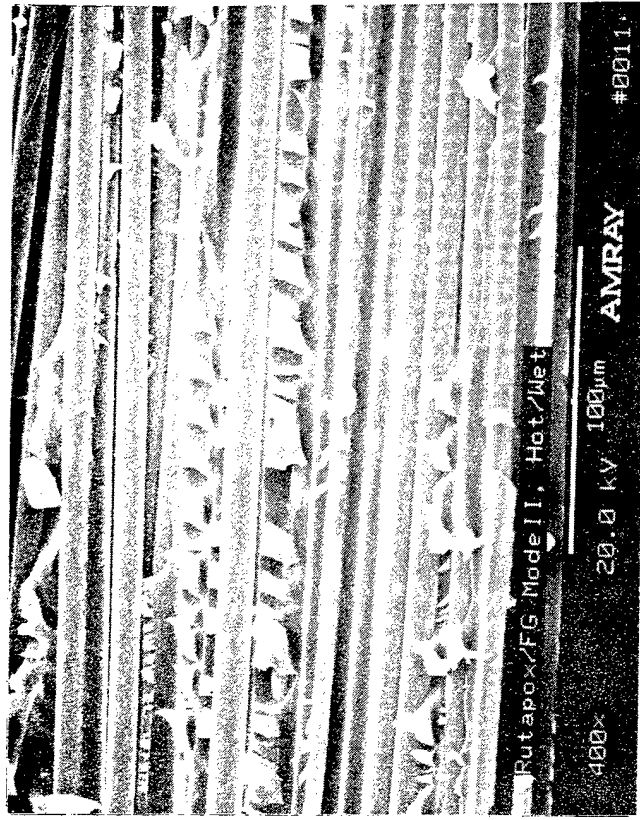


Figure 3.6-6. SEM Fractographs of a Rutapox/FG Fabric Interlaminar Mode II (Shear) Hot/Wet Fracture Surface, RT

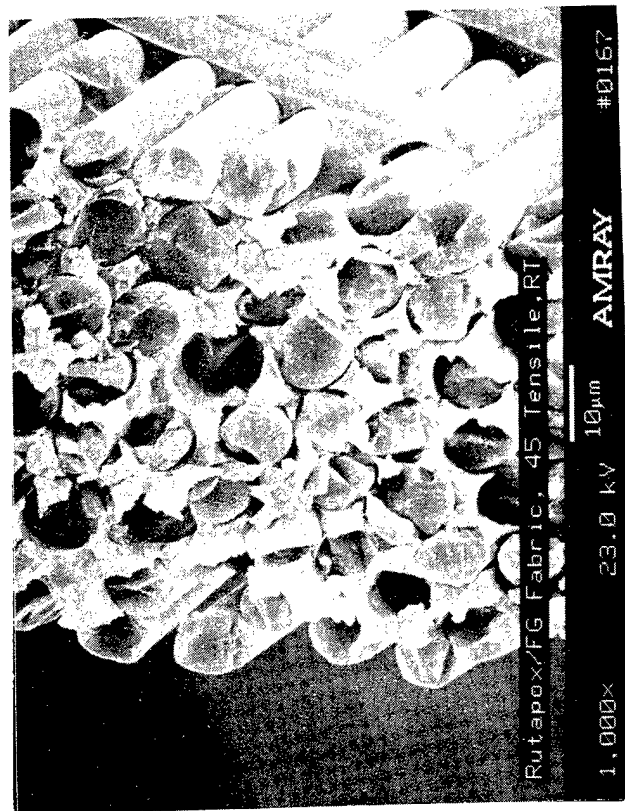
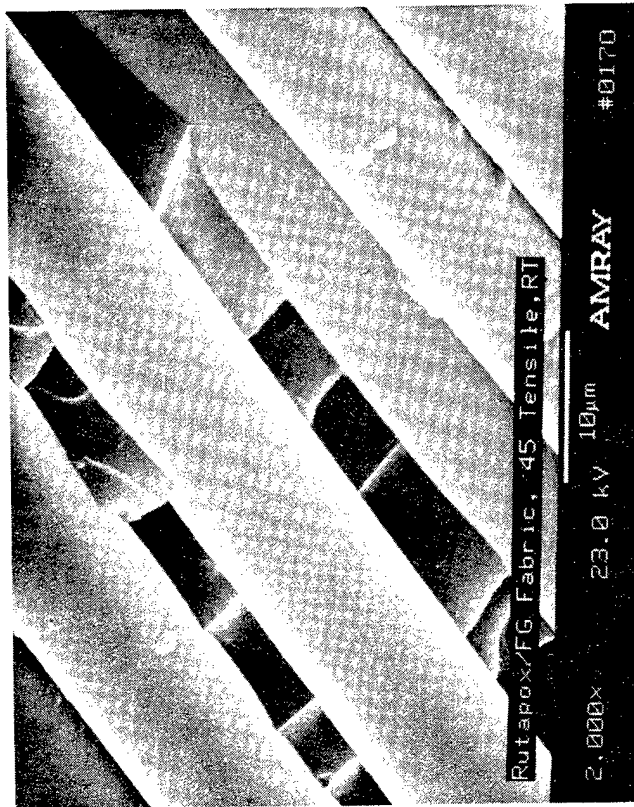
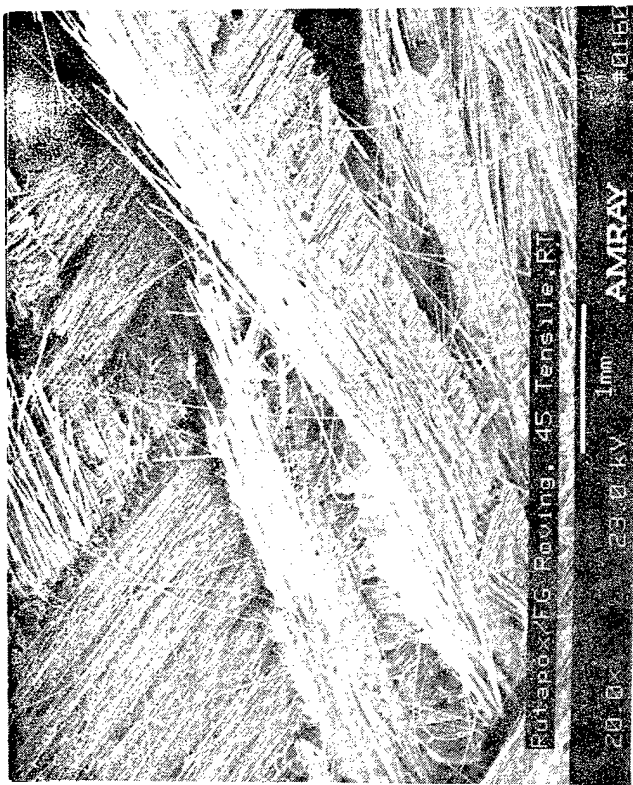


Figure 3.6-7. SEM Fractographs of a Rutapox/FG Fabric  $\pm$  45° Tensile Fracture Surface, RT



Mechanically Induced  
Crack Direction

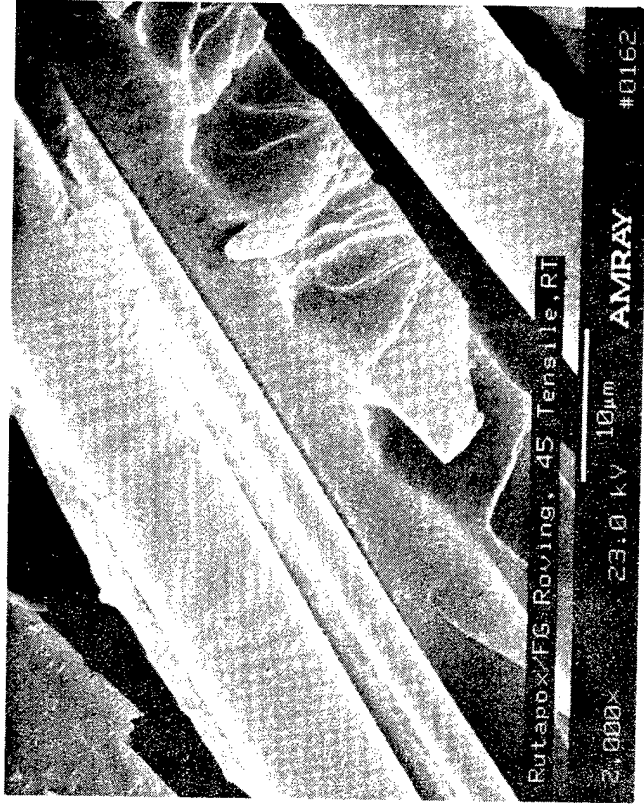


Figure 3.6-8. SEM Fractographs of a Rutapox/FG Rovings  $\pm$  45° Tensile Fracture Surface, RT

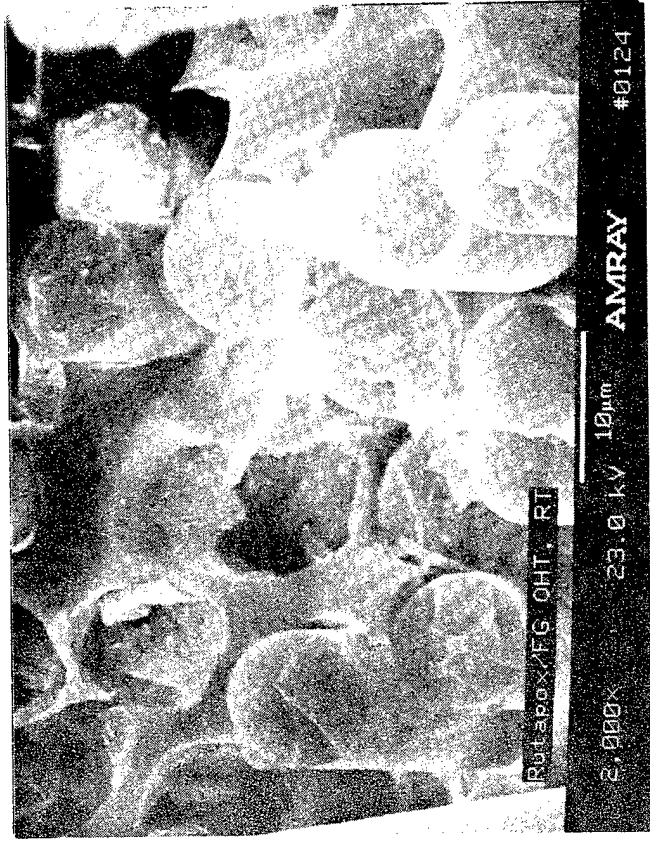
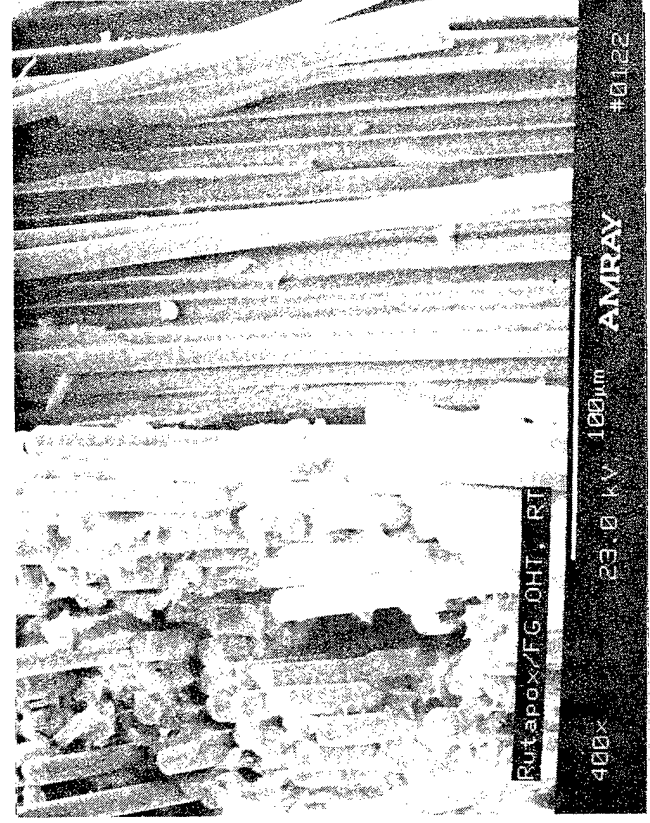


Figure 3.6-9. SEM Fractographs of a Rutapox/FG Fabric Open Hole Tension Fracture Surface, RT

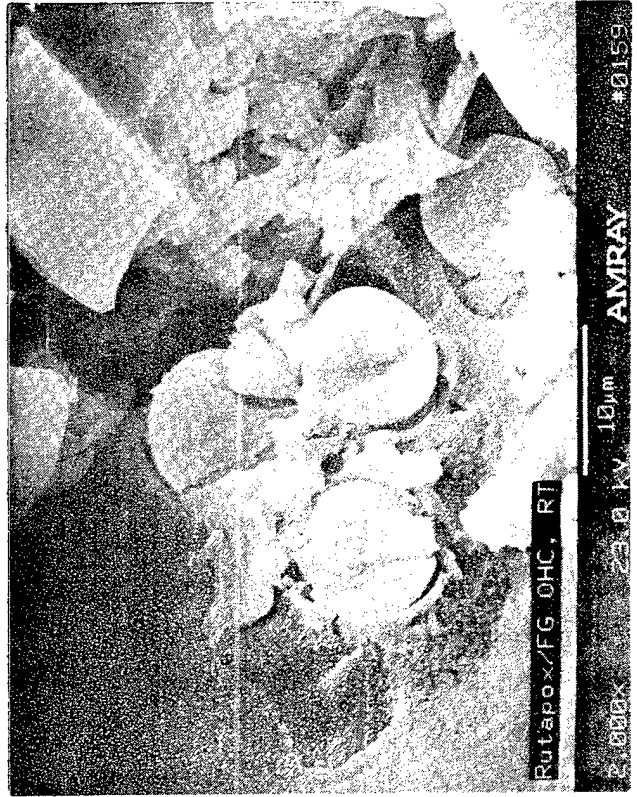
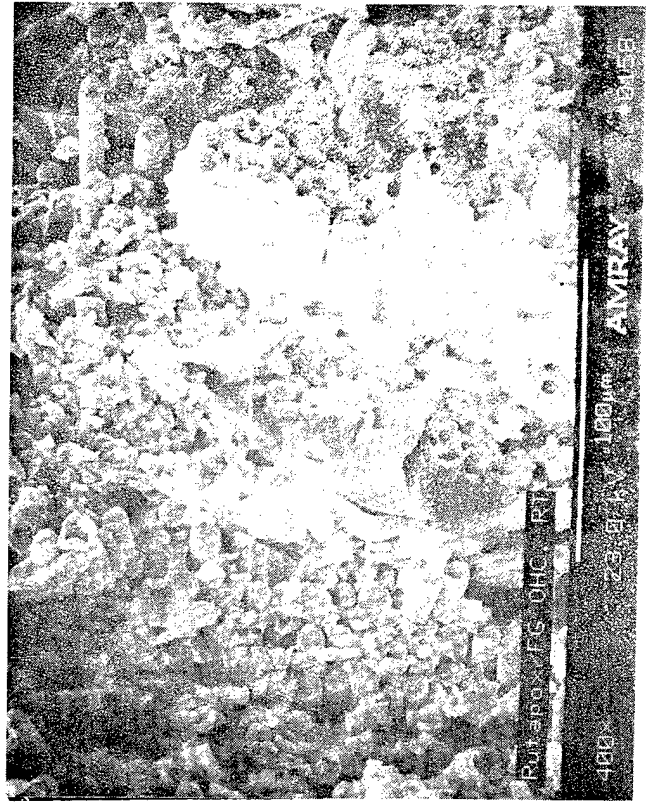
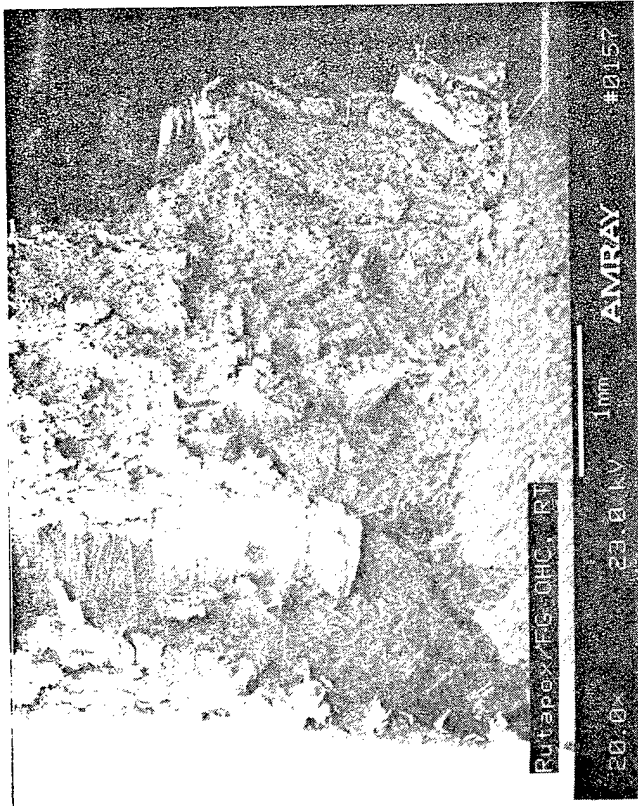
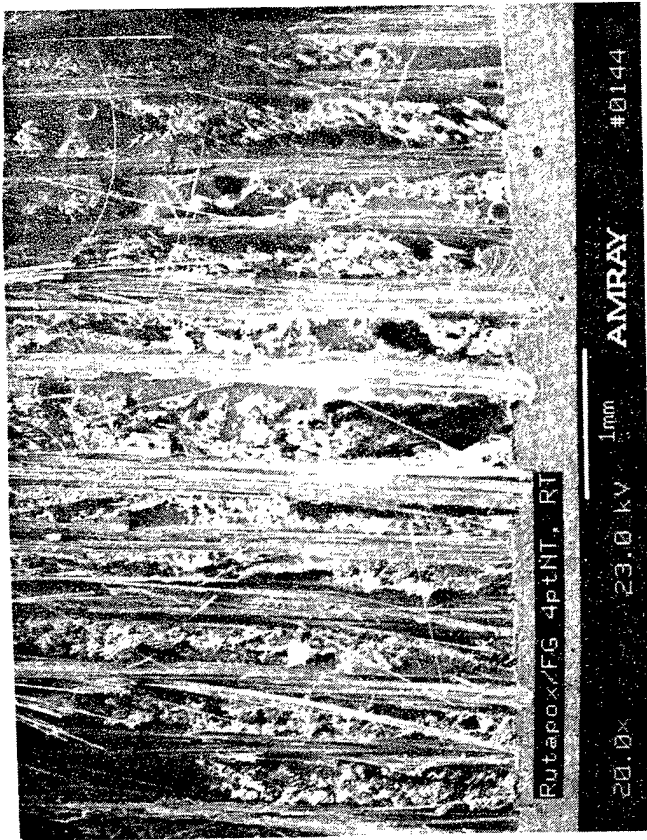


Figure 3.6-10. SEM Fractographs of a Rutapox/FG Rovings Open Hole Compression Fracture Surface. RT





Mechanically Induced  
Crack Direction

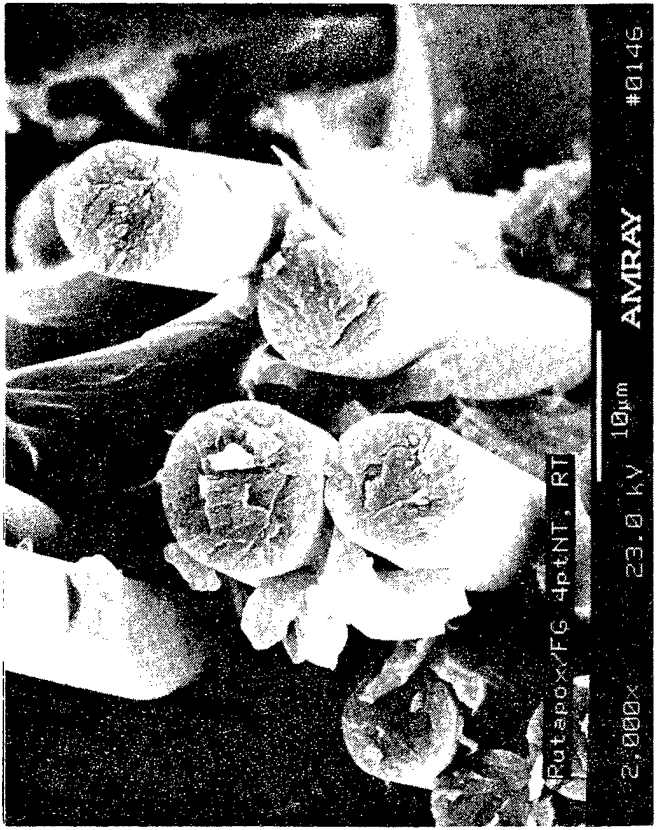
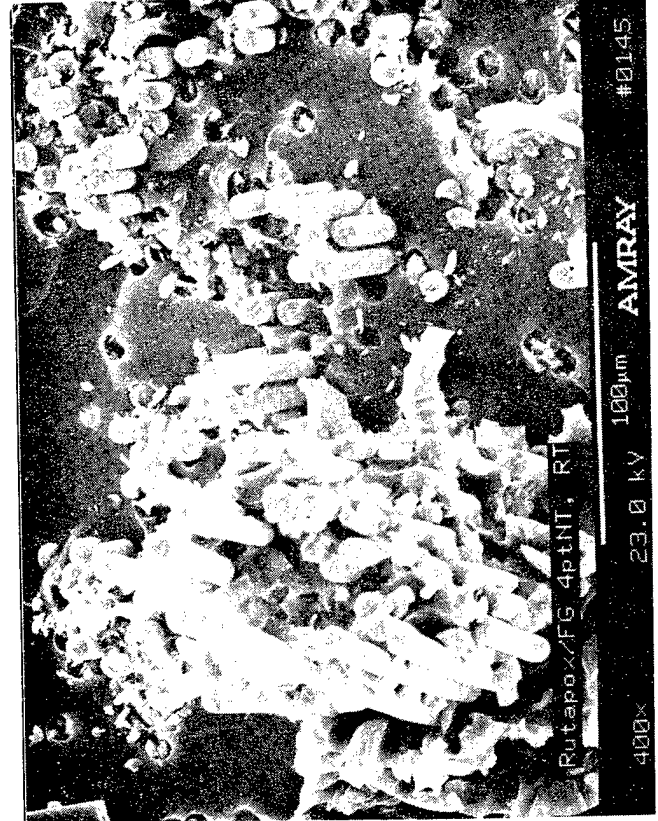
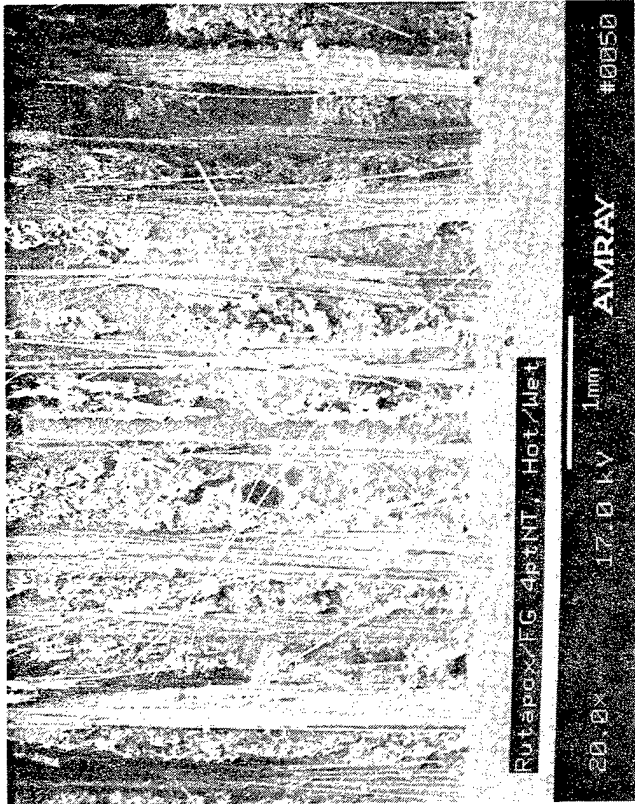


Figure 3.6-11. SEM Fractographs of a Rutapox/FG Roving 4ptNT Specimen Fracture Surface, RT



Mechanically Induced  
Crack Direction  
↑

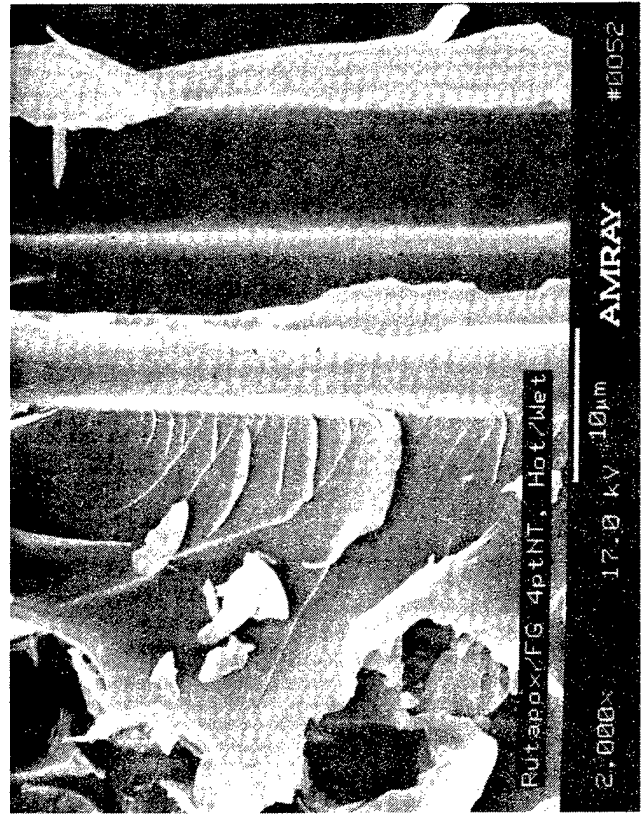
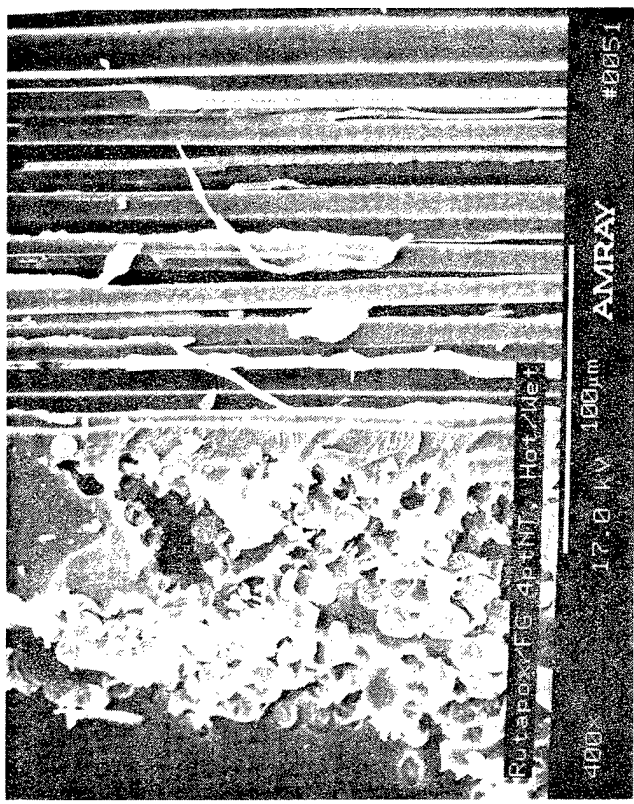
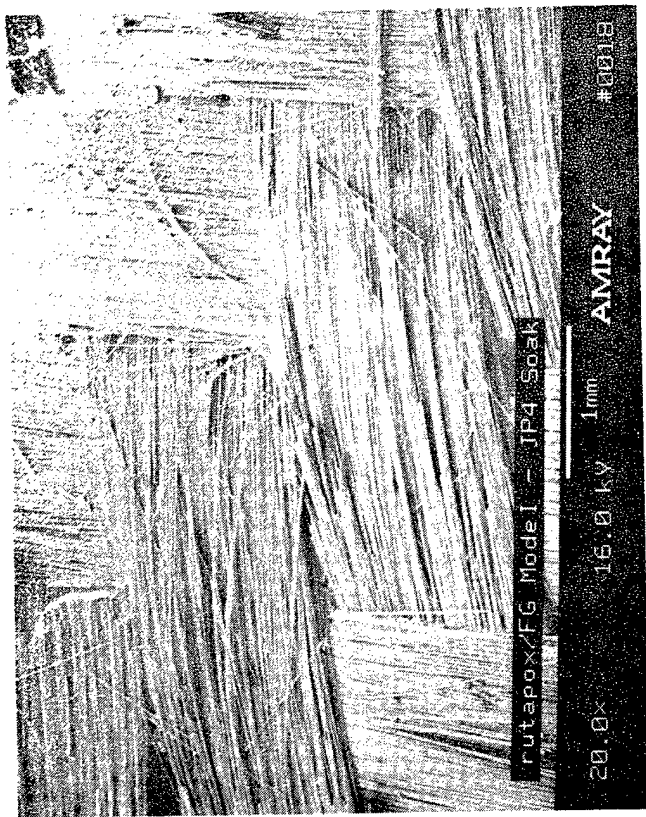


Figure 3.6-12. SEM Fractographs of a Rutapox/FG Roving 4ptNT Fracture Surface, Hot/Wet



Mechanically Induced  
Crack Direction  
↓

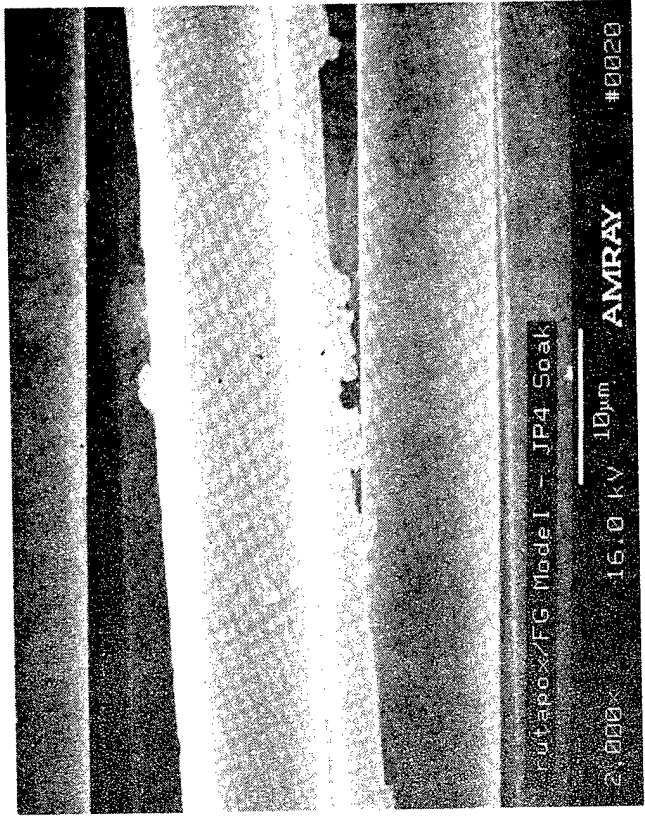
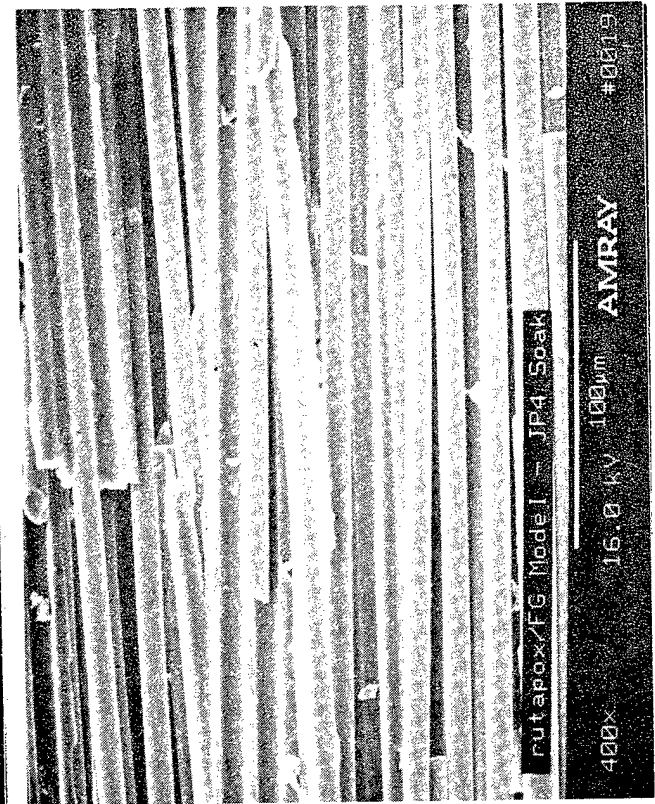
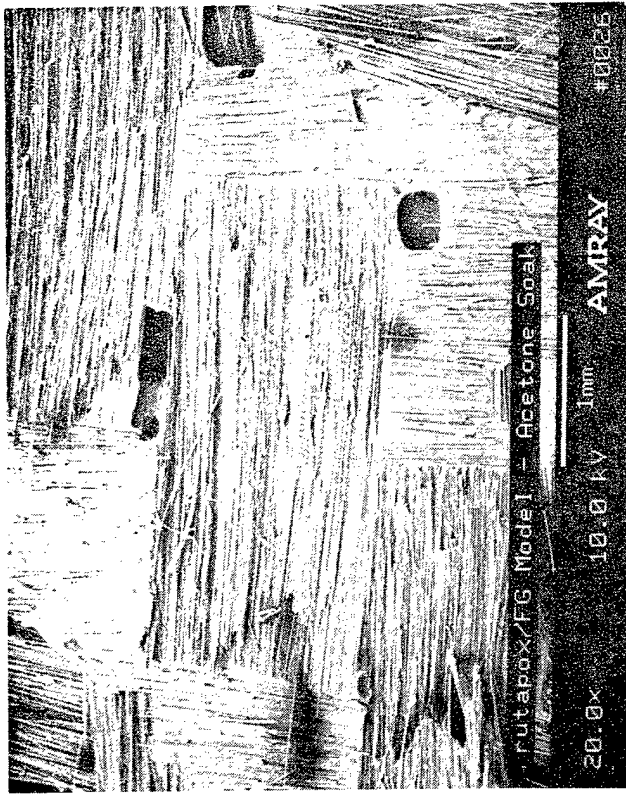


Figure 3.6-13. SEM Fractographs of a Rutapox/FG Fabric Interlaminar Mode I (Tensile) Fracture Surface Exposed to JP4 Jet Fuel for 7 days



Mechanically Induced  
Crack Direction  
↓

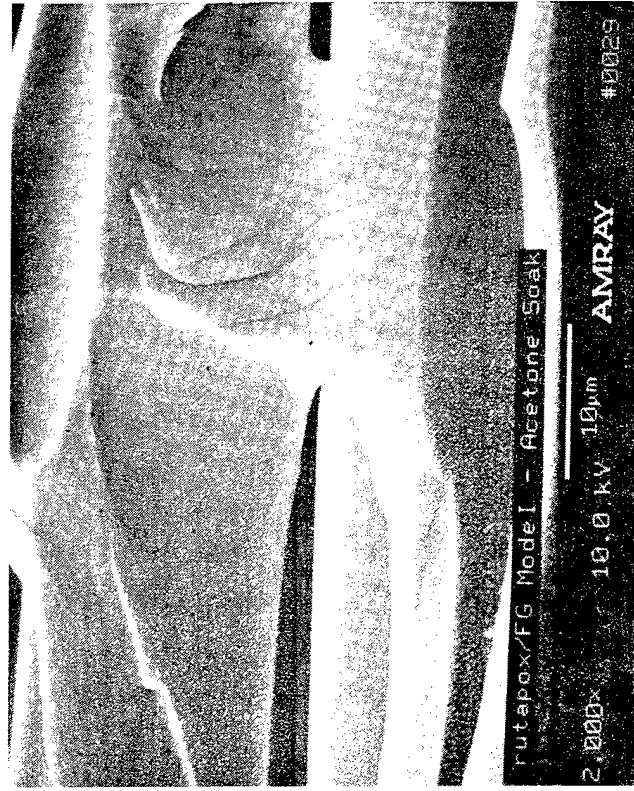
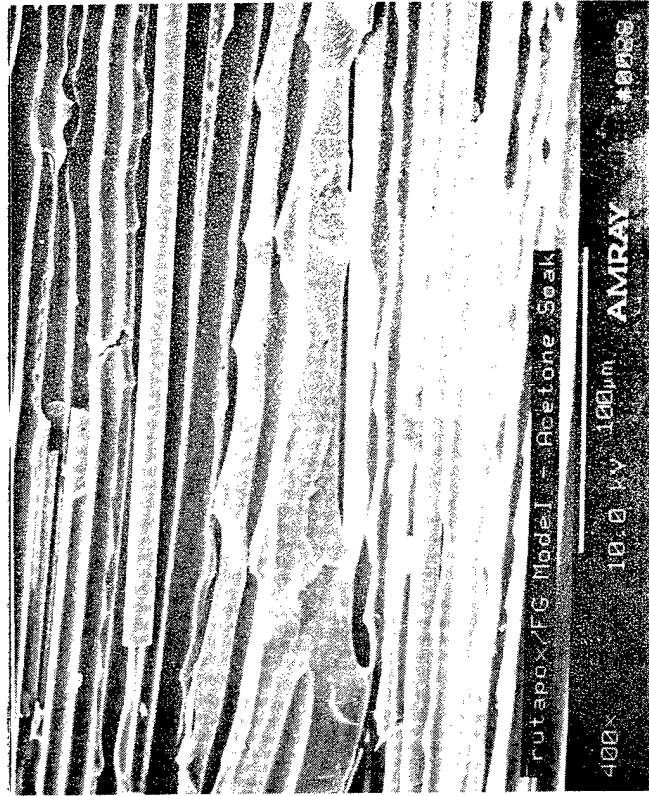
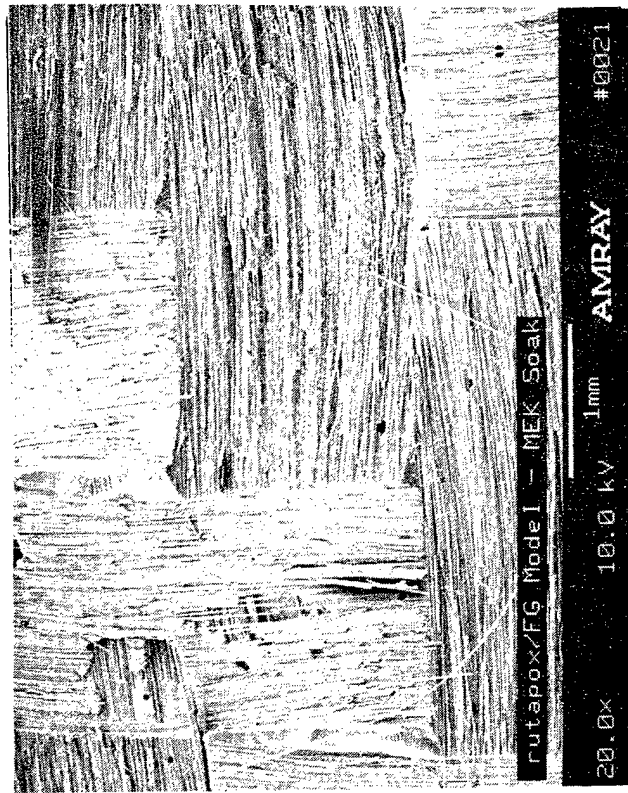


Figure 3.6-14. SEM Fractographs of a Rutapox/FG Fabric Interlaminar Mode I (Tensile) Fracture Surface Exposed to Acetone for 7 days



Mechanically Induced  
Crack Direction  
↓

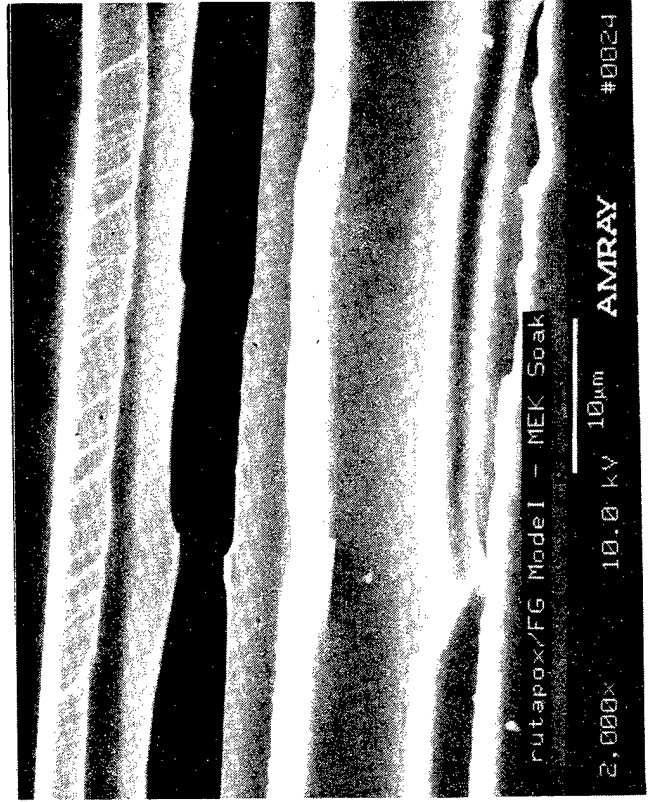
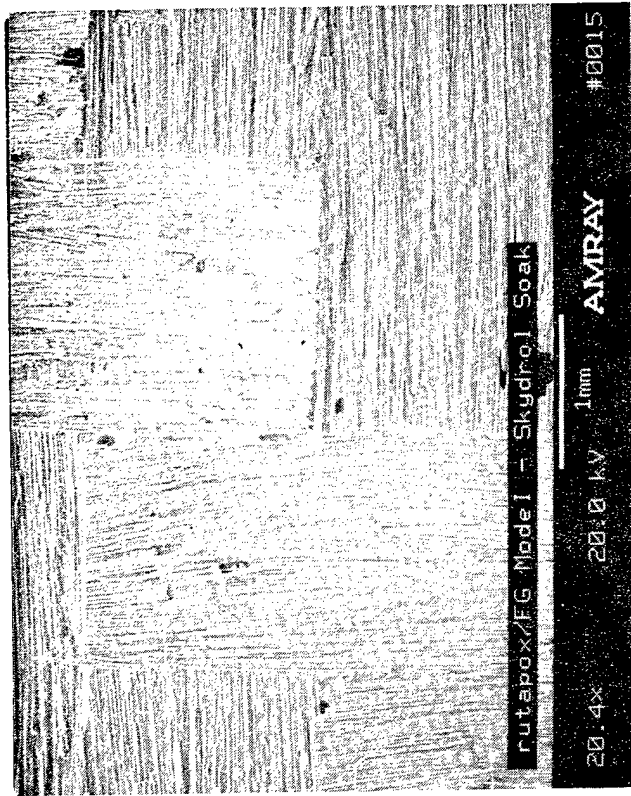


Figure 3.6-15. SEM Fractographs of a Rutapox/FG Fabric Interlaminar Mode I (Tensile) Fracture Surface Exposed to MEK for 7 days



Mechanically Induced  
Crack Direction  
↓

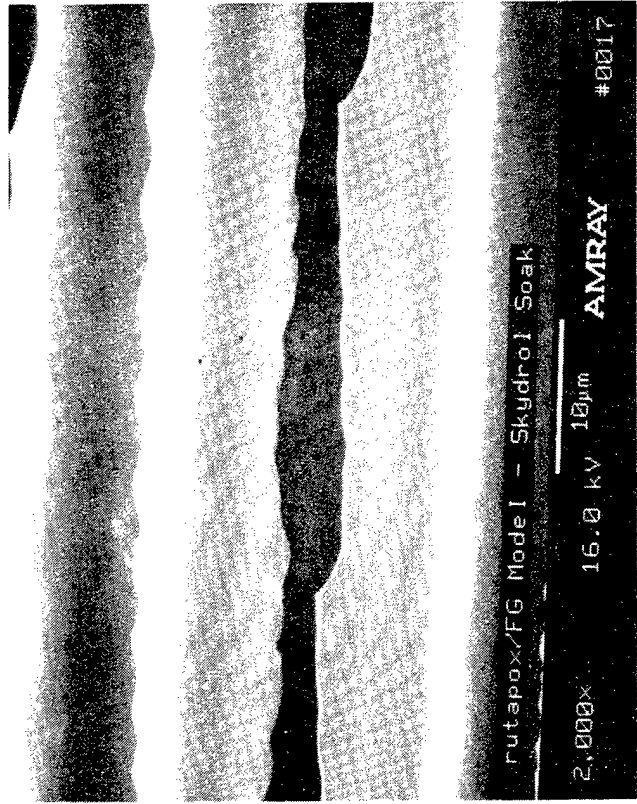
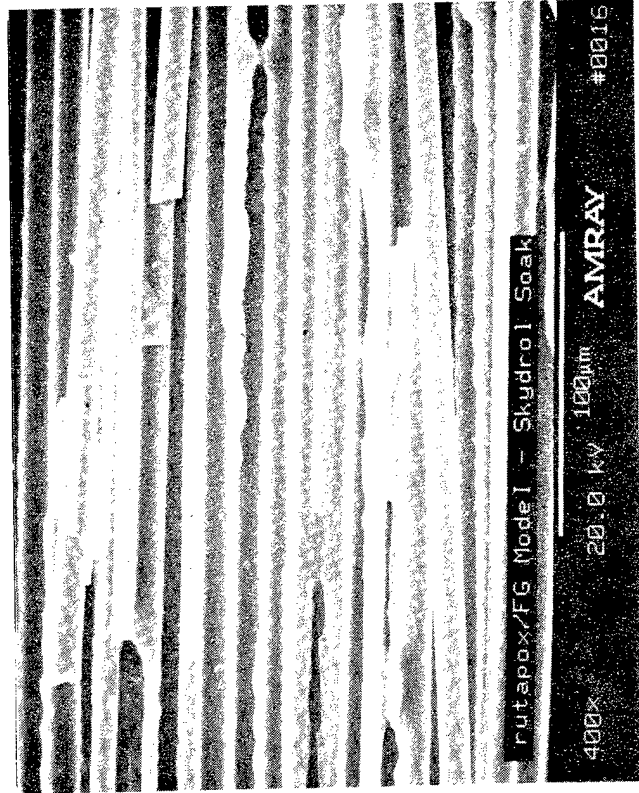


Figure 3.6-16. SEM Fractographs of a Rutapox/FG Fabric Interlaminar Mode I (Tensile) Fracture Surface Exposed to Hydraulic Fluid for 7 days

**SECTION 3.7**  
**CARBON/THERMOSET**  
**HTA-5131-12K/RUTAPOX L-20/SL**

**3.7.1 Introduction**

This section presents the fractographic examination of the HTA-5131-12K/Rutapox L-20/SL (Gr/Rutapox) test specimens. This system is also used on lightweight aircraft manufactured by Grob Industries, although primarily on a high-altitude research version. Similar to the fiberglass system, these aircraft structures are fabricated primarily using carbon fiber fabric. Consequently, most of the test specimens were fabricated using fabric for the interlaminar (DCB and ENF) fracture specimens, made using a wet hand lay-up technique. However, to evaluate other basic fractographic morphologies, additional specimens were machined from panels that were fabricated using fiber rovings. One unique feature of the fabric was that these carbon fibers were slightly oval and contained numerous longitudinal ridges. These features were not seen in the carbon fiber rovings nor were they present in the fiberglass fibers of either the fabric or the rovings.

**3.7.2 Static Loading**

**Interlaminar Mode I (Tension), Normal and High Strain Rate RT/Dry**

The fracture surface (Figure 3.7-1 & 3.7-2) contained numerous resin-rich regions with voids distributed throughout the surface. These voids were likely the result of panel processing rather than a specific material attribute. This resulted in an overall shiny appearance when examined visually. SEM examination (Figure 3.7-1) revealed numerous rivermarks in the resin-rich regions indicating the crack growth direction. The resin between the fibers perpendicular to the fracture direction was composed of hackles with no specific discernible fracture direction.

The high strain rate specimen fracture surfaces (Figure 3.7-3 & 3.7-4) were similar to the normal rate specimens, but the river patterns were more evident.

**Interlaminar Mode II (Shear), RT/Dry and Hot/Wet**

The visual appearance was generally rough similar to the mode I surfaces but with fewer shiny regions (Figure 3.7-5 & 3.7-6). The fracture surfaces were similar to the fiberglass specimens with the exception of the carbon fiber features as mentioned above. The fabric tows parallel to the crack propagation orientation contained the hackles typical of a shear loading and the tows perpendicular to the crack direction exhibited the ribbons of resin. The torn ends of the resin were generally bent towards the crack propagation direction.

The fracture surface of the RT/dry specimen was composed mainly of resin which indicates that the crack propagated through the interface between the fabric surface (as seen in the Hot/Wet fractographs) and

the resin. This resin fracture surface also contained translaminar cracks, perpendicular to the fibers, which are typical of shear cracked resin surfaces. In addition, voids were also present at the fabric tow intersections.

#### **Translaminar Mode I (Tensile), 4ptNT, Rovings, RT/Dry & Hot/Wet**

Both fracture surfaces (Figures 3.7-7 & 3.7-8) were similar and both contained slightly oval fibers with longitudinal striations. There was little correlation between the fiber end fractures and the macroscopic fracture direction. In addition, even there was fairly good wetting of the fibers by the resin, it was difficult to determine the fracture direction on the ply surfaces parallel the fracture direction. Few fracture morphology features were evident on the these surfaces.

#### **$\pm 45^\circ$ Tensile Fracture Surface Rovings and Fabric, RT**

The overall appearance of the fabric surface exhibited both mode I and II fractures features (Figure 3.7-9). The orientation of the hackles did not give an obvious indication of the overall crack propagation direction.

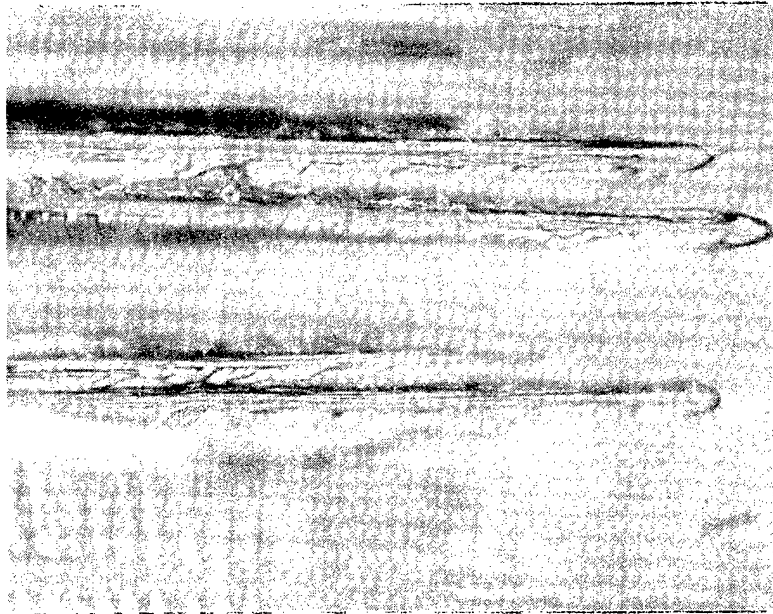
#### **Open Hole Tension, Fabric, RT**

The fiber ends did not clearly indicate the overall crack direction from examination of a small sample (Figure 3.7-10). The fibers were oval and contained distinct longitudinal ridges. Tracer yarns in the fabric were clearly visible and were initially confused with some type of fiber pull-out condition. The plies parallel to the crack direction had hackles on the surfaces, but it generally appeared that these tow regions were pulled apart in a mode I.

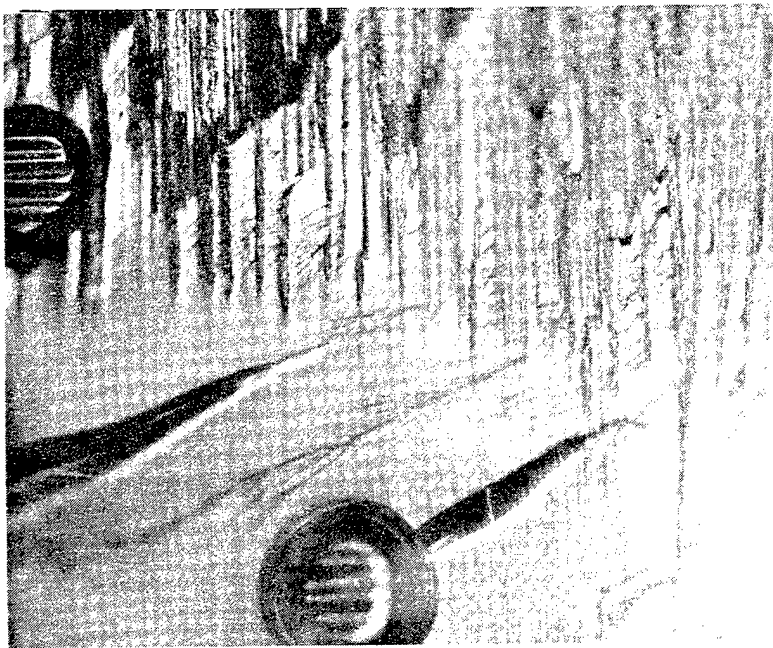
#### **Open Hole Compression**

Two distinct regions were present on the fracture surfaces (Figure 3.7-11). The region adjacent to the hole contained a great deal of rubble covered with small sections of fractured fibers. The regions further away from the hole exhibited the classic compression fracture morphology with the distinct centerline through the fibers. In addition, some of the fibers were actually split along their centerline to an unknown depth.





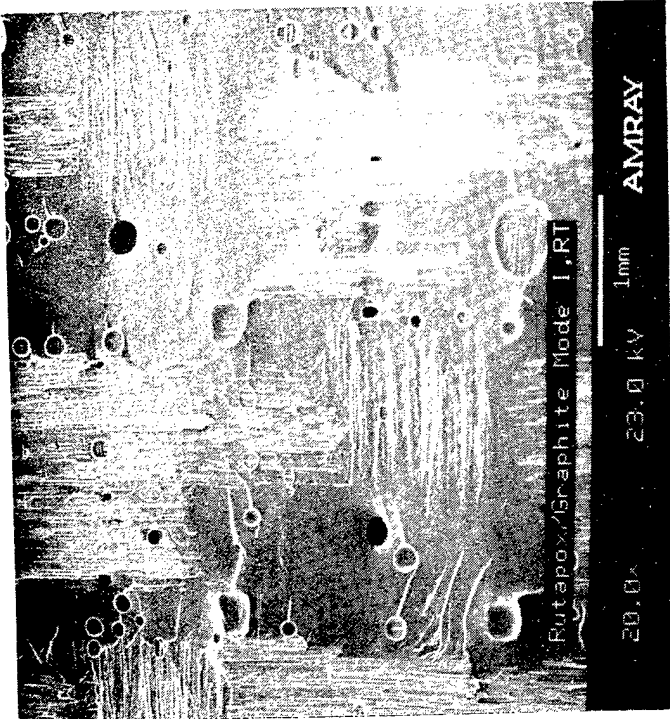
400X



100X



Figure 3.7-1. Optical Fractographs of a Rutapox/Graphite Fabric Interlaminar Mode I (Tensile) Fracture Surface, RT



Mechanically Induced  
Crack Direction  
↑

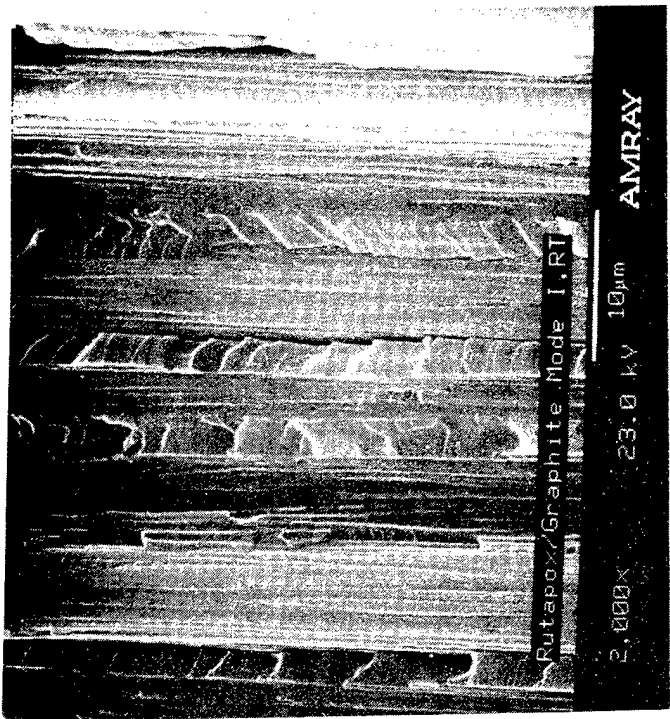
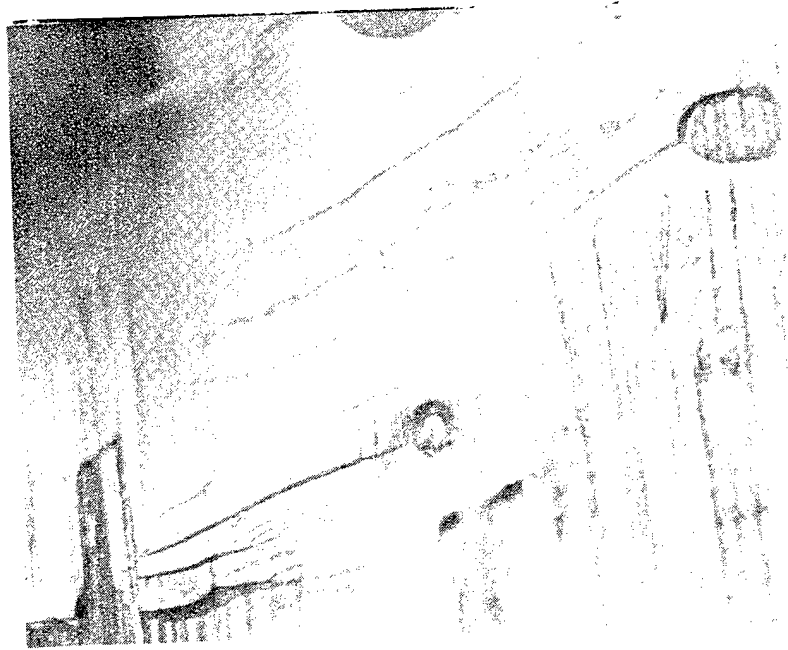


Figure 3.7-2. SEM Fractographs of a Rutapox/Graphite Fabric Interlaminar Mode I (Tensile) Fracture Surface, RT



400X



100X

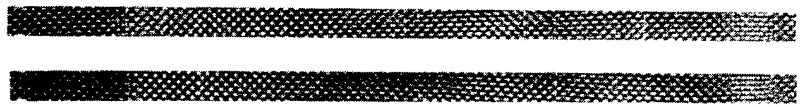
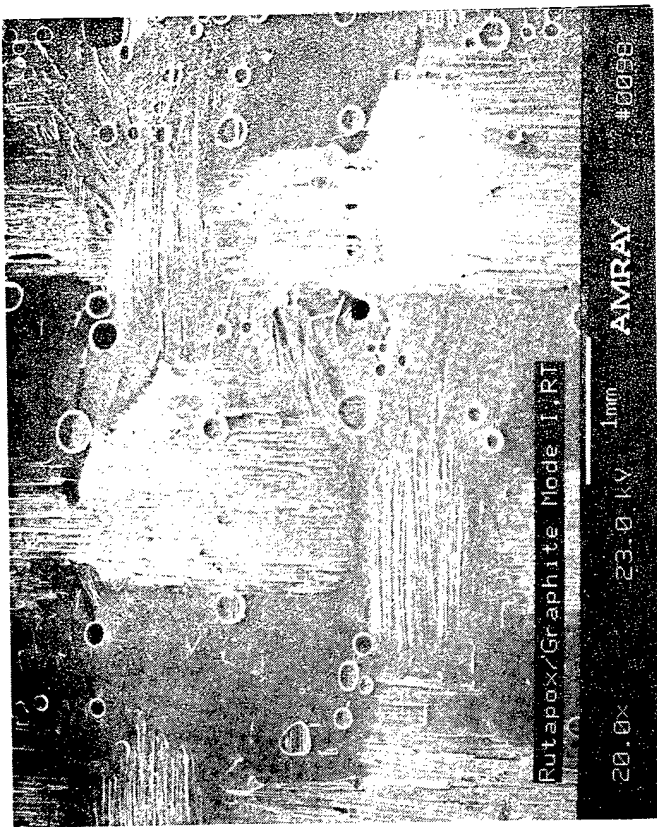


Figure 3.7-3. Optical Fractographs of a Rutapox/Graphite Fabric Interlaminar Mode I (Tensile) High-Rate Fracture Surface, RT



Mechanically Induced  
Crack Direction  
↑

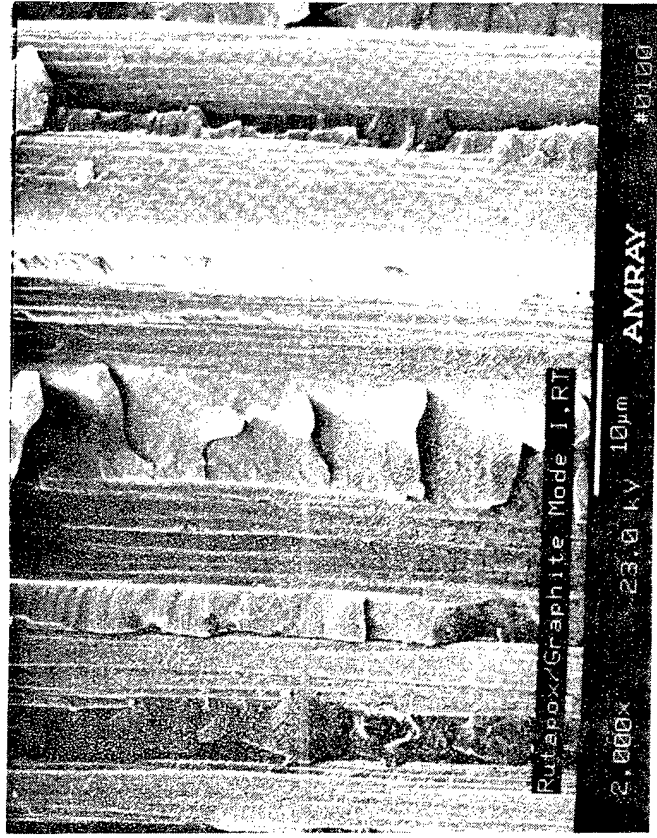
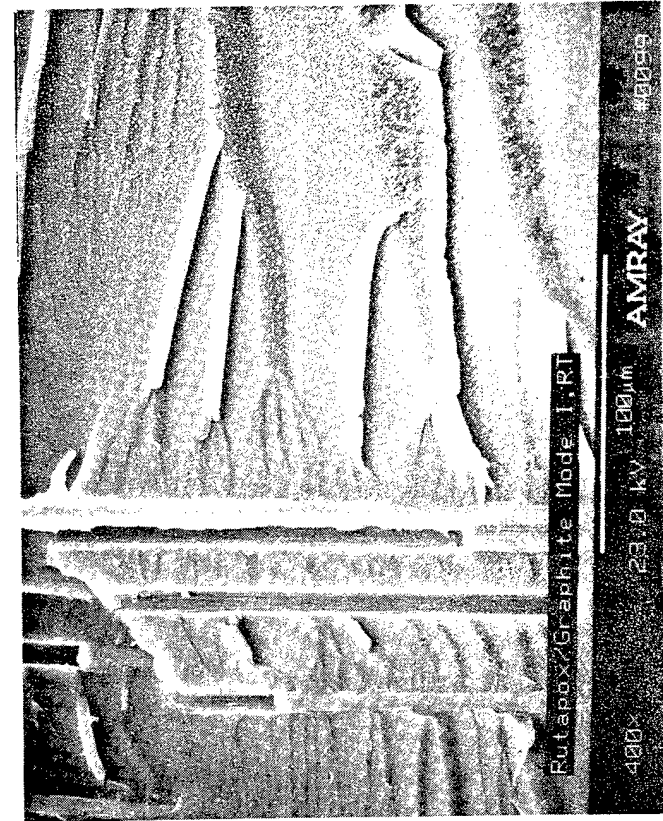
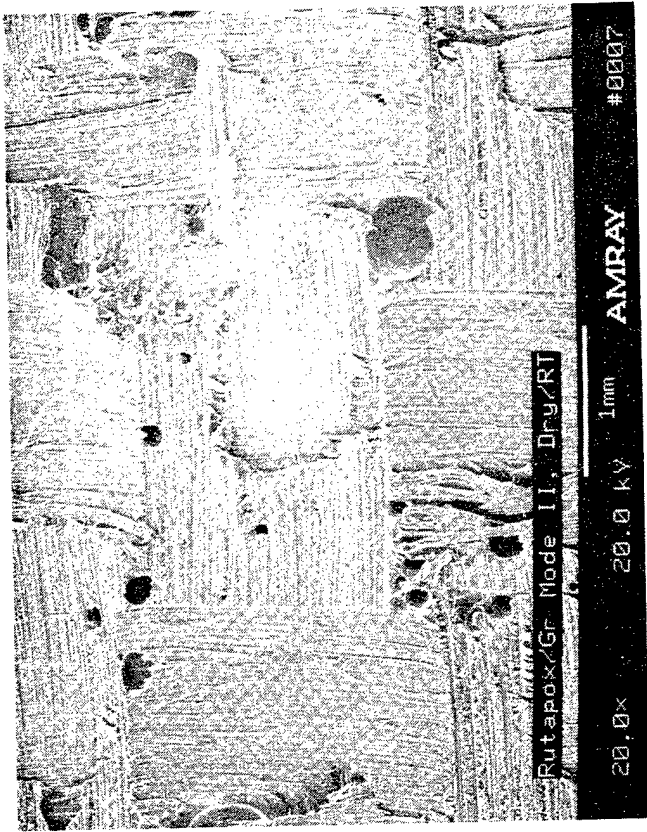


Figure 3.7-4. SEM Fractographs of a Rutapox/Graphite Fabric Interlaminar Mode I (Tensile) High-Rate Fracture Surface, RT



Mechanically Induced  
Crack Direction →

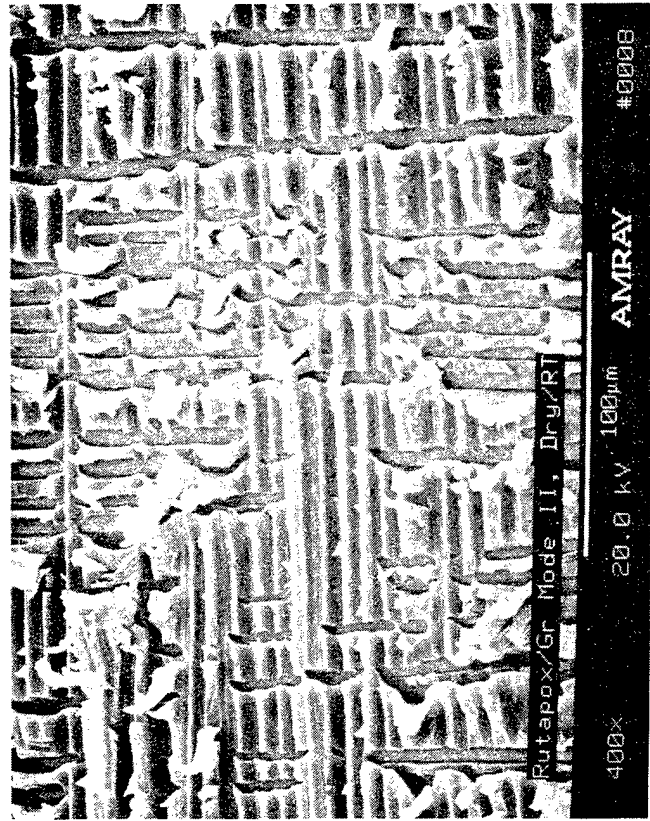
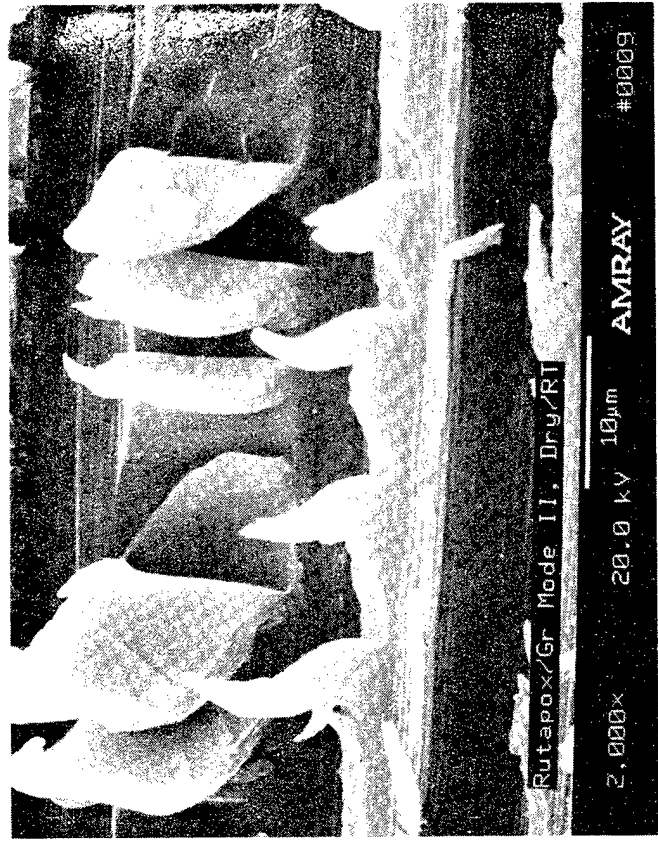


Figure 3.7-5. SEM Fractographs of a Rutapox/Graphite Fabric Interlaminar Mode II (Shear) Fracture Surface, RT

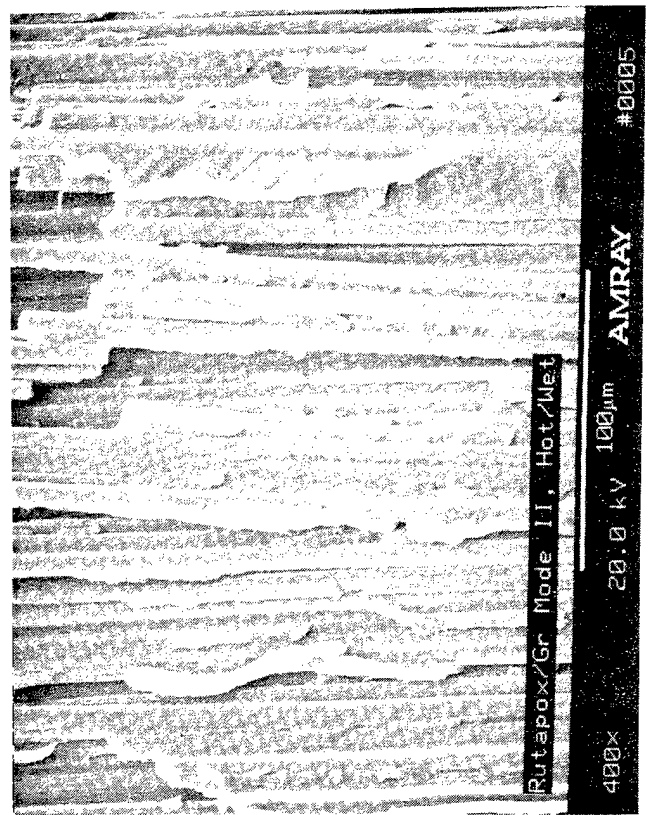
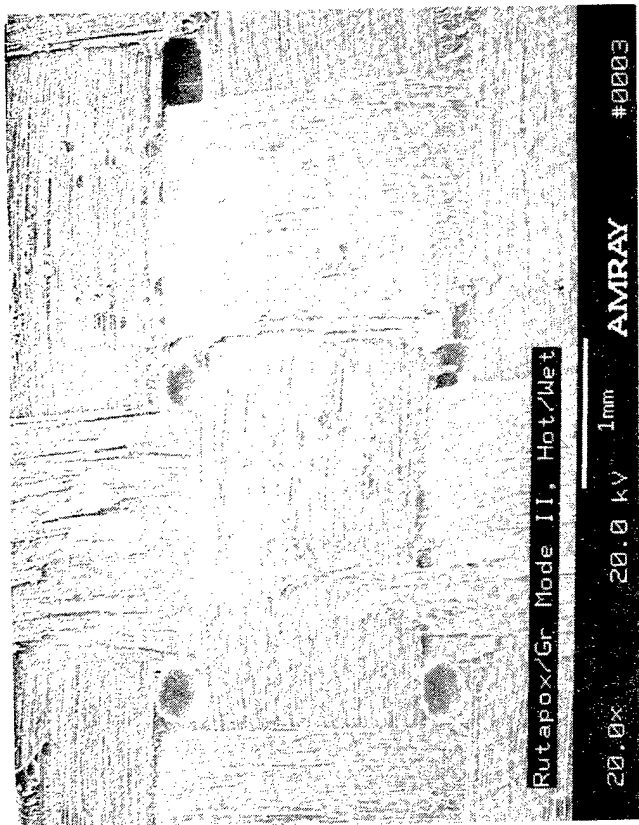
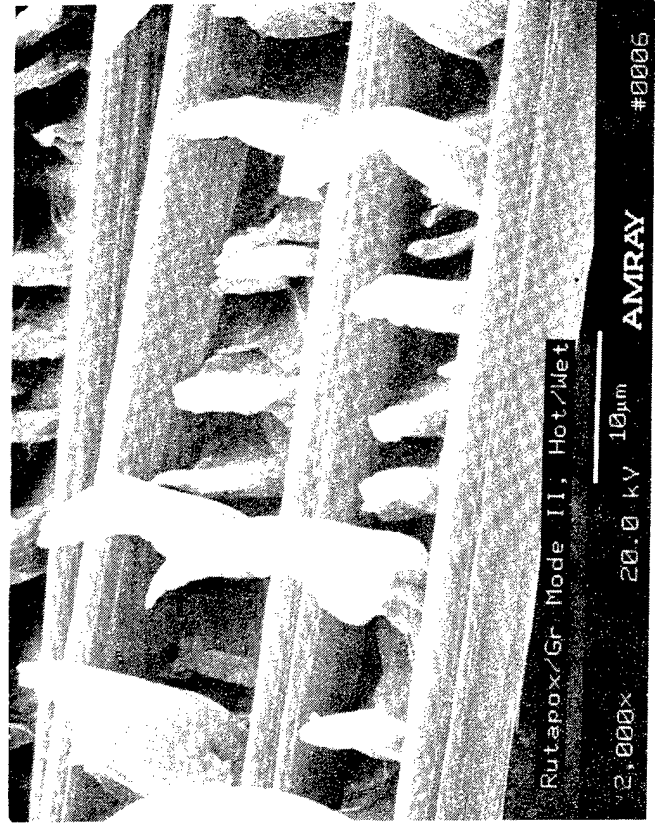
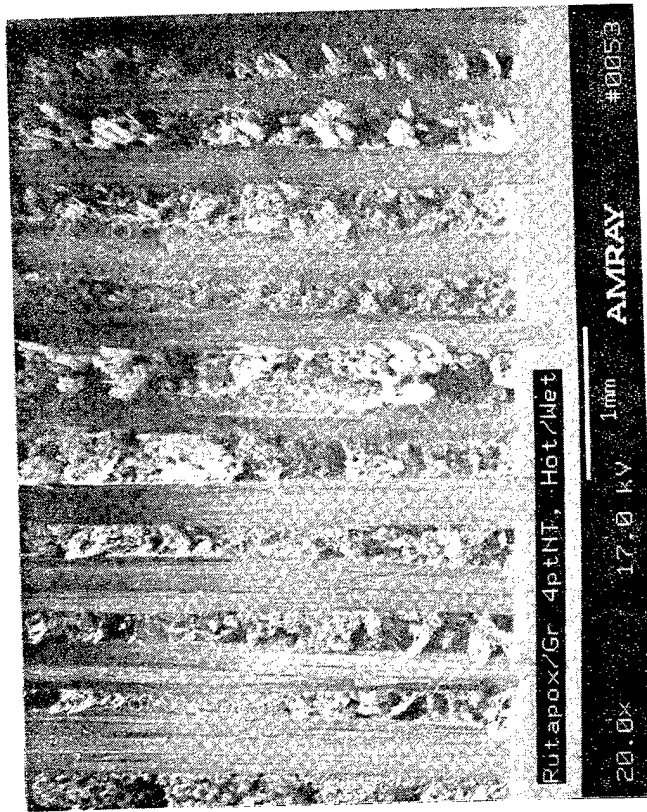


Figure 3.7-6. SEM Fractographs of a Rutapox/Graphite Fabric Interlaminar Mode II (Shear) Hot/Wet Fracture Surface, RT



Mechanically Induced  
Crack Direction  
↑

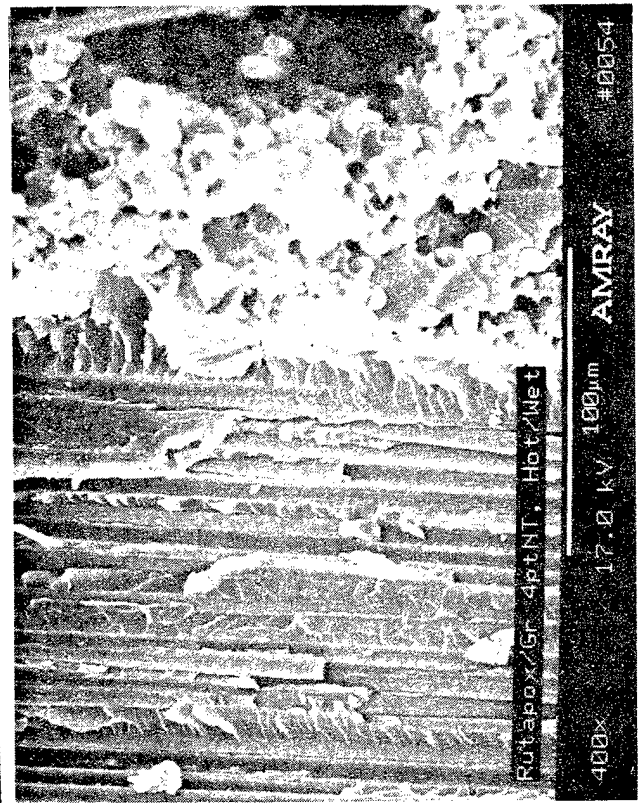
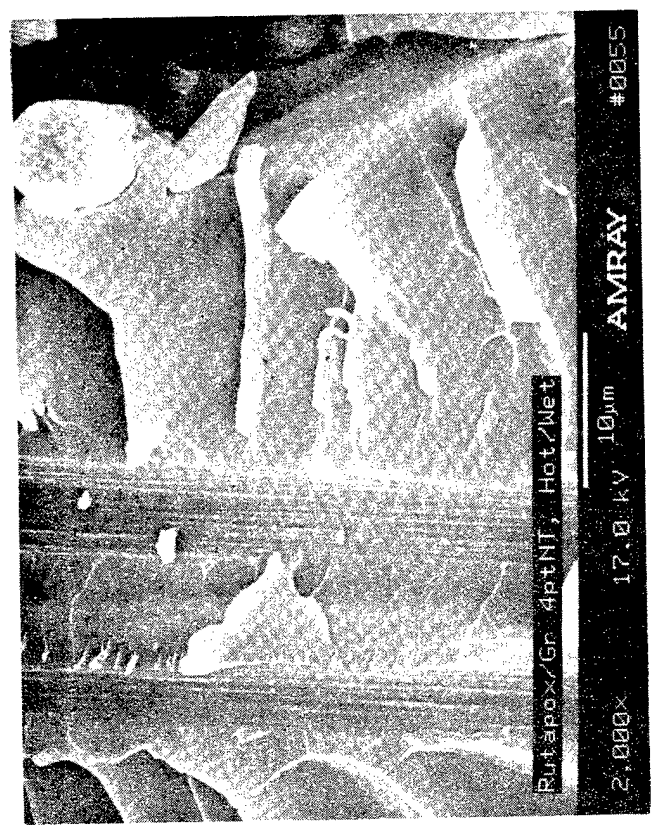
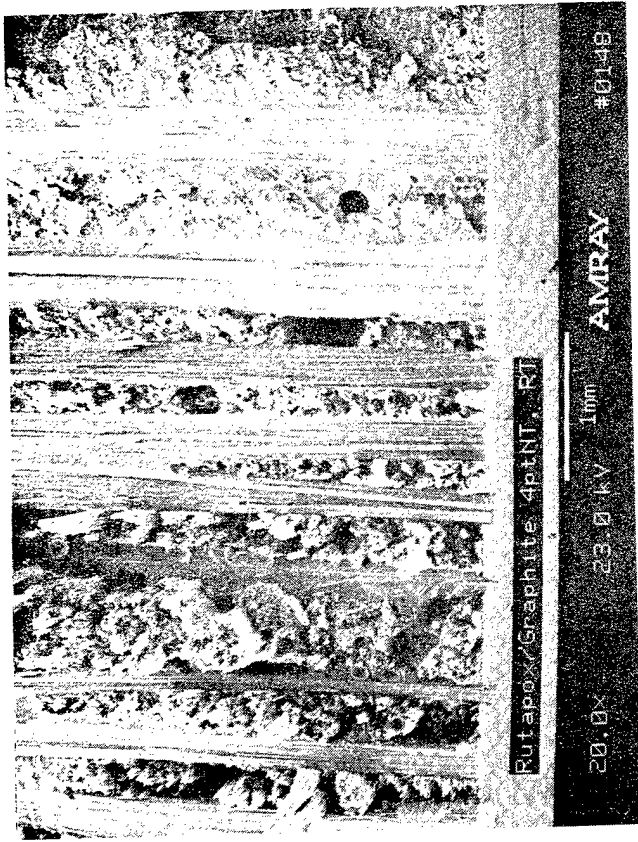


Figure 3.7-7. SEM Fractographs of a Rutapox/Graphite Roving 4ptNT Fracture Surface, Hot/Wet



↑  
Mechanically Induced  
Crack Direction

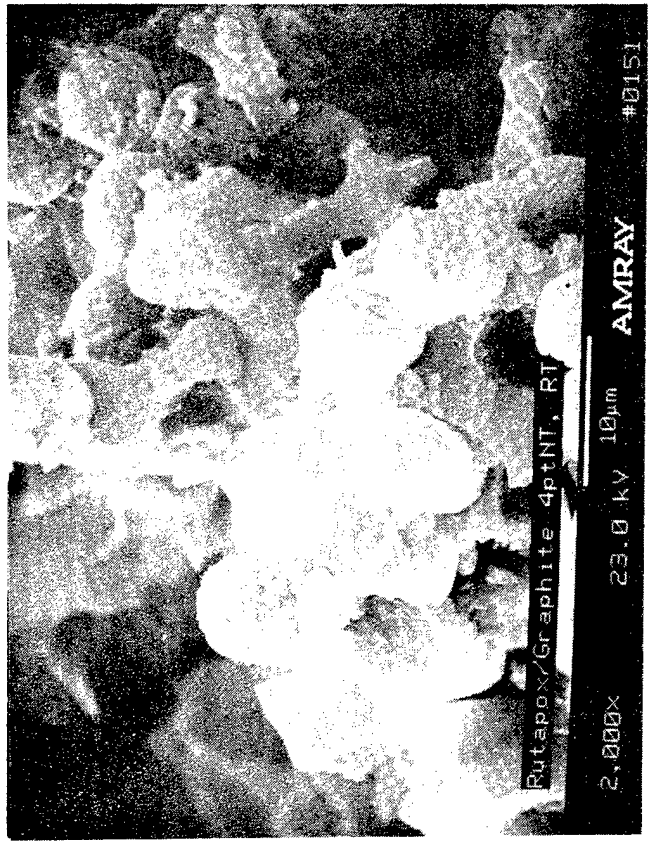
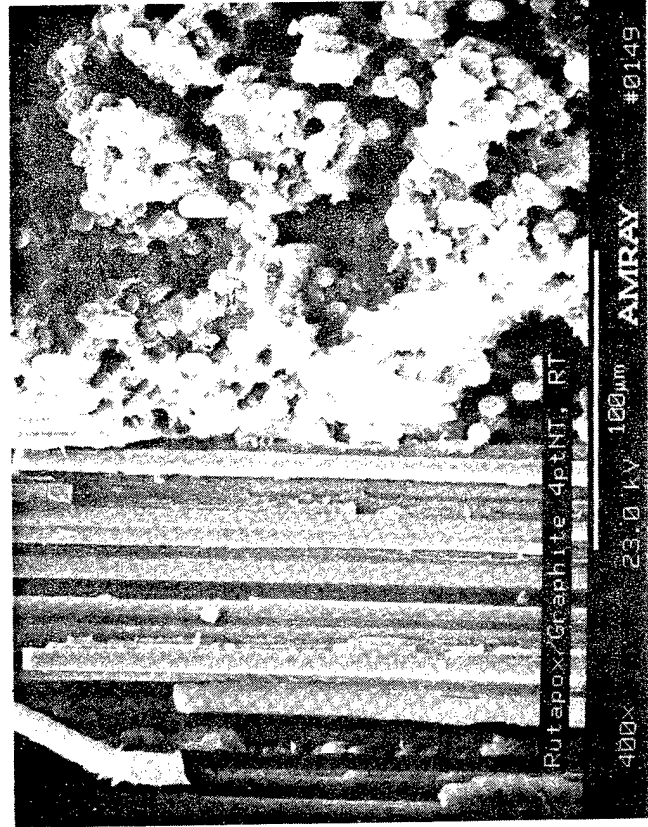


Figure 3.7-8. SEM Fractographs of a Rutapox/Graphite Roving 4ptNT Fracture Surface, RT



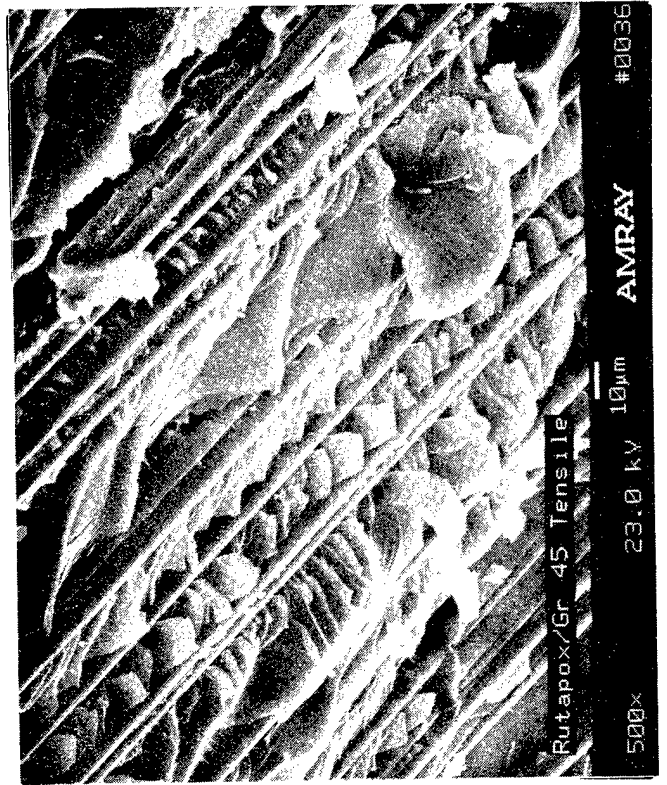
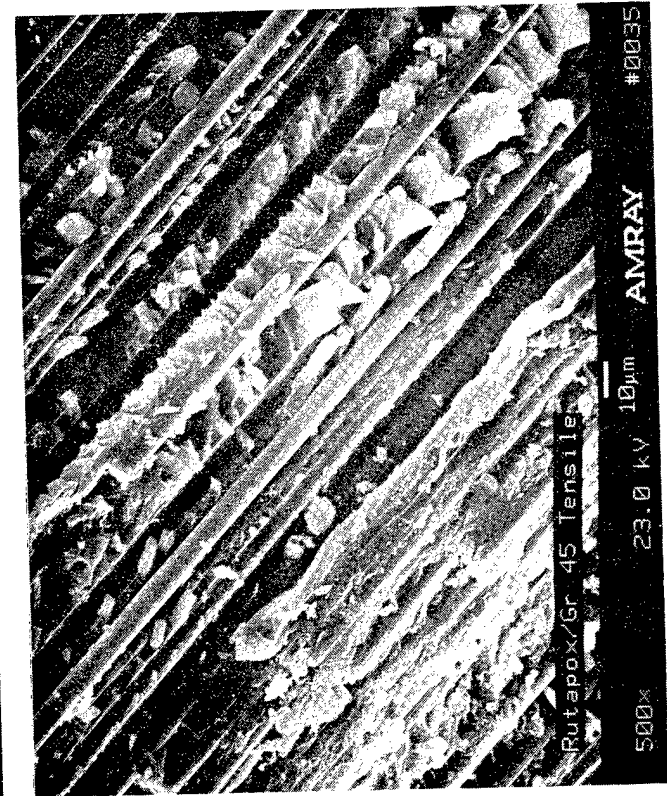
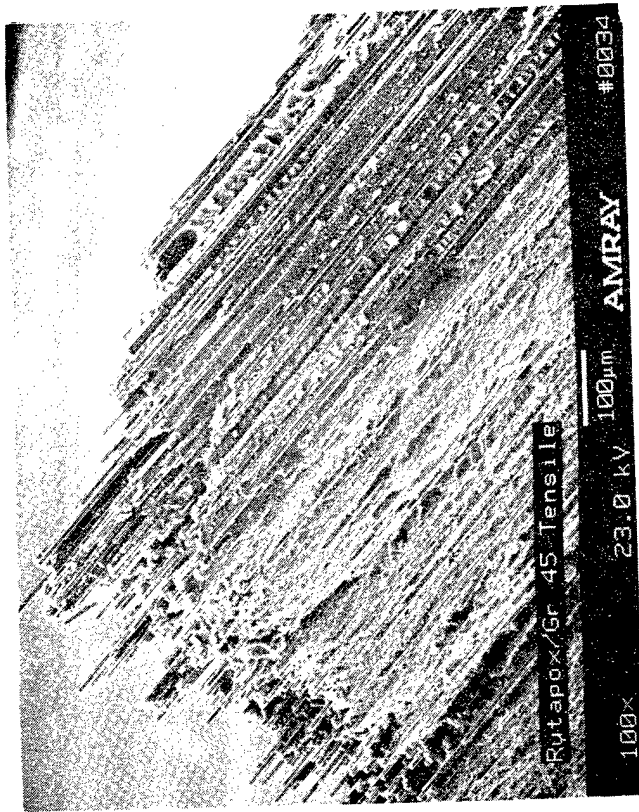


Figure 3.7-9. SEM Fractographs of a Rutapox/Graphite Fabric  $\pm 45^\circ$  Tensile Fracture Surface, RT

Mechanically Induced  
Crack Direction  
→

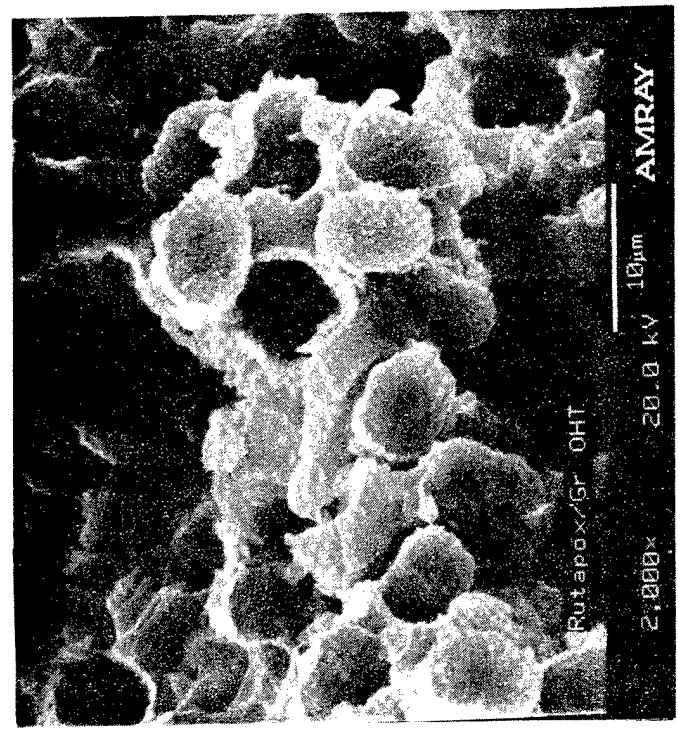
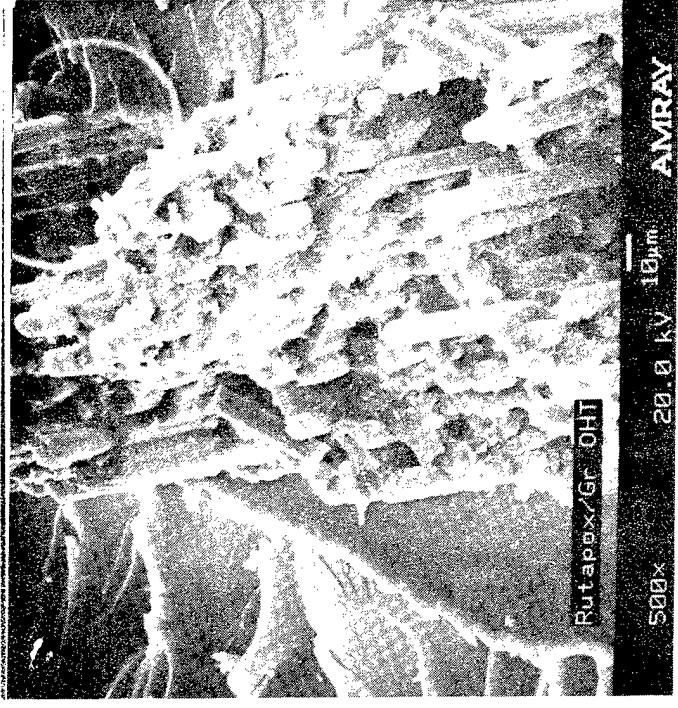


Figure 3.7-10. SEM Fractographs of a Rutapox/Graphite Fabric Open Hole Tension Fracture Surface, RT

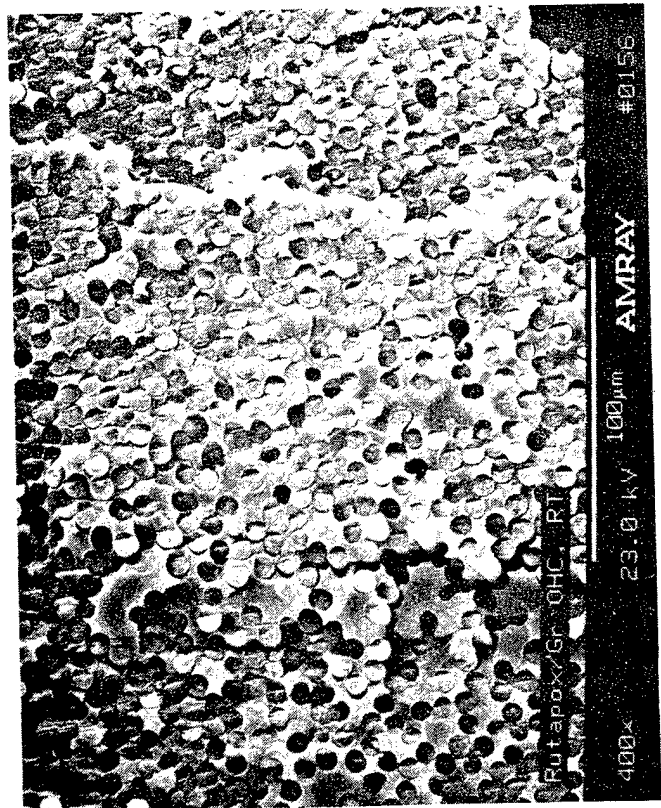
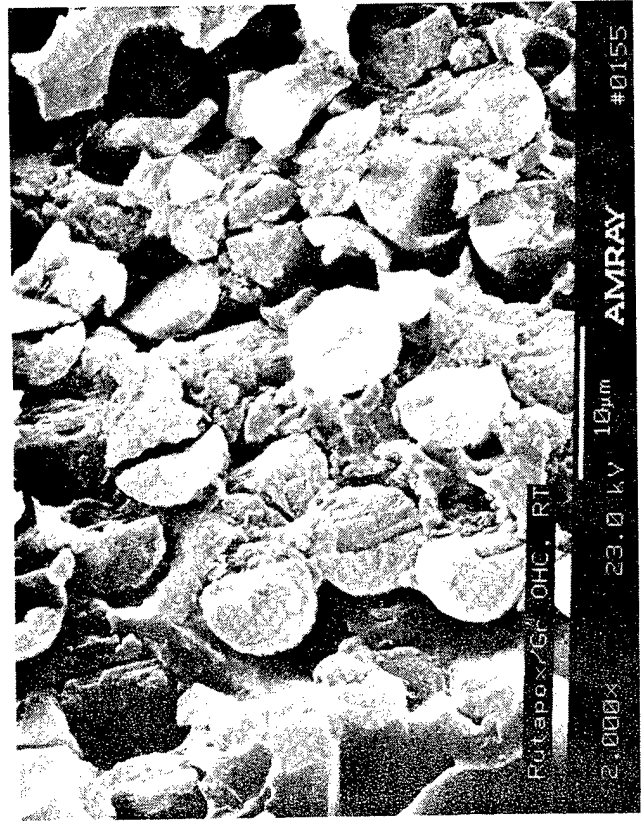


Figure 3.7-11. SEM Fractographs of a Rutapox/Graphite Rovings Open Hole Compression Fracture Surface, RT

**SECTION 3.8**  
**HONEYCOMB STRUCTURES**  
**3501-6 FACE SHEETS/NOMEX HONEYCOMB**

**3.8.1 Introduction**

This section presents the fractographic characterization of failed 3501-6/Nomex honeycomb sandwich components. The tests performed consisted of single cantilevered beam and three-point bending shear test coupons. For each type of test condition, a fractographic analysis technique was developed that described the various fracture modes and how to determine the failure mode and possibly the cracking direction or directions. In addition to providing baseline data for the failure analysis development, processing variables and environmental conditions were also investigated.

**3.8.2 Single Cantilevered Beam**

**Determining Failure Propagation Direction**

Failure propagation in honeycomb material is best determined by examination of the fiber pullout and by the direction in which the fiber is bent. As the honeycomb fails, the fiber and resin fail separately. The fiber is often freed from the resin by the failure and is drawn plastically in the direction of the displacement due to the propagation of the failure. For tensile failure this displacement is nearly normal to the direction of propagation, with a slight bias in the direction of propagation. The bias can result in plastic deformation of the side of the fiber away from the propagation direction or breakage of the fiber with the propagation direction of the crack in the fiber the same as that in the honeycomb. The result of these effects is that the propagation direction is indicated by the lay of the loose ends of fibers along the failed surface (see Figure 3.8-1). Studying the crack propagation directions in the resin meniscus where the honeycomb ribbons join is a more difficult method of determining the failure propagation direction.

The locations where the ribbons join have a double ribbon thickness and additional resin to strengthen that location (see Figure 3.8-2). The resin meniscus is a trilobate structure, with its weakest points at the terminations of these lobes or arms, which are directed 120 degrees from one another. In all the test specimens, the loading occurred such that propagation direction for the failure would be parallel to the ribbon direction. The failure could propagate only along one of three paths. Two of these paths were along single plies of ribbon oriented at 60 degrees from the line of the ribbon junctures. The other direction was that of the ribbon juncture (see Figure 3.8-3). Whenever one of these juncture areas failed, both menisci were involved. If the failure was the result of a traveling failure front, then one of the menisci broke from the juncture outward (the trailing meniscus) and one broke from one of the arms along the single-ply edge of the cell (see Figure 3.8-4). This meniscus set thereby indicates the propagation direction for that joint. The propagation direction for any one meniscus set may not be consistent with the overall direction of failure. The failure propagation

front is not always a straight line (see Figure 3.8-5), which can result in local areas where the failure front may temporarily loop back on itself before jumping back to the main front. This would generate a meniscus pair with a failure propagation direction that was the reverse of the general propagation direction for the panel. Other possibilities include patterns that would indicate a direction of propagation at right angles to the ribbon direction (Figure 3.8-6) or vertical, with both menisci breaking in toward the center (Figure 3.8-7). As a result, the propagation direction on the scale of an individual honeycomb cell based on the meniscus resin failures would not reliably indicate the overall direction of the failure. Multiple sets of menisci would have to be examined to be confident in the overall direction of failure.

### **Fractography of the Specimens**

Visual observations were documented before more detailed analysis. These observations included the general appearance of the adhesive layer, indications of any adhesive failure, amount of failure in a plane, and fiber burst in the honeycomb failure. Figure 3.8-8 shows some of the visual observations on the mode I honeycomb sandwich specimens. The failure surfaces were then examined microscopically to document the fractography of the resin surfaces and the crack propagation directions.

**Control Specimen.** No adhesive or cohesive failures were seen in these specimen types. As shown in Figure 3.8-9, 100% core failure was observed.

**Aged Adhesive Specimen.** The honeycomb cells appeared to be more distorted in these specimens than in the others. It has not been determined if this is the result of processing or testing. The amount of burst fibers was less than that seen in the control specimen. As shown in Figure 3.8-10, the failure was in the honeycomb.

**Eight-Pound Core Specimen.** The failure occurred primarily in the adhesive layer. Both adhesive and cohesive failure was evident. The adhesive failure, between the adhesive and the face sheet, occurred near the center of the specimen. Approximately 25% of the core failure was observed in these specimens. Optical fractographs taken at 200X showed a lower velocity fracture characteristic as evidenced by the mirror and mist fracture features shown in Figure 3.8-11.

**Undercured Adhesive Specimen.** There was more burst fiber on the failure surface in this sample than in most of the others, except the control specimens, (Figure 3.8-12).

**Undercured Face Sheet Specimen.** The honeycomb material embossed the face sheet, and there was more evidence of out gassing in the form of many bubbles in the adhesive layer, as shown in Figure 3.8-13.

### 3.8.3 Three-Point Bending Shear Test

Samples were photographed as received, and surface failure pattern was documented graphically (see Figure 3.8-14). The pattern of the visible distortion on each of the sides related to the failure is schematically represented. The illustration of the labeled side of the panel is in the same orientation as the photograph of the panel. The edge illustrated just below the labeled side illustration is of the right edge with the labeled side of the panel on the top. The left end of the right-edge view is the lower section of the view, while the right side is higher along the edge. The illustration of the unlabeled side is drawn as though viewed from the labeled side to indicate the relative pattern of the failure on the two sides. The associated photograph is a mirror image of the illustration in this case. The left edge is illustrated below the illustration of the unlabeled side. The left end of the left-edge view is the higher section of the view, while the right side is lower along the edge.

The crack pattern in the honeycomb is illustrated in the edge view drawings. The alternating light and dark vertical bands signify individual cell walls of the honeycomb; walls normal to the edge are now shown. The lines indicate visible cracks in the honeycomb walls, and the thickened surface sheets indicate delamination of the carbon fiber/resin composite, cohesive failure of the adhesive, adhesive failure of the adhesive, or honeycomb fracture at the adhesive meniscus. The type of failure at that surface is identified in Figure 3.8-15. Figures 3.8-16 through 3.8-30 show the specimens and the crack diagrams.

The extent of damage to the honeycomb within the panel was evaluated with a water intrusion technique. The approach was to place the panel in a beaker of water and weigh it down so that the crack area was submerged. This was then placed in a vacuum bell jar, and a vacuum was created. The vacuum was held until the escape of gas bubbles from the panel ceased. The bell jar was then repressurized and the panel was reweighed. After weighing, the process was repeated to ensure complete filling of the damaged area. More gas bubbles were generally released, suggesting this procedure may be causing the cracks to continue to propagate. This approach is still being evaluated. A related approach is the use of silicone rubber intrusion methods to create a rubber cast of the failure site.

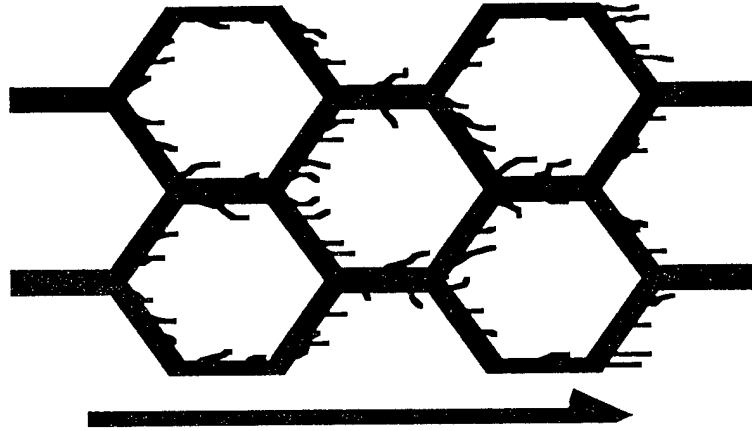


Figure 3.8-1. *Fibers Torn and Bent in the Direction of the Propagation of the Failure*

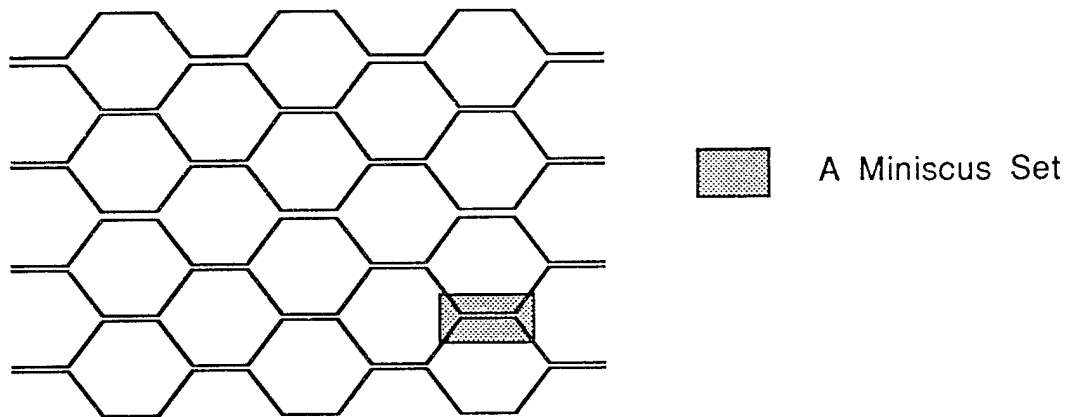


Figure 3.8-2. *Orientation of the Continuous Ribbons in the Honeycomb Denoting the Ribbon Direction and the Associated Miniscus Set*

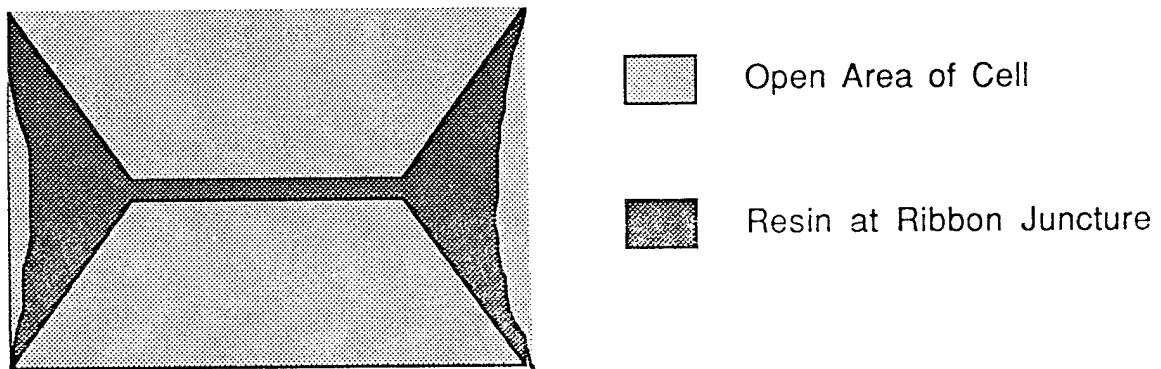


Figure 3.8-3. *Trilobate Resin Structure at the Ribbon Juncture Forming a Pair of Menisci or a Meniscus Set*

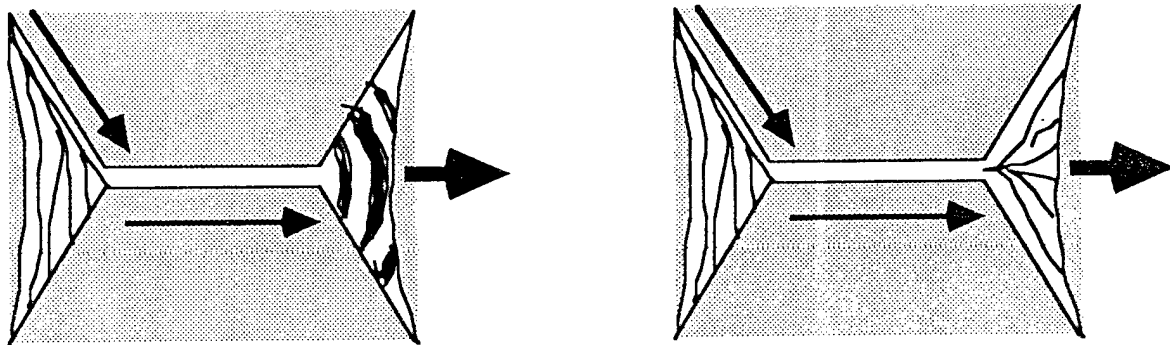


Figure 3.8-4. Failure Patterns in the Resin Menisci Indicating the Propagation Directions

The illustration on the left shows "Wallner" lines indicating the failure initiated at the apex of the upper arm of the meniscus. It then propagated across the joint and caused a conchoidal fracture in the trailing meniscus. The illustration on the right shows the same type of event but with a Wallner line failure pattern at the trailing meniscus.

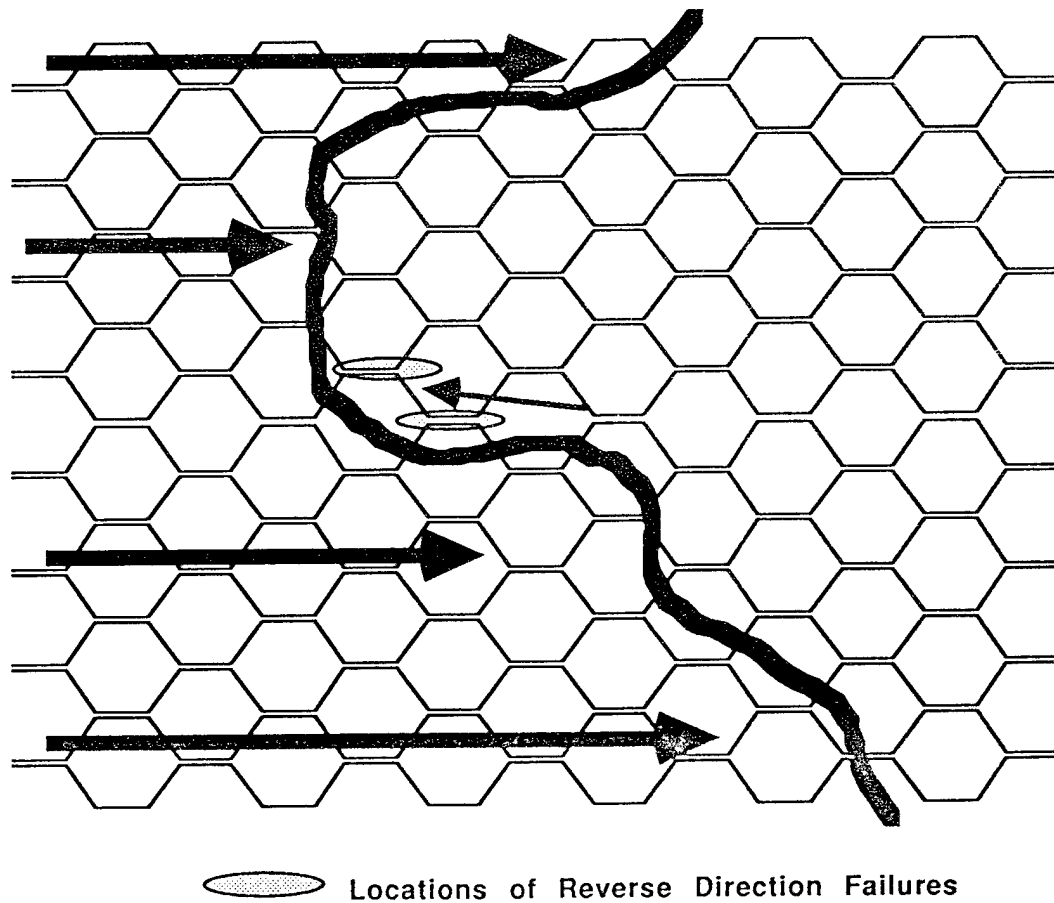


Figure 3.8-5. The Failure Front Doesn't Travel as a Straight Line and May, for Short Distances, Change Direction



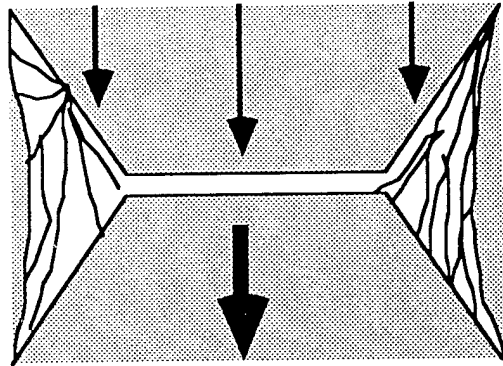


Figure 3.8-6. The Wallner Line Pattern for a Failure Propagating Normal to the Ribbon Direction

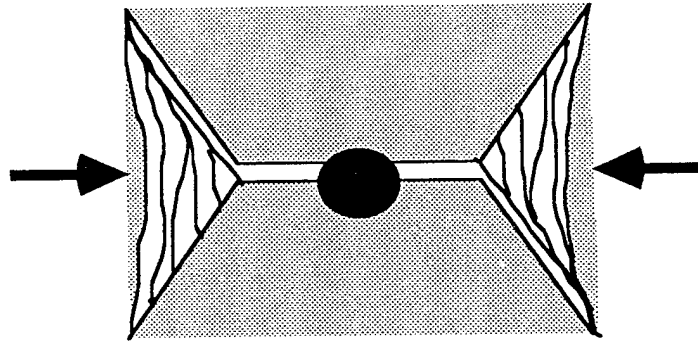
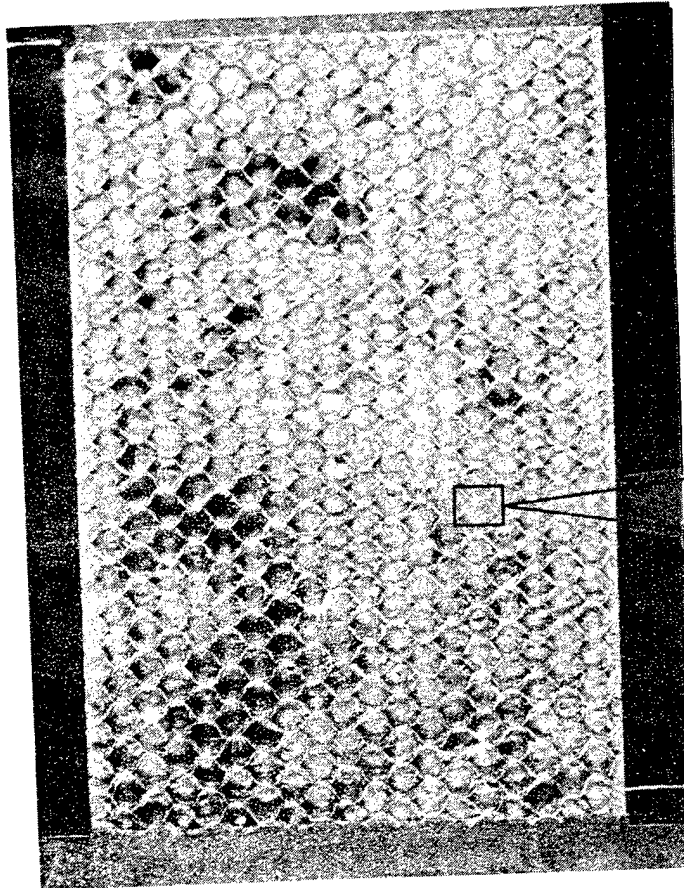


Figure 3.8-7. The Wallner Line Pattern for a Failure Propagating Inward From Both Sides Indicating a Vertical or Twisting Failure

Specimen type	Percent of failure type			Presence of green adhesive	Comment
	Core failure	Cohesive failure	Adhesive failure		
Control	100%			Yes	
Aged adhesive	100%			Yes	
Eight-pound core	25%	55%	20%	Yes	
Undercured adhesive	100%			No	
Undercured facesheet	100%			Yes	

Figure 3.8-8. Failure Type for Mode I Honeycomb Sandwich Failures

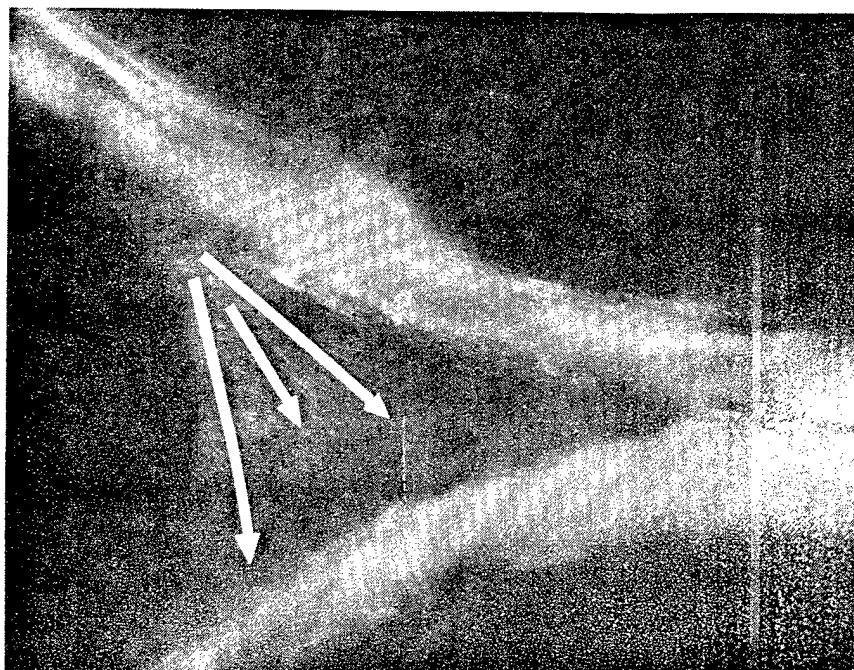
04-L7220-AA0p  
XW-VP2-012191



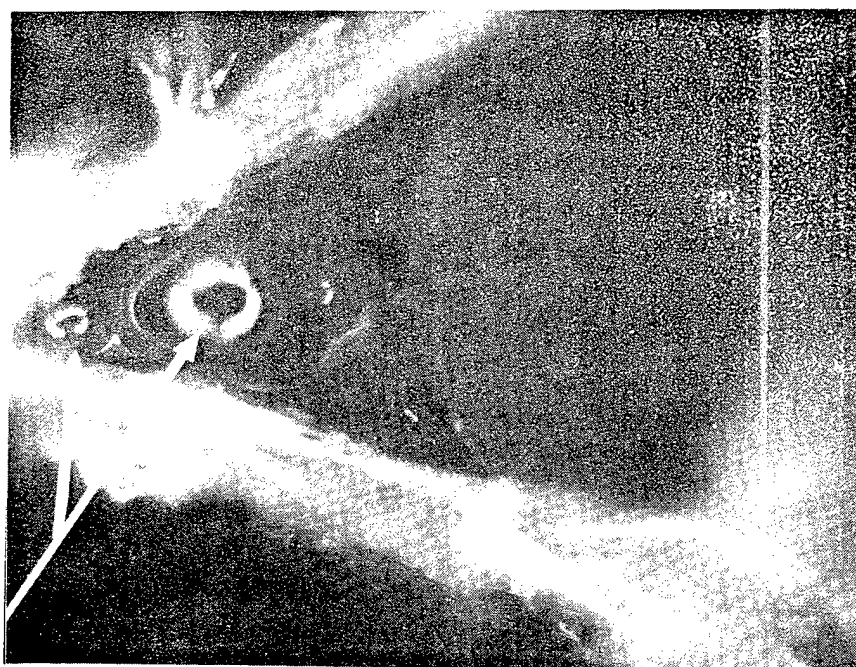
See 200X magnification  
on next page

Sample 1A

Figure 3.8-9. *Optical Fractographs of Mode I Sandwich, Control Specimen  
Sheet 1 of 2*



200X

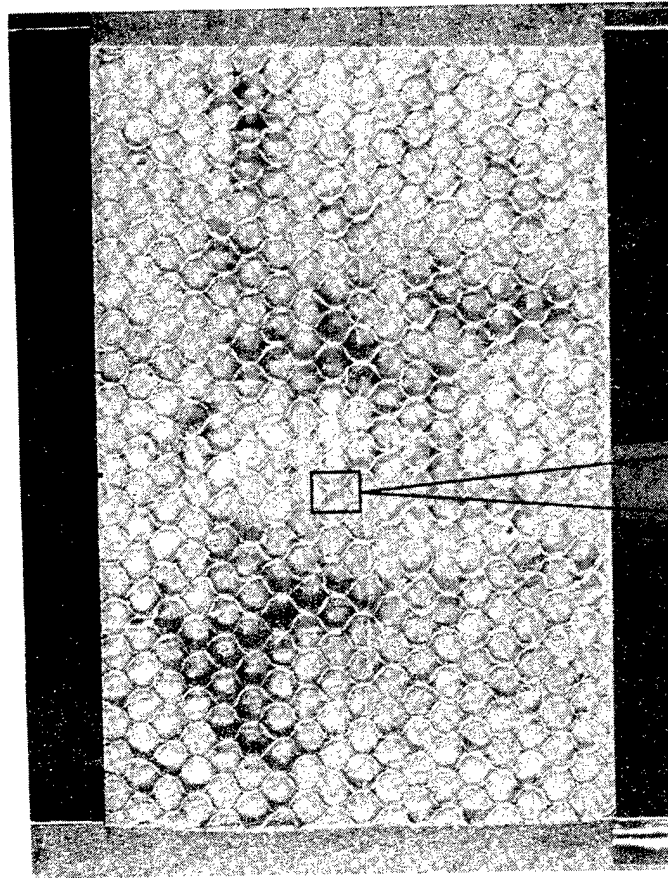


Bubbles

Sample 1A-1

200X

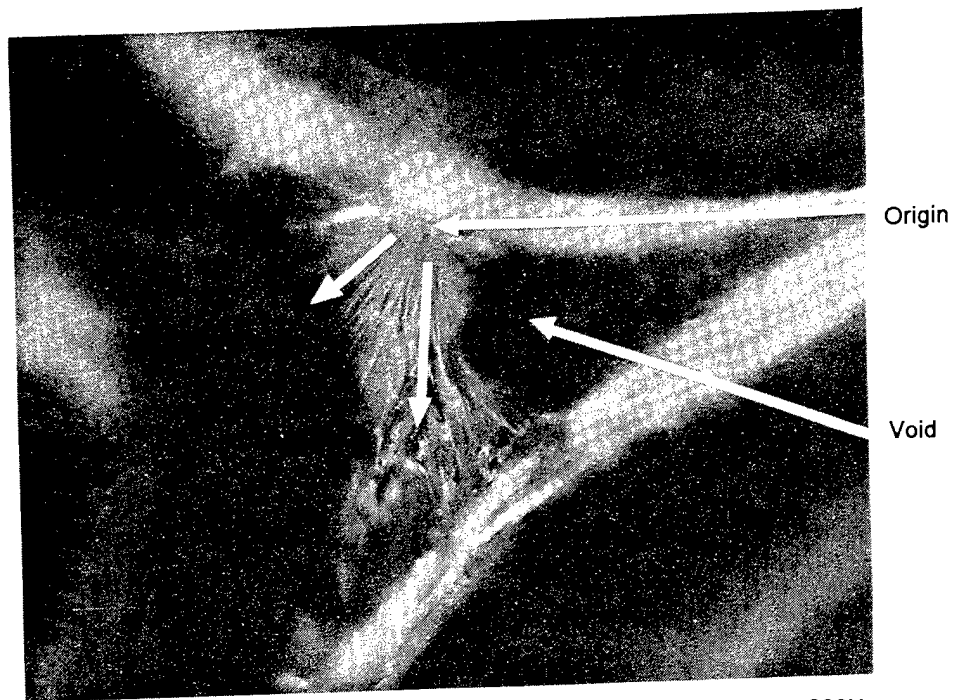
Figure 3.8-9. *Optical Fractographs of Mode I Sandwich, Control Specimen*  
Sheet 2 of 2



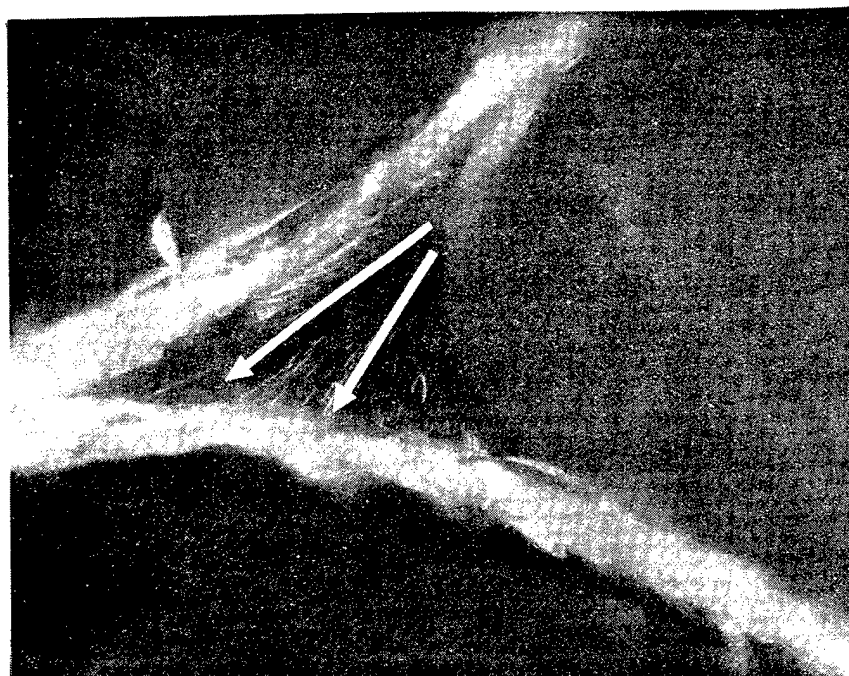
See 200X  
magnification  
on next page

Sample 2B

*Figure 3.8-10. Optical Fractographs of Mode I Sandwich, Aged Adhesive Specimen  
Sheet 1 of 2*



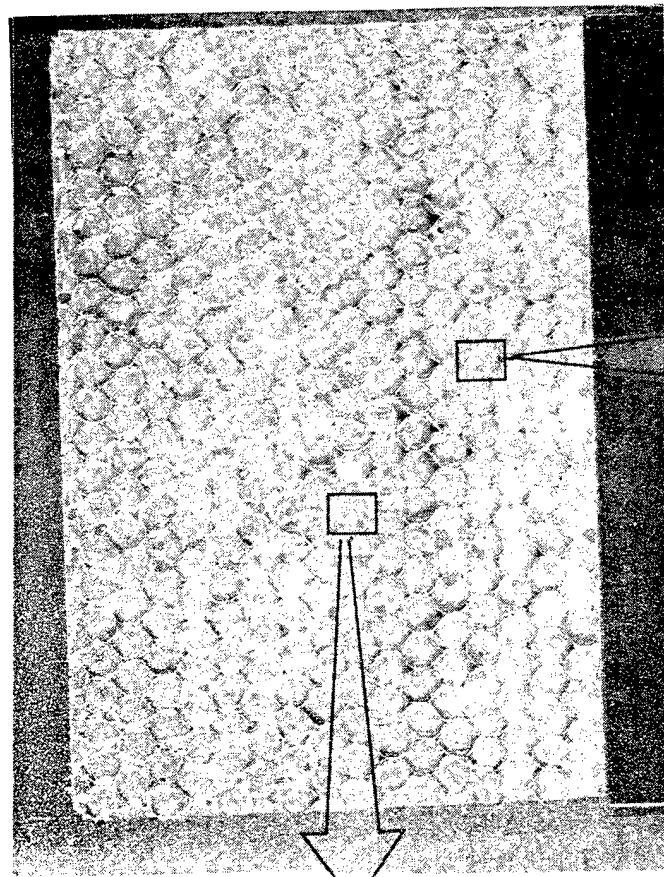
200X



200X

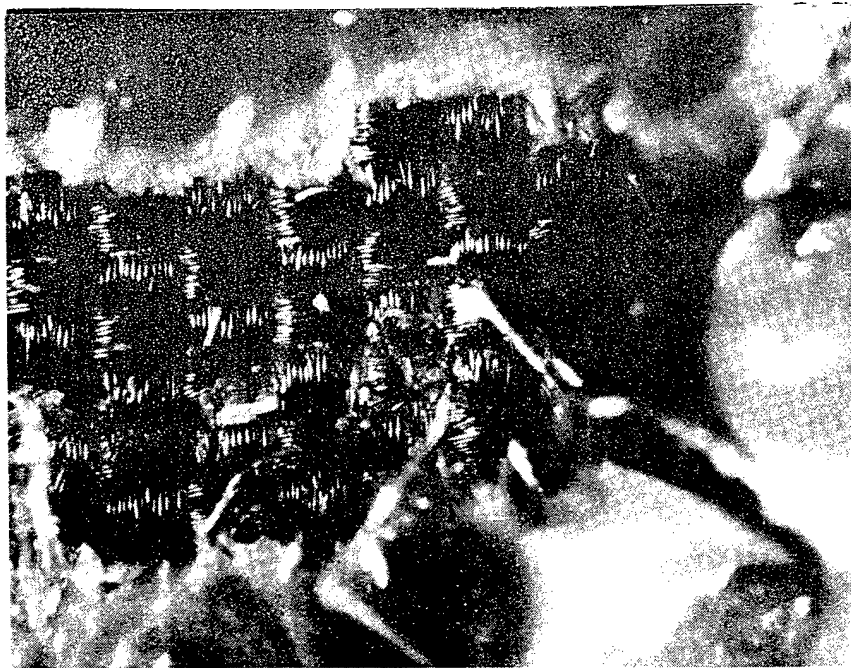
Sample 2B-2

*Figure 3.8-10. Optical Fractographs of Mode I Sandwich, Aged Adhesive Specimen (Sheet 2 of 2)*



See 100X  
magnification  
on next page

Sample 3B see magnification below

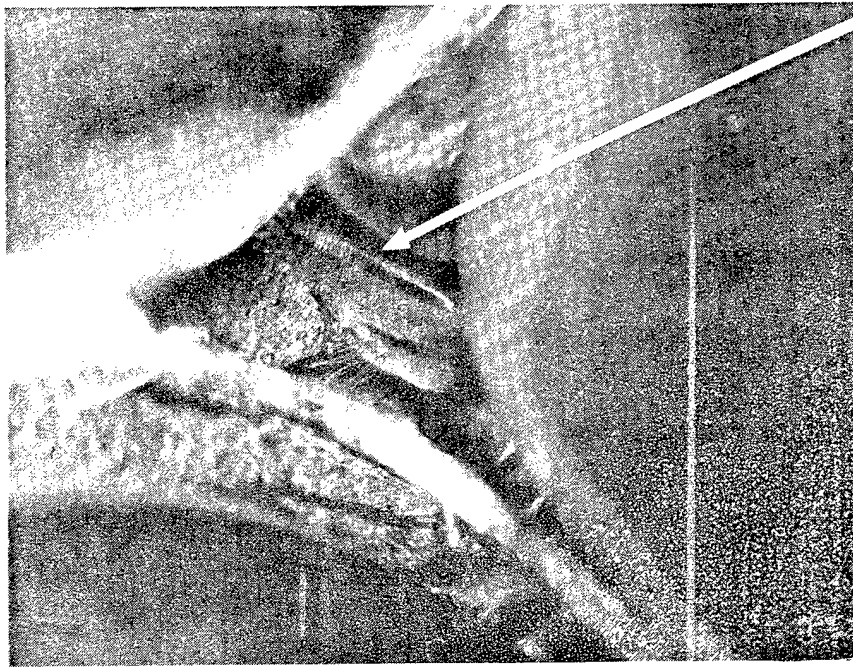


50X

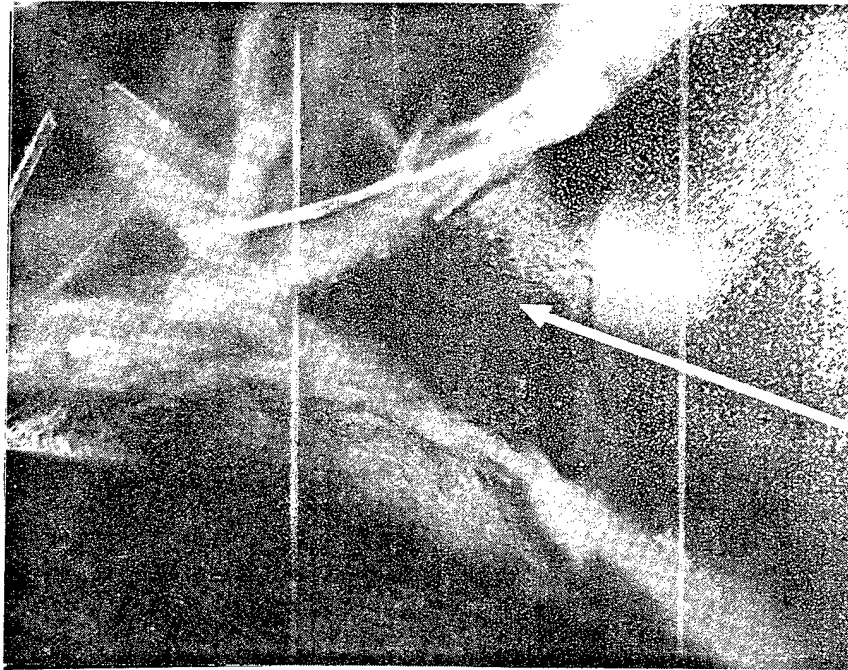
Sample 3A-2

Figure 3.8-11. *Optical Fractographs of Mode I Sandwich, Stronger Core Used (8-lb) Specimen Sheet 1 of 2*

Wallner  
lines



100X



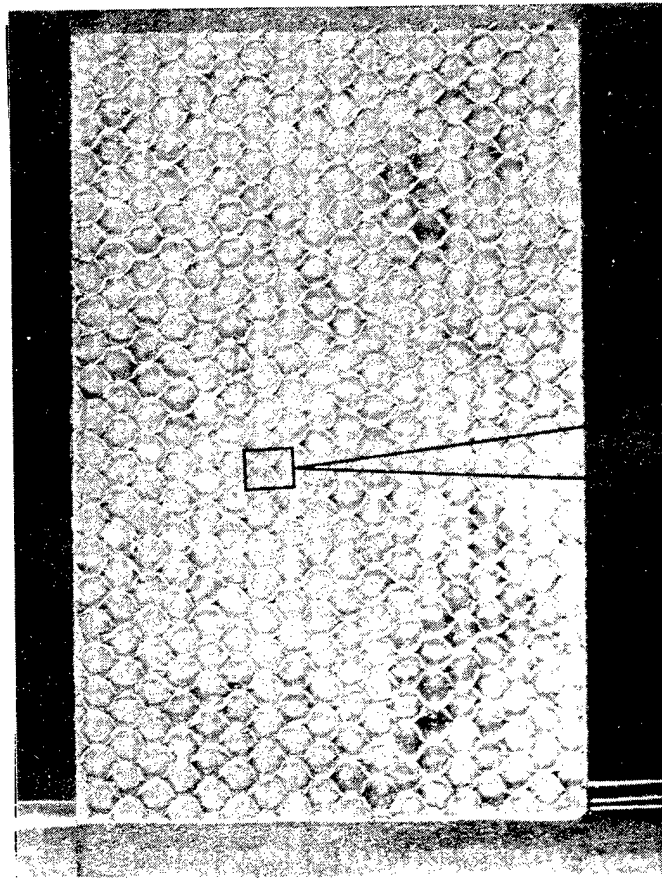
Mist

100X

Sample 3B-3

Figure 3.8-11. Optical Fractographs of Mode I Sandwich, Stronger Core Used (8-lb) Specimen  
Sheet 2 of 2

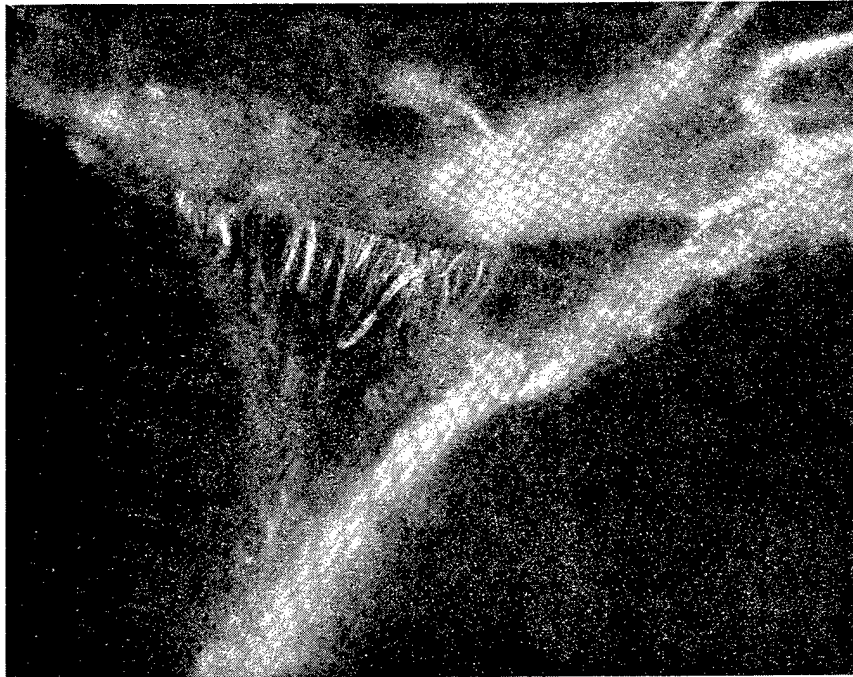




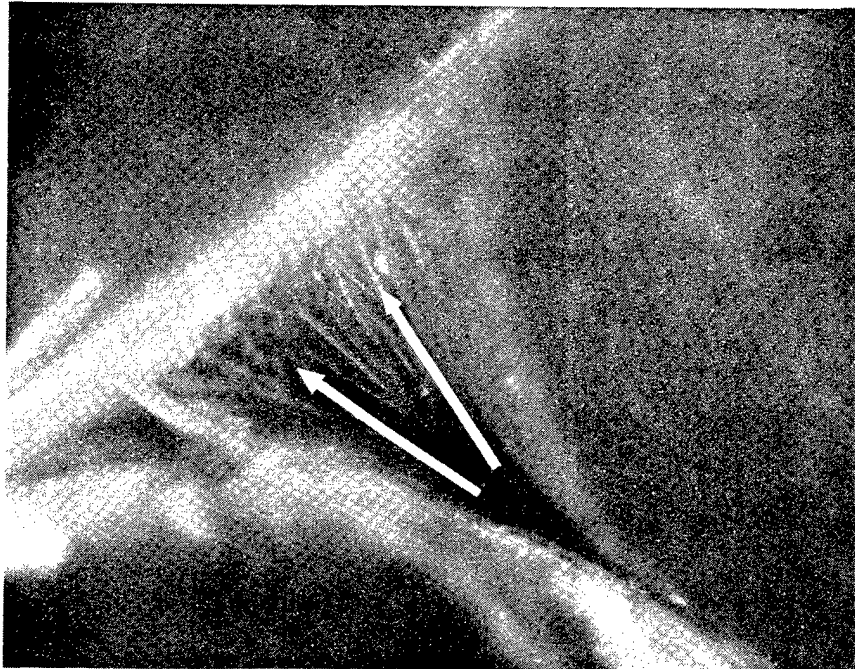
See 200X  
magnification  
on next page

Sample 4B

Figure 3.8-12. *Optical Fractographs of Mode I Sandwich Specimen, Undercured Adhesive*  
Sheet 1 of 2



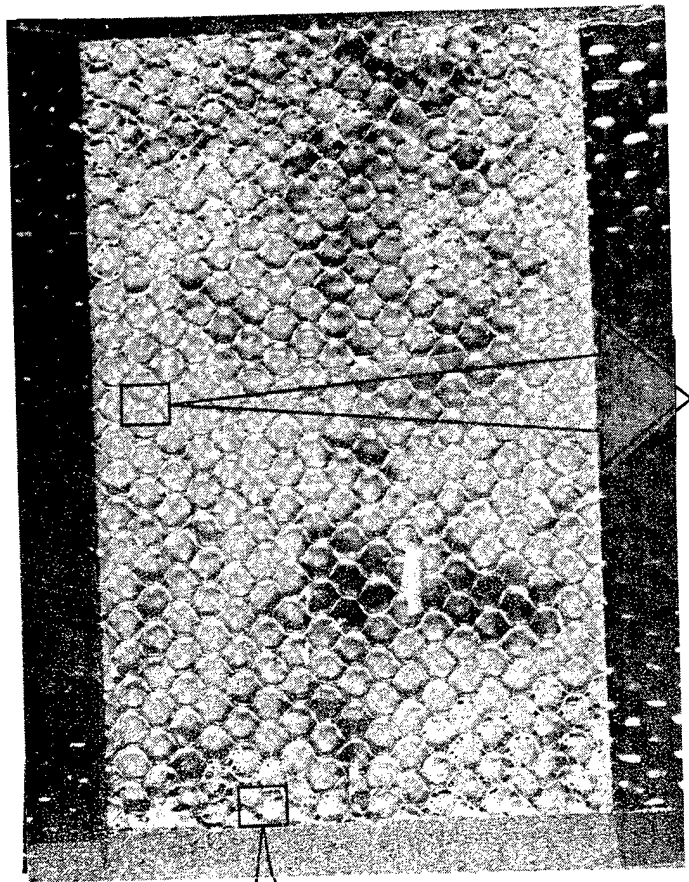
200X



200X

Sample 4B-2

*Figure 3.8-12. Optical Fractographs of Mode I Sandwich Specimen, Undercured Adhesive*  
Sheet 2 of 2

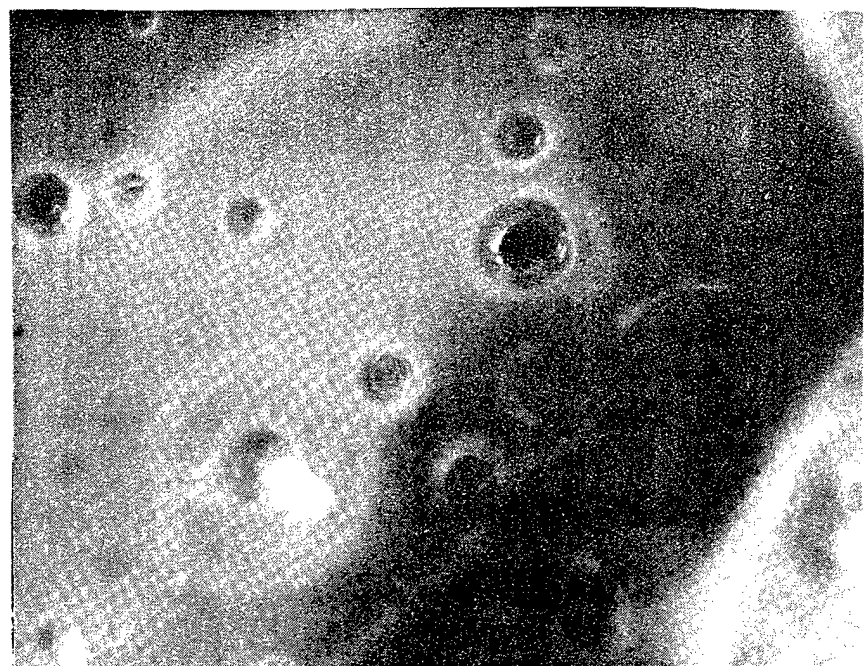


See 200X magnification on next page

Bubbles in adhesive layer

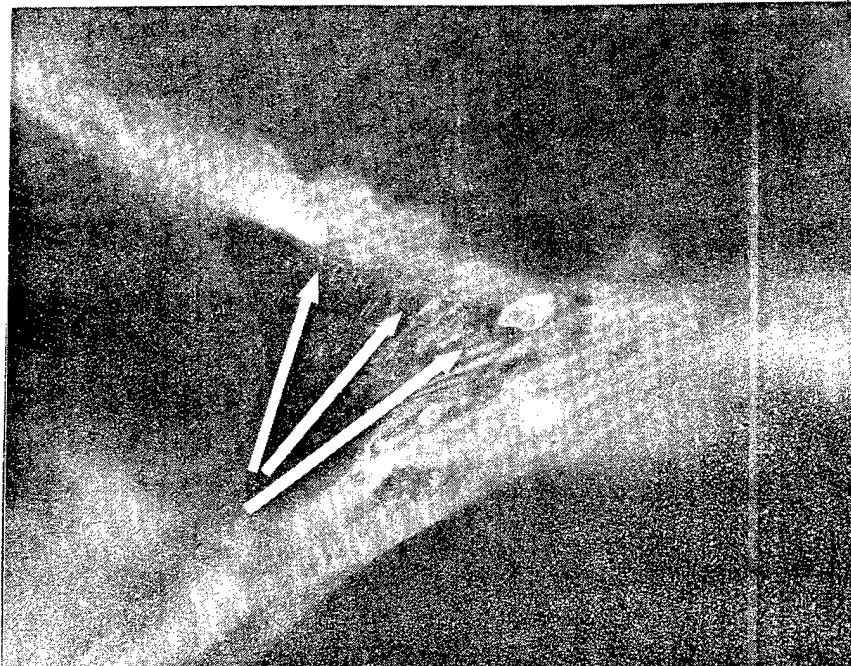
Sample 5A

See magnification below

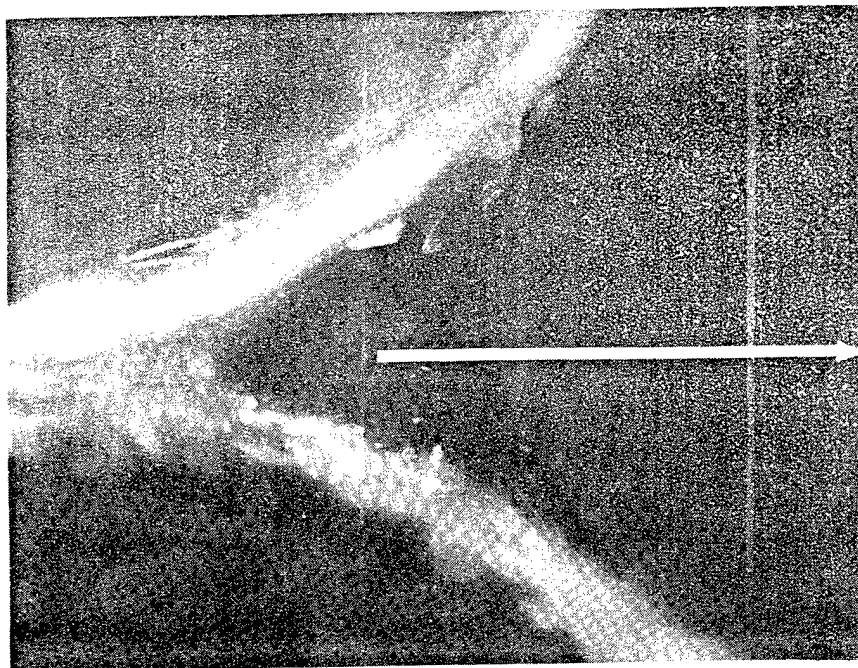


50X

Figure 3.8-13. Optical Fractographs of Mode I Sandwich Specimen, Undercured Face Sheet Sheet 1 of 2



200X



Mirror

Sample 5A-1

200X

Figure 3.8-13. Optical Fractographs of Mode I Sandwich Specimen, Undercured Face Sheet  
Sheet 2 of 2

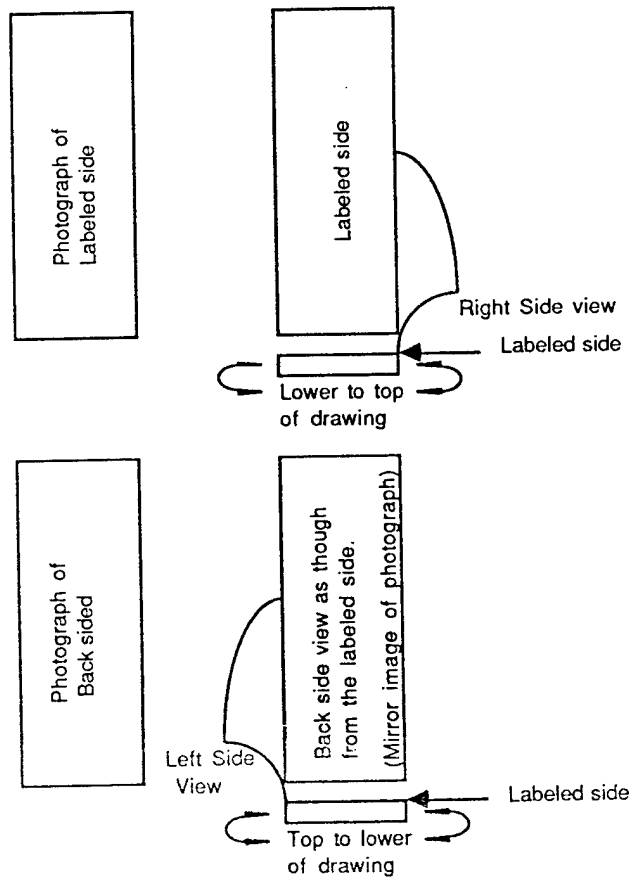


Figure 3.8-14. Illustration of the Position of the Two Photographs and Four Drawings of Each Sample

SAMPLE NUMBER	TREATMENT	PERCENT BREAKAGE AT							
		CARBON/RESIN		ADHESIVE		MENISCUS		HONEYCOMB	
		LEFT	RIGHT	LEFT	RIGHT	LEFT	RIGHT	LEFT	RIGHT
1	CONTROL					13		87	100
2							75	100	25
3						56	50	44	50
6A1	AGED ADHESIVE							100	100
6A2							33	67	CRUSH
6A3								25	75
7A1	IMPROPER CORE	33	33	67	67				
7A2		33	10		40			67	50
7A3		20	20		80	80			
8A1	UNDERCURED ADHESIVE						10	100	90
8A2							40	100	60
8A3									CRUSH
9A1	UNDERCURED FACE SHEET						80	100	20
9A2									100
9A3						18	4	82	96

Figure 3.8-15. Linear Distribution of the Three Crack Modes Near the Honeycomb/Adhesive/Carbon Fiber Composite Interface and the Amount of Cracking Through the Honeycomb

The failure visible at the edge of the sample is reported in terms of the linear percent of the length for each crack mode. The Carbon/Resin category indicates delamination in the face sheet composite. The subcolumns indicate the left and right sides respectively as indicated on the schematic sheet for that sample. The Adhesive category indicates cohesive failure in the adhesive layer itself. The Meniscus category indicates that the honeycomb failed at the point of the adhesive meniscus. The final category, Honeycomb, indicates the percentage of failure in the honeycomb material away from the face sheets.

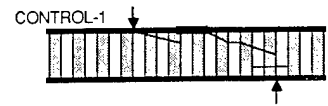
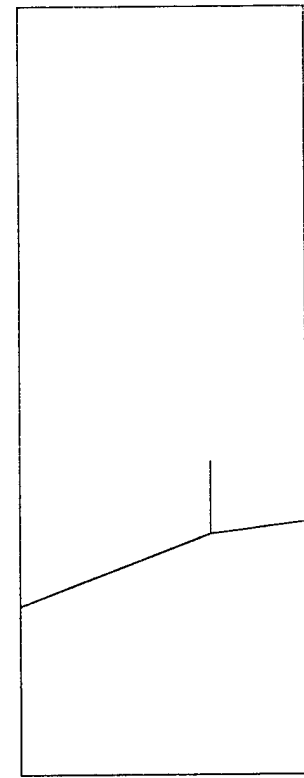
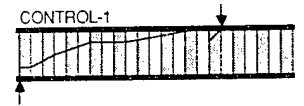
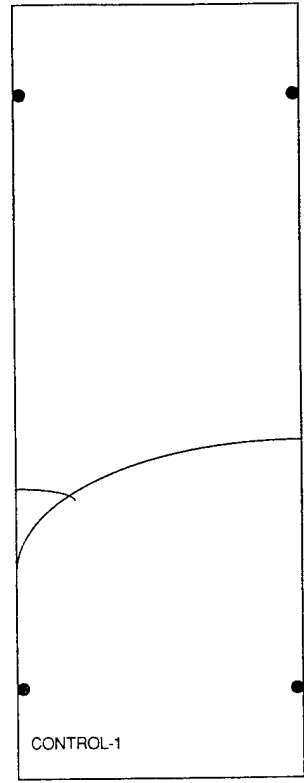
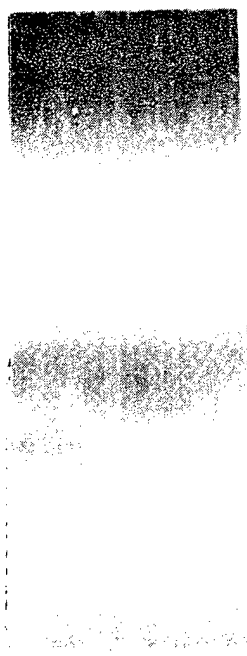
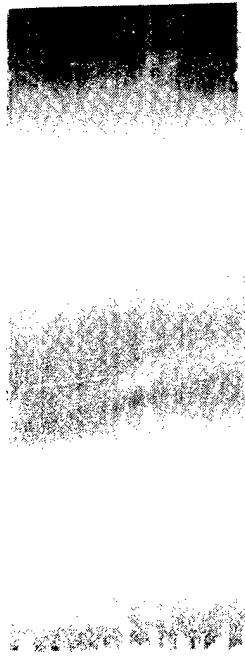


Figure 3.8-16. Control Sample 1—2.4X Reduction

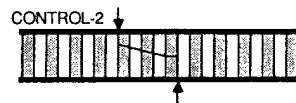
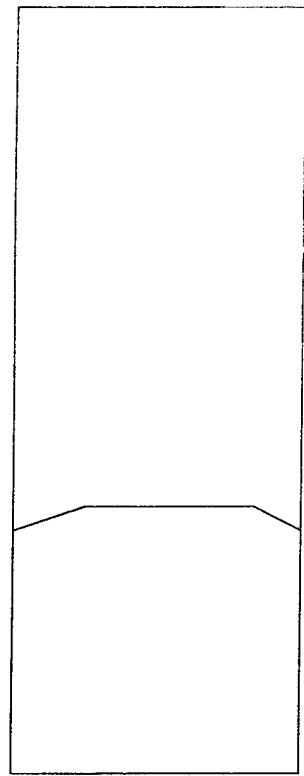
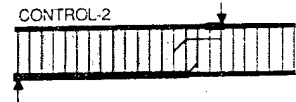
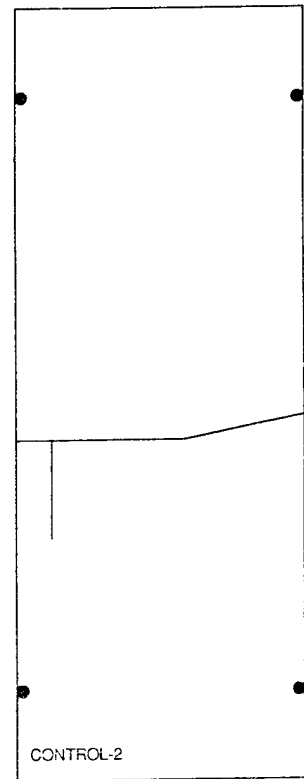
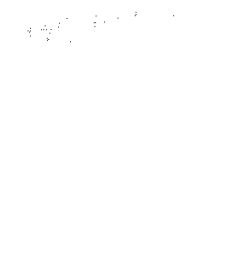
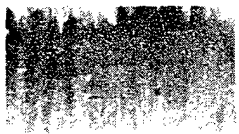
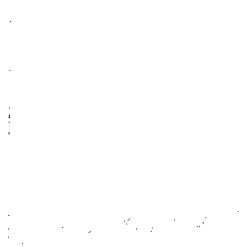


Figure 3.8-17. Control Sample 2—2.4X Reduction



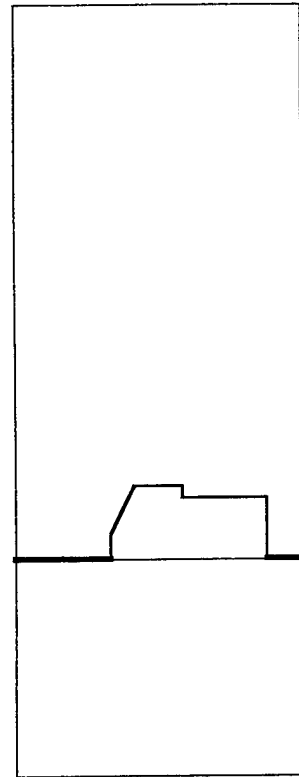
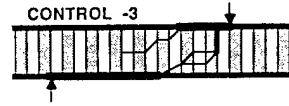
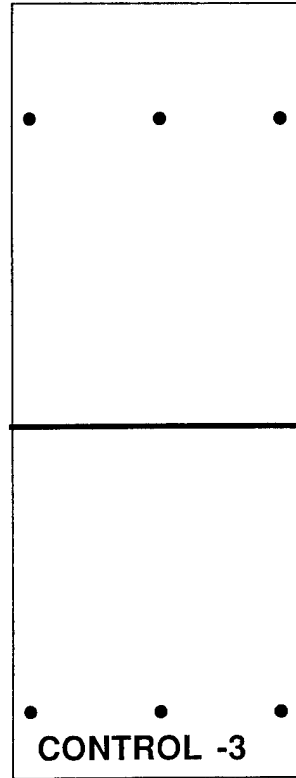
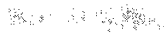
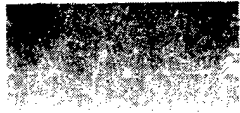


Figure 3.8-18. Control Sample 3—2.4X Reduction

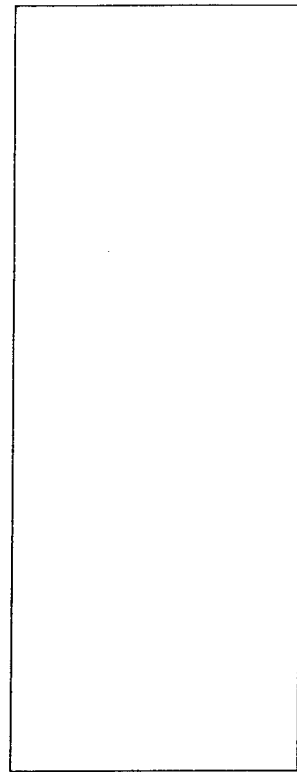
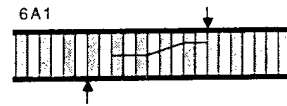
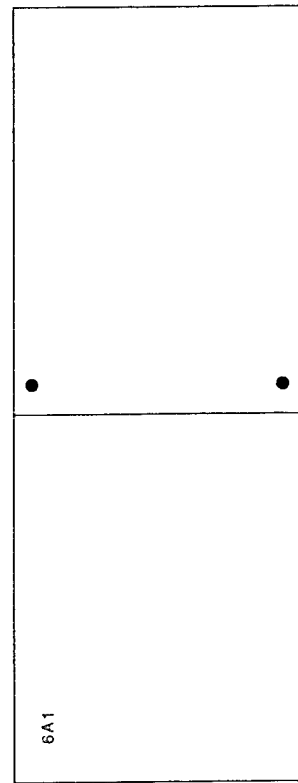
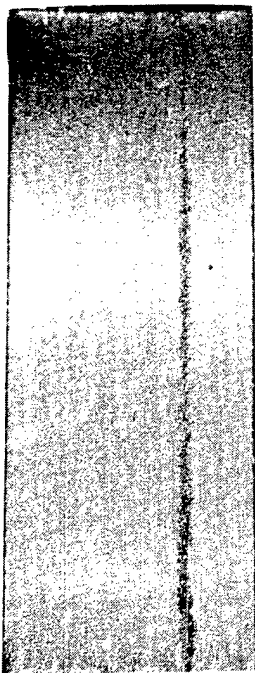
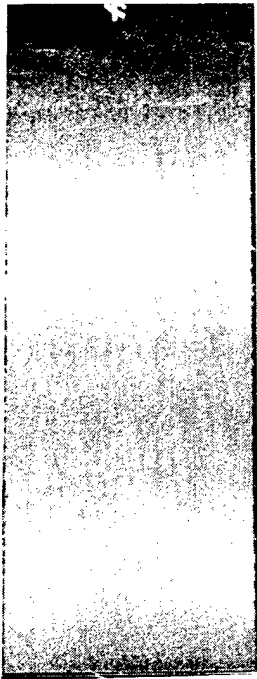


Figure 3.8-19. Aged Adhesive Sample 6A1—2.4X Reduction

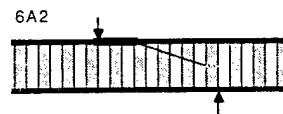
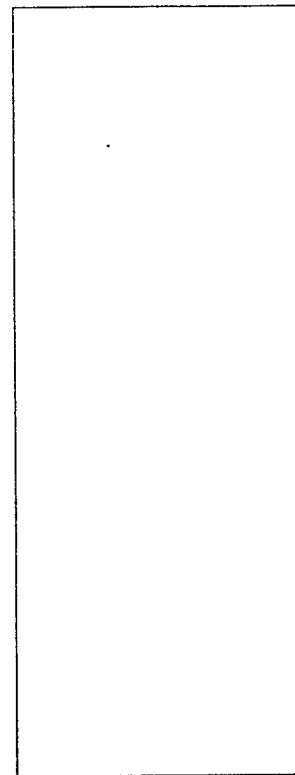
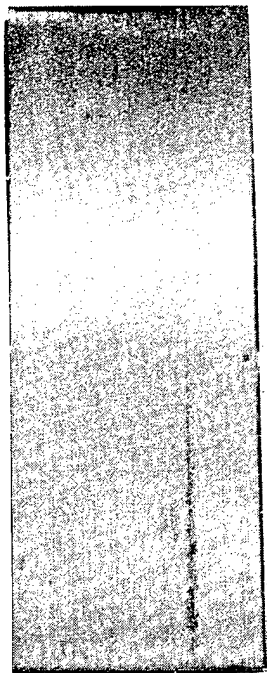
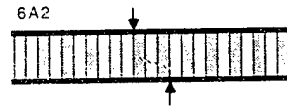
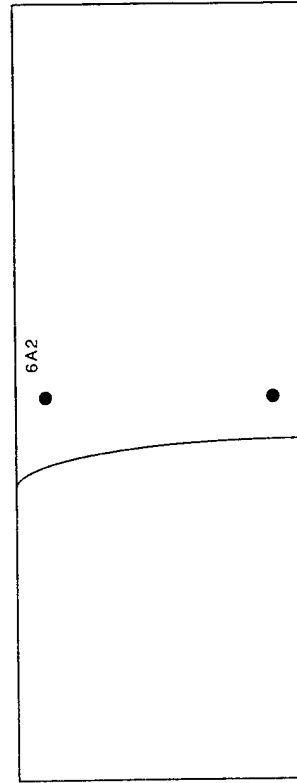
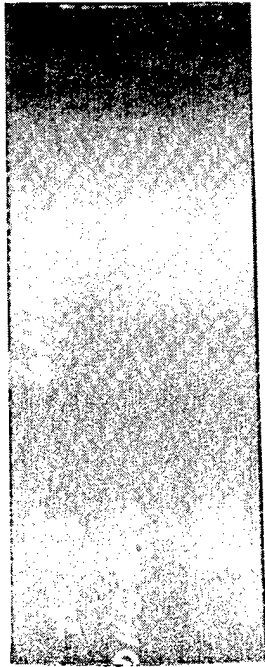


Figure 3.8-20. Aged Adhesive Sample 6A2—2.4X Reduction

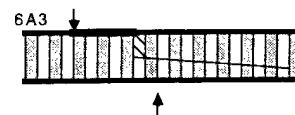
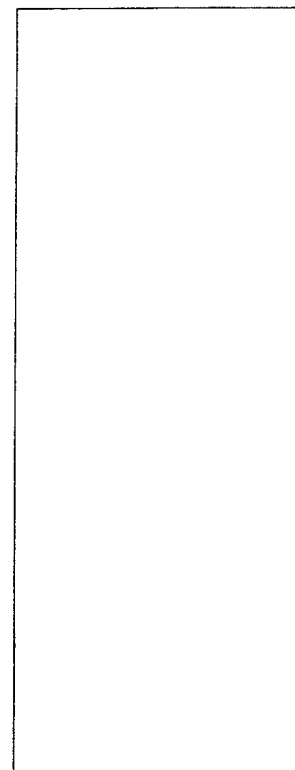
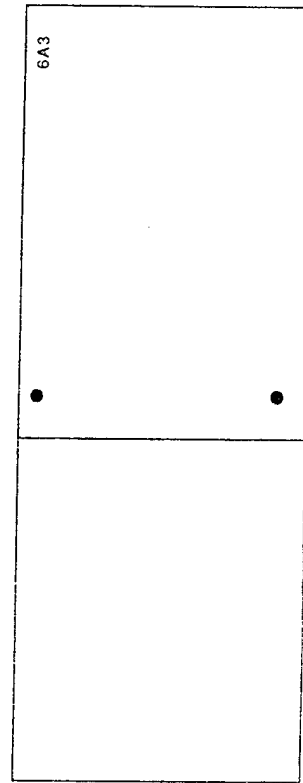
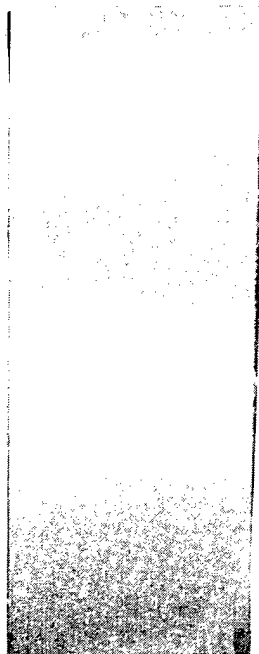
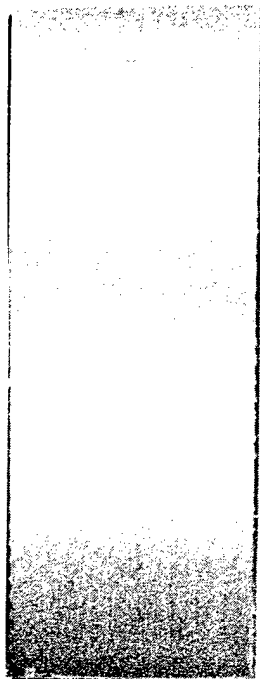


Figure 3.8-21. Aged Adhesive Sample 6A3—2.4X Reduction

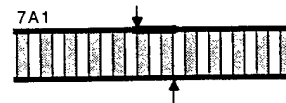
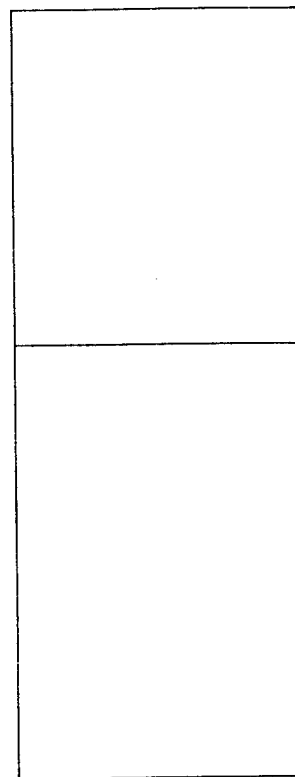
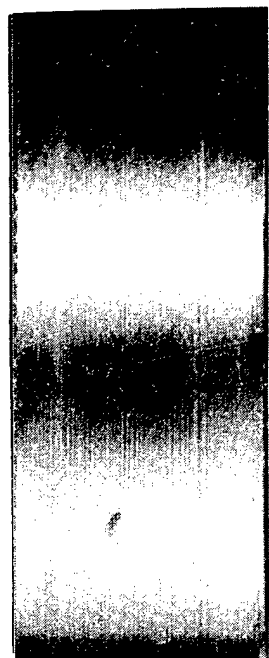
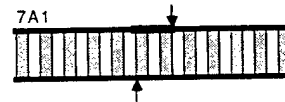
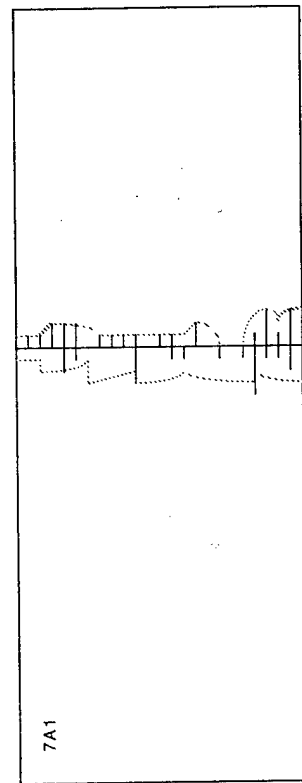
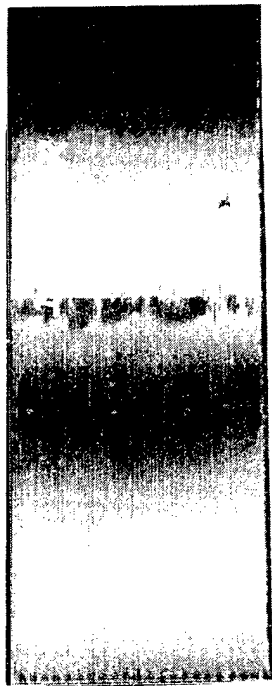


Figure 3.8-22. Improper Core Sample 7A1—2.4X Reduction

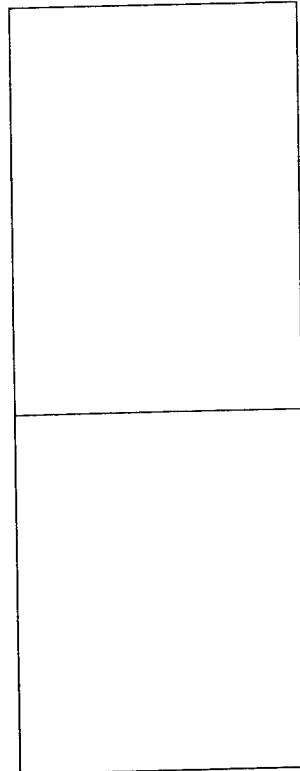
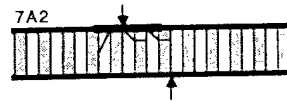
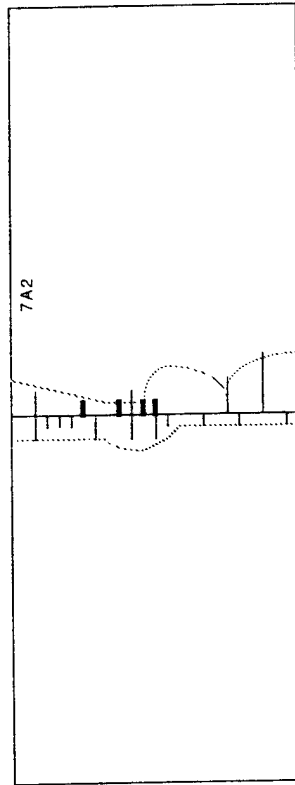
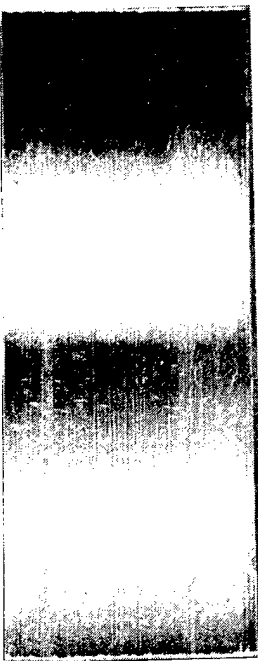
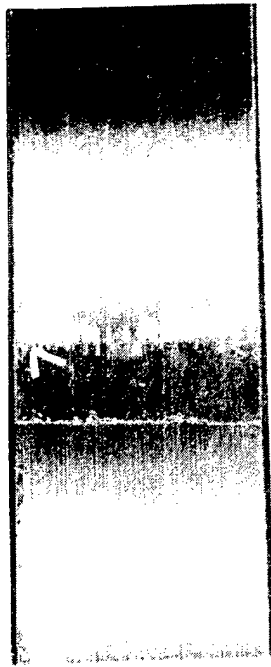


Figure 3.8-23. Improper Core Sample 7A2—2.4X Reduction

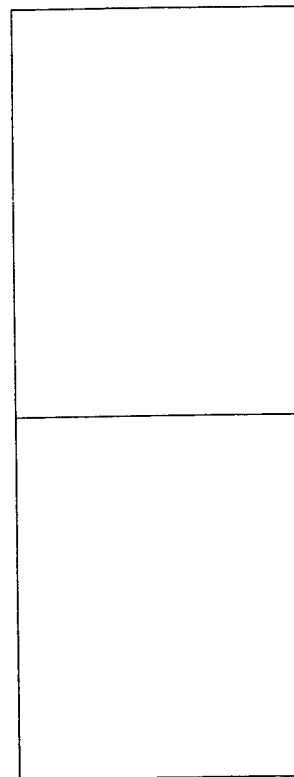
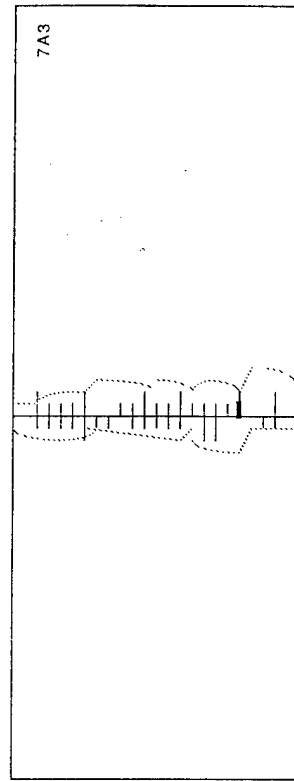
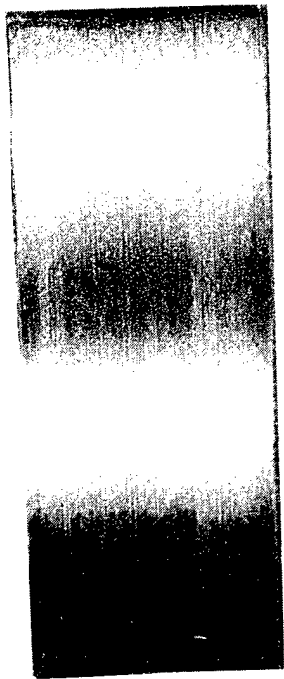
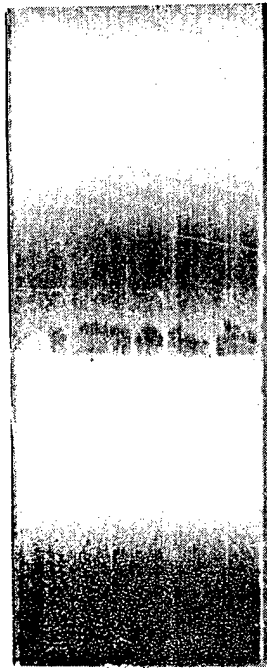


Figure 3.8-24. Improper Core Sample 7A3—2.4X Reduction

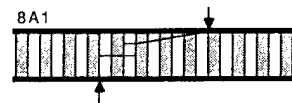
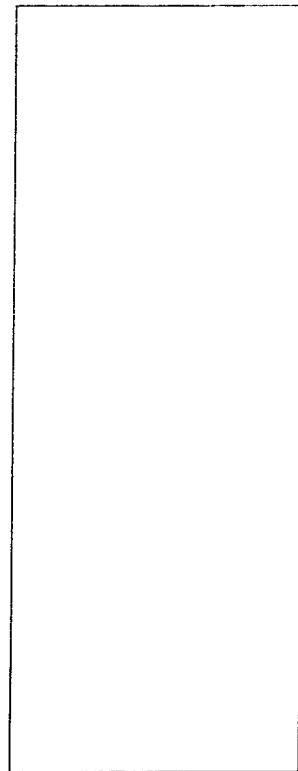
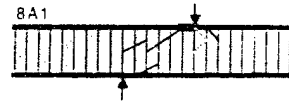
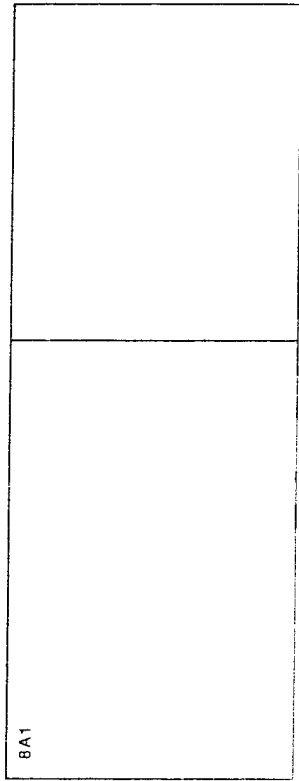
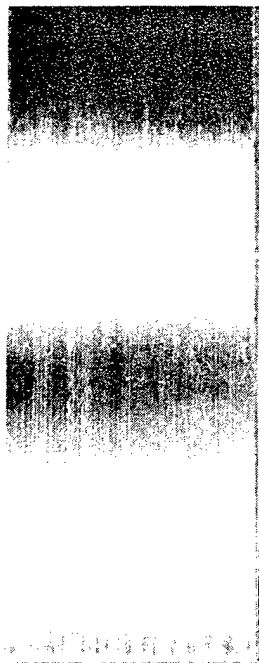
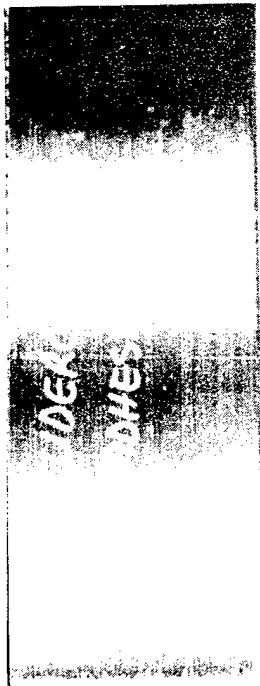


Figure 3.8-25. Undercured Adhesive Sample 8A1—2.4X Reduction



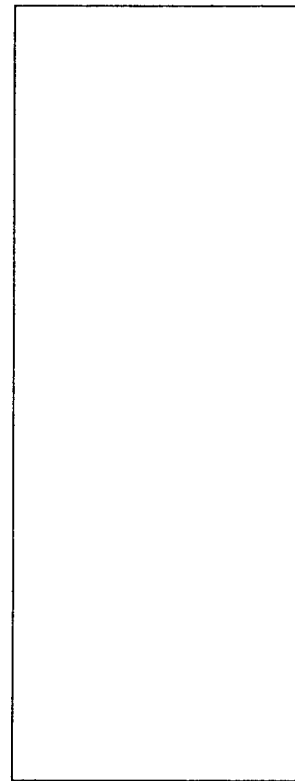
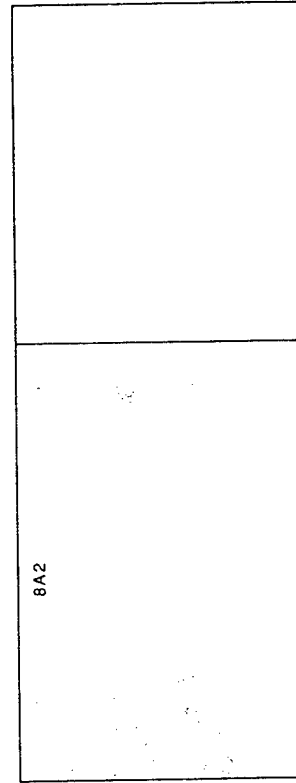
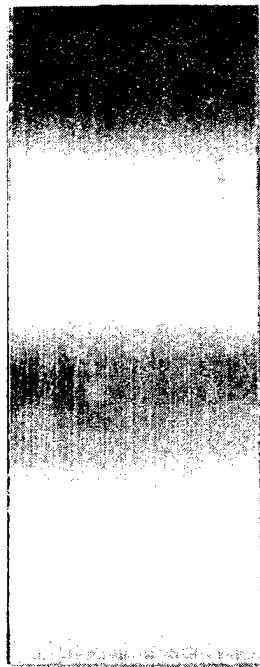
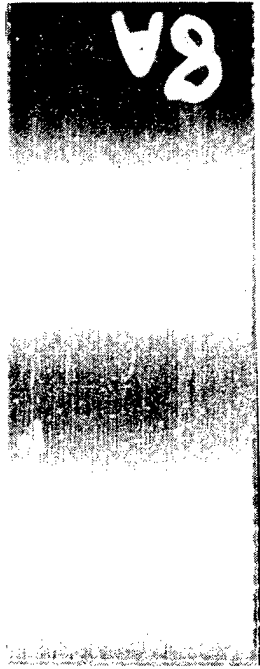


Figure 3.8-26. Undercured Adhesive Sample 8A2—2.4X Reduction

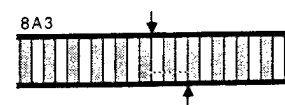
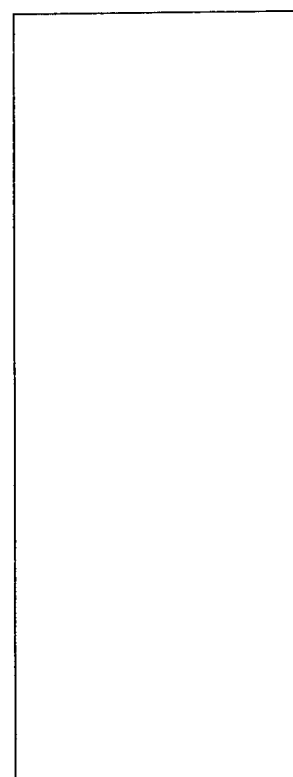
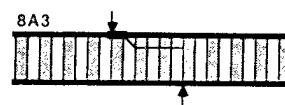
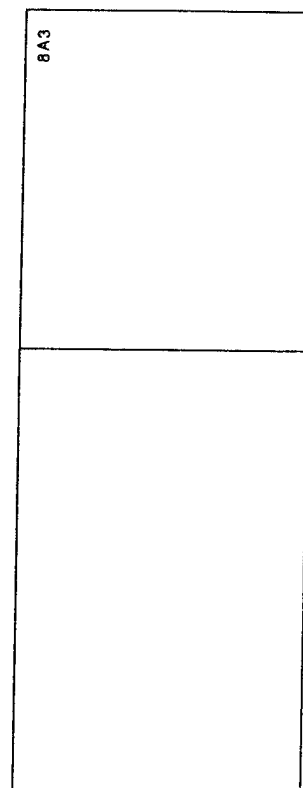
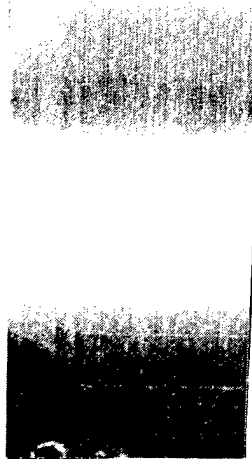
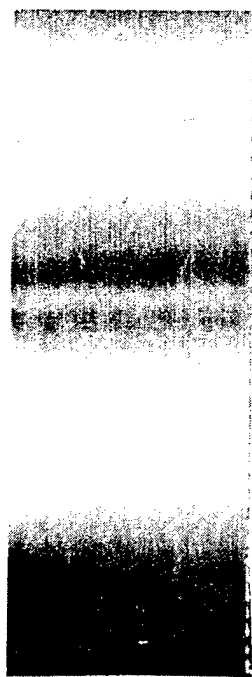


Figure 3.8-27. Undercured Adhesive Sample 8A3—2.4X Reduction

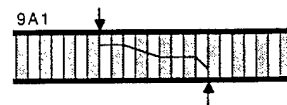
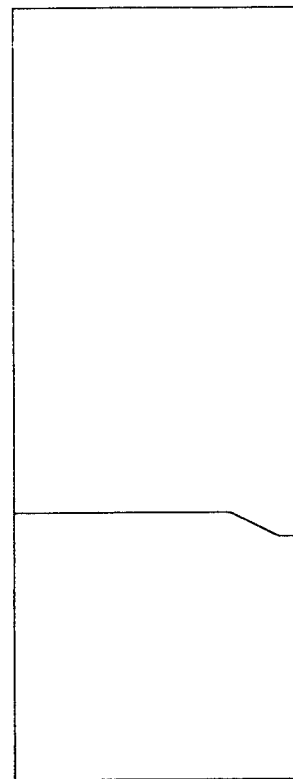
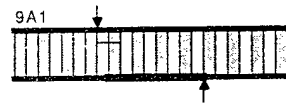
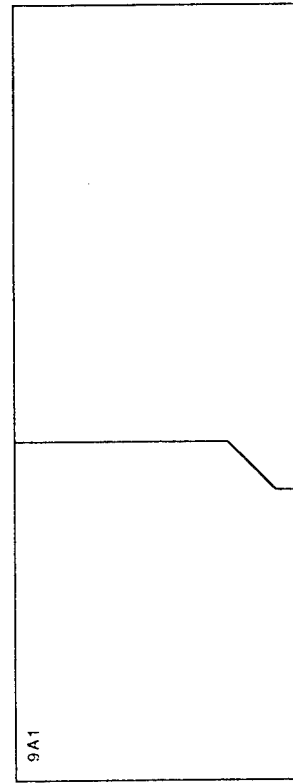
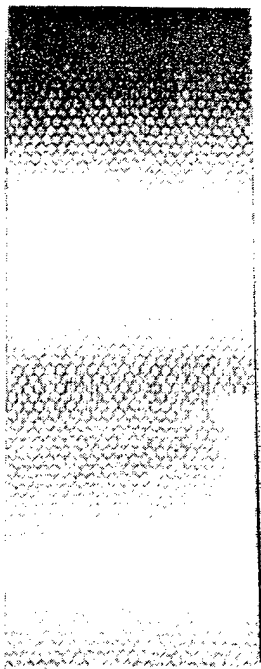
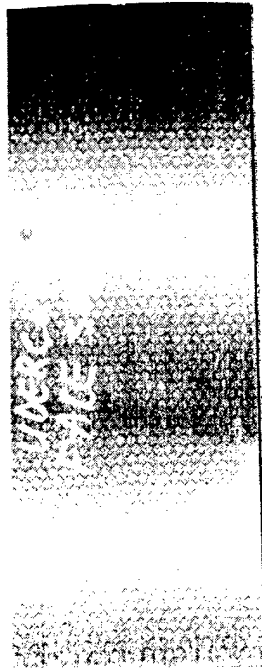


Figure 3.8-28. Undercured Face Sheet Sample 9A1—2.4X Reduction

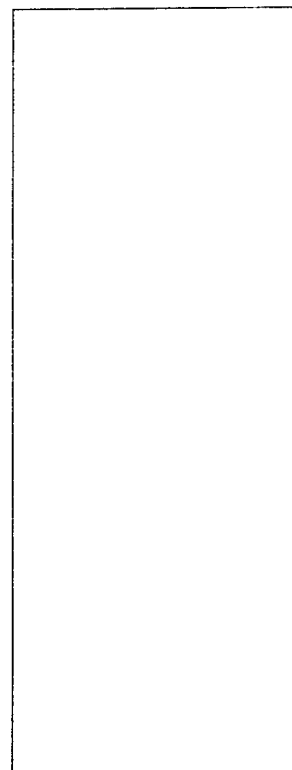
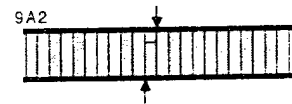
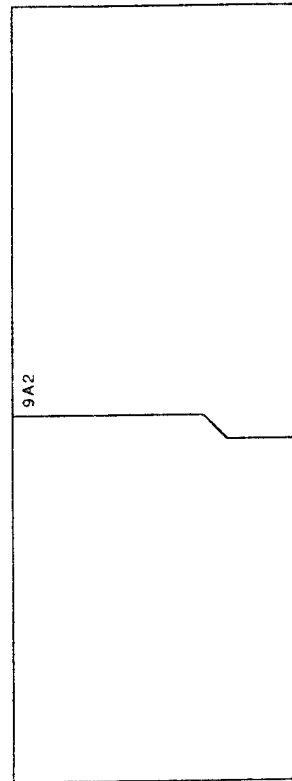
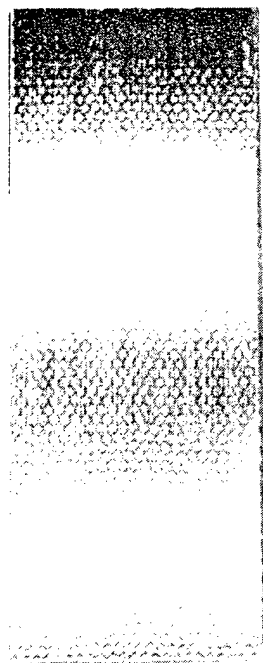
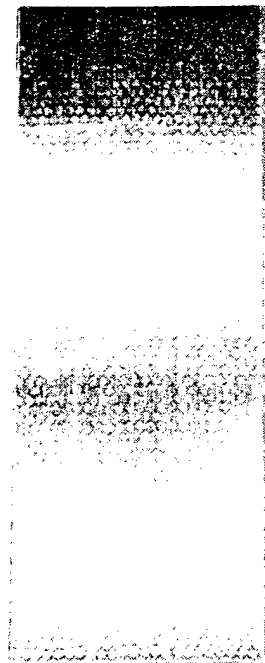


Figure 3.8-29. Undercured Face Sheet Sample 9A2—2.4X Reduction

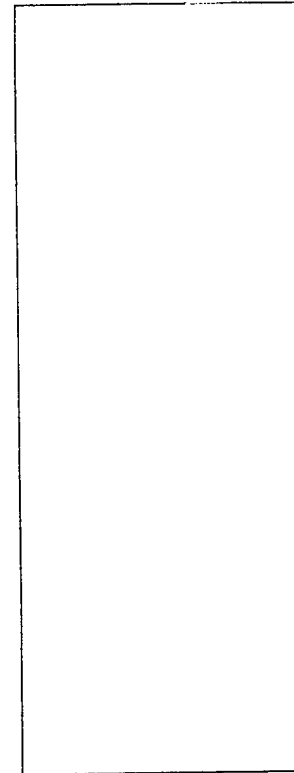
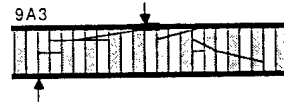
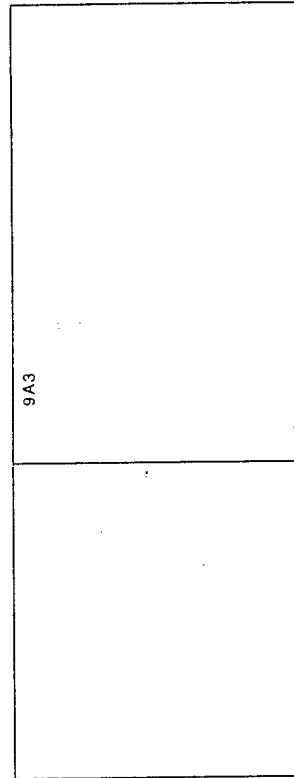
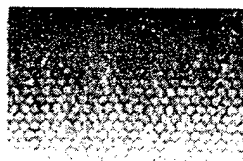
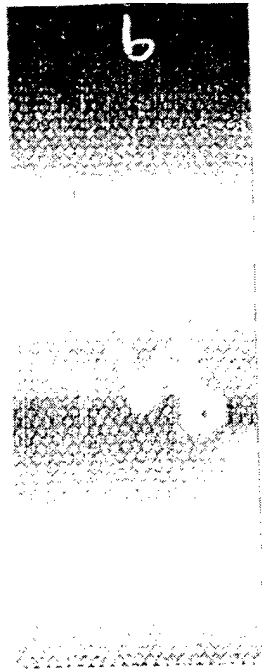


Figure 3.8-30. Undercured Face Sheet Sample 9A3—2.4X Reduction

## SECTION 4

### TASK 6: VERIFICATION OF THE COMPOSITE FAILURE ANALYSIS SYSTEM

#### 4.1 Objective

The objective of this task was to determine the capabilities and effectiveness of the composite failure analysis handbook by demonstrating the use of the handbook on actual components.

#### 4.2 Approach

Two simple components were fabricated, tested, and submitted by the Air Force to Boeing for failure analysis. To make this analysis more realistic, various aspects regarding the background of the fabrication and testing of these components were withheld from the investigator. The failure analyses would then be compared with the known causes of failure, resulting in a more effective evaluation of the procedures and techniques in the handbook.

#### 4.3 Reports

The failure analysis performed on a simple angle component is in Appendix A, a metal core honeycomb sandwich analysis in Appendix B and a fracture analysis of a GROB wing section in Appendix C.

**APPENDIX A**  
**SIMPLE ANGLE COMPONENT**

UNCLASSIFIED  
THE BOEING COMPANY

CAGE CODE 81205

THIS DOCUMENT IS:

CONTROLLED BY

ALL REVISIONS TO THIS DOCUMENT SHALL BE APPROVED  
BY THE ABOVE ORGANIZATION PRIOR TO RELEASE.

PREPARED UNDER

CONTRACT NO. F33615-86-C-5071

IR&D

OTHER

PREPARED ON Macintosh Word

FILED UNDER L-9990

DOCUMENT NO. D180-31996-2

MODEL

TITLE Composite Failure Analysis Handbook  
Failure Analysis of Air Force Component (CDRL Item 7)

ORIGINAL RELEASE DATE 22 November 1991

ISSUE NO.

TO

DATE



THE INFORMATION CONTAINED HEREIN IS NOT PROPRIETARY.



THE INFORMATION CONTAINED HEREIN IS PROPRIETARY TO THE BOEING COMPANY  
AND SHALL NOT BE REPRODUCED OR DISCLOSED IN WHOLE OR IN PART OR USED  
FOR ANY DESIGN OR MANUFACTURE EXCEPT WHEN SUCH USER POSSESSES  
DIRECT, WRITTEN AUTHORIZATION FROM THE BOEING COMPANY.

ANY ADDITIONAL LIMITATIONS IMPOSED ON THIS DOCUMENT  
WILL BE FOUND ON A SEPARATE LIMITATIONS PAGE.

PREPARED BY

*Gregory M. Walker*  
Gregory M. Walker

L-1205

1-14-90

CHECKED BY

\_\_\_\_\_

\_\_\_\_\_

\_\_\_\_\_

SUPERVISED BY

\_\_\_\_\_

\_\_\_\_\_

\_\_\_\_\_

APPROVED BY

*Donald F. Sekits*  
Donald F. Sekits

9-5575

1-15-90

SIGNATURE

ORGN

DATE



THE BOEING COMPANY

ABSTRACT

As a requirement for the Composite Failure Analysis Handbook contract, a small-scale component was fabricated, mechanically tested, and submitted to Boeing for failure analysis. The purpose of this analysis was to demonstrate and evaluate the procedures to be included in the handbook, including the Fracture Analysis Logic Network (FALN). As part of the evaluation, information was withheld from the investigator regarding the loading parameters and fabrication specifications. By comparing the analysis with the actual event, improvements can be made to the procedures and techniques which will provide more accurate analyses in the future.

The analysis followed the simplified FALN since the component was not considered a complex part which did not require an extensive investigation. Visual and optical examination revealed multiple delaminations as the primary damage incurred by testing. Chemical characterization indicated that some sections of the part may have been undercured during fabrication. High magnification optical and scanning electron microscopic examination of the fracture surfaces revealed the presence of two fracture modes emanating from the angle region and propagating toward the flange edges. A possible scenario describing the test conditions was developed to explain the cause of the damage and the multiple propagation fracture sequence.

KEY WORDS

composites

failure analysis

delamination

THE BOEING COMPANY  
TABLE OF CONTENTS

	PAGE
1. INTRODUCTION	5
2. TECHNICAL	6
2.1 Background and History	6
2.2 Nondestructive Evaluation	6
2.3 Material Characterization	14
2.4 Fractography	17
2.5 Stress Analysis	17
3. CONCLUSIONS	21

THE BOEING COMPANY

LIST OF FIGURES

FIGURE		PAGE
1	Diagram Showing the Simplified Fracture Analysis Logic Network	7
2	Photographs of the As-Received Component	8
3	Photographs of the Edge of the Component Showing the Extent of Delamination	9
4	Micrographs Showing the Regions of Surface Fibers Delamination and Cracking Along the Middle and Edges of the Inner Radius	10
5	Micrograph of the Indentations and "Tracks" Along the Inner Radius	11
6	CT Image Showing the Imaging Artifacts and Some of the Actual Delaminations	12
7	Photograph Showing the Regions of Intact Laminates Identified Using Pulse Echo	12
8	TTU Scan Before Sealing. Water Has Penetrated the Laminates From the Edges Causing Incorrect Readings	13
9	Photograph of the Part After the Edges and Fastener Holes Were Sealed Before the Second Series of TTU Scans	14
10	TTU Scan, After Drying and Sealing the Component, Exhibiting Delamination Regions Similar to the Pulse-Echo Examination	15
11	IR Spectrum From a Sample of Hercules 3501-6 350°F Cure Epoxy Resin	16
12	IR Spectrum From a Sample of the Resin From the Component	16
13	SEM Micrograph Showing a Section of the Delaminated Surface Which Initiated at the Peel Ply	18
14	SEM Micrograph of the Mode II-Type (Shear) Fracture Surface in Region 4 Adjacent to the Peel Ply	19
15	SEM Micrograph of the Mode I-Type (Tension) Fracture Surface in Region 2	19
16	SEM Micrograph of the Mode II-Type (Shear) Fracture Surface in Region 1	20

## THE BOEING COMPANY

### 1. INTRODUCTION

This report summarizes the failure analysis of the angle component provided by the Air Force. This work was conducted under task 6 of the add-on contract to F33615-86-5071, Composite Failure Analysis Handbook. The add-on expands tasks 3, 6, and 7. Tasks 1, 2, 4, and 5 were completed under the original contract.

The overall program objective is to create a failure analysis handbook containing the procedures, techniques, and data necessary to conduct failure analysis of fiber-reinforced composite structures. In addition, the handbook will describe a limited number of documented case histories conducted on small-scale components. Contract F33615-86-5071 is an expansion of WRDC Contract F33615-84-C-5010 Postfailure Analysis Compendium for Composite Structures. The present contract consists of the following tasks:

- a. Task 1: Development of Handling and Data Gathering Techniques for Field Representatives
- b. Task 2: Expansion of Fractographic Techniques in Composite Failure Analysis
- c. Task 3: Expansion of the Fractographic Database
- d. Task 4: Development of Data Formats
- e. Task 5: Documentation of Materials Properties
- f. Task 6: Verification of the Composite Failure Analysis System (by performing a demonstration of two structural demonstration items)
- g. Task 7: Documentation
- h. Task 8: Administrative Management
- i. Task 9: Meetings

The technical direction for the contract is provided by Patricia L. Stumpff, Wright Research and Development Center, Wright-Patterson Air Force Base (WPAFB), Ohio. Donald F. Sekits is the Boeing program manager and Gregory M. Walker is the principal investigator.

Other contributors for this report include: G. Georgeson and J. Linn, Nondestructive Inspection; J. Chen, Chemical and Thermal Analysis; G. Tuss, Surface Analysis; D. Banning, Scanning Electron Microscopy.

2. TECHNICAL

2.1 Background and History

The submitted composite part was one of two small-scale components that were to be analyzed by Boeing. The analysis is to demonstrate the concepts and procedures which are to be included in the Composite Failure Analysis Handbook, such as the Fracture Analysis Logic Network (fig. 1).

To evaluate the effectiveness of the procedures, various details regarding the history and background of the component were withheld from the investigator such as; intentional defects, information regarding the original dimensions and drawing specifications, and process specifications. Testing parameters and the loading configuration were also unknown to the investigator such as; the failure criteria, the loading direction and component orientation, and the loading spectrum. After comparing the analysis to the actual event, improvements to the procedures and techniques can be made to provide more accurate analyses in the future.

2.2 Nondestructive Evaluation

Various techniques were used for the nondestructive evaluation of the component including: visual and low magnification inspection, X-ray computed tomography, pulse echo, and through-transmission ultrasound. Each technique provides different types of information; however, for this investigation, the visual inspection and the pulse echo examination provided the most data.

a. Visual Examination

The submitted component (shown in fig. 2) was approximately 14 inches long with 5-inch wide flanges. The thickness was approximately 0.17 to 0.20 inch. The angle between the two flanges was approximately 95 to 100 degrees. The overall color and appearance was indicative of a carbon fiber-reinforced plastic system.

A "padup" strip was placed along the inner and outer radius of the knee region. The depressed regions, containing the fastener holes and probably used for grips, appeared to be thinner due to the absence of plies. However, closer examination revealed that it was actually the result of the same number of plies being compressed closer together.

Internal delaminations, observe from both ends of the part, extended from the "knee" or angle region to the edges of the flanges (fig. 3). A 3-inch long delamination was located along the center plies. This delamination extended from an inserted ply placed within the center of the fiber plies at the knee region.

Surface fibers within the inner radius of the "knee" were cracked (fig. 4). Deformations, such as rippling and buckling, were also present along the entire length of the inner radius of the knee. Small indentations and elongated depressions or "tracks" were present along the inner knee surface (fig. 5). The surface of the depressions was shiny indicating that the depressions probably occurred during the fabrication process. Some of the "tracks" contained cracks which went through the surface ply. There were no surface defects or anomalies on the outside surface of the component. Strain gages were located on both sides of one of the flanges.

THE BOEING COMPANY

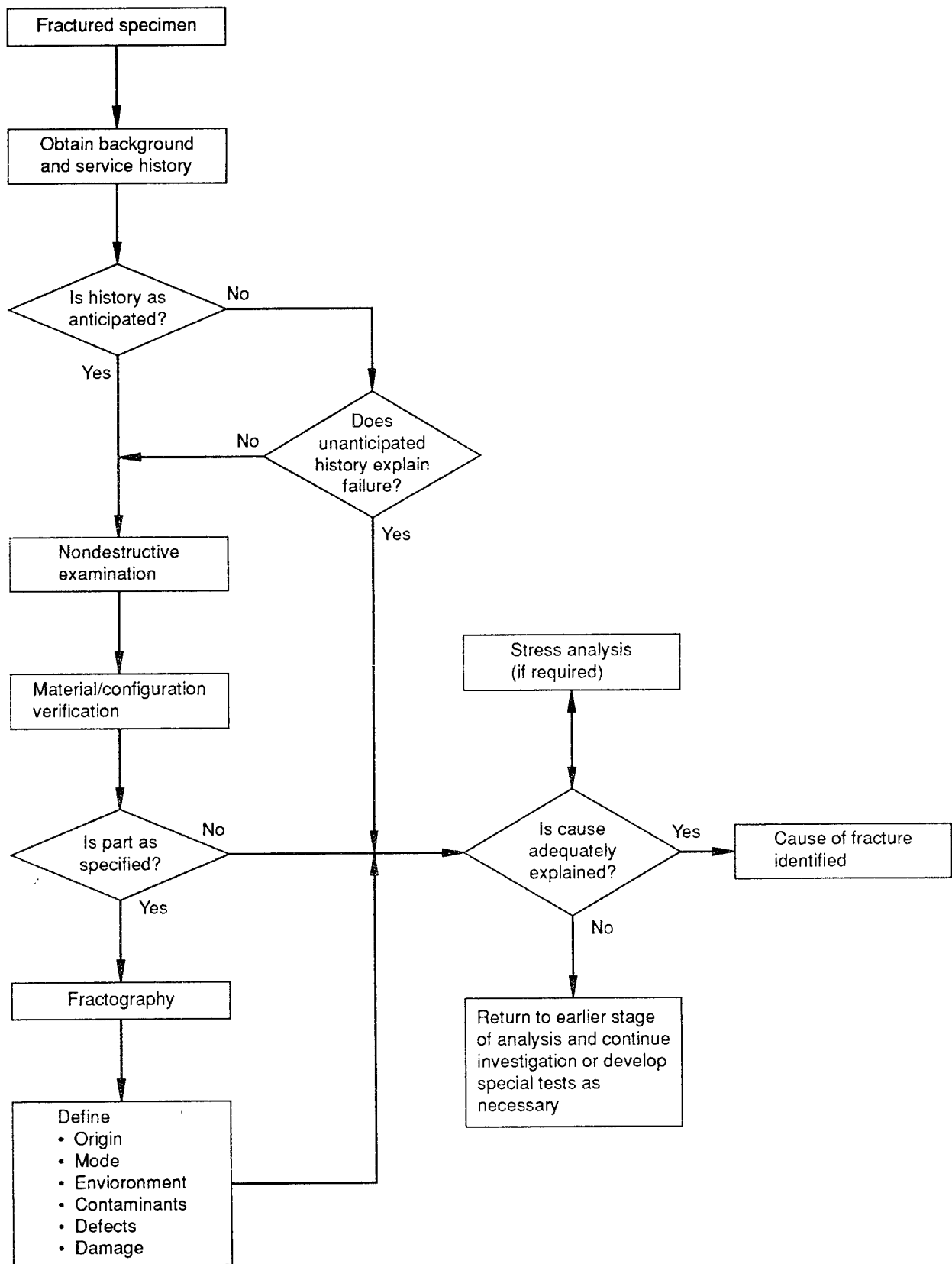
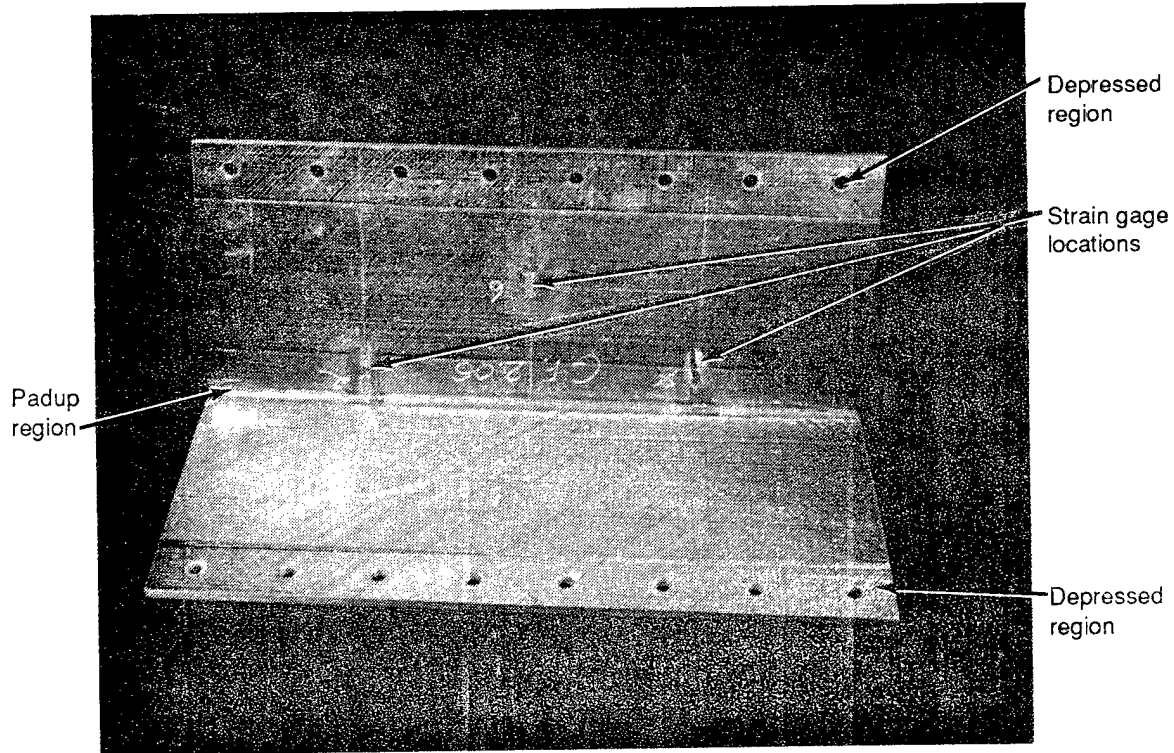
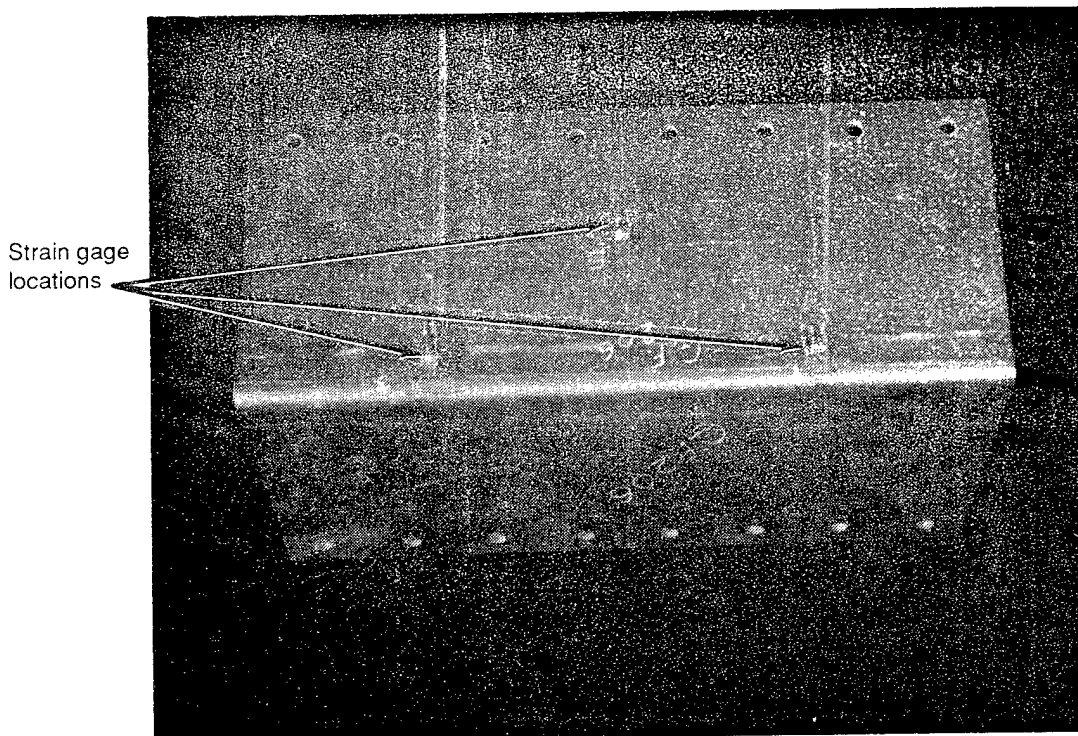


Figure 1. Diagram Showing the Simplified Fracture Analysis Logic Network

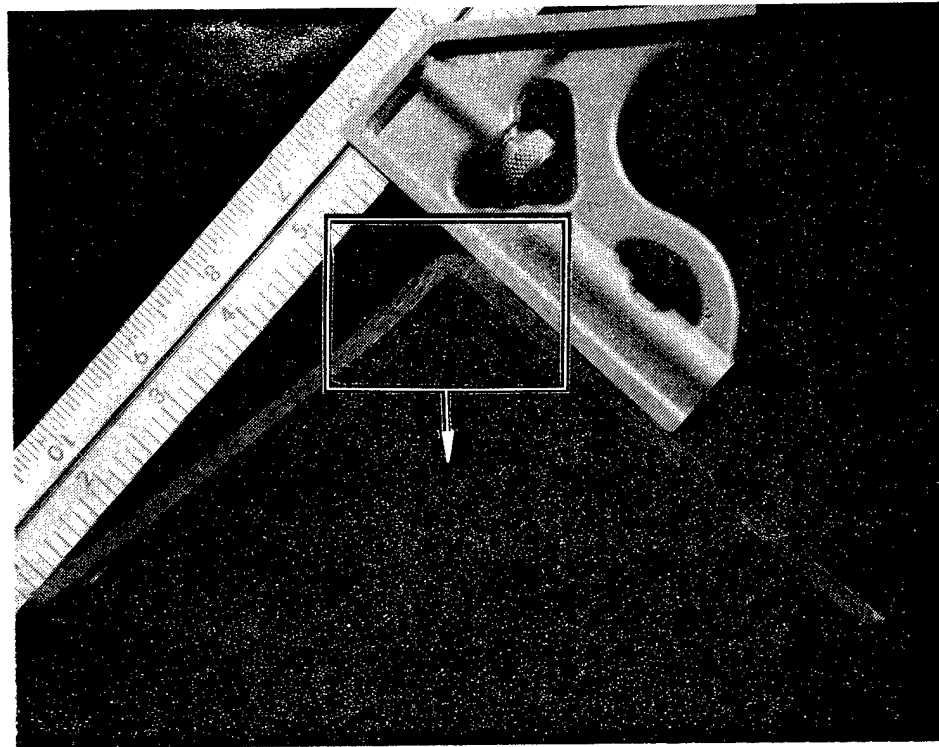


(a) Front Side

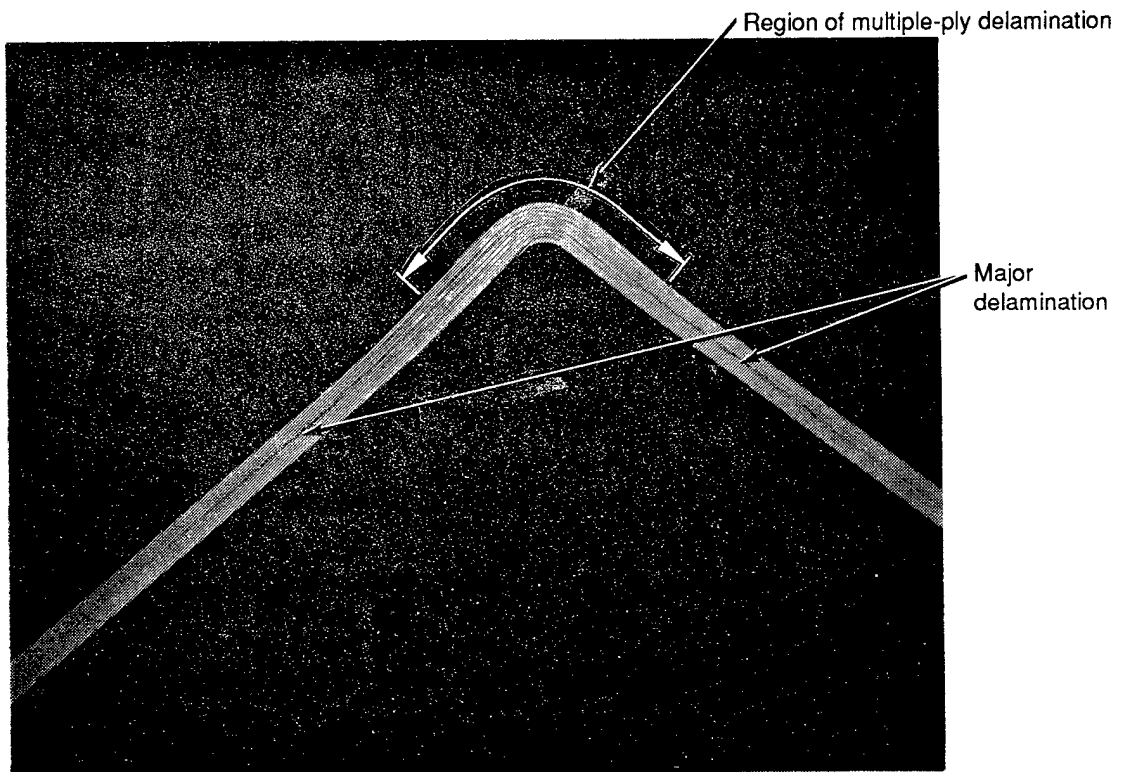


(b) Back Side

Figure 2. Photographs of the As-Received Component



(a) Overall View of the Edge



(b) Close-Up View of the Delaminated Regions

Figure 3. Photographs of the Edge of the Component Showing the Extent of Delamination



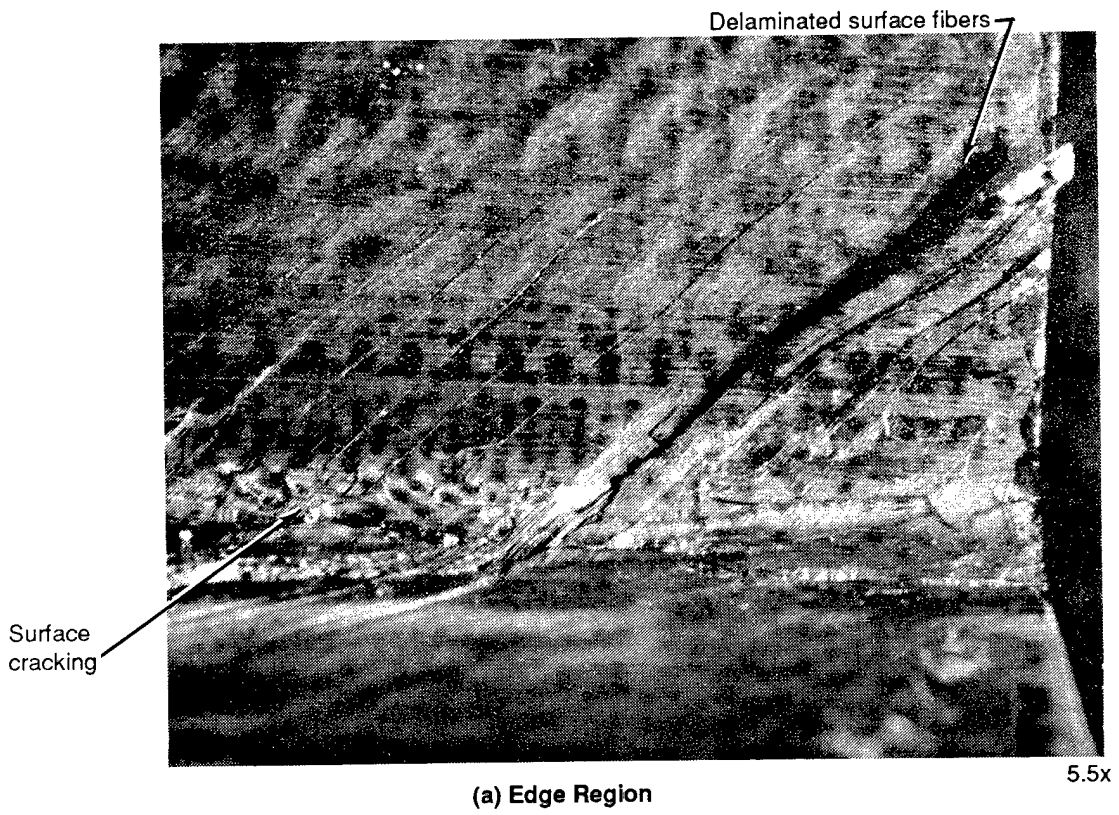
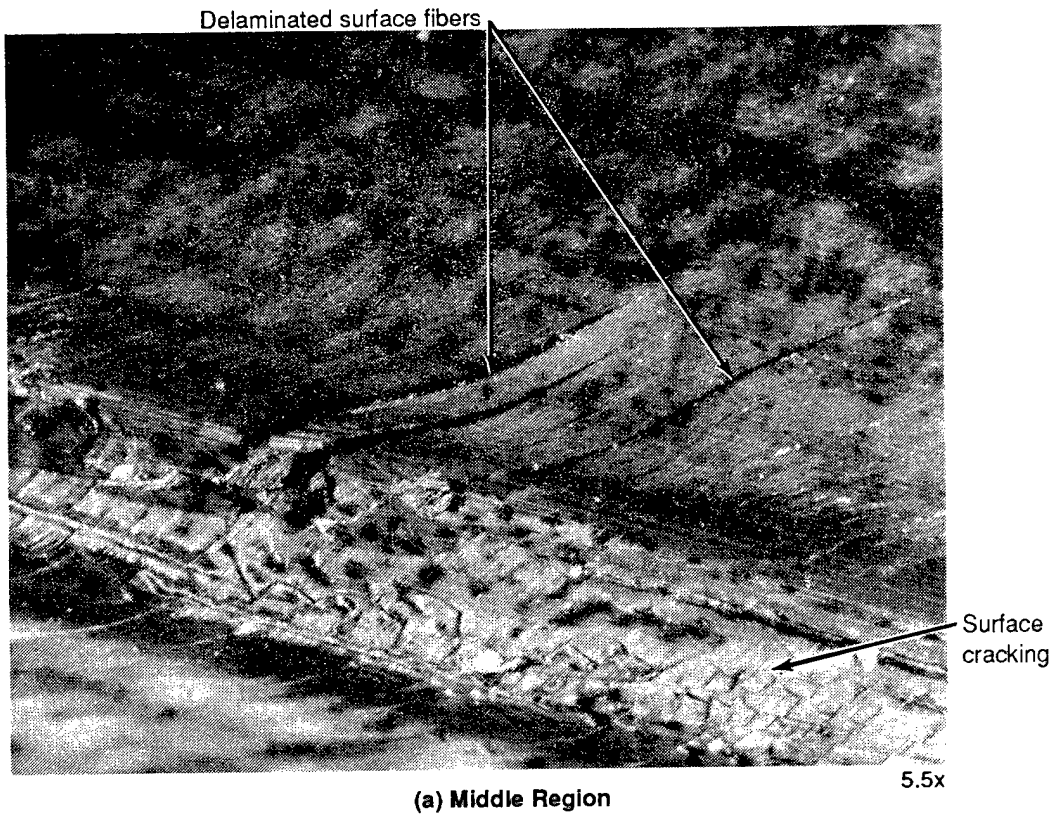


Figure 4. Micrographs Showing Regions of Surface Fibers Delamination and Cracking Along the Middle and Edges of the Inner Radius

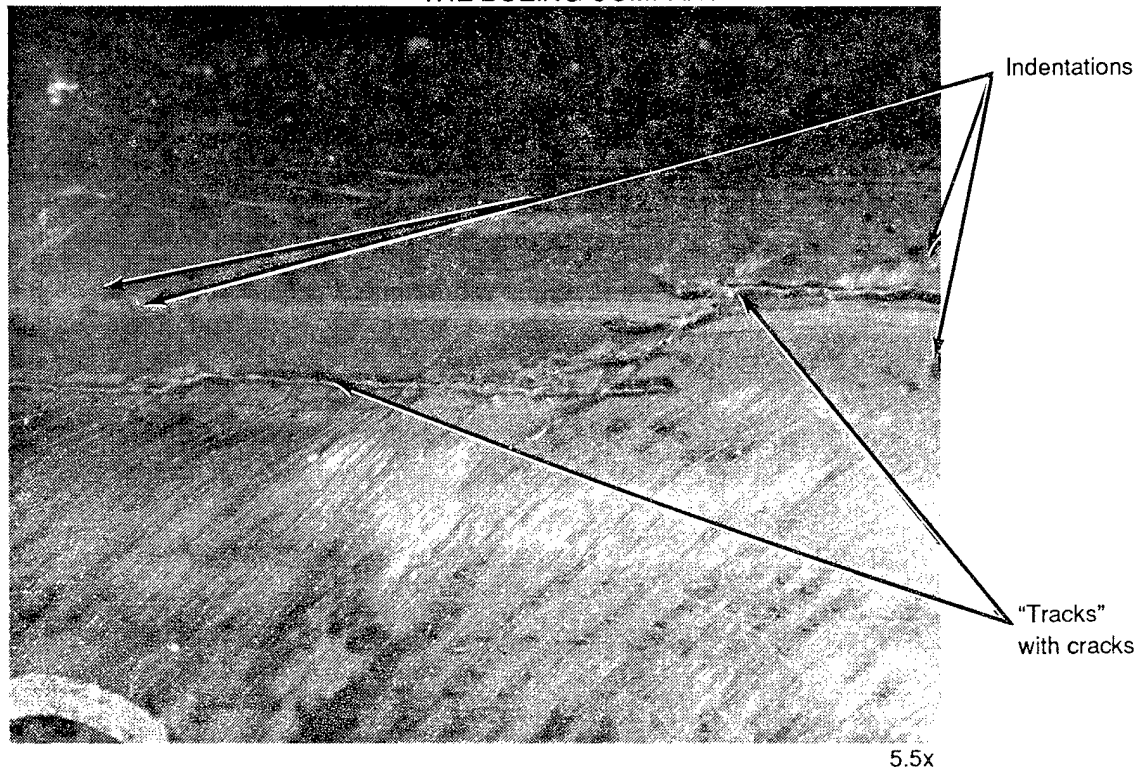


Figure 5. Micrograph of the Indentations and "Tracks" Along the Inner Radius

b. X-Ray Computed Tomography (CT)

Computed tomography was performed on the angle component to determine the extent of internal cracking and delamination. The results of the CT scan are shown in figure 6. The "L" geometry is not well suited for CT examination/evaluation. Artifacts, such as the dark horizontal streak in the CT image, were caused by the "L" geometry. Even with these artifacts, some delaminated regions were identified which were located along the length of the part and concentrated at the knee region.

c. Pulse Echo

Examination using a handheld pulse-echo unit (C-scan) with a .25-inch transducer identified delaminations throughout the component (see fig. 7) except at certain locations along the region containing the fastener holes.

d. Through-Transmission Ultrasound (TTU)

An attempt was made to further characterize the extent of delaminations using TTU (C-scan). However, since the part was exposed to water jets to perform the TTU analysis, large amounts of water entered the part through the edges and caused incorrect indications of delaminations and damage (fig. 8). These were grossly inconsistent with the pulse-echo analysis.

The part was subsequently dried in an oven at 90°F for 30 minutes before another set of scans was performed. This time the edges were sealed, the surface of the part was sprayed with a lacquer, and the fastener holes were plugged (fig 9). The part was then rescanned which revealed that it was almost completely delaminated (fig. 10). The grip areas were not delaminated as observed in the pulse-echo analysis.

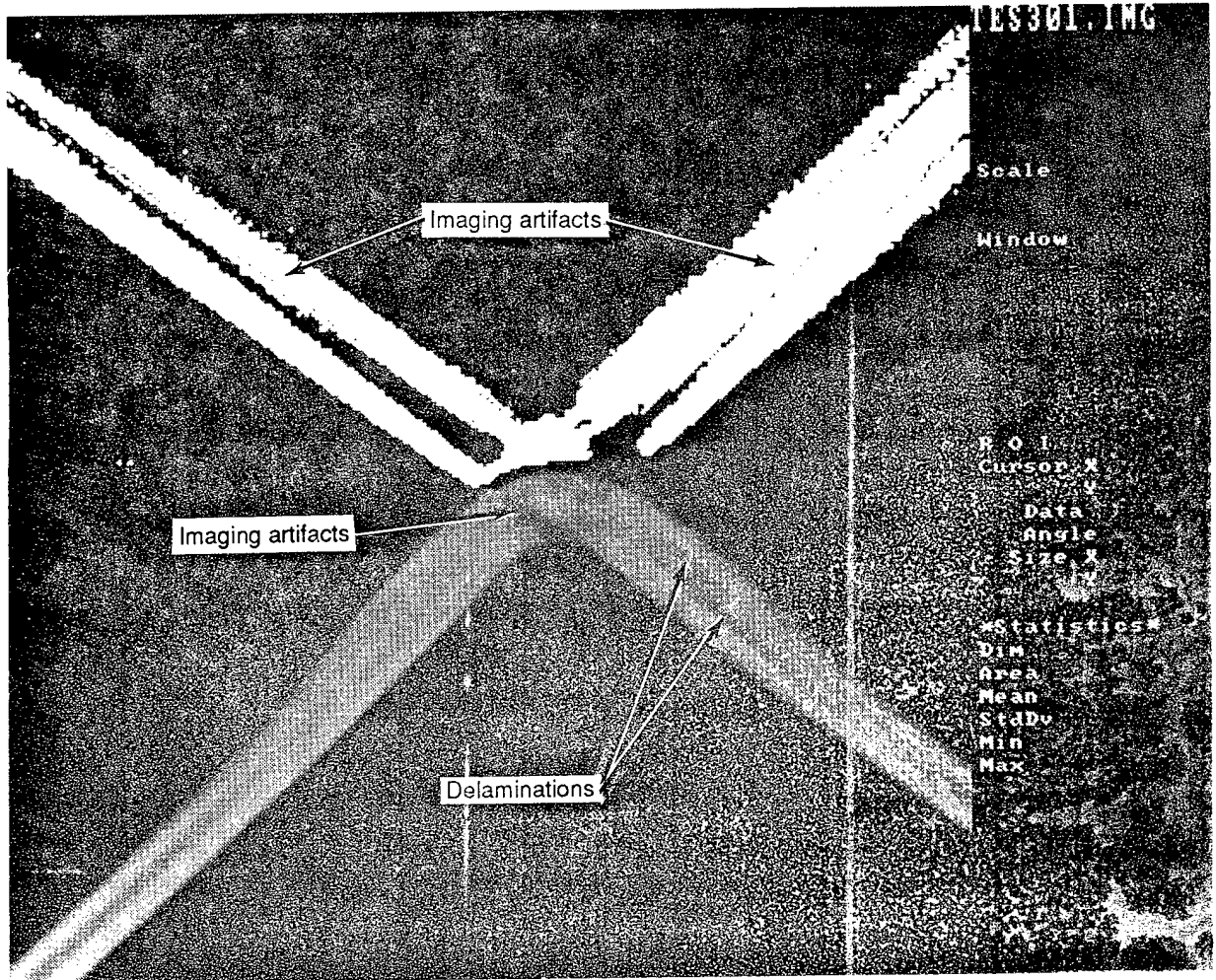


Figure 6. CT Image Showing the Imaging Artifacts and Some of the Actual Delaminations

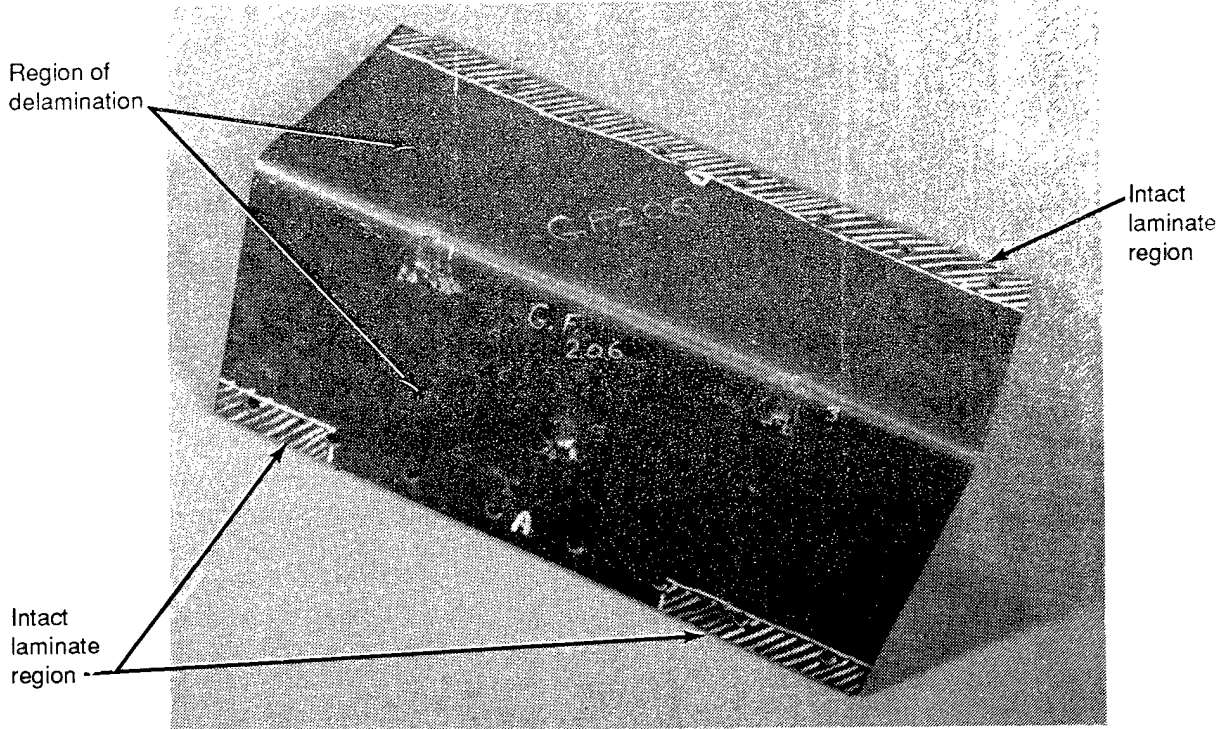


Figure 7. Photograph Showing the Regions of Intact Laminates Identified Using Pulse Echo

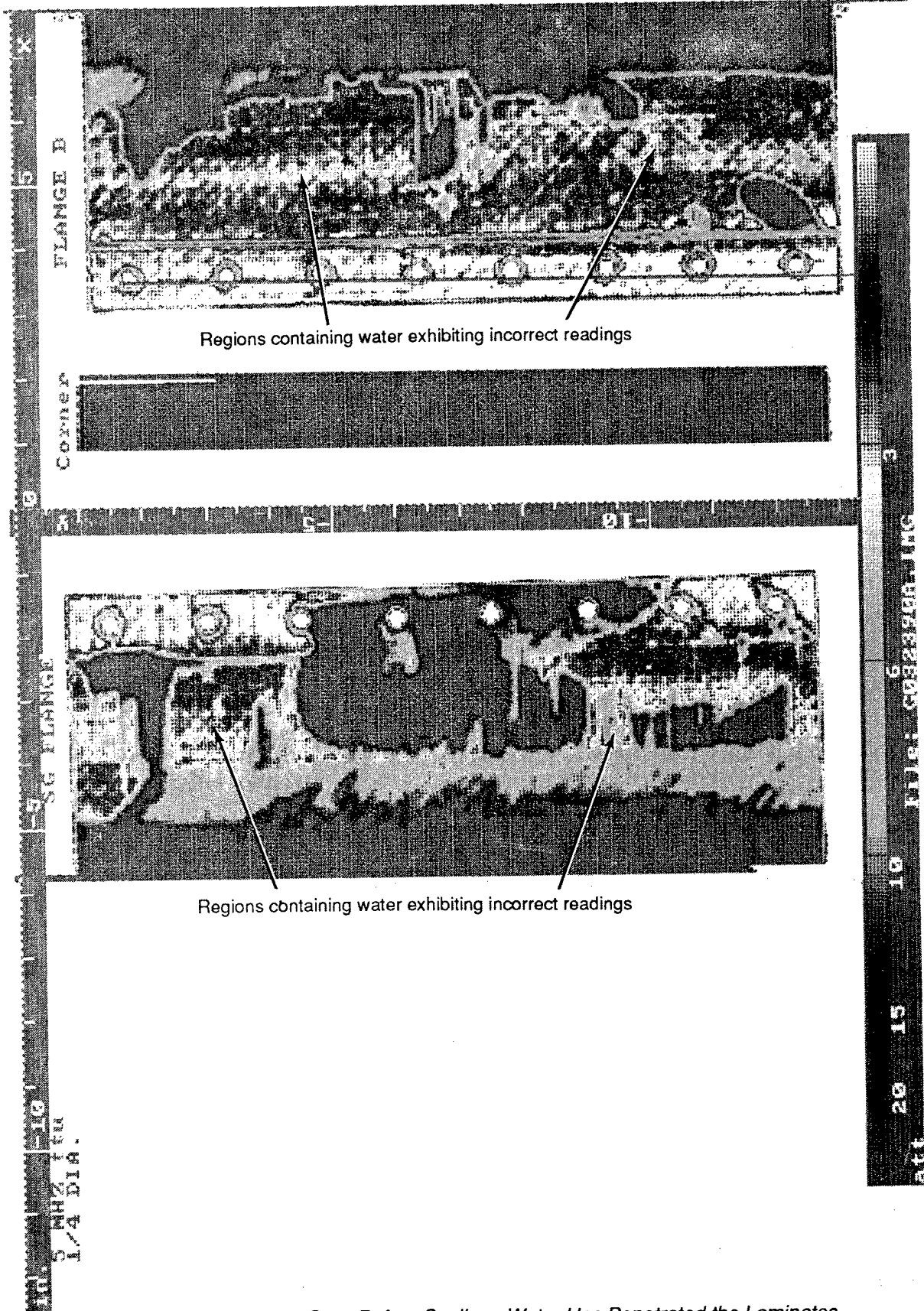
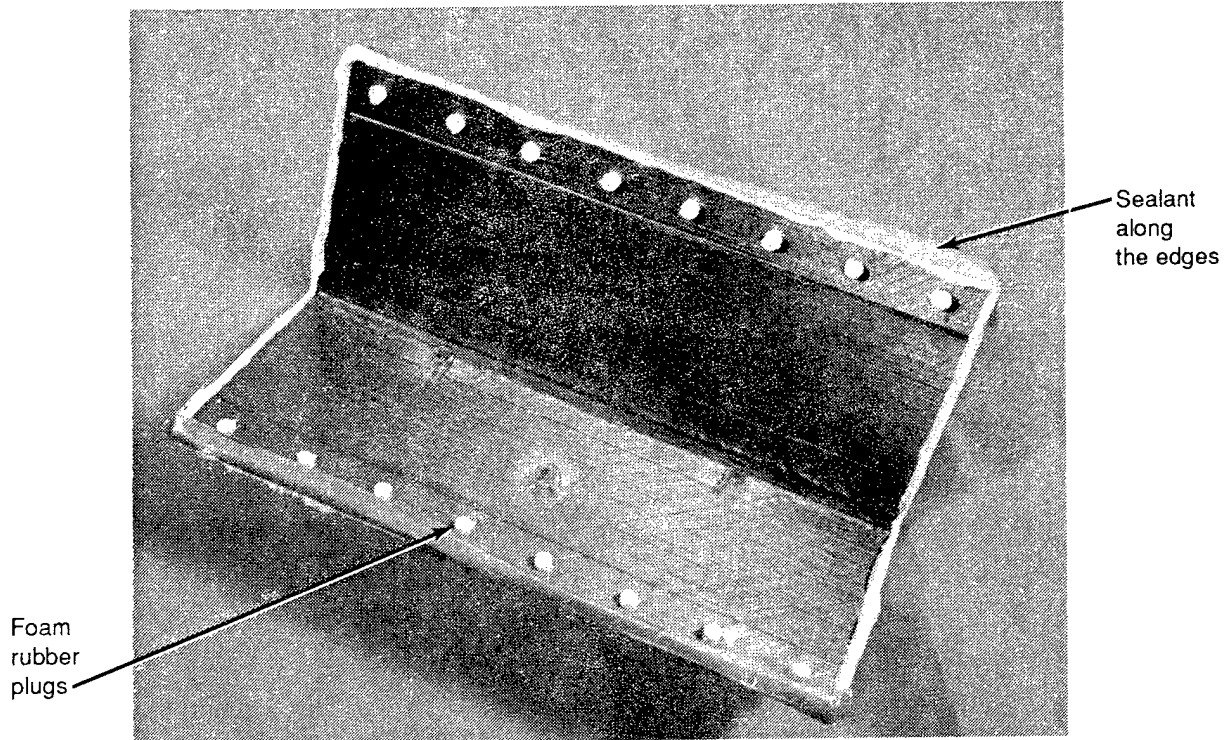


Figure 8. TTU Scan Before Sealing. Water Has Penetrated the Laminates From the Edges Causing Incorrect Readings



*Figure 9. Photograph of the Part After the Edges and Fastener Holes Were Sealed Before the Second Series of TTU Scans*

### 2.3 Material Characterization

#### a. Material Identification

The resin material was examined using infrared spectroscopy analysis (IR). This identified the material as similar to the Hercules 3501-6 epoxy resin system (figs. 11 and 12). This material has a curing temperature of 350°F. IR also identified the peel ply material to be a Teflon/Fiberglass film.

The fibers within epoxy resin system were identified to be carbon using a surface analyzer.

#### b. Glass Transition Temperature (T<sub>g</sub>) and Extent of Cure

Both differential scanning calorimetry (DSC) and thermomechanical analysis (TMA) were used to determine the glass transition temperature of the composite. Specimens analyzed using TMA revealed peaks at 343°F and at 357°F which indicates that the part may have been undercured in some locations. In addition, during cutting of a section to obtain specimens for TMA, the section split into two halves. The T<sub>g</sub> was consistently at 156°C for some halves and at 185°C for others. This indicates that some regions of the component might have been undercured. DSC analysis did not detect any appreciable heat of curing which indicates the part was fully cured. However, because of the low resin content of the composite, the residual heat of curing may not have been detectable.

#### c. Resin Content

The resin content was determined to be 26.79% by weight using the acid digestion method.

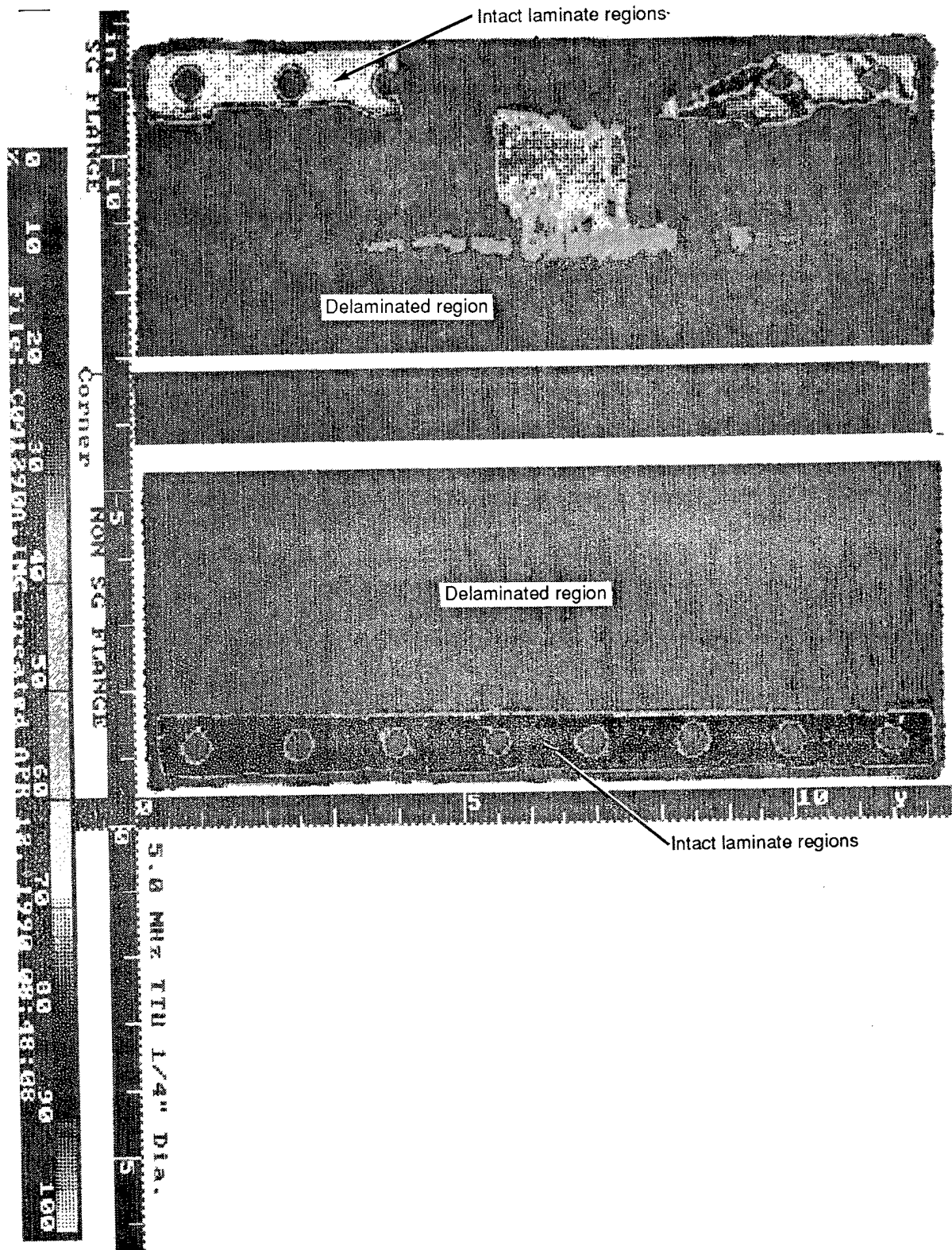


Figure 10. TTU Scan, After Drying and Sealing the Component, Exhibiting Delamination Regions Similar to the Pulse-Echo Examination

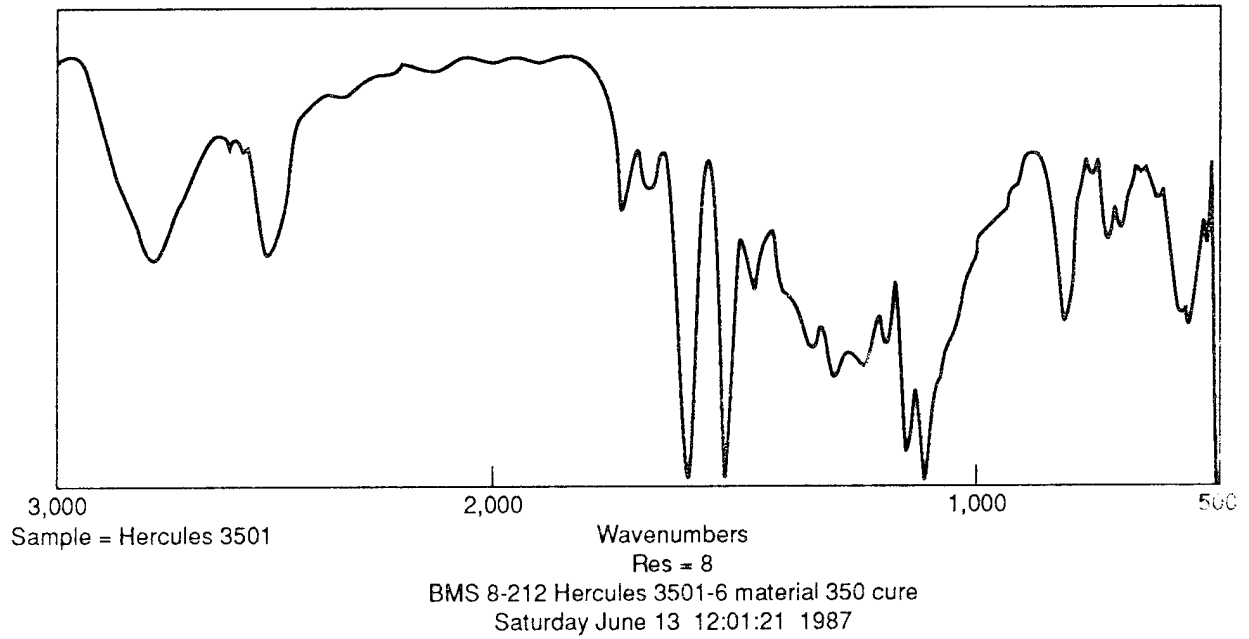


Figure 11. IR Spectrum From a Sample of Hercules 3501-6 350°F Cure Epoxy Resin

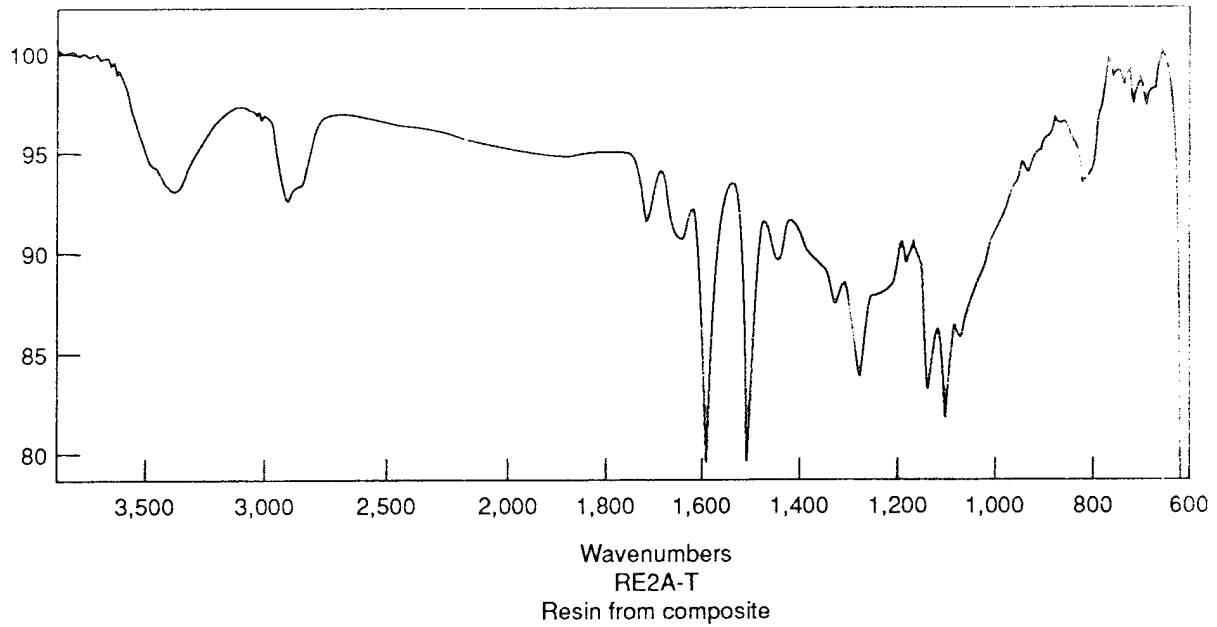


Figure 12. IR Spectrum From a Sample of the Resin From the Component

d. Density

The density was determined to be 1.596 g/cc using the displacement method.

e. Microscopic Examination

Cross sections of the component were examined at 100X. No anomalies or features, such as voids, that could contribute to fracture were found. The stacking sequence was: [+45, 0, 90, -45]<sub>4</sub> \*Peel Ply\* [-45, 90, 0, +45]<sub>4</sub>, for a total ply thickness of 32 (plus the peel ply). The peel ply extended approximately 1 inch from the knee into both flanges. The plies also appeared to be properly aligned in their respective orientations.

2.4 Fractography

a. Optical Examination

The component was sectioned and peeled apart to expose the delaminated fracture surfaces. High magnification (100X to 400X) optical examination of the crack surfaces revealed the presence of two different fracture modes; mode I which is caused by a tensile loading and mode II which is caused by shearing. The most prevalent fracture mode observed was the mode II shearing mechanism. The results of translamellar crack mapping indicate that the delaminations initiated at the edge of the peel ply and propagated towards the flange edges.

Some fracture surfaces exhibited a change in fracture modes from shearing to a tensile mechanism then back to the shearing mode. As seen in figure 13, the crack initiated at the edge of the peel ply and propagated along the flanges to their edge while changing its crack propagation mode.

b. Scanning Electron Microscopy (SEM) Examination

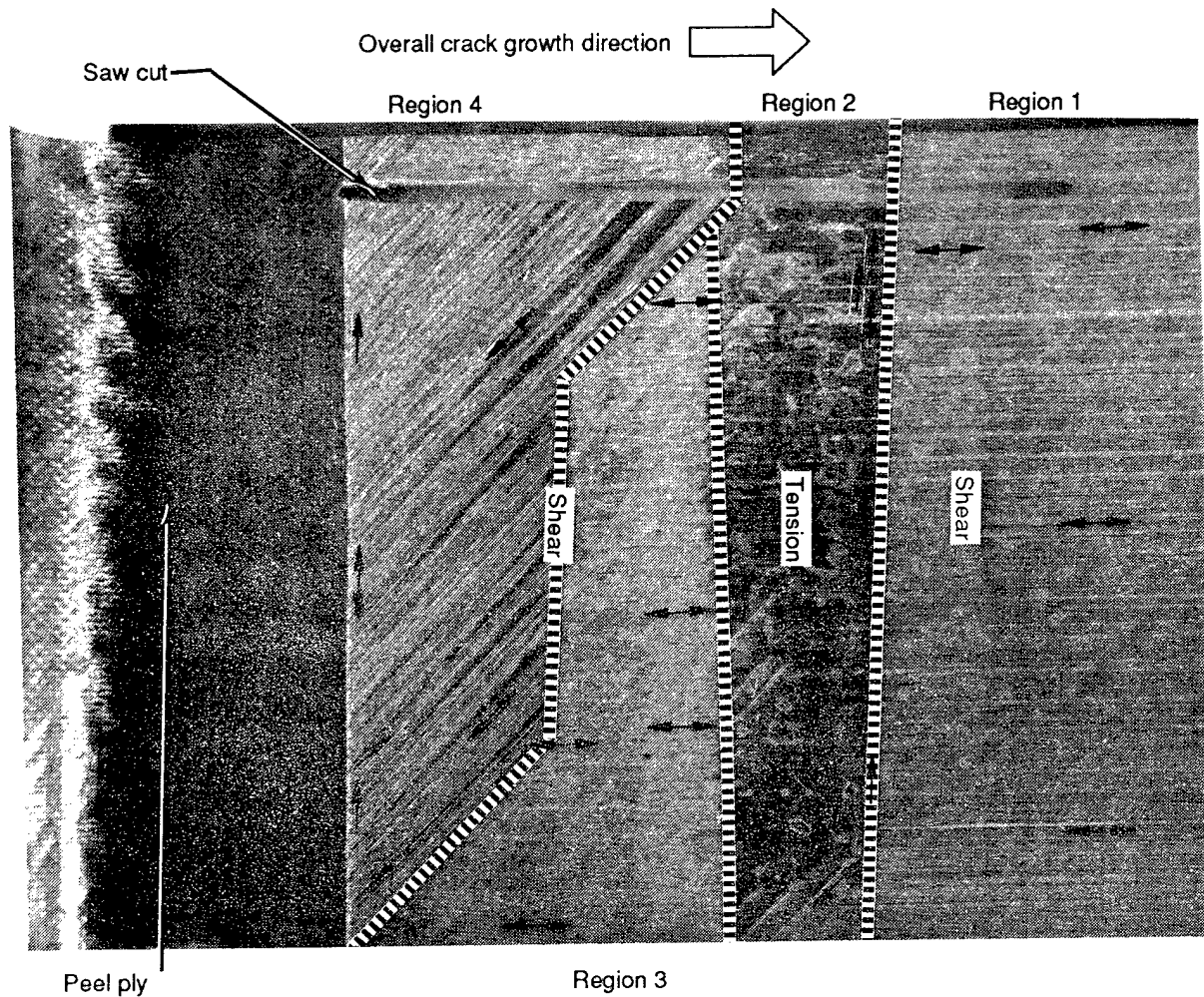
Examination using the SEM confirmed that the fracture modes identified visually were correct. SEM micrographs of the surfaces in the different regions in figure 13 are shown in figures 14 through 16. Comparison of the micrographs with a fractographic database reveals that the component was most likely tested at room temperature in a dry air environment.

2.5 Stress Analysis

Given the fact that the actual test parameters and fixtures were unknown, the following is a proposed loading configuration based on the information that had been collected. This assumes that the component was originally fabricated with a 90-degree angle and that the testing resulted in a permanent deformation.

Initially, the component was gripped at the edges of the flanges using the fastener holes. As loading began, one edge was pulled away from the other edge which induced an initial shear loading condition inside the component at the edge of the peel ply. The presence of the peel ply in the center (where the maximum shear stress occurred) provided a high stress concentration region which allowed the cracks to initiate. As the edges were pulled further apart, the cracks continued to propagate by shear.





Note: Four regions are identified, exhibiting two different fracture modes:

- Region 1: Mode II (shear)
- Region 2: Mode I (tension)
- Region 3: Mode II (shear) 0-degree fibers
- Region 4: Mode II (shear) 45-degree fibers

The arrows show the crack growth directions or orientations at those locations determined using high magnification optical examination.

*Figure 13. SEM Micrograph Showing a Section of the Delaminated Surface Which Initiated at the Peel Ply*

For the one flange, the crack propagated entirely by shear. However, the cracking on the other flange changed modes because the stress orientation had altered significantly enough, due to the component's deformation, to continue the shearing mechanism. As a result, localized buckling occurred which caused a change in the propagation mode from shear to tensile. After further displacement, deformation of the part again changed the loading orientation which changed the propagation mode back to the more energetically favorable shearing mode. Also, the stresses were now sufficient at this point to cause additional delaminations to initiate and propagate in the knee region. This continued until the crack reached the gripped region which was clamped and restricted further crack propagation.

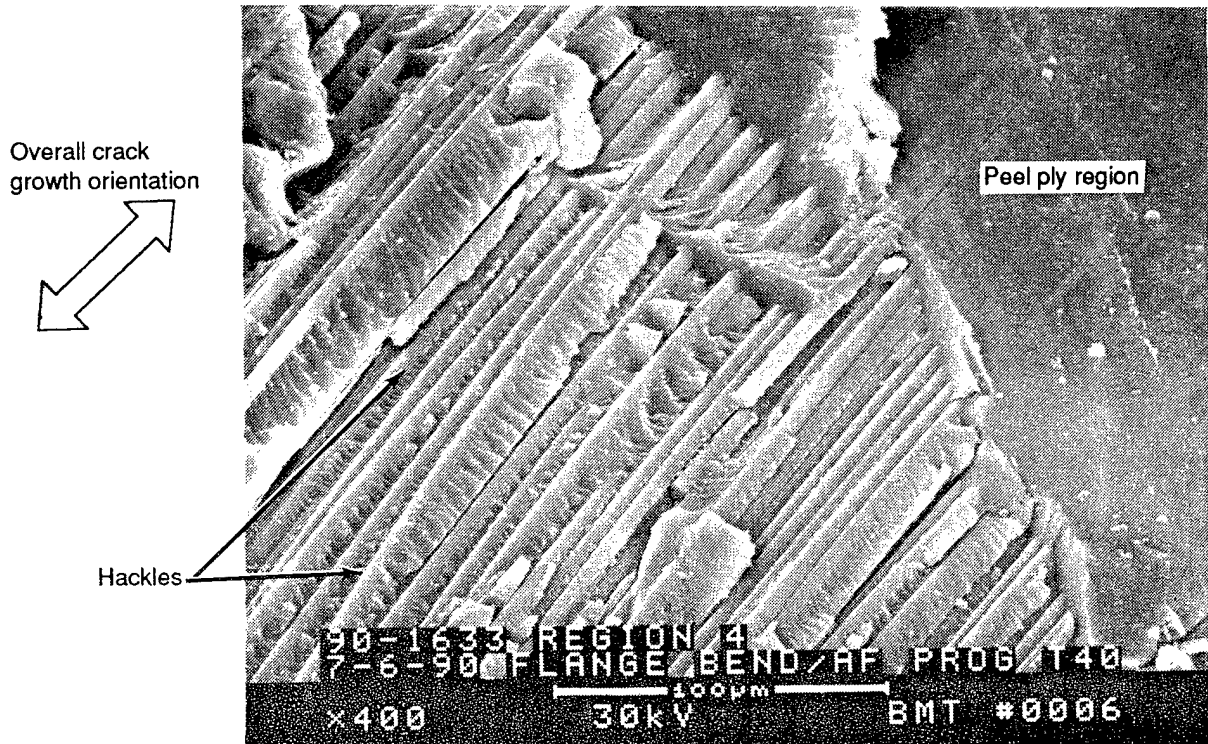


Figure 14. SEM Micrograph of a Mode II-Type (Shear) Fracture Surface in Region 4 Adjacent to the Peel Ply



Figure 15. SEM Micrograph of a Mode I-Type (Tension) Fracture Surface in Region 2

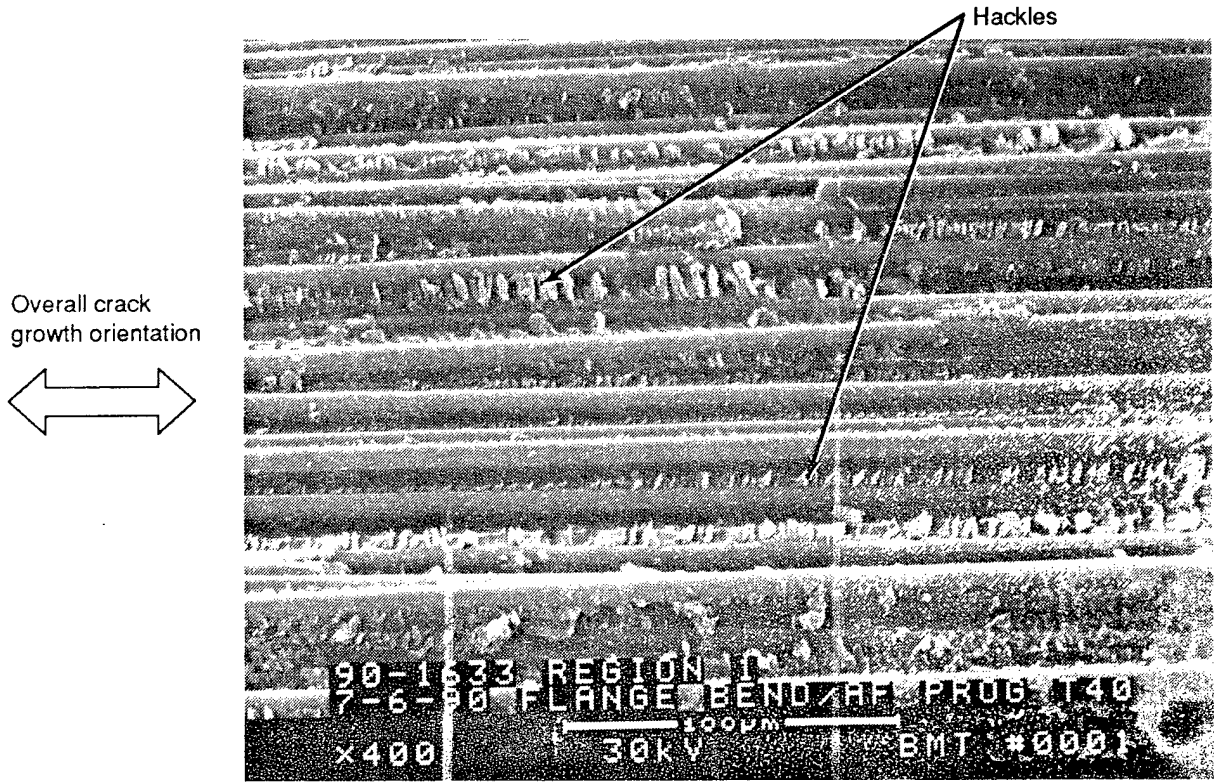


Figure 16. SEM Micrograph of a Mode II-Type (Shear) Fracture Surface in Region 1

3. CONCLUSIONS

- a. Nondestructive evaluation revealed that delaminations were present throughout the component with a major delamination emanating from the knee of the component in the center.
- b. Based on the infrared analysis, the material is a 350°F cure epoxy/graphite fiber composite which is similar to the Hercules 3501-6 resin. A Teflon peel ply was observed at the knee region extending approximately 1 inch into both flanges.
- c. TMA identified some undercured regions in the component. It could not be determined whether this contributed to fracture initiation.
- d. The fracture surface exhibited different modes of crack propagation initiating from the peel ply.
- e. Because the actual testing configuration was not given, a scenario was developed to explain the fracture sequence. The component was gripped at both edges and then pulled apart. This caused a crack to initiate primarily in the center adjacent to the peel ply and propagate by a shearing mechanism (mode II). In some regions, changing stress conditions and material constraints caused the crack propagation mode to change to a mode I (tensile) and back to mode II.

**APPENDIX B**  
**METAL CORE HONEYCOMB SANDWICH**

## ABSTRACT

As a requirement for the composite Failure Analysis Handbook contract, two small-scale components were fabricated, mechanically tested and submitted to Boeing for failure analysis. The purpose of this analysis was to demonstrate and evaluate the procedures in the handbook on a failed part.

This analysis was performed on a small rectangular metal honeycomb sandwich panel with carbon fiber reinforced plastic facesheets. This represents the second part of the two small scale components. For this analysis, a simplified version of the Fracture Analysis Logic Network (FALN) was used.

Following the steps of the FALN, the part was initially examined by non-destructive methods which revealed damage throughout the panel, including damage to the honeycomb core and a major delaminated region was located in the middle of one of the panel orientated across the transverse direction. There were no failures between the cell walls and the adhesive material.

Material analysis of the panel identified; the face sheets were CFRP similar to the 3501-6/IM6 material, the honeycomb was a 5000 series aluminum alloy, and the adhesive was an epoxy with additional compounds. A microstructural examination of the face sheets revealed porosity uniformly distributed throughout the matrix.

Based on the information obtained in the examination, the most probable explanation which would account for the damage would have been a simple longitudinal compressive loading. In addition, because no evidence of prior damage was found, it was assumed that all of the damage was a result of this compressive loading.

## TABLE OF CONTENTS

Section	Page
1.0 INTRODUCTION .....	4
2.0 TECHNICAL.....	4
2.1 Background and History .....	4
2.2 Non-Destructive Evaluation .....	6
2.3 Materials Characterization.....	12
2.4 Destructive Examination .....	16
2.5 Fractography .....	22
2.6 Discussion.....	22
3.0 CONCLUSIONS .....	23

## LIST OF FIGURES

Figure	Page
1 Diagram Showing the Simplified Fracture Analysis Logic Network.....	5
2 Photographs Showing the Top and Bottom Surfaces of the As-Received Component.....	7
3 Photographs Showing the Front, Back and Sides of the Component.....	8
4 Buckled Surface Showing the Angled Slit Lighting Contours.....	9
5 Smooth Surface Showing the Angled Slit Lighting Contours.....	10
6 The Vertical Displacement is Equal to 0.39X of the Horizontal Displacement of the Slit Image. Horizontal Displacement of the Slit Image as a Function of Length.....	11
7 Diagram Showing the Approximate Locations Where the Honeycomb Panel was Scanned by the CT System.....	11
8 CT Images of the Transverse Scan Through the Delaminated Zone.....	13
9 CT Images of the First Longitudinal Scan.....	14
10 CT Images of the Second Longitudinal Scan.....	15
11 CT Image of the Third Longitudinal Scan.....	15
12 FTIR Plots of the, (a) Resin From the Honeycomb Panel, and (b) From a Data File of Hercules 3501-6.....	17
13 DSC Plots of the (a) Composite and (b) the Adhesive.....	18
14 EDS Spectrum Showing the Major Elements That Have Been Detected and a Semi-quantitative Analysis of the Material.....	19
15 Cross-Sectional Micrograph of the CFRP Face Sheets Showing the Extent of Porosity and the Lay-Up Sequence.....	20
16 Photographs of Cross Sections Through the Panel Corresponding to the CT Scans: (a) CT Slice 3 (b) CT Slice 2 (c) CT Slice 1.....	21
17 Diagram Showing the Probable Loading Configuration and Subsequent Deformation of the Panel.....	23



## **1.0 INTRODUCTION**

This report is a Technical Operating Report (TOR) describing the failure analysis of a honeycomb sandwich component provided to Boeing by the Air Force. As a requirement for the Composite Failure Analysis Handbook contract, two small-scale and one large-scale components were fabricated, mechanically tested and submitted to Boeing for failure analysis. This work was conducted under the Add-on contract to the F33615-86-5071 contract. The overall contract program objective is to create a handbook containing the procedures, techniques, and data necessary to conduct failure analysis of fiber reinforced composite structures. In addition, the handbook will include case histories demonstrating the use of these techniques and procedures.

As part of this demonstration, certain aspects of the design, fabrication, and testing of the component were withheld from this investigation. The primary reason for this was to provide a number of unknown factors which will allow for a more realistic analysis of a component that has failed. In addition, by comparing the failure analysis results and conclusion with the known parameters, an evaluation of the procedures and technique utilized in the investigation could be made. Since the part was considered a "small-scale" component, only the simplified fracture analysis logic network (FALN) was utilized (Figure 1). This network illustrates the most effective sequence of steps to perform a complete and thorough analysis.

## **2.0 TECHNICAL**

### **2.1 BACKGROUND AND HISTORY**

As explained above, various aspects of the fabrication and testing of the components were withheld from the investigator. As a consequence there is essentially no background or history available for this analysis.

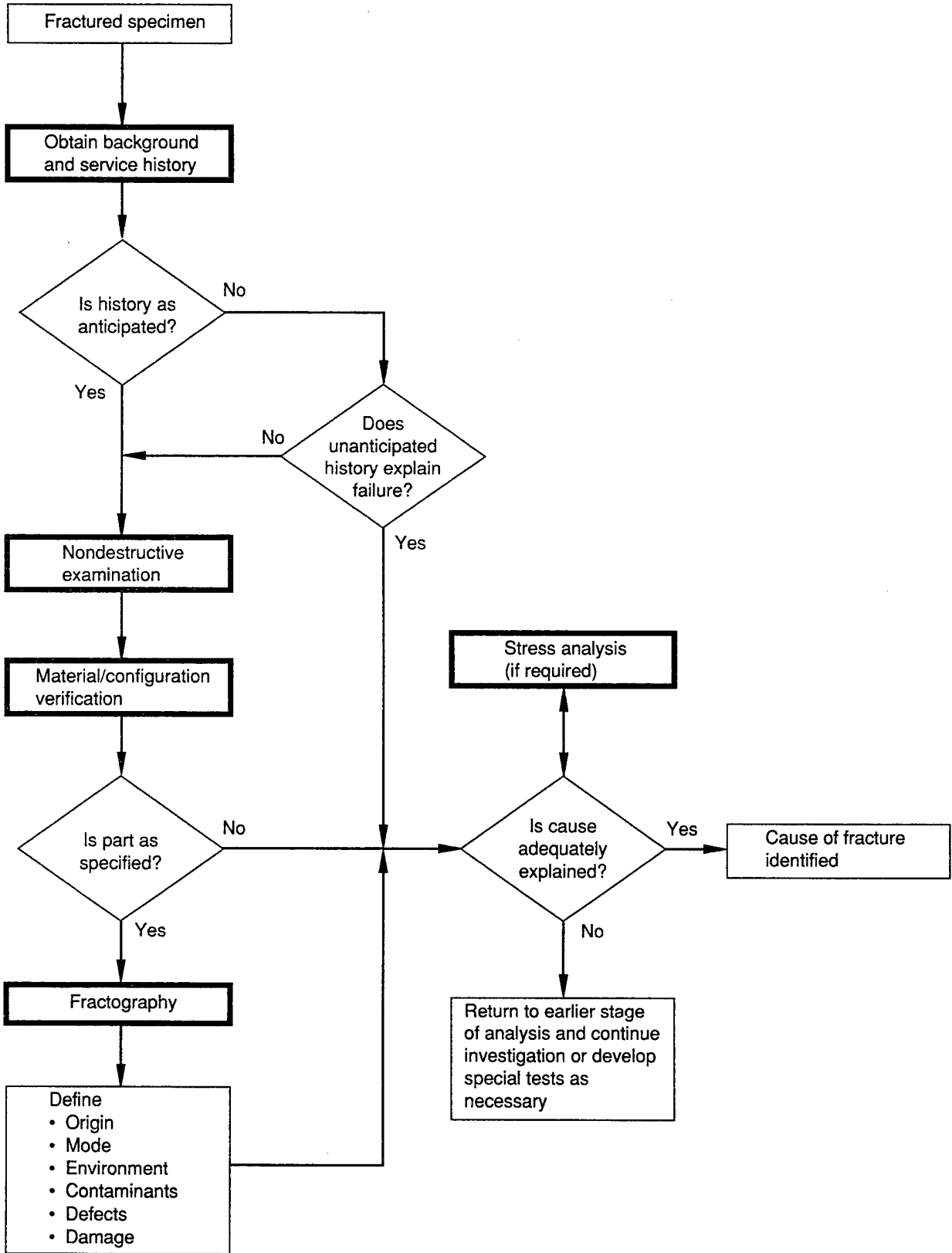


Figure 1. Diagram Showing the Simplified Fracture Analysis Logic Network

## **2.2 NON-DESTRUCTIVE EVALUATION / EXAMINATION (NDE)**

### **Optical Examination**

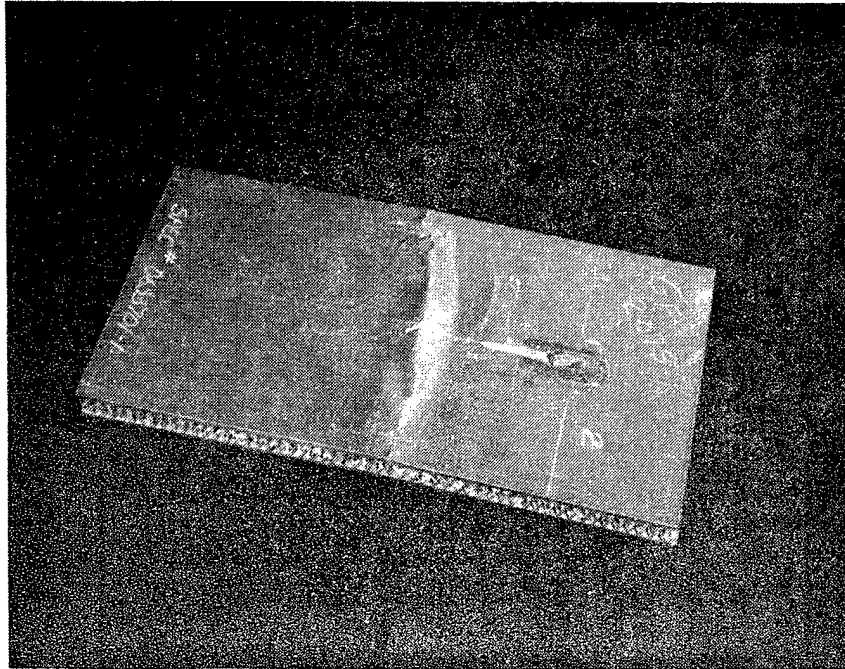
The component was a rectangle metal honeycomb sandwich panel with carbon fiber composite face sheets. It was approximately 0.6 inch thick, measuring 9.0 inches by 6.0 inches (see Figures 2 & 3). The top surface contained a transverse bulge located in the middle of the panel approximately 1 inch wide. The bottom surface was generally warped. Examination of the honeycomb core along the edges revealed that all of the honeycomb core was damaged (see Figure 3). However, no honeycomb/adhesive failures were observed, only the cell walls were deformed with the bonds to the facesheets being intact.

### **Slit Illumination Photography**

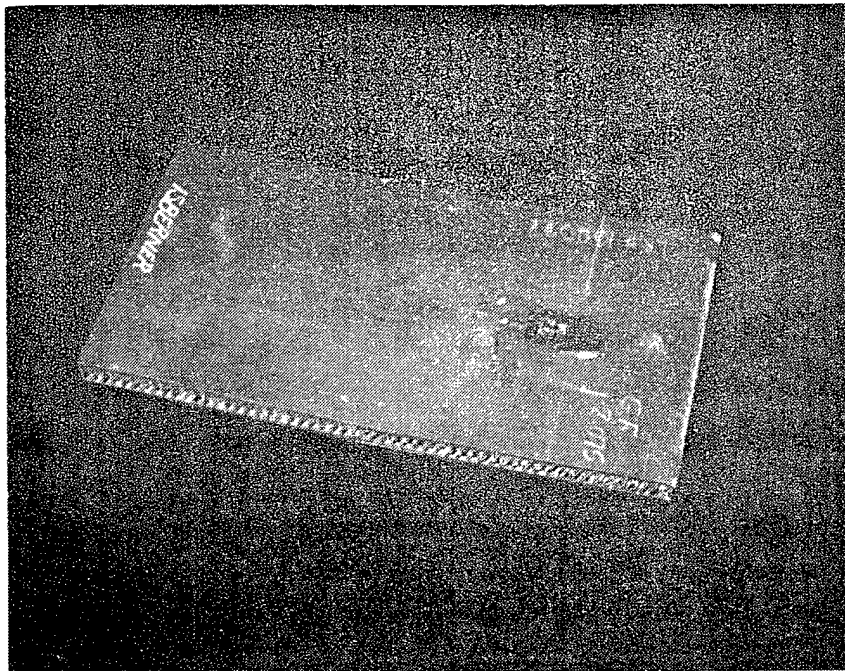
Following the visual examination, the surface of the component was analyzed using slit illumination photography. This technique involves photographing a series of beams of light projected at an angle onto the panel (Figures 4 & 5). Variations in the surface are seen as curvatures of the slit of light which have been calibrated to correspond to the variations in depth and height of the surface. This allows for quantitative documentation of the surface deformation as shown in Figure 6. Examination of the data reveals that the entire back side of the panel was warped. This is shown as both in a twisting and buckling type of deformation. It also indicates that no region of the panel was undamaged.

### **Computed Tomography**

Because the structure of the honeycomb core does not lend itself very well to a number of commonly used NDE techniques, the component was examined using Computed Tomography. This technique involves the use of multiple x-ray images of the specimen which are then mathematically reconstructed to produce a 3-D image. This allows for the examination of "slices" of the internal structure at various angles and depths. The CT system employed for this analysis was the Boeing ACTIS system using a 2mm beam thickness. Figure 7 illustrates the approximate locations of these scans.



(a) Top

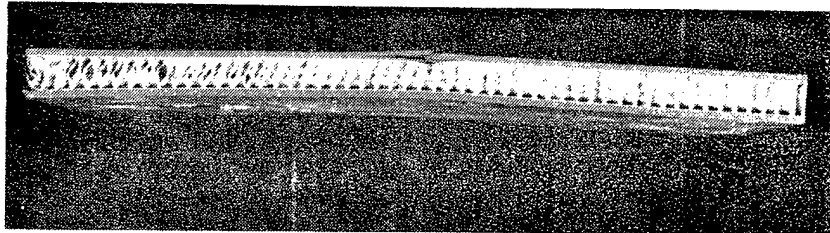


(b) Bottom

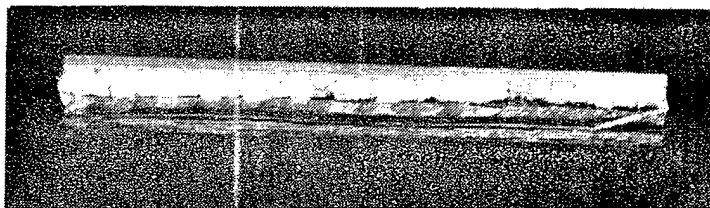
Figure 2. Photographs Showing the Top and Bottom Surfaces of the As-Received Component



(c) Left side



(d) Right side

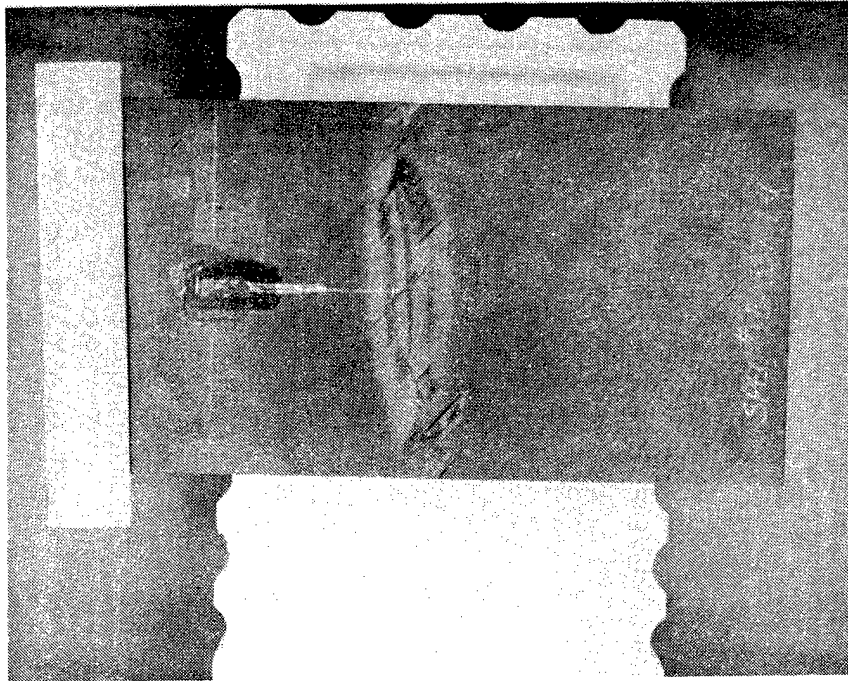


(a) Front

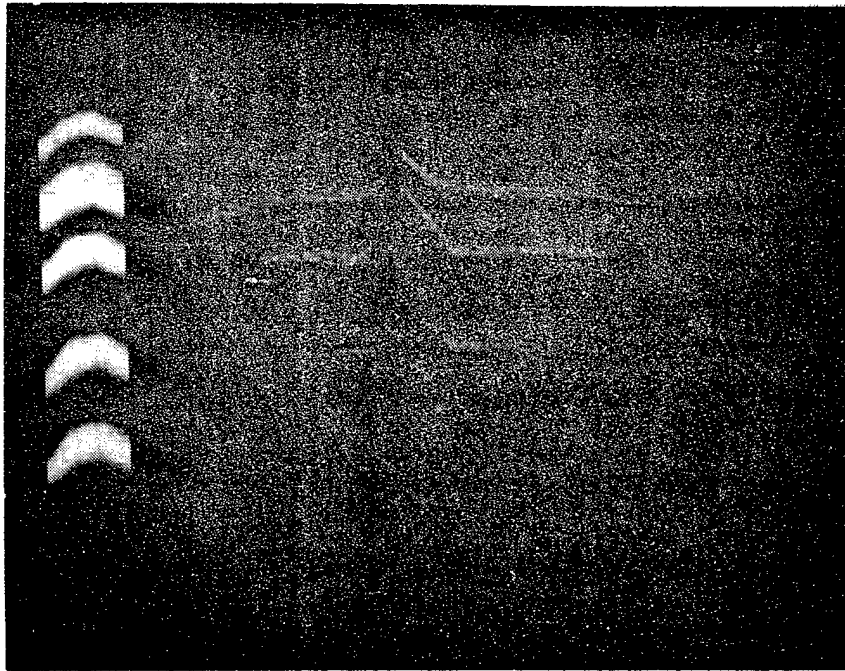


(b) Back

Figure 3. Photographs Showing the Front, Back and Sides of the Component

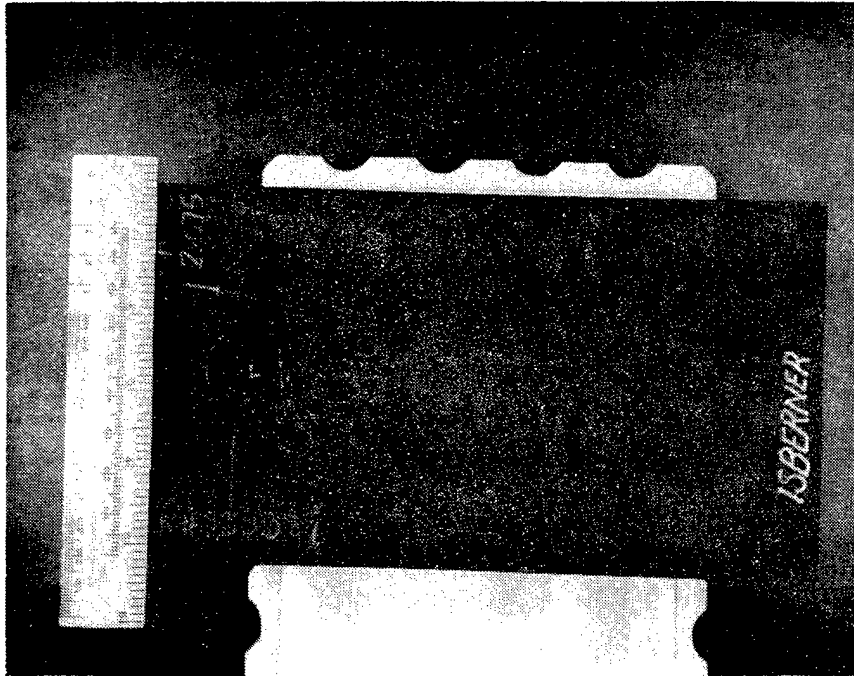


(a)

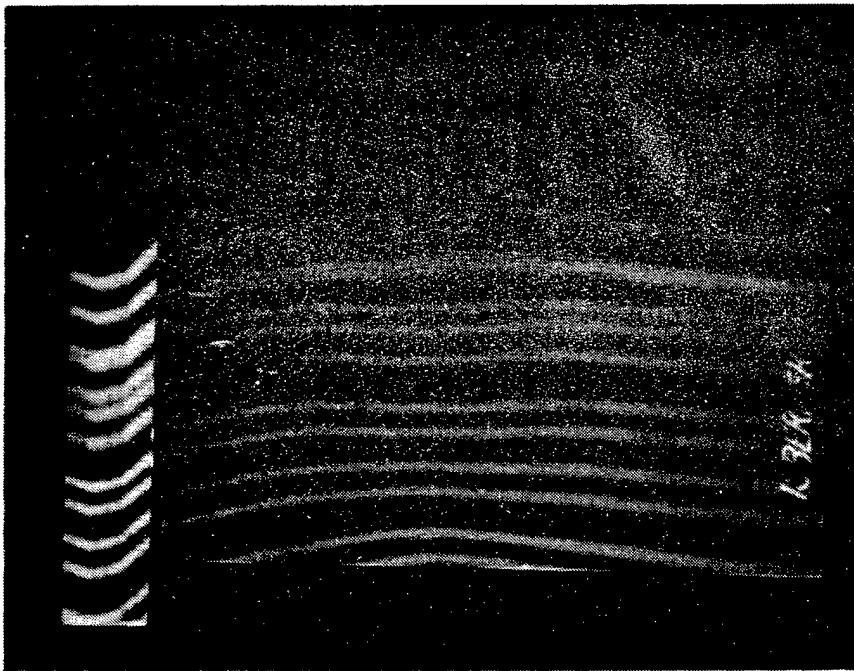


(b)

*Figure 4. Buckled Surface Showing the Angled Slit Lighting Contours*



(a)



(b)

*Figure 5. Smooth Surface Showing the Angled Slit Lighting Contours*

Horizontal displacement of lines 1 through 11 in millimeters at intervals of one inch along the length of the panel

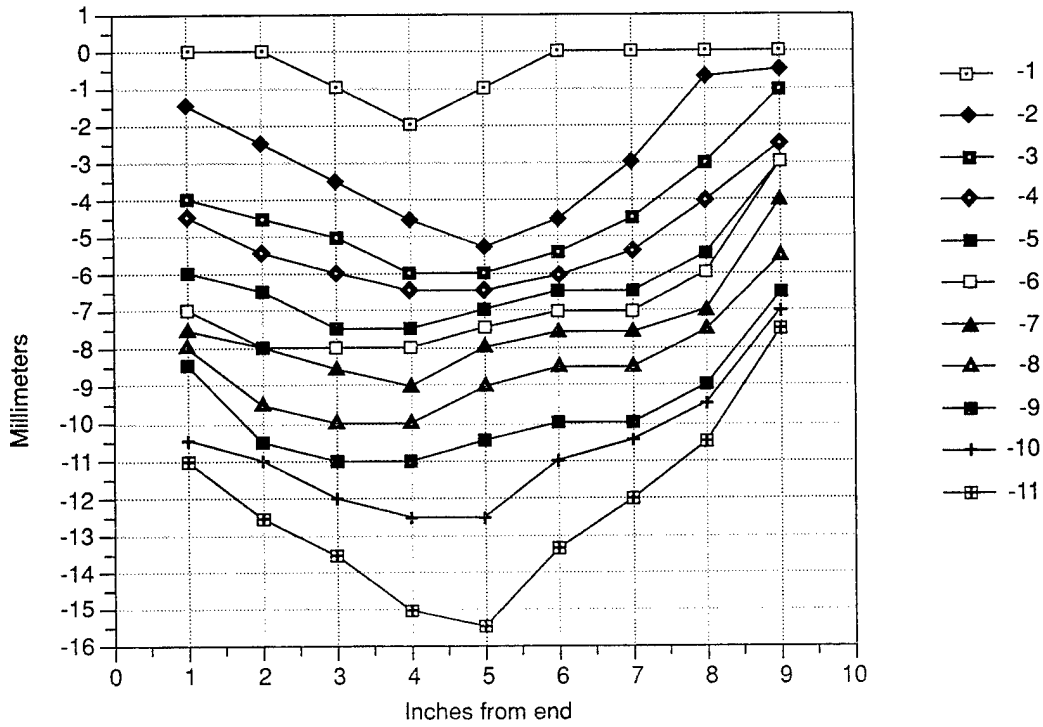


Figure 6. The Vertical Displacement is Equal to 0.39X of the Horizontal Displacement of the Slit image. Horizontal Displacement of the Slit Image as a Function of Length.

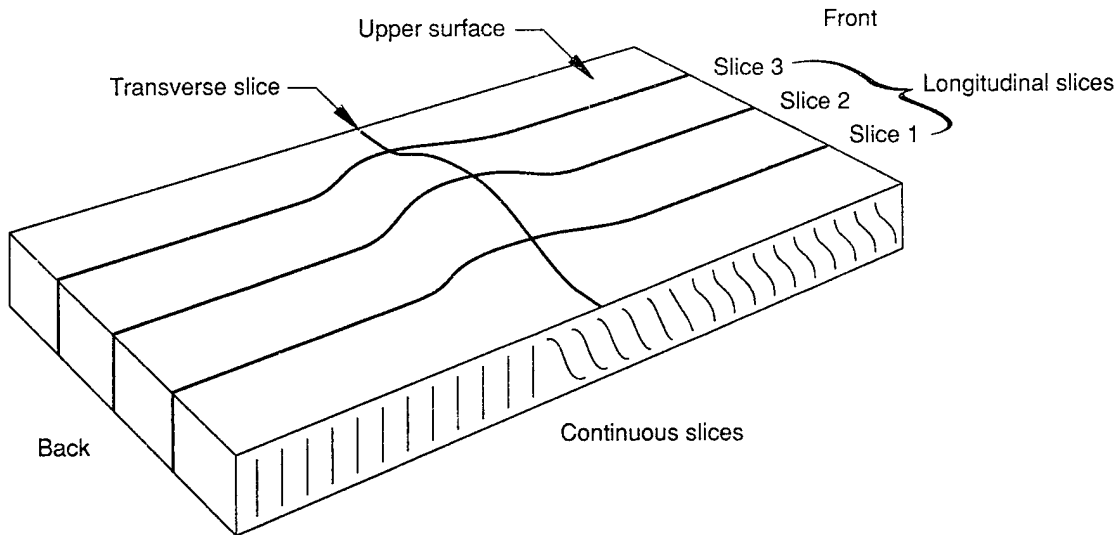


Figure 7. Diagram Showing the Approximate Locations Where the Honeycomb Panel was Scanned by the CT System



Figures 8 through 11 through show the various images of the slices through the component. The longitudinal slices 1, 2, & 3 show the damage present in the honeycomb regions in the center of the component. The front half of the panel appears to have been crushed by a macroscopic shearing of the upper front half of the facesheet. The back half exhibited little if no damage. However near the bulge, the core appeared to be crushed in the short transverse direction. There was no evidence showing any longitudinal buckling trends to either end (from one end to the other). This transverse damage was located all along the back half of the component.

In addition, there was no evidence indicating that any honeycomb/adhesive failures occurred. All of the fractures in the core were located in the middle of the cell walls. This result is similar to the optical examination on the exposed edges of the panel.

### **Through Transmission Ultrasound Analysis**

Because there was a major delamination in the center of the part, no TTU analysis was performed. The damaged regions would have allowed excessive water to enter the honeycomb cell causing false indications of voids and delaminations. Pulse Echo was not performed for similar reasons.

## **2.3 MATERIALS CHARACTERIZATION**

### **Chemical Analysis**

A sample of the panel was removed and submitted for chemical analysis. The facesheet and the adhesive materials were examined using an Infra-red Fourier Transform instrument for chemical identification. Determination of the honeycomb core of the material was done by Energy Dispersive Spectroscopy (EDS) in a microprobe instrument. A Differential Scanning Calorimetry (DSC) instrument was used to determine the glass transition temperature ( $T_g$ ) and moisture content.

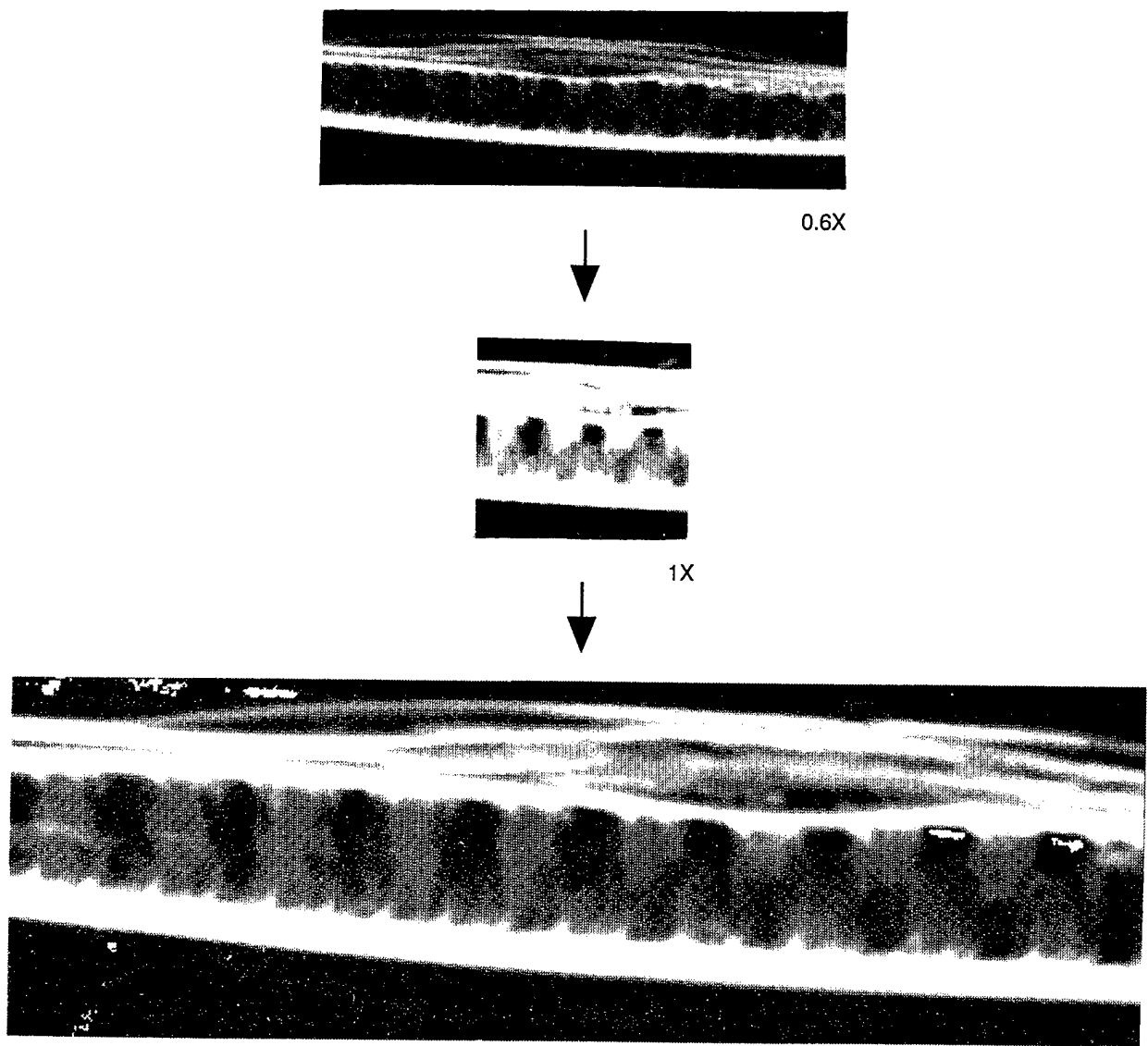


Figure 8. CT Images of the Transverse Scan Through the Delaminated Zone

1.5X

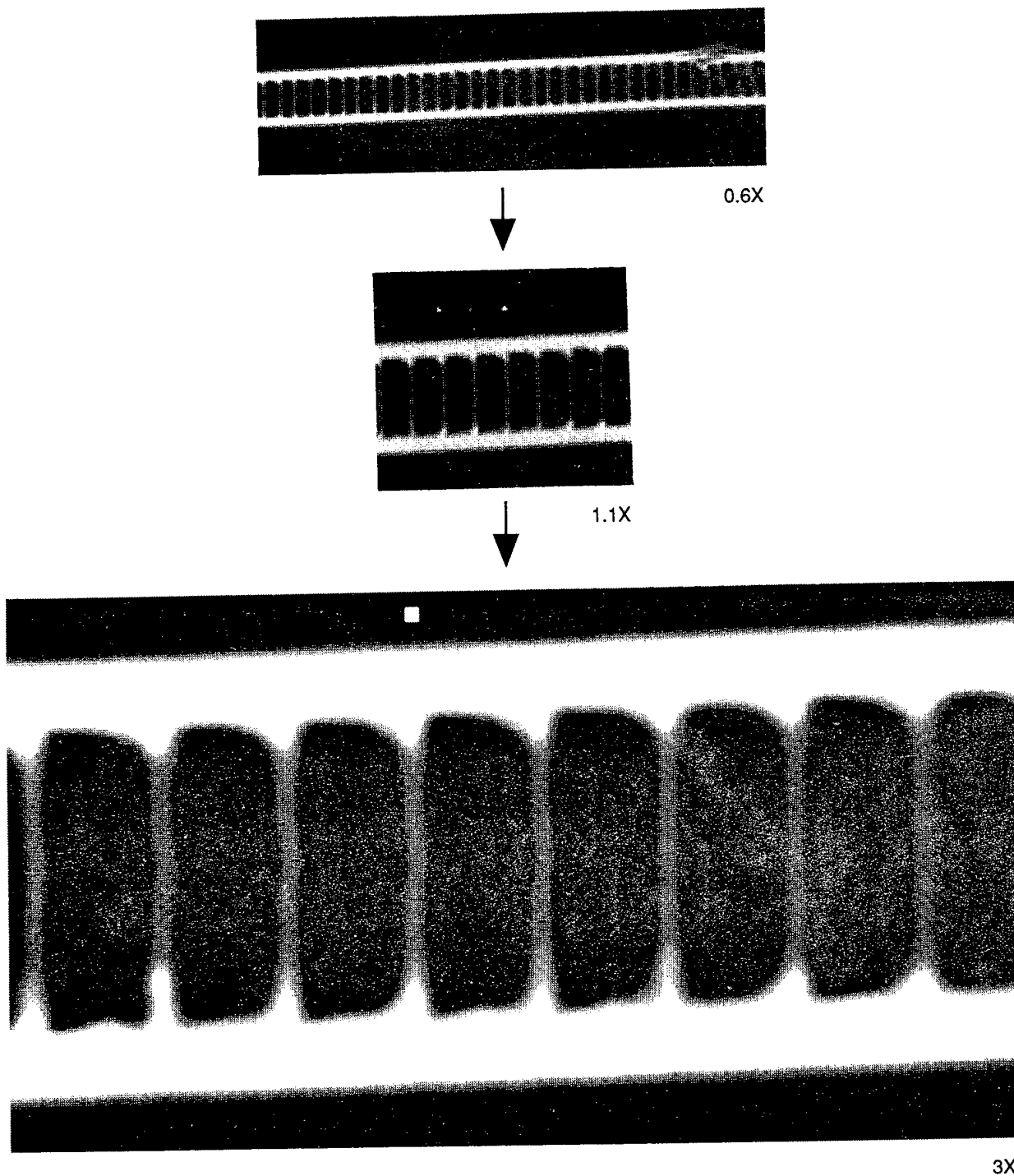
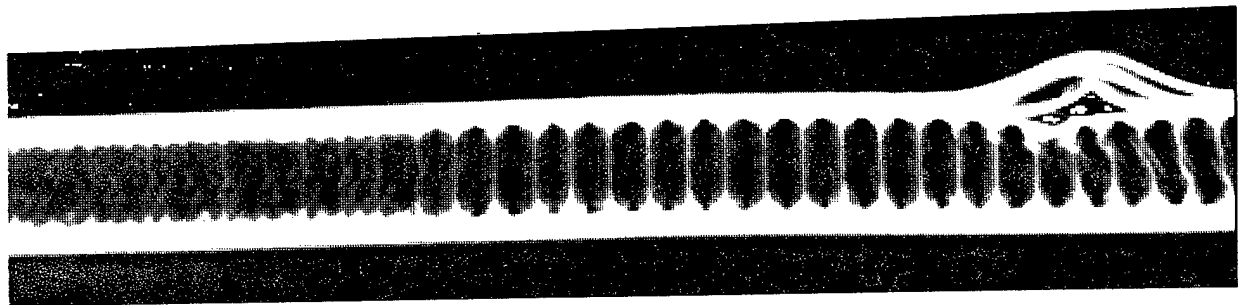
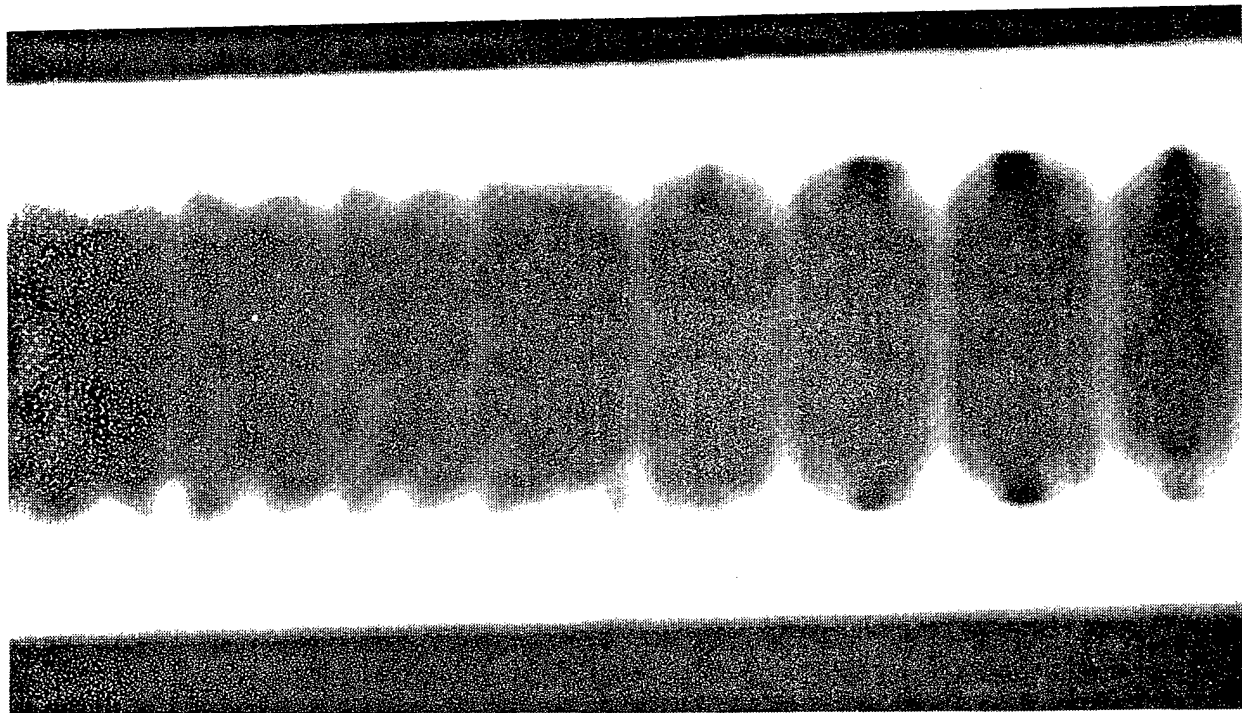


Figure 9. CT Images of the First Longitudinal Scan

3X

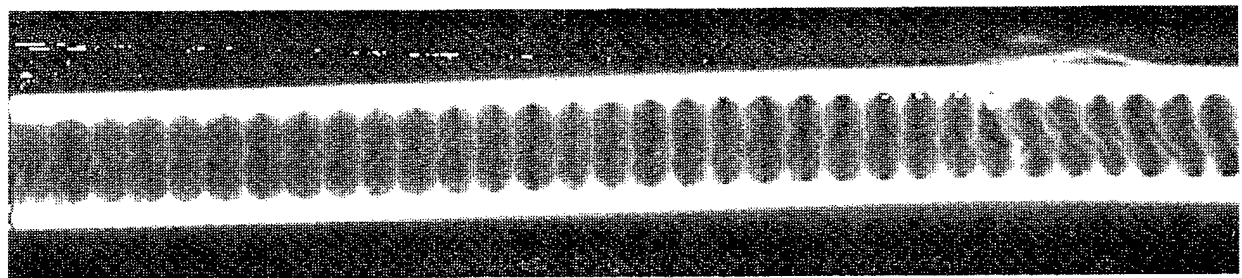


1.2X



4.8X

*Figure 10. CT Images of the Second Longitudinal Scan*



1.2X

*Figure 11. CT Image of the Third Longitudinal Scan*

The following are the results of the analysis:

- **Facesheets**

The facesheets were composed of carbon fibers in a 350° F cure epoxy resin system similar to the Hercules 3501-6 resin (see Figure 12 ). DSC analysis of the resin system revealed that the resin was fully cured (as shown in Figure 13a).

- **Adhesive**

The adhesive was identified as an epoxy with additional compounds (Figure 13b). DSC plots revealed an endotherm peak which was determined to be the result of melting. Further analysis indicated that the adhesive was fully cured.

- **Honeycomb**

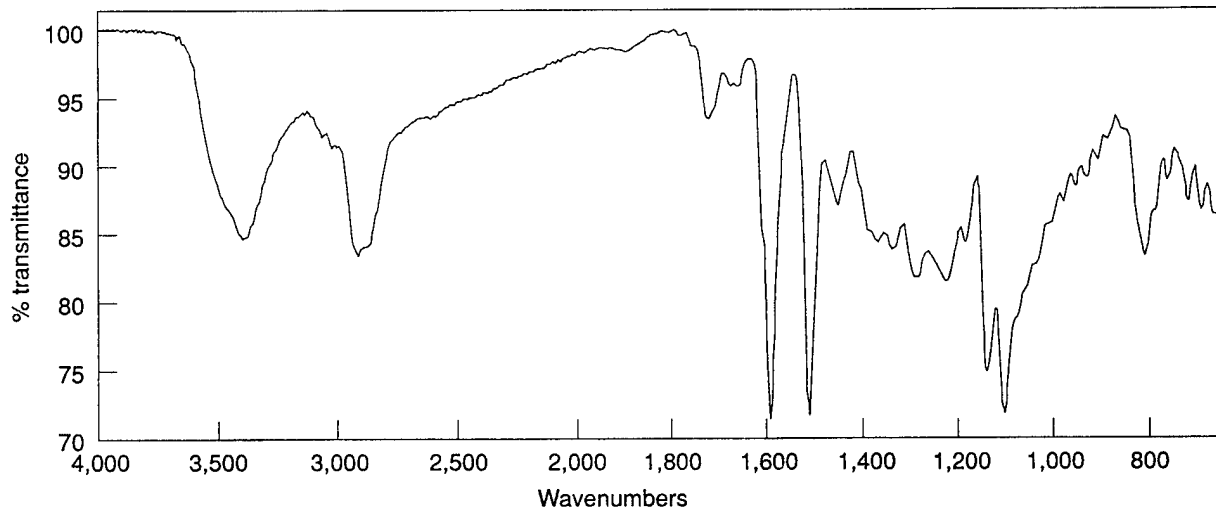
The honeycomb core was composed of a 5000 series aluminum as determined by the EDS analysis (Figure 14). Although aluminum honeycomb cores are usually made from 5000 type alloys, the EDS instrument is not accurate enough to identify the specific alloy in this series.

## **Microstructural Analysis**

A small section of the panel was cut, mounted, ground and polished. The facesheet ply orientation sequence was:  $[(+45/90/0/-45)2]_s$ . Major voids were observed throughout the facesheet (see Figure 15). This could be the result of incorrect processing of the composite material prior to assembly of the entire component because the adhesive bond appeared to have been processed correctly.

## **2.4 DESTRUCTIVE EXAMINATION**

The component was sectioned longitudinally along the same three locations as the CT scan slices to obtain a more detailed examination of the damage within the panel. Figure 16 shows the cross-section at the right edges of each section which correspond to the CT images in Figures 9 to 11. Examination of the surfaces reveal damage similar to the CT images.



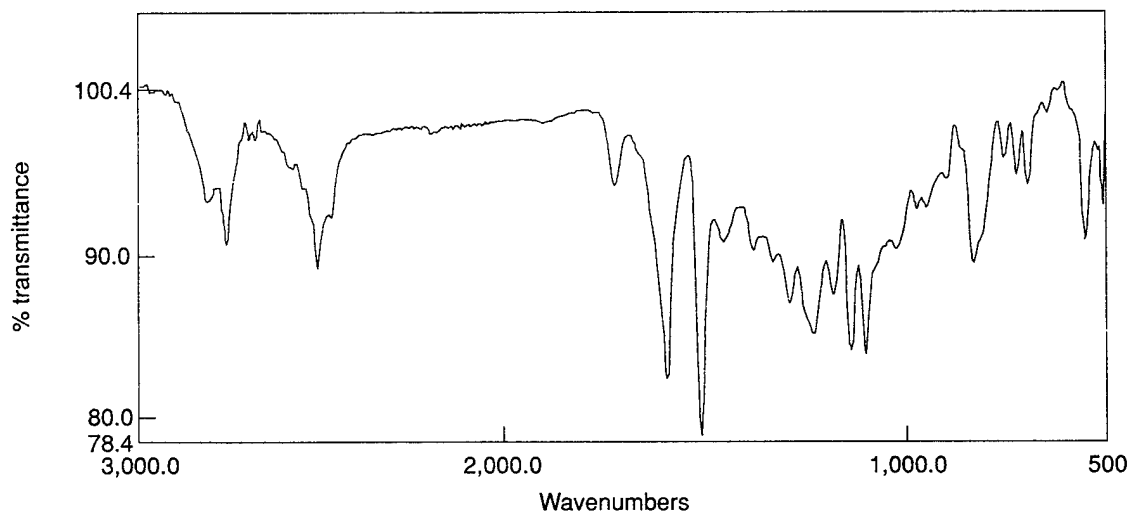
CPA-RESIN2;  
Resin from prepreg surface

Res = 8.0

Created = Thursday, Aug 6, 17:09:32 1992

Scans = 64

(a)



SAMP = SKFIRT35-1

Res = 8.0

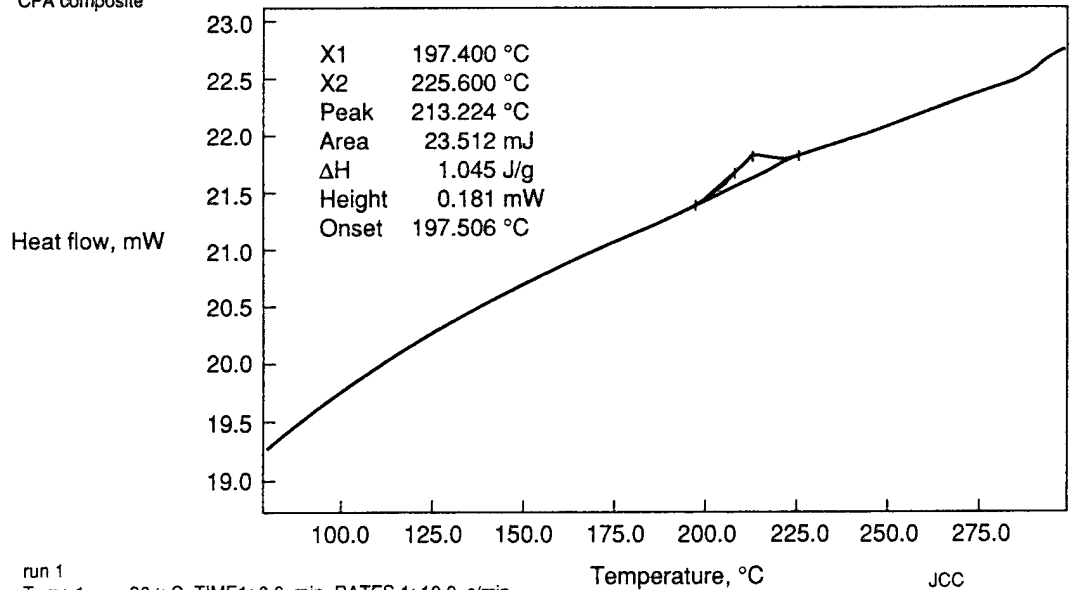
Scans = 64

(b)

Figure 12. FTIR Plots of the, (a) Resin From the Honeycomb Panel, and (b) From a Data File of Hercules 3501-6

Curve 1: DSC  
 File info: cfa1  
 Sample Weight: 11.970 mg  
 CFA composite

Tue Aug 18 16: 03: 18 1992



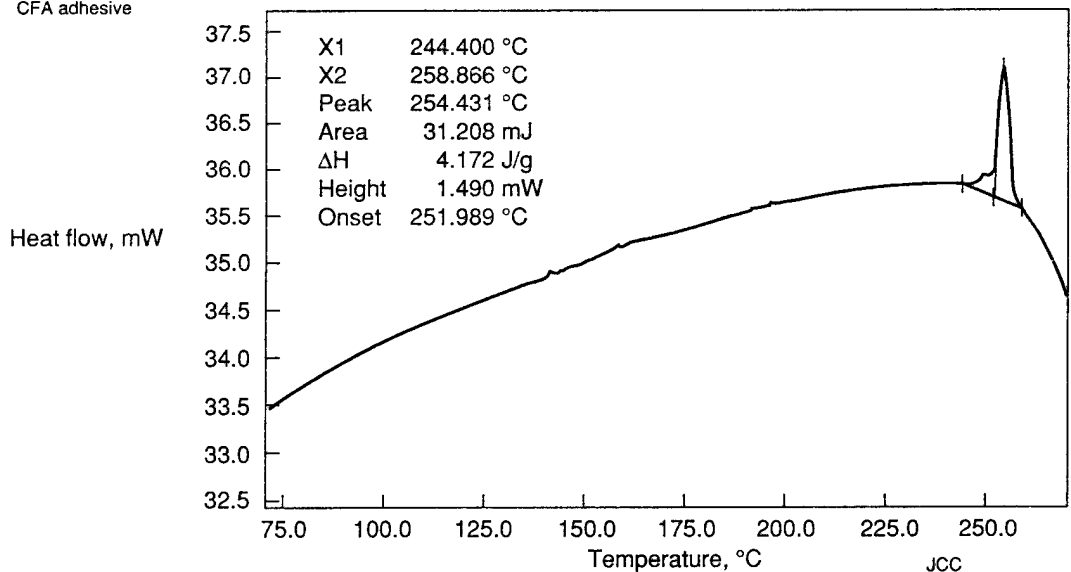
run 1  
 Temp 1: 30.0 C TIME1: 0.0 min RATES 1: 10.0 c/min  
 TEMP 2: 320.0 C

JCC  
 PEAKIN-ELMER  
 7 Series Thermal Analysis System  
 Tue Aug 18 16: 13: 58 1992

(a)

Curve 1: DSC  
 File info: adh3  
 Sample Weight: 7.480 mg  
 CFA adhesive

Wed Aug 19 17: 16: 39 1992

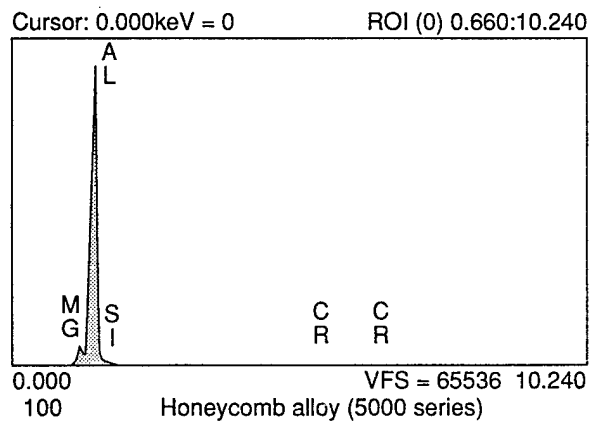


run 3, no ABO  
 Temp 1: 40.0 C TIME1: 0.0 min RATES 1: 10.0 c/min  
 TEMP 2: 275.0 C

JCC  
 PEAKIN-ELMER  
 7 Series Thermal Analysis System  
 Wed Aug 18 17: 17: 42 1992

(b)

Figure 13. DSC Plots of the (a) Composite and (b) the Adhesive

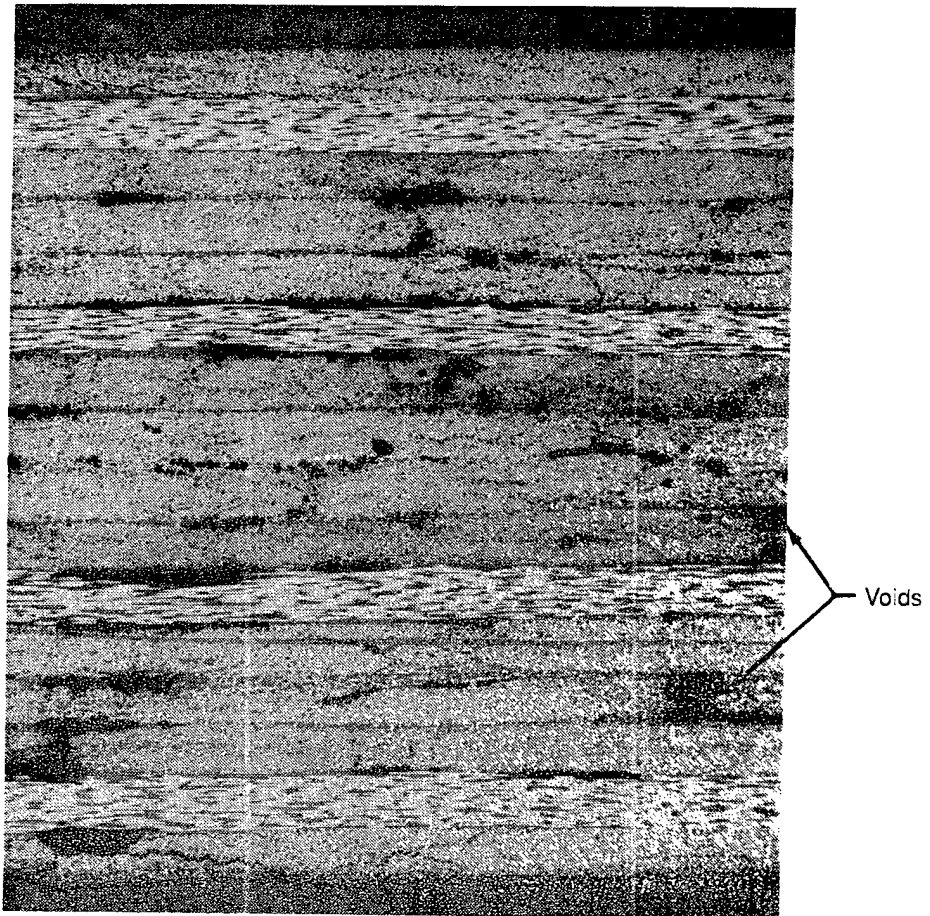


PRZ correction 20.00 kV 40.00 deg  
No. of iterations = 6

Element	K-ratio	Z	A	F	ZAF	Atom %	Wt%
Al-K	0.848	0.998	1.107	1.000	1.105	94.48	93.63
Mg-K	0.036	0.963	1.129	0.957	1.040	4.17	3.72
Si-K	0.000	0.975	2.929	1.000	2.856	0.00	0.00
Cu-K	0.001	1.186	1.001	1.000	1.187	0.04	0.10
Mn-K	0.001	1.156	1.020	1.000	1.179	0.06	0.13
Cr-K	0.018	1.131	1.032	1.000	1.167	1.09	2.07
Ni-K	0.000	1.127	1.004	0.999	1.131	0.02	0.05
Zn-K	0.001	1.188	0.999	1.000	1.187	0.06	0.15
Ti-K	0.001	1.122	1.073	0.997	1.201	0.08	0.13
						Total	100.00%

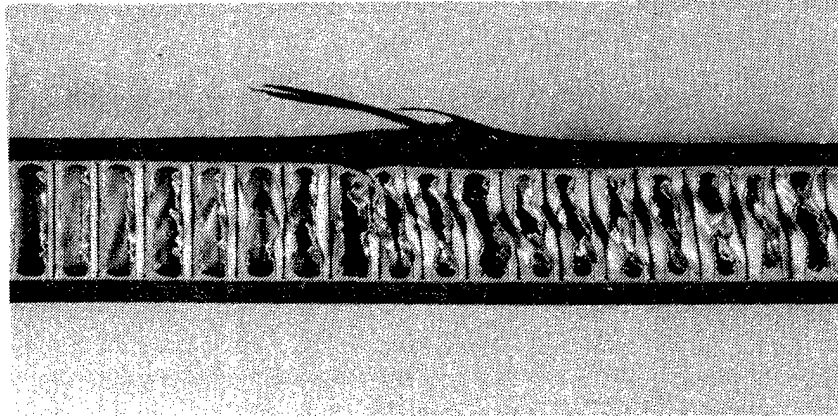
Figure 14. EDS Spectrum Showing the Major Elements That Have Been Detected and a Semi-quantitative Analysis of the Material



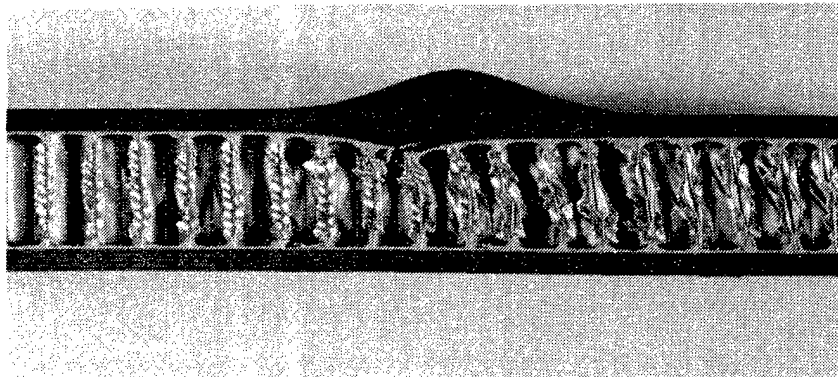


50x

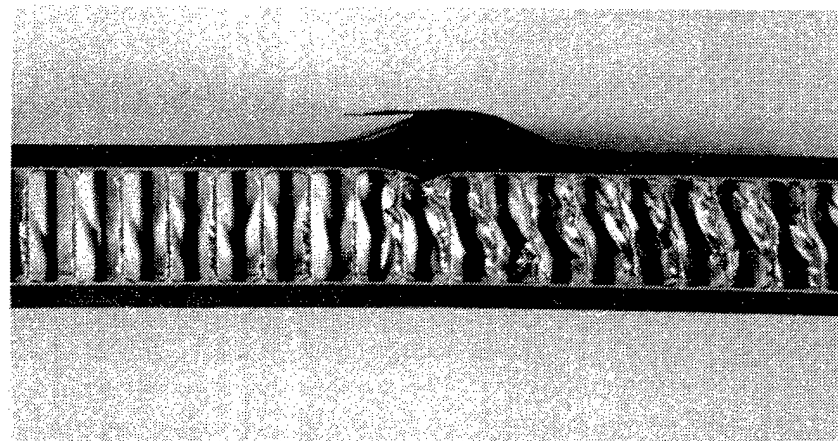
*Figure 15. Cross-Sectional Micrograph of the CFRP Face Sheets Showing the Extent of Porosity and the Lay-Up Sequence*



(a)



(b)



(c)

*Figure 16. Photographs of Cross Sections Through the Panel Corresponding to the CT Scans:  
(a) CT Slice 3  
(b) CT Slice 2  
(c) CT Slice 1*

## 2.5 FRACTOGRAPHY

Because the facesheets buckled in a uniform manner typical of a compression loading, no fractographic examination was done.

## 2.6 DISCUSSION

The transverse delamination region of the facesheets is indicative of compressive loading. There are two general ways in which the panel could have been loaded in order to cause a compressive loading; the first would be a three point loading configuration; the other would be a simple longitudinal compressive loading applied to the ends of the panel. If the component had been loaded in the three point loading configuration, the bottom side should exhibit tensile cracking and the honeycomb core on either side of the transverse delaminated region would not have been damaged or deformed. However, examination of the internal structure by both the CT scans and the sectioning revealed a non-uniform deformation. The longitudinal compressive loading configuration would most likely have produced this type of damage. Figure 17 shows a diagram of the panel illustrating a plausible loading sequence that could account for the damage to the panel. As the load was applied to both ends of the panel, the top facesheet began to delaminate and eventually buckle. Then the front half of the top facesheet shifted towards the back, deforming the honeycomb core in the process. This in turn caused the panel to bend with the back half of the panel remaining relatively straight while the front half twisted downward which resulted in the edge of the bottom facesheet being frayed. The downward twisting movement also deformed the bottom of the panel.

This description of the fracture sequence assumes that all of the damage to the panel was caused by the simple compressive loading. The porosity in the facesheets was the only anomaly discovered on the panel that wasn't the result of the loading. However these voids did not appear to have influenced the placement of the origins or crack propagation direction, they probably only effected the overall strength of the panel. If there was evidence of damage in the panel prior to the compression loading, it would have been destroyed by the subsequent loading.

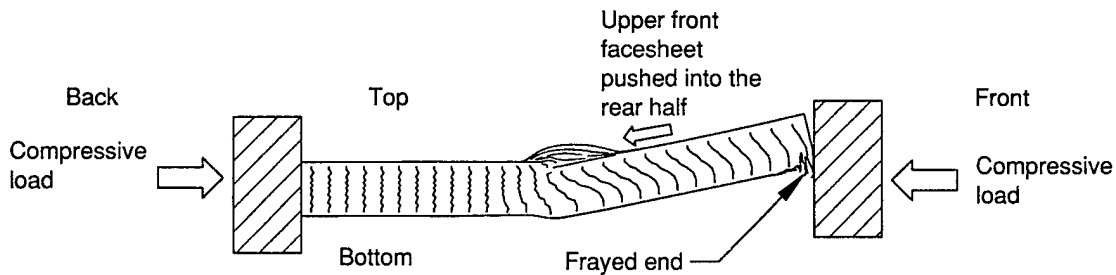


Figure 17. Diagram Showing the Probable Loading Configuration and Subsequent Deformation of the Panel

### 3.0 CONCLUSIONS

- a. Optical examination of the panel revealed a transverse delamination across the panel with the metal honeycomb deformed along the edges of the panel.
- b. Non-destructive and subsequent destructive evaluation of the panel revealed that the honeycomb core was deformed throughout the panel.
- c. Analysis of the materials identified the facesheets to be fabricated from a CFRP material similar to a 3501-6/IM6 system, the metal honeycomb core was a 5000 series aluminum alloy and the adhesive was a typical epoxy with additional compounds.
- d. There was a uniform distribution of voids or porosity throughout the CFRP face sheets.
- e. Damage to the honeycomb core was either deformation or fracturing. In both cases, the damage only occurred in the center of the cell walls and not at the core-adhesive region.
- f. Based on the information collected from the examination, the damage most likely occurred as a result of longitudinal compressive loading.
- g. Other than the porosity, no other anomalies were identified that could have caused premature failure or crack initiation.

**APPENDIX C**  
**GROB AIRCRAFT WING**

## TABLE OF CONTENTS

Section	Page
LIST OF FIGURES.....	3
1.0 INTRODUCTION.....	4
2.0 TECHNICAL .....	4
2.1 Background and History .....	4
2.2 Non-Destructive Evaluation.....	4
2.3 Materials Chacterization .....	7
2.4 Destructive Examination.....	11
2.5 Fractography .....	11
2.6 Discussion .....	19
3.0 CONCLUSIONS.....	19

## LIST OF FIGURES

Figure	Page
1 FALN Diagram .....	5
2 Photographs of the Outer Surfaces of the Wing Section .....	6
3 Photograph of the Inner Surfaces of the Wing Section .....	8
4 Photographs of the Pulse Echo Results.....	9
5 FTIR Plots of the Wing Section Specimen and the Rutapox .....	10
6 DSC Plots of the Non-Post-Cured Rutapox Sample .....	12
7 DSC Plots of the Wing Section Specimen .....	13
8 TMA Plots of the Non-Post-Cured Rutapox Sample .....	14
9 TMA Plots of the Wing Section Specimen .....	15
10 Cross Section through a Crack in the Upper Wing Skin .....	16
11 Cross Section through a Crack in the Upper Wing Skin .....	17
12 SEM Photographs of the Crack Surfaces .....	18
13 Diagram Showing the Probable Loading Configuration.....	20

## 1.0 INTRODUCTION

As part of the Composite Failure Analysis Handbook Contract (5071) a full scale test article was fractured and submitted for failure analysis. The purpose of this effort is to demonstrate and evaluate the effectiveness of the Failure Analysis Logic Network (FALN) outlined in the Composite Failure Analysis Handbook (Figure 1). In addition, to more effectively evaluate this analysis tool, some of the facts pertaining to the actual test parameters and component configurations were withheld from the investigator. This provided a more realistic situation for the investigator to apply the FALN to this analysis. After the failure analysis, the results will be compared to the actual test parameters. From this comparison, the FALN can be modified if necessary.

## 2.0 TECHNICAL

### 2.1 BACKGROUND AND HISTORY

The test article was a small wing section manufactured by Grob Industries, Germany. The section was composed of an upper and a lower skin joined together by a leading edge cap and two spars (Figure 2). The wing section was 8.5 inches thick with a 42 inch cord. This test article is a 16 inch wide and appears have been cut from a larger wing specimen because of machine cuts on both ends.

### 2.2 NON-DESTRUCTIVE EVALUATION / EXAMINATION (NDE)

**Outer Wing Surface** - The upper wing skin was composed of a paper honeycomb core with layers of fiberglass plies on both sides. White Gelcoat was present on the outer surfaces. The upper skin contained two long cracks and one small crack. One long crack extended approximately three quarters of the way from the leading edge towards the aft. The other long crack was located between the mid spar and the aft spar. The small crack was located on the edge of the wing section near the middle of the wing section. In addition to the cracks; a large section of the surface, located adjacent to one edge and between the leading edge and the mid spar, had been sanded through the gelcoat.

The lower skin, fabricated identically to the upper skin, contained five regions which appeared to be in various stages of repair. Two of the regions (one ~5.5 and the other ~3.0 inch square) were located in the main section of the lower skin. Both contained exposed honeycomb and white potting compound along the perimeter of the exposed regions. In addition, the surfaces adjacent to these two regions were sanded. Another region (~2.0 inch square) simply had the honeycomb removed down to the inner surface skin. Finally, two sanded regions were located on the edge of the lower skin, one at the spar cap and the other aft of the mid-spar. Both of these regions were approximately 2 inch square and had also been sanded through the Gelcoat.



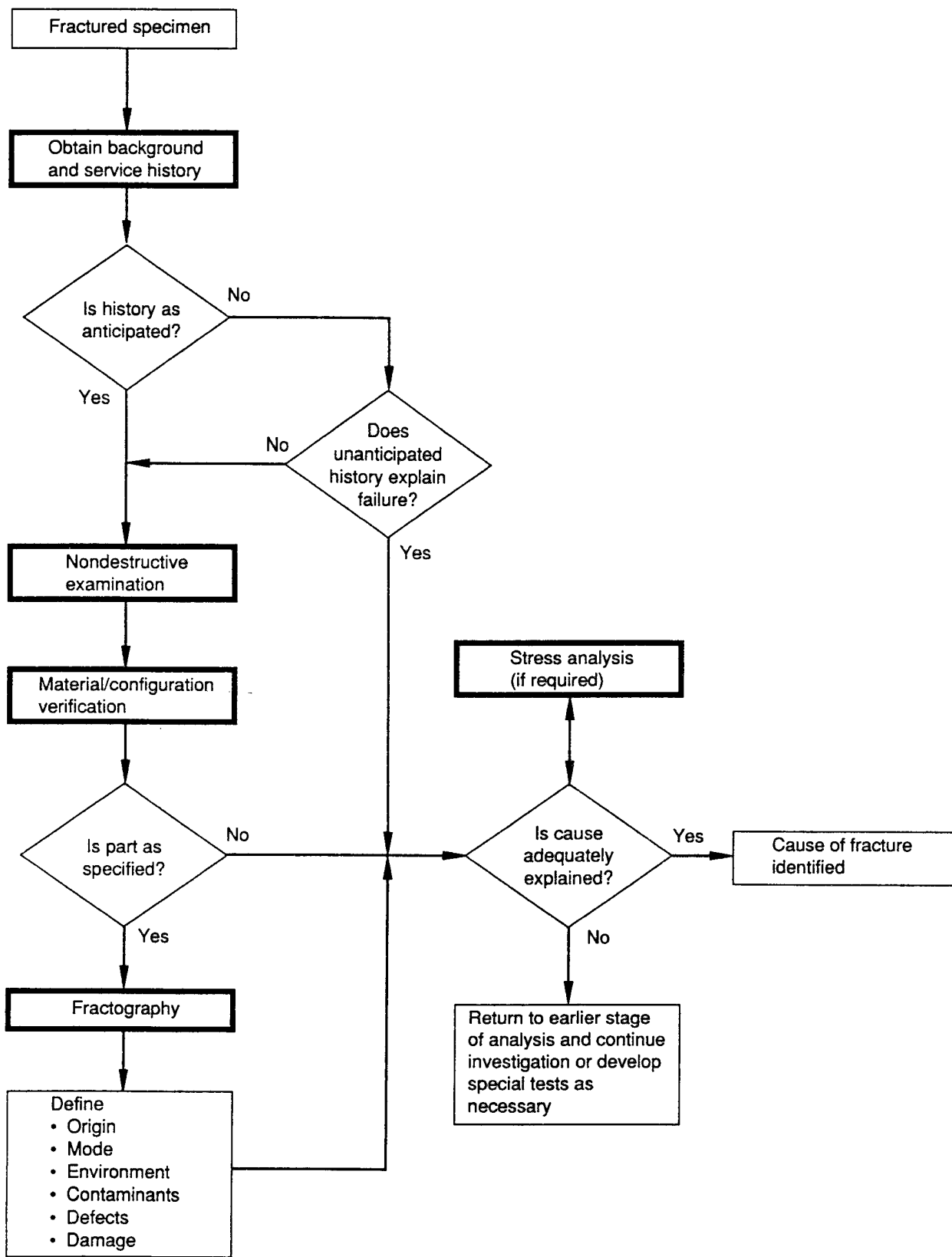
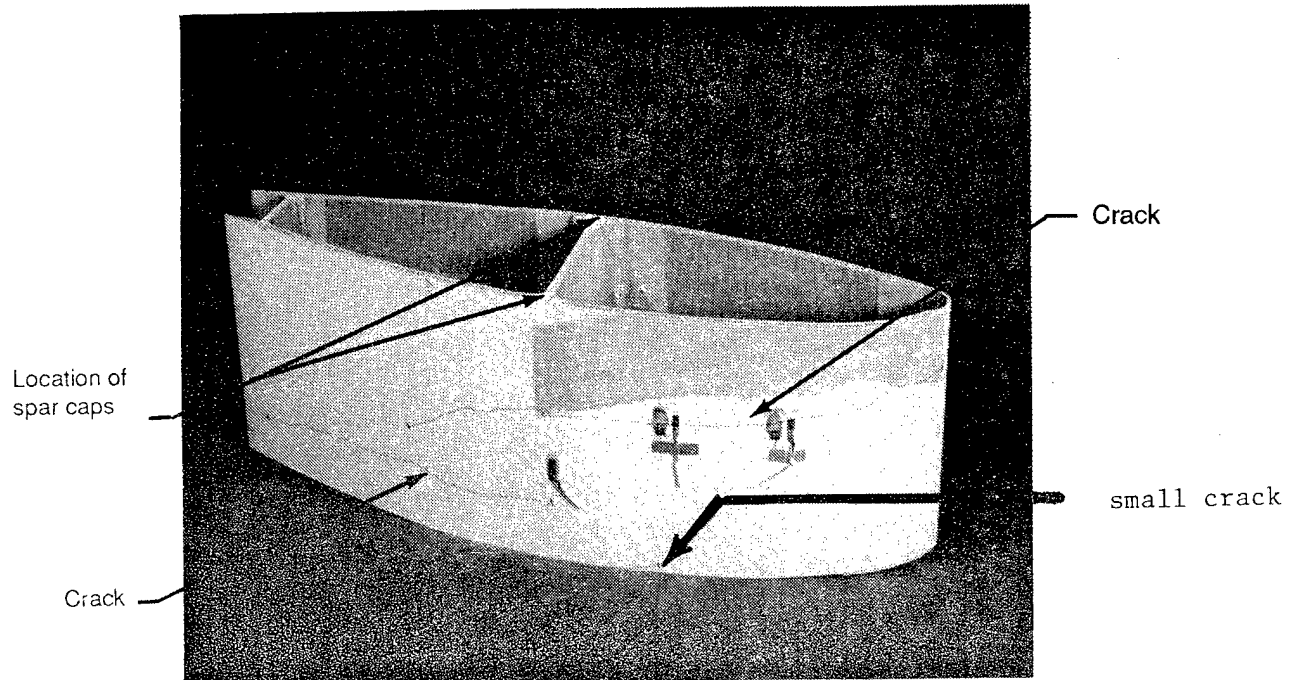
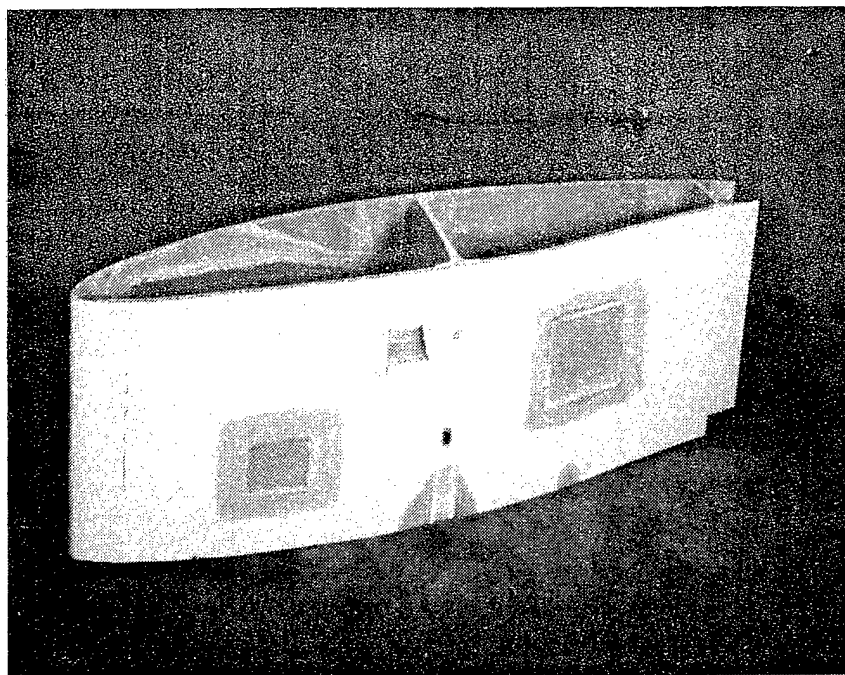


Figure 1. Diagram Showing the Simplified Fracture Analysis Logic Network



(a)



(b)

Figure 2. Photographs of the Outer Surfaces of the Wing Section  
a) Upper Surface  
b) Lower Surface

**Inner Wing Surfaces** - Since no Gelcoat was present on these surfaces, the plies were transparent enough to see the honeycomb structure. In addition, numerous cracks and delaminated regions were present on the inner side of the upper wing skin (Figure 3). Of these, the smaller delaminated regions corresponded to a crack on the outer surface. Another large delamination region in this section also corresponded to the sanded region on the outer surface. The section between the main spar and the aft spar contained only a few cracks with one large crack extending between the two spars. None of the cracks in this section corresponded to any on the outer surface.

No cracks were observed in the lower wing skin, however, there were two built up regions of plies and resin corresponding to two of the "repaired regions" on the outer surface.

The main spar was fabricated from a foam core with fiberglass plies on either side. Caps, consisting of unidirectional plies of fiberglass approximately 1 inch wide by 0.5 inch deep, were attached to the top and bottom of this spar. The rear spar consisted of a honeycomb core with fiberglass laminates on either side and attached to the upper and lower wing surfaces only using the fabric and resin. This was supported by a small brace of fabric and plies located in the center of the test article.

#### **PULSE ECHO**

The surface along the crack was analyzed using a hand held Pulse Echo instrument to determine the extent of delamination caused by the crack. Figure 4 shows the results of the examination. There appeared to be a fairly consistent delamination extending about 1 inch on either side of the crack. No non-destructive evaluation was performed on the inner surfaces because the cracks and delamination regions were visible through the transparent fabric plies and were noted in the preliminary observations.

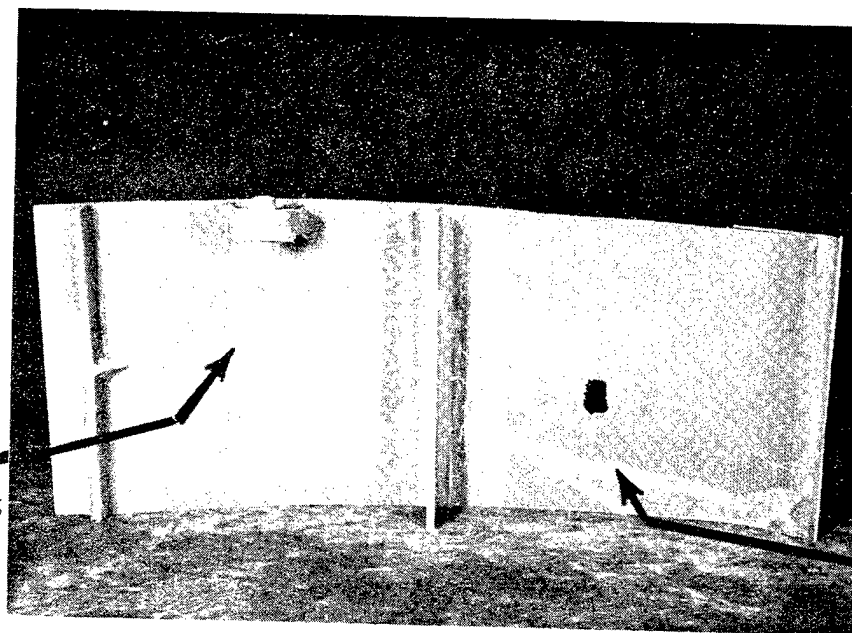
### **2.3 MATERIAL CHARACTERIZATION**

#### **Chemical Analysis**

A Fourier Transformation Infrared (FTIR) analysis, used for determining the formulation of polymers, was performed on a sample of the resin used in the skins and compared to a sample of a partially cured Rutapox resin. The analysis indicated that both samples were essentially identical, confirming that wing section was fabricated using the Rutapox resin system (Figure 5).

Differential Scanning Calorimetry (DSC) analysis was used to determine the extent of curing and the glass transition temperature (T<sub>g</sub>). A sample of un-cured epoxy resin was analyzed two times with an exothermic reaction occurring on the first pass. An exothermic reaction did not occur on the second pass but a T<sub>g</sub> of 112° C was observed. The next specimen from the wing section was also analyzed twice. No exotherms were

small delaminated  
region corresponding  
to the crack on the  
outer surface



large delaminated  
region corresponding  
to a sanded region  
on the outer surface

*Figure 3. Photograph of the Inner Surface of the Upper Wing Surface*

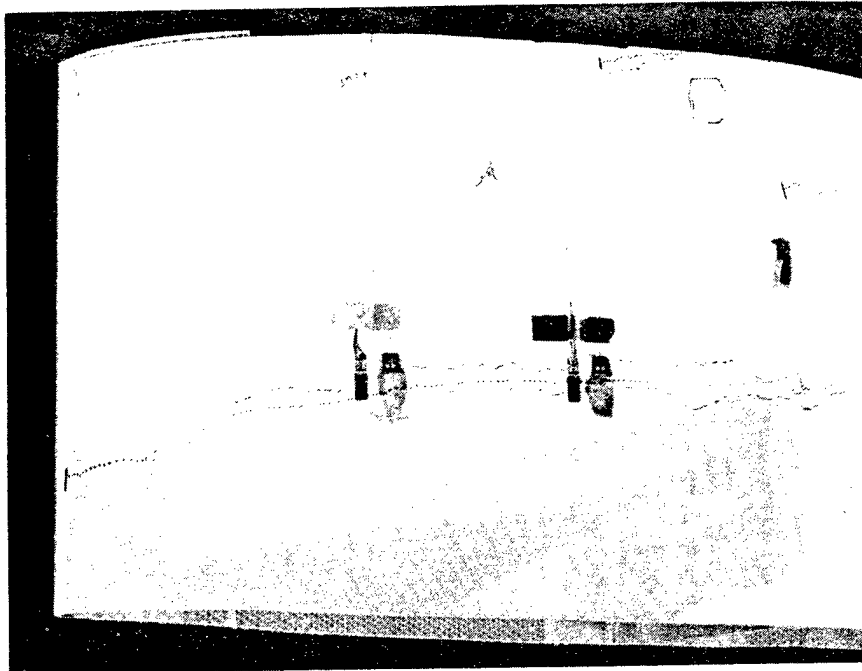


Figure 4. Photographs of the Pulse Echo Results. The long dashed lines delineate the extent of the delaminations

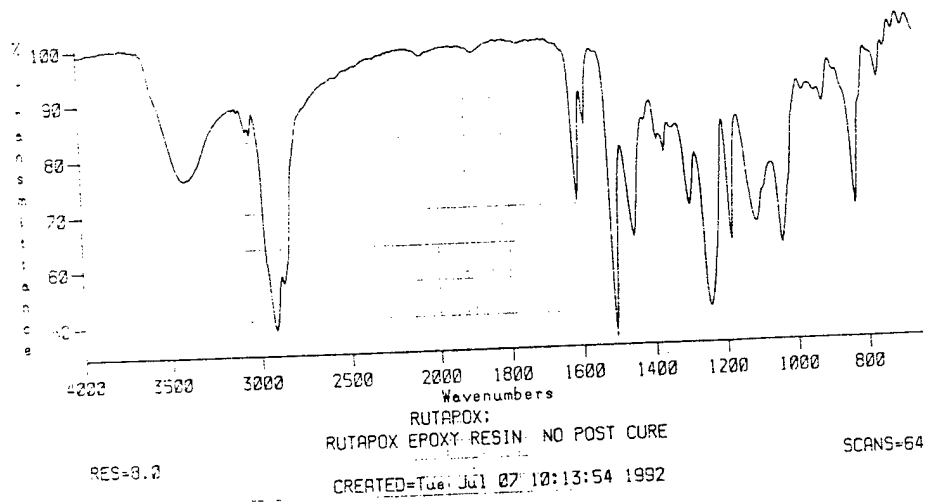
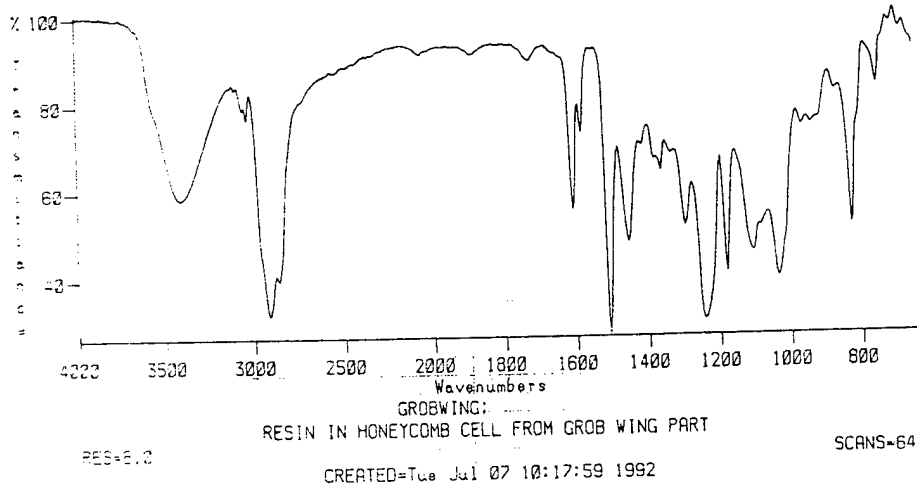


Figure 5. FTIR Plots of the Wing Section Specimen and the Rutapox  
 a) Wing Section Sample  
 b) Non-Post-Cured Rutapox Resin Sample

observed on either analyses and the Tg was 103° C and 115° C for the first and second tests respectively. This indicates that the resin in the wing section had been fully cured (Figure 6 & 7).

Thermo-mechanical Analysis (TMA) is another method to determine the Tg of a polymer. Again two specimens were tested; a non-post cured sample and a sample from the wing section. The first heat cycle of the non post-cured specimen revealed a definite Tg indication at 59°C. Testing of the resin from the wing revealed a Tg of 110°C and 107°C from the first and second runs, respectively. The difference between these two tests confirmed that the wing sample was fully cured because the Tg values were similar to the DSC analysis and that the uncured specimen exhibited a lower Tg and an exotherm. (Figure 8 & 9).

### **Microstructural Analysis**

The fiber volume of the composite sections in the honeycomb was determined to be approximately 43% by wt. using an acid digestion technique.

## **2.4 DESTRUCTIVE EXAMINATION**

Cross sectional analysis was performed on the specimens from two of the cracks on the upper wing skin (Figure 10 & 11). The outer and inner surface of the upper wing skin consisted of a layer of Gelcoat and two plies of fiberglass fabric, oriented in a 0/90 direction. The honeycomb core was attached to the plies by the same resin as the plies. The honeycomb core had a cell size approximately 3/16 inch from side to side.

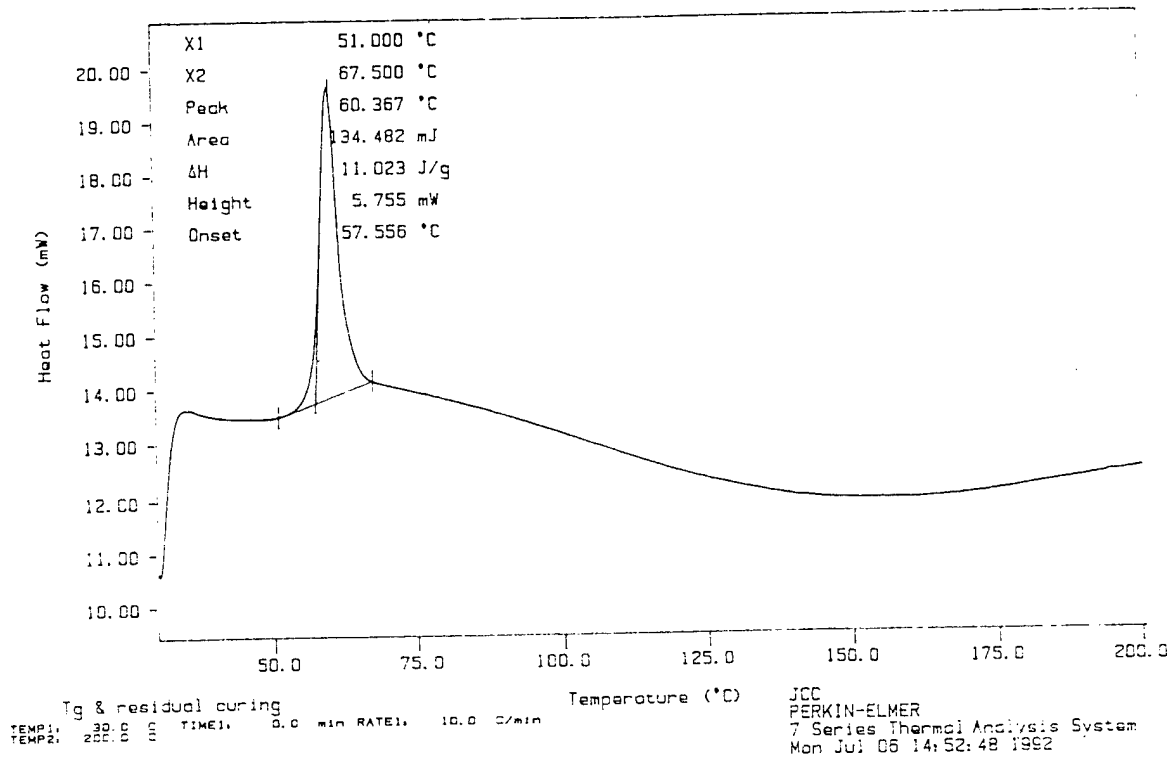
The cracked regions appeared to have been the result of a buckling of the upper skin. In some regions where a crack was present on both sides of the skin, the honeycomb core was fractured diagonally also consistent with a buckling load.

## **2.5 FRACTOGRAPHY**

Sections of the upper wing section containing the cracks were cut out for scanning electron microscopy (SEM). These sections were assumed to be representative of the crack along its length, three from the forward crack, three from the aft crack and one from the edge crack. After removing these samples from the wing skin, they remained intact and had to be further machined to expose the crack surfaces for examination. This was accomplished by cutting through the backside facesheet and the honeycomb of the specimens. On three of these sections, it was impossible to separate them without inducing further damage into the existing crack.

The two specimens that were able to be separated were coated with Au-Pd and examined using a SEM. The fracture surfaces were frayed with numerous loose fibers pulled from the crack surfaces (Figure 12). The fabric tows perpendicular to the crack direction were bent upward. Closer examination of these fiber ends revealed fractures consistent with compression failure, initiating at the bottom of the fibers. The dominate fracture

Curve 1: DSC  
 File info: rutal Mon Jul 06 14:37:17 1992  
 Sample Weight: 12.200 mg  
 Rutapox resin



Curve 1: DSC  
 File info: rhrutal Mon Jul 06 15:11:50 1992  
 Sample Weight: 12.200 mg  
 Rutapox heated to 200 C

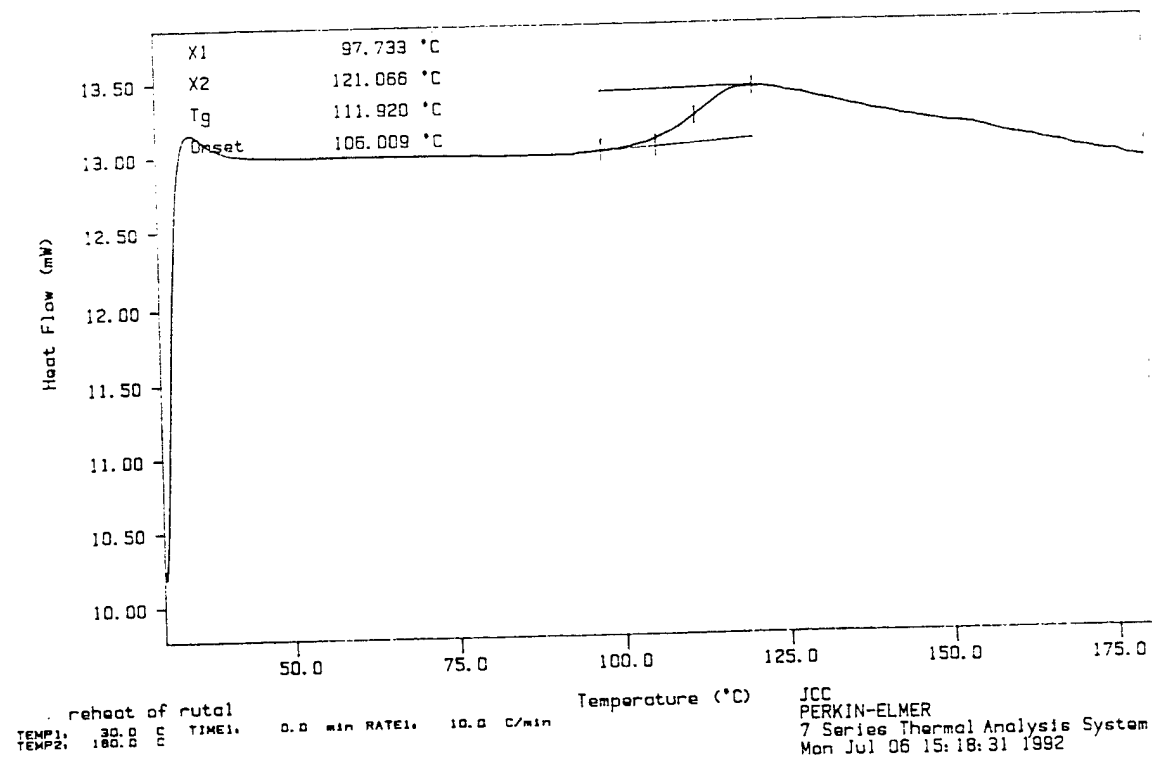
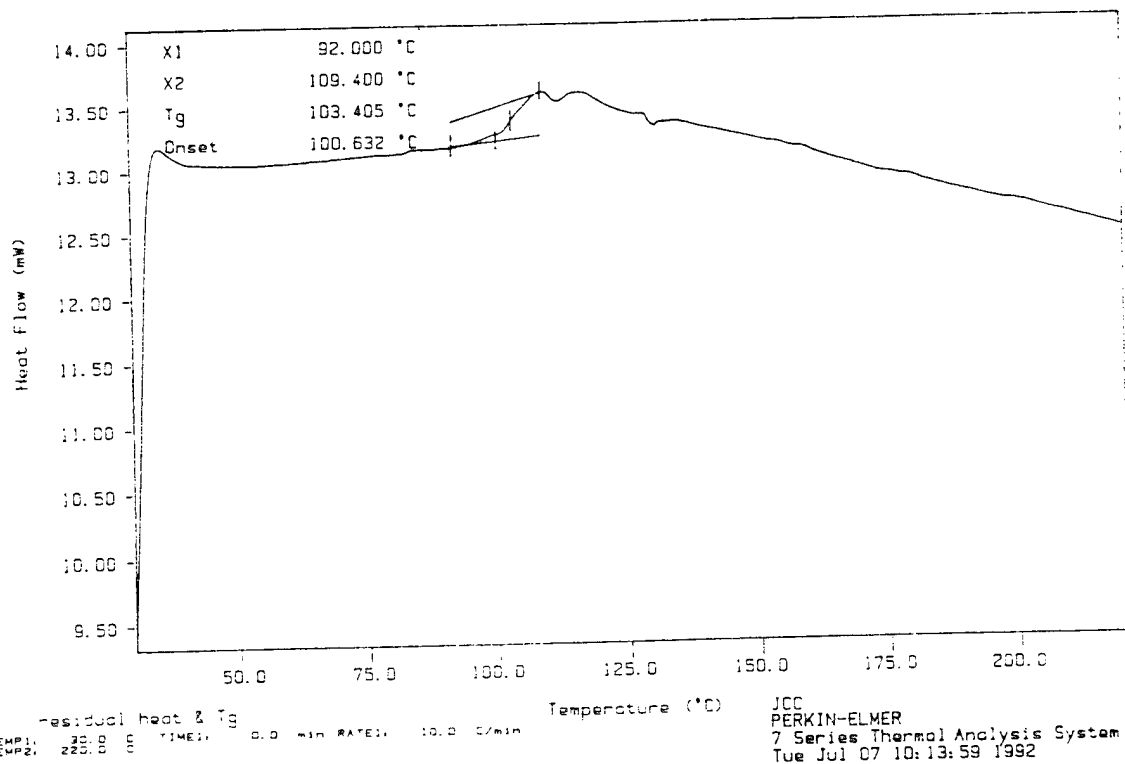


Figure 6. DSC Plots of the Non-Post-Cured Rutapox Sample



Curve 1: DSC  
 File info: grobl Tue Jul 07 10:01:59 1992  
 Sample Weight: 7.780 mg  
 resin fr. Grob wing section



Curve 1: DSC  
 File info: shgrob Tue Jul 07 10:34:02 1992  
 Sample Weight: 7.780 mg  
 resin fr. Grob wing section

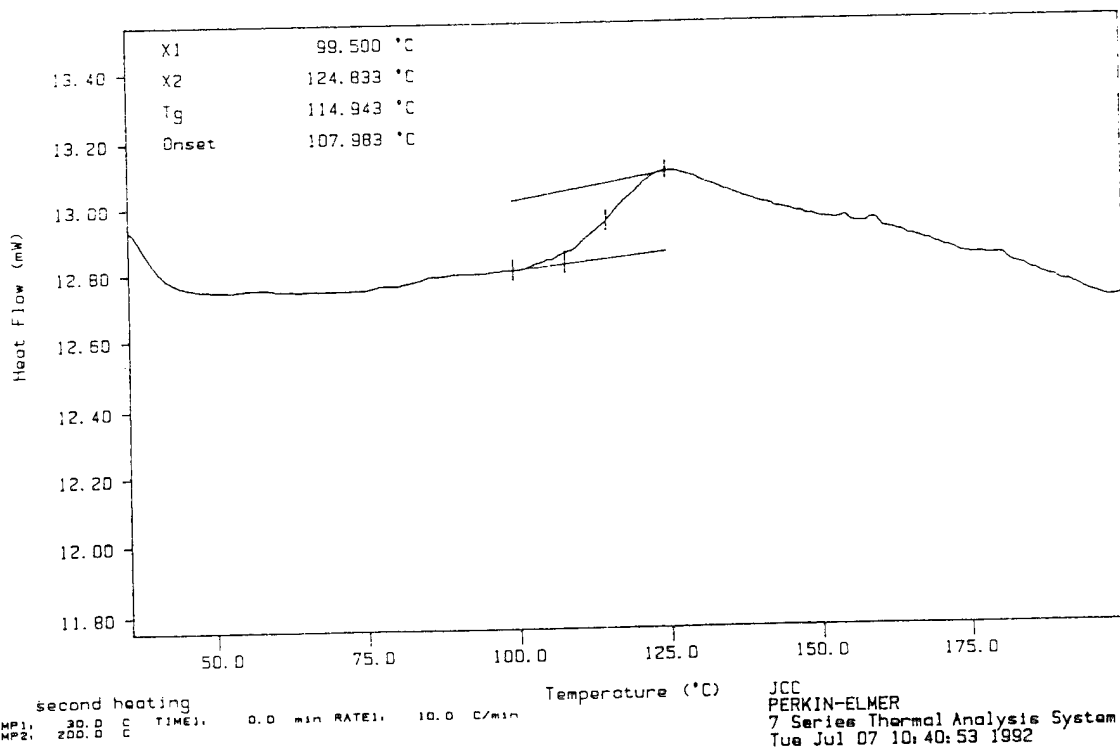
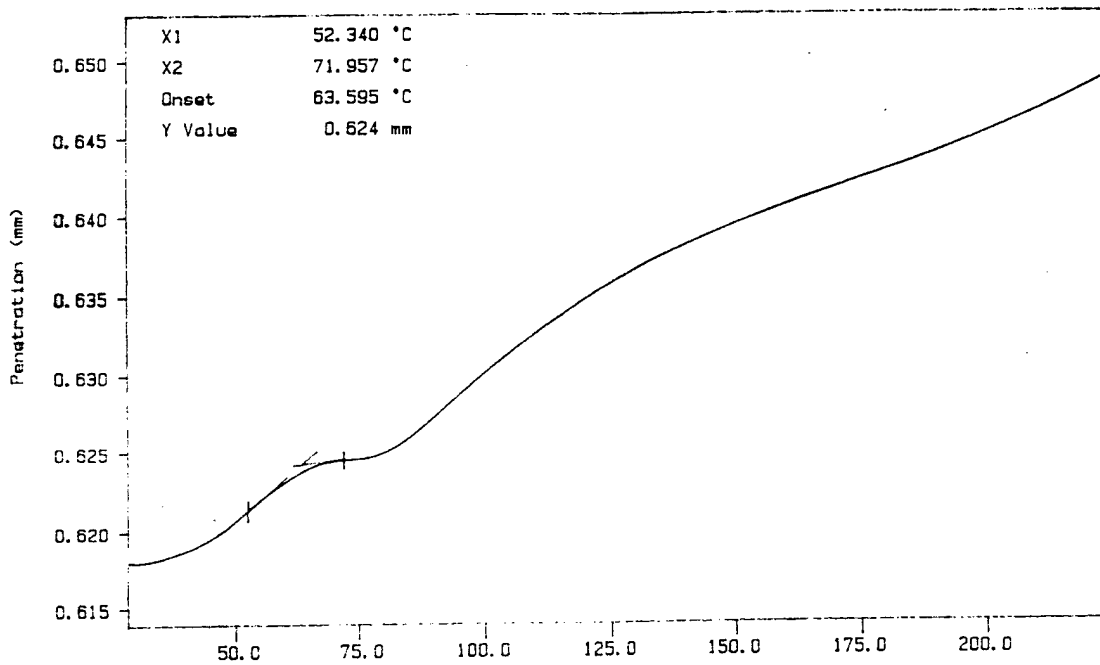


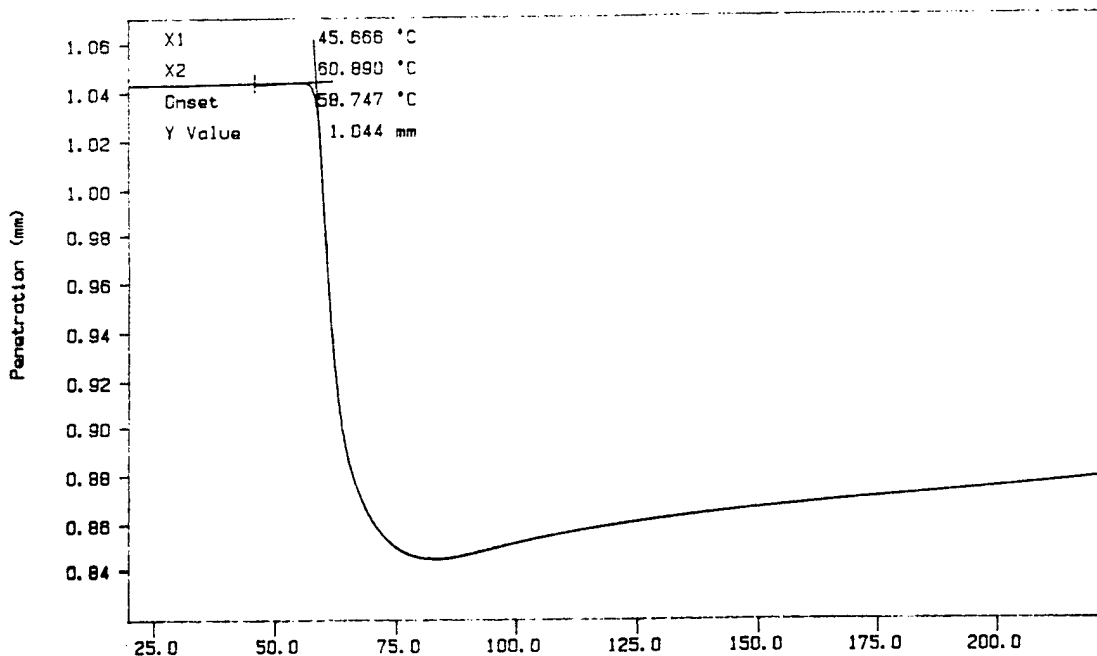
Figure 7. DSC Plots of the Wing Section Specimen

Curve 1: TMA in Penetration  
 File info: ruta2 Mon Jul 06 13:48:25 1992  
 Sample Height: 0.818 mm  
 Rutapox -No Post Cure



Tg Run 2  
 TEMP1: 30.0 °C TIME1: 0.0 min RATE1: 10.0 C/min  
 TEMP2: 225.0 °C  
 G Duschl  
 PERKIN-ELMER  
 7 Series Thermal Analysis System  
 Mon Jul 06 13:50:29 1992

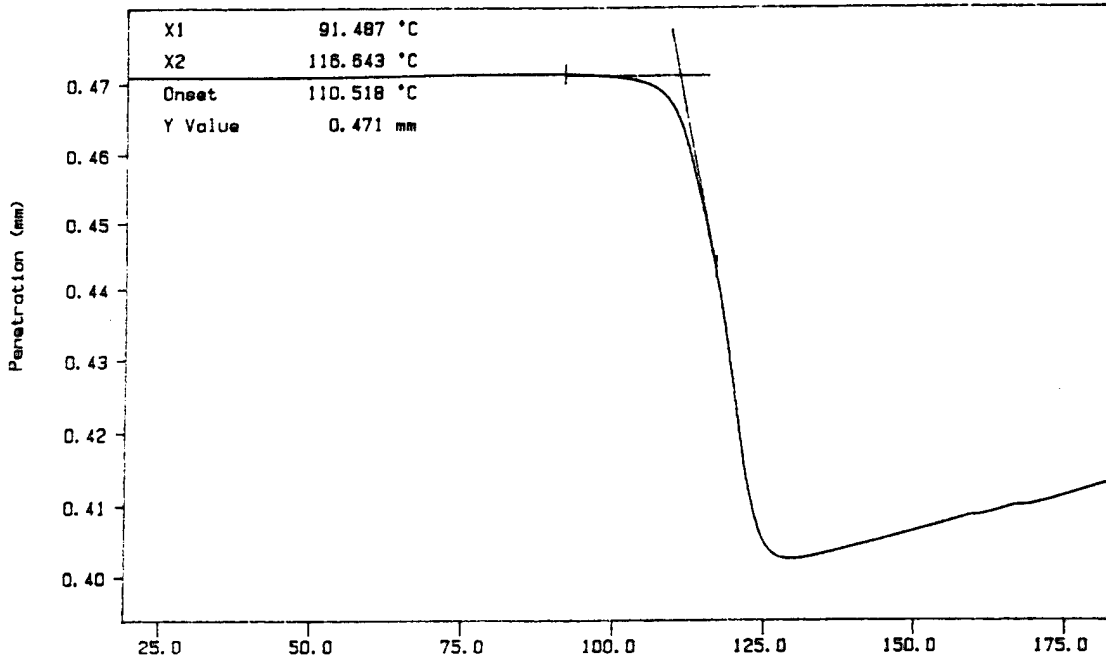
Curve 1: TMA in Penetration  
 File info: ruta1 Mon Jul 06 13:15:21 1992  
 Sample Height: 1.044 mm  
 Rutapox -No Post Cure



Tg Determination  
 TEMP1: 30.0 °C TIME1: 0.0 min RATE1: 10.0 C/min  
 TEMP2: 225.0 °C  
 G Duschl  
 PERKIN-ELMER  
 7 Series Thermal Analysis System  
 Mon Jul 06 13:53:45 1992

Figure 8. TMA Plots of the Non-Post-Cured Rutapox Sample

Curve 1: TMA in Penetration  
 File info: wing1 Mon Jul 06 14:39:18 1992  
 Sample Height: 0.819 mm  
 Grob Wing- Resin inside Cell

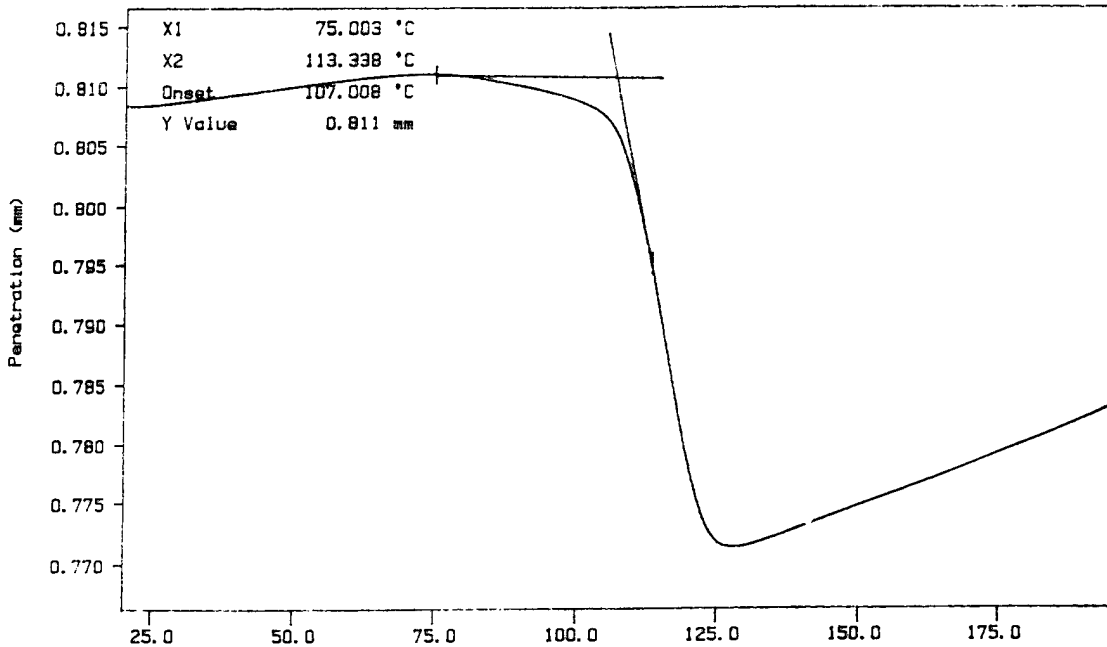


Tg determination  
 TEMP1: 20.0 °C TIME1: 0.0 min RATE1: 10.0 °C/min  
 TEMP2: 225.0 °C

Temperature (°C)

G Duschl  
 PERKIN-ELMER  
 7 Series Thermal Analysis System  
 Mon Jul 06 14:40:21 1992

Curve 1: TMA in Penetration  
 File info: wing2 Mon Jul 06 15:11:58 1992  
 Sample Height: 0.819 mm  
 Grob Wing- Resin inside Cell



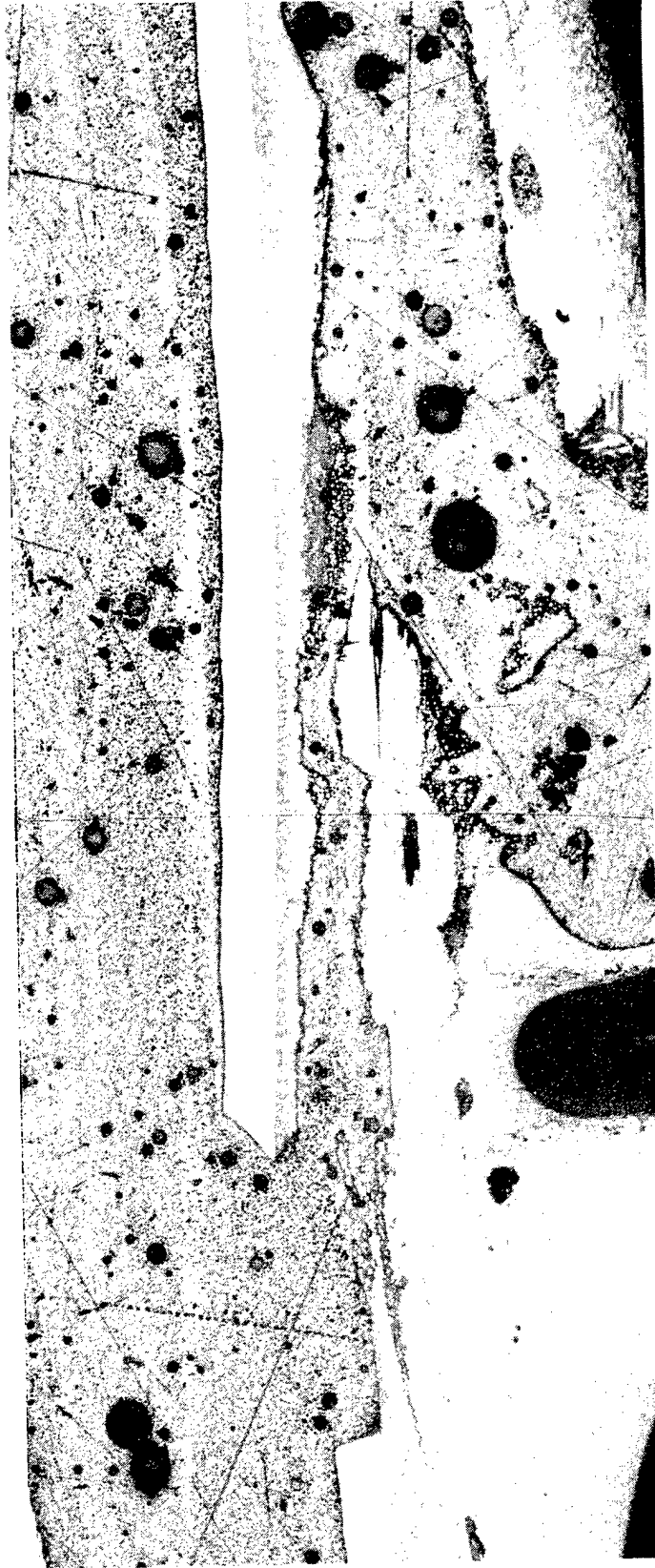
Tg determination  
 TEMP1: 20.0 °C TIME1: 0.0 min RATE1: 10.0 °C/min  
 TEMP2: 225.0 °C

Temperature (°C)

G Duschl  
 PERKIN-ELMER  
 7 Series Thermal Analysis System  
 Mon Jul 06 15:17:30 1992

Figure 9. TMA Plots of the Wing Section Specimen

Outer Surface



Honeycomb Side

Figure 10. Cross Section through a Crack in the Upper Wing Skin

Outer Surface



Honeycomb Side

Figure 11. Cross Section through a Crack in the Upper Wing Skin

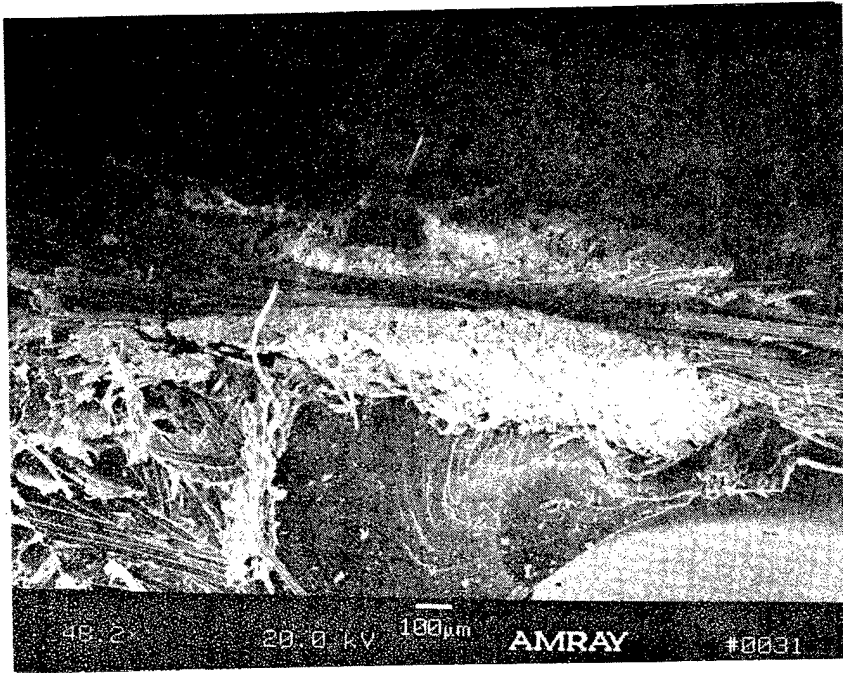


Figure 12. SEM Photographs of the Crack Surfaces

feature on the both the fibers parallel and perpendicular to the crack were the hackles indicating a mode II (shear) loading.

## 2.6 DISCUSSION

The fractures were most likely the result of a buckling of the upper skin that bent the edges upwards in relation the center of the wing section. This buckling was likely caused by either a general three point bending configuration or a longitudinal compression loading (Figure 13). In the case of the compression loading, it's assumed that the test grips or plates were removed prior to this investigation because no indication of crushed skin or honeycomb were seen on the edges.

However, the fact that no cracks or delaminations are present on the lower skin, the spars, or the leading edge is not consistent with either proposed loading configuration. All of these components would have been also subjected to some type of loading with the upper skin loading, but they did not suffer any damage. One possible explanation is that this wing section was loaded cyclically in bending or compression. This could initiate and propagate localized cracks before general cracking occurred throughout the part. On the other hand, no fracture features indicative of fatigue loading were observed along the crack. Examination of the disbond regions, on either side of the crack, might have found these features however it was not possible to access the surfaces without further damaging them.

## 3.0 CONCLUSIONS

1. The wing section contained two major cracks which extended from the leading edge of the wing to the aft edge. Another small crack was located at the edge, in the middle of the wing section. All of the cracks were on the upper wing skin.
2. Chemical analysis of the materials did not reveal any anomalies in the materials. No material or fabrication anomalies which could have contributed to crack initiation were found.
3. Cross-sectional and SEM analysis revealed the fractures were caused by buckling of the upper skin. The specific cause of the buckling could not be determined.

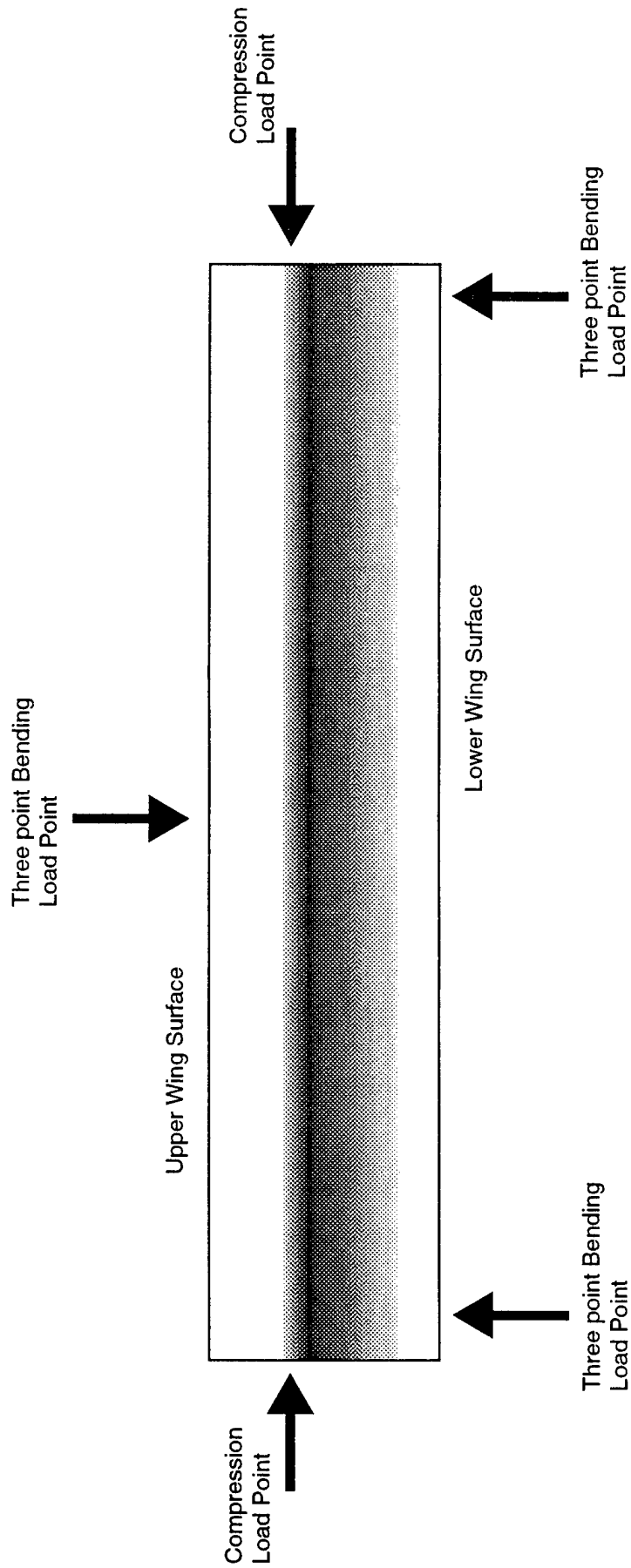


Figure 13. Diagram of the two Proposed Loading Configurations Which could Cause the Upper surface to Buckle